Imperial College
London

Imperial College
London

INVESTIGATION OF FLOW PARAMETERS IN RESIN TRANSFER MOULDING

Ngugi Kiuna

February 2003

Department of Chemical Engineering and Chemical Technology
Imperial College London
London SW7 2AZ

A thesis submitted in partial fulfillment of the requirements for the degree of Doctor of Philosophy of the University of London and for the Diploma of Membership of Imperial College

UNIV.

To Mum, Dad and Gachao. Love you always.

"The pure and simple truth is rarely pure and never simple."

-Oscar Wilde

ABSTRACT

Resin transfer moulding (RTM) is a production method used for the manufacture of continuous fibre-reinforced thermoset composites for aerospace, automotive, marine and civil applications. Production of large and thick composite structures is becoming increasingly essential, hence the simulation of composite processing is seen as a key design tool in the efforts to enhance efficiencies and improve product quality. This thesis addresses some of the key flow parameters in the resin transfer moulding process. The flow parameters studied are; resin viscosity, curing behaviour, flow front progression and micro scale flow filling properties.

Rheological characterisation studies were performed on typical RTM resins as very little information exists on these systems. In addition to the characterisation studies, a model has been proposed for the advancement of the rheology during cure. This model is based on viscosity-time experimental measurements taken at constant temperature. The key advantage of this model compared with most other proposed models is that it is not explicitly dependent on the extent of cure.

Velocity field analysis studies were conducted by micro-scale simulation of the influx of resin into the mould by visualising flow through a Perspex cell with a hexagonal arrangement of rods. A model fluid whose refractive index was matched with the Perspex was used in this study. The local velocity fields were analysed by taking images of the fluid flow seeded with aluminium dust. Micro-scale flow front tracking experiments were conducted using the Perspex flow cell in order to characterise the shape of the flow front during filling in RTM.

Finally, experiments were conducted using the *SMARTweave* flow monitoring system to determine the progression of the flow front for different fibre fill scenarios. The experiments were carried out on an industrial scale mould at QinetiQ[a].

[aa] *QinetiQ*, Cody Technology Park, Farnborough, Hampshire, GU14 OLX, UK

ACKNOWLEDGEMENTS

First and foremost I would like to express my deepest gratitude to my three principal supervisors, Professor Chris Lawrence, Dr Peter Lee and Dr Thomas Selerland. Your guidance, support, encouragement and friendship throughout this whole project are deeply cherished. I am forever indebted to you for all your efforts in making this project a success.

I would also like to extend my gratitude to Dr Peter Spelt who played an integral part in this project and for his timeless assistance whenever required. Also, Stuart McCallum with whom I spent many hours carrying out the industrial phase of this research. I am also grateful to Joanna Woods and Krios Yeung for their assistance in conducting some of the experimental work.

This project would not have been possible without the financial and technical support of the Industrial affiliates, namely, QinetiQ, BAE Systems, Dowty Aerospace Propellers, Vosper Thornycroft and AEA Technology. Many thanks to them for their assistance throughout the entirety of this work. I am also grateful for the financial assistance offered by Universities UK through the Overseas Research Studentship award.

My thanks also go to all the academic, administrative and technical support staff in both the Departments of Chemical Engineering and Materials Engineering.

I'm grateful to my parents and my brother for all their support, love and understanding throughout the years that I've been away from home. Thank you and I dedicate this to you.

Last but not least I would like to thank all my friends, both past and present, who have meant so much to me during my time at Imperial. Wailid, Flo, Pris, Colin, Tzuu, Mike, Tahsin, Bin, Lan, Tony and so many others that I couldn't possibly list them all. Thanks to all of you and I'd like to take this opportunity to wish you all the best in your future endeavours.

TABLE OF CONTENTS

ABSTRACT.....1

ACKNOWLEDGEMENTS.....3

TABLE OF CONTENTS.....5

LIST OF FIGURES.....12

LIST OF TABLES.....30

NOMENCLATURE.....32

1. INTRODUCTION.....35

References.....39

2. BACKGROUND.....41

2.1. Permeability Measurement.....41

2.1.1. Aligned and Continuous Fibre Bundles.....44

2.1.2. Woven and Cross-Ply Fibrous Structures.....47

2.1.3. Random and Stitched Fibre Mats.....49

2.1.4. Capillary Pressure.....50

2.1.5. Summary.....51

2.2. Permeability Experiments.....52

2.2.1. Parallel Flow Experiments.....54

2.2.2. Radial Flow Experiments.....55

2.2.3. Permeability Measurement Through Several Layers.....55

2.3. Numerical Methods.....56

2.3.1. Circular Cylinders.....56

2.3.2. Ellipsoid Shaped Tows.....60

2.4. Flow Phenomena.....63

2.4.1. Void Formation.....64

2.4.2. Race-Tracking.....65

2.5. Preform Compression.....67

2.6. Fibre Wetting.....69

2.7. Computational Simulations.....71

2.7.1. Simulations of Flow Transverse to Circular Cylinders.....71

2.7.2. Flow Simulations for Other Geometries.....76

2.7.3. Flow through an Array of Rectangular Fibres.....79

2.8. Summary.....80

2.9. References.....81

3. EXPERIMENTAL DESIGN.....90

3.1.1. Rheological Measurements.....90

3.1.2. Resin Systems.....90

3.1.3. Rheometers.....91

3.2. The Flow Cell.....92

3.2.1. Velocity Profile Consideration.....92

3.2.2. Fibre Volume Fraction (V_f).....95

3.2.3. Pressure Drop in the Flow Cell.....95

3.2.4. Particle Image Velocimetry.....98

3.2.5. Flow Front Tracking.....101

3.3. Semi Industrial Scale RTM.....102

3.3.1. RTM Moulds.....102

3.3.2. Processing of Liquid and Injection Process.....105

3.3.3. Fabric Material.....106

3.3.4. Dielectric Analysis.....108

3.3.5. *SMARTweave*.....110

3.4. Summary.....117

3.5. References.....118

4. RHEOLOGY AND CURE MODELLING OF RESIN SYSTEMS.....119

4.1. Introduction.....119

4.1.1. Kinetic Analysis.....119

4.1.2. Chemoviscosity.....120

4.1.3. Gel Effects.....121

4.1.4. Cure Modelling.....121

4.2. Rheology.....124

4.2.1. Shear Stress Ramp Results.....125

4.2.2. Shear Rate Ramp Results.....126

4.2.3. Oscillatory Stress Sweep.....126

4.2.4. Frequency Sweep.....127

4.2.5. Strain Amplitude Sweep.....128

4.2.6. Shear Rate Ramp – Forward and Reverse.....129

4.2.7. Discussion.....129

4.3. Proposed Viscosity Model.....130

4.3.1. Model.....130

4.3.2. Isothermal Experiments.....131

4.3.3. Simple Exponential Fits.....134

4.3.4. Non-isothermal Experiments.....135

4.3.5. Higher Order Fits.....138

4.4. Summary.....140

4.5. References.....141

5. ANALYSIS OF FLOW IN FULLY SATURATED MEDIA.....144

5.1. Introduction.....144

5.1.1. The Use of PIV and Other Fluid Flow Analysis Techniques.144

5.1.2. Accuracy of PIV and Image Analysis.....147

5.2. Numerical Model.....148

5.3. Error Analysis.....150

5.4. Results and Discussion.....151

5.4.1. Redistributed Data Points.....156

5.4.2. Contour Plots.....160

5.4.3. Comparison with Numerical Simulation Results.....169

5.5. Summary.....172

5.6. References.....173

6. FLOW FRONT TRACKING.....174

6.1. Fundamentals of Flow Modelling.....174

6.1.1. Surface Tension and Contact Angle.....175

6.2. Contact Angle Measurement.....178

6.3. Surface Tension Measurement.....181

6.4. Flow Front Tracking for a Hexagonal Array of Cylinders – Results.182

6.5. Comparison with Numerical Simulation Results.....190

6.6. Summary.....192

6.7. References.....193

7. SEMI INDUSTRIAL SCALE RTM.....195

7.1. Introduction.....195

7.2. Background.....197

7.3. Experiments.....197

7.4. Error Analysis.....199

7.5. Results.....200

7.5.1. Run 1.....203

7.5.2. Run 2.....207

7.5.3. Run 3.....208

7.5.4. Run 4.....210

7.5.5. Run 5.....211

7.5.6. Run 6.....212

7.5.7. Run 7.....213

7.5.8. Run 8.....214

7.5.9. Run 9.....218

7.5.10. Run 10.....222

7.6. Estimation of the Permeability Measurement.....223

7.7. Discussion.....228

7.7.1. Effect of Variations in Preform Properties.....229

7.7.2. Influence of orientation of the Tool.....231

7.8. Dielectric Cure Monitoring.....232

7.9. Summary.....236

7.10. References.....236

8. CONCLUSIONS AND RECOMMENDATIONS FOR FUTURE WORK.....238

8.1. Summary.....238

8.2. Future Work.....241

8.3. References.....242

LIST OF FIGURES

1. INTRODUCTION

Figure 1.1 – Schematic diagram showing the principal steps of the RTM process[4]…36

2. BACKGROUND

Figure 2.1 – Cross-section of a unidirectional laminate on a micro-scale showing the variation in fibre diameter……42

Figure 2.2 – Cross-section of a unidirectional laminate on an intermediate scale[1]…..42

Figure 2.3 - Optical microscope image of a resin transfer moulded sample with unidirectional layers……44

Figure 2.4 – Optical microscope image of resin transfer moulded sample with woven fabric……47

Figure 2.5 – Schematic diagram of Radial flow (on the left) and Parallel flow (on the right) experiments used to determine the permeability of fibre preform (for process description see sections 2.2.1 and 2.2.2)……..52

Figure 2.6 - Computed results (shown by solid line) of Sangani et al.[53] compared with numerical results from [2.21] (dashed line) and [2.22] (dashed/dotted line).....58

Figure 2.7 - Comparison of hybrid model results and computationally simulated results obtained by Bruschke et al.[3] for Newtonian (n=1) and power-law (n=0.5) fluids.....59

Figure 2.8 - Sketch of square fibre array in a unidirectional reinforcement where R is the rod radius, D is the rod spacing and L is the length/width of the unit cell[55].....60

Figure 2.9 - The general configuration of a grating of elliptic cylinders used by Kuwabara[59] to calculate drag and lift coefficients.....62

Figure 2.10 - Variation of C_D (drag coefficient) and C_L (lift coefficient) with b when h=10, a=p/2 and Re=0.4 and 1.0 obtained by Kuwabara[59] using a method proposed by Imai.....62

Figure 2.11 - Schematic diagram of an elliptical tow giving parameters used by Phelan and Wise[60] for lubrication analysis of cross flow.....63

Figure 2.12 – Diagram showing the progression of the flow front both within and between fibre tows[69].....65

Figure 2.13 – Typical development of a liquid drop wetting a porous media[98].....70

Figure 2.14 - Square (top) and hexagonal (bottom) unit cells used by Bruschke and Advani[3] in their computer simulations.....72

Figure 2.15 - Mesh used by Nagelhout et al.[99] to simulate fluid flow perpendicular to cylinders in sparse arrays.....73

Figure 2.16 - Velocity vector diagram[99] (a) and pressure contour diagram (b) for numerical simulation of flow normal to circular cylinders in a square array where *Re* = 5 and g_L = 0.99.....73

Figure 2.17 - Finite element mesh (left) used by Edwards et al. and pressure contour map (right) obtained for a square array of cylinders[100].....74

Figure 2.18 - Computed particle trajectories (streamlines) in a unit cell for an impermeable tow (a) and a bundle of 61 fibres (b) where the intra-tow porosity is 60% in both cases and fluid flow is from left to right[101].....75

Figure 2.19 - Change in pressure per unit length ($\Delta P/L$) obtained by Epstein and Masliyah[102] at various orientation ratios (*O.R.*) for creeping flow perpendicular to elliptical cylinders with solid volume fraction *c*.....76

Figure 2.20 - Rows of elliptical cylinders used by Epstein and Masliyah[102] to form a square array of pitch *h*.....76

Figure 2.21 - Comparison of total drag coefficient, C_{DT}, calculated for elliptical cylinders by the zero vorticity cell model and by the isolated-rows-in-series model for creeping flow[102]. *O.R.* is the orientation ratio and *c* is the solid concentration.....77

Figure 2.22 - Streamlines obtained by Larson and Higdon[103] for flow through a square array of elliptical cylinders with area fraction 0.3.....77

Figure 2.23 - Normalised principal permeabilities k_1 and k_2 for elliptical inclusions of aspect ratio (a/b) for different lattice geometries at two concentrations, c. From Larson and Higdon[103,104].....78

Figure 2.24 - Geometry (left) and partition into two regions (right) used by Wang[106] to examine Stokes flow through an array of rectangular fibres.....80

Figure 2.25 - Normalized drag D as a function of solid fraction e for square fibres in a square array obtained by Wang[106] (solid line) compared with values obtained by Sangani and Acrivos[53] for circular cylinders in a square array (dashed line).....80

3. EXPERIMENTAL DESIGN

Figure 3.1 – The geometry of the gap between rods in the flow cell.....93

Figure 3.2 - Graph of variation of dimensionless velocity with $\hat{y}$ at constant $\hat{x} = 0.5$ for aspect ratio $b/a = 2,3,4,5$.....94

Figure 3.3 – Full velocity profile for aspect ratio $b/a = 5$.....94

Figure 3.4 - The triangular unit cell in the hexagonal arrangement of rods.....95

Figure 3.5 – Geometry of the flow cell used for pressure drop calculation.....96

Figure 3.6 - Final design of the flow cell (dimensions in mm).....97

Figure 3.7 – General set-up of PIV Experiment.....98

Figure 3.8 - Schematic diagram of the experimental set-up for flow front tracking..101

Figure 3.9 - Detailed drawing of the RTM mould used in the dielectric cure monitoring studies. The mould thickness is 4mm and has a length and width of 300mm. The single injection port is seen on the right-hand side of the drawing and the three vent ports are on the left-hand side.....103

Figure 3.10 – Detailed drawing of the RTM mould used in the *SMARTweave* studies. The mould thickness is 30mm and has a length and width of 400mm. The single injection port is seen on the right-hand side of the drawing and the three vent ports are on the left-hand side.....104

Figure 3.11 – The Isojet RTM injection pot used to pump the liquid into the mould.....105

Figure 3.12 - Glass fibre spool stack.....106

Figure 3.13 - Liba weaving machine used in the manufacture of the unidirectional glass fabric used in the experiments.....107

Figure 3.14 – Image of the unidirectional glass fabric material (724g/m^2 ET-760)°.....107

Figure 3.15 - Cutting table used to cut the glass fabric sheet to the mould dimensions of 400mm by 400mm. This was performed at Dowty Aerospace Propellers, Gloucester, GL2 9QL, UK.....108

Figure 3.16 – An IDEX dielectric sensor.....110

Figure 3.17 - Sensing gap between excitation and sensing lines.....111

Figure 3.18 - Sensing grid.....112

Figure 3.19 - Through-thickness sensor positioning for case 1.....113

Figure 3.20 – Schematic showing the sensor positioning in each plane for experiments where three planes were used to monitor the flow. All lengths shown are dimensionless because the X and Y variables changed for different experiments depending on the dimensions of the fabric used.....114

Figure 3.21 – Schematic of the sensor positioning in each plane for experiments where five planes were used to monitor the flow. All the fabric dimensions in this case were 360mm×360mm.....115

Figure 3.22 - Voltage-time history for Derakane 411-C50.....116

4. RHEOLOGY AND CURE MODELLING OF RESIN SYSTEMS

Figure 4.1 - Time temperature transformation diagram (*TTT*) (from Halley and Mackay[9]).....121

Figure 4.2 - RTMLY5052/HY5052 Shear Stress Ramp at 30°C from 1-100Pa for 20pts at 1min/pt.....125

Figure 4.3 - RTMLY5052/HY5052 Shear rate ramp at 30°C from 0.1/s to 200/s for 30pts at 1min/pt.....126

Figure 4.4 - RTMLY5052/HY5052 Oscillatory Stress Sweep, Frequency 1Hz.....126

Figure 4.5 - RTMLY5052/HY5052 Frequency Sweep from 0.01-10Hz at Oscillatory Stress Amplitude of 3Pa.....127

Figure 4.6 - RTMLY5052/HY5052 Strain amplitude sweep from 0.02 to 10 at 0.1Hz and 30°C for 20pts.....128

Figure 4.7 - RTMLY5052/HY5052 Strain amplitude sweep from 0.02 to 10 at 10Hz and 30°C for 20pts.....128

Figure 4.8 - Shear rate ramp from 0.03/s - 10/s at 1min/pt for 20pts at 30°C.....129

Figure 4.9 - Isothermal viscosity-time curves for LY5052/HY5052 at constant shear rate of 5/s for different temperatures.....132

Figure 4.10 - Master Curve for LY5052/HY5052. Dimensionless viscosity against dimensionless time. Isothermal data for several temperatures in the range 20°C – 70°C are shown.....133

Figure 4.11 - Arrhenius plot of initial viscosity, η_0, and rate constant, k, for LY5052/HY5052.....133

Figure 4.12 - Viscosity-time curves for LY5052/HY5052, for constant shear rate of 5/s at 35°C and 40°C.....135

Figure 4.13 - Temperature step change from 20-60°C after 4000s for LY5052/HY5052.....136

Figure 4.14 - Temperature step change from 40-30°C after 1500s for LY5052/HY5052.....136

Figure 4.15 - Modified temperature profiles for Figures 4.13 and 4.14 incorporating time lags between the plate temperature (Expt.) and the fluid sample temperature (Model).....137

Figure 4.16 - Comparison of experiment with current model and with Lee and Hahn[24] method for a complex temperature profile simulating a typical processing cycle for PR500.....138

Figure 4.17 - Temperature step change from 40-30°C after 1500s comparing linear and third order fits (LY5052/HY5052).....139

Figure 4.18 - Comparison of exponential model with linear fit for isothermal (25°C) data for Derakane Momentum 411-C50.....140

5. ANALYSIS OF FLOW IN FULLY SATURATED MEDIA

Figure 5.1 - Schematic of a typical particle image velocimetry set-up[2].....145

Figure 5.2 - Schematic of the experimental set-up using volume illumination with particle image velocimetry[4].....146

Figure 5.3 - The laser induced fluorescence technique and particle image velocimetry technique.....147

Figure 5.4 - Image shift in particle image velocimetry and calibration picture used to reduce this effect.....148

Figure 5.5 - Image of particle streaks in the flow cell for a shutter speed of 1s and fluid volumetric flow rate of 16cm^3/s (the cylinder diameter is 16mm).....152

Figure 5.6 - Unit cell used to normalise the raw experimental data by rotating the original image, shifting the origin and rescaling the image size.....153

Figure 5.7 – Particle streaks of Aluminium dust showing the velocity field of the liquid flowing through a hexagonal array of cylinders (global volumetric flow rate of 9.4cm^3/s).....154

Figure 5.8 - Particle streaks of Aluminium dust showing the velocity field of the liquid flowing through a hexagonal array of cylinders (global volumetric flow rate of 13cm^3/s).....155

Figure 5.9 - Particle streaks of Aluminium dust showing the velocity field of the liquid flowing through a hexagonal array of cylinders (global volumetric flow rate of 16cm^3/s).....156

Figure 5.10 – Schematic diagram showing each of the four quadrants used in the redistribution of data points.....157

Figure 5.11 - Particle traces mapped to one-quarter of the unit cell (global flow rate of 9.4cm^3/s).....157

Figure 5.12 - Particle traces mapped to one-quarter of the unit cell (global flow rate of 13cm^3/s).....158

Figure 5.13 - Particle traces mapped to one-quarter of the unit cell (global flow rate of 16cm^3/s).....159

Figure 5.14 – Contour plot of the velocity field within the unit cell for a global volumetric flow rate of 9.4cm^3/s. The black arrows indicate the velocity vectors for each data point.....160

Figure 5.15 - Contour plot of the velocity field within the unit cell for a global volumetric flow rate of 13cm^3/s. The black arrows indicate the velocity vectors for each data point.....162

Figure 5.16 - Contour plot of the velocity field within the unit cell for a global volumetric flow rate of 16cm^3/s. The black arrows indicate the velocity vectors for each data point.....163

Figure 5.17 – Contour plot of the velocity field for a condensed data set at a global volumetric flow rate of 9.4cm^3/s. Each data point is plotted in all four quadrants of the unit cell.....164

Figure 5.18 - Contour plot of the velocity field for a condensed data set at a global volumetric flow rate of 13cm^3/s. Each data point is plotted in all four quadrants of the unit cell.....165

Figure 5.19 - Contour plot of the velocity field for a condensed data set at a global volumetric flow rate of 16cm^3/s. Each data point is plotted in all four quadrants of the unit cell.....166

Figure 5.20 - Contour plot of the velocity field for a combined data set at all of the respective flow rates, 9.4cm^3/s, 13cm^3/s and 16cm^3/s.....167

Figure 5.21 - Contour plot of the velocity field for a combined data set at all of the respective flow rates, 9.4cm^3/s, 13cm^3/s and 16cm^3/s. In this case a no-slip boundary condition is applied around the cylinder walls.....168

Figure 5.22 – Contour plot of the velocity field produced by the numerical simulation code1 for the flow of a Newtonian fluid through a hexagonal array of cylinders at a volume fraction of 58%. The black arrows indicate the velocity vectors.....170

Figure 5.23 – Comparison of the contour plot of the velocity field produced by the numerical simulation code[1] on the left and the experimental result of the velocity field within the flow cell on the right.....171

6. FLOW FRONT TRACKING

Figure 6.1 – Stages in the wetting-out of an array of cylinders by capillary flow due to surface tension (t is time).....176

Figure 6.2 - Images of the behaviour of the flow front during filling.....177

Figure 6.3 - Schematic diagram of flow front tracking set-up.....178

Figure 6.4 – Illustration of the image analysis technique showing the position of the glycerine droplet relative to the Perspex surface in *x*-*y* coordinates.....179

Figures 6.5 – Glycerine droplet on a flat (a) and inclined (b) Perspex surface.....180

Figure 6.6 – Surface free energy of Derakane 411–C50[a].....181

Figure 6.7 - Overall image of the flow front passing through a hexagonal array.....183

Figure 6.8(a-j) - Sequence of images of the progressing flow front at a superficial velocity of 0.45cm/s and a frame rate of 0.2s/frame.....185

Figure 6.9 – Close-up of image sequences in Figure 6.8 from 0.4s to 1s showing more clearly the shape of the flow front.....186

Figure 6.10(a-c) - Flow front profiles for 3 different superficial velocities (a = 0.63cm/s, b = 0.45cm/s and c = 0.28cm/s).....187

Figure 6.11 - Graph showing the average contact angle vs. the surface distance of cylinder.....189

Figure 6.12 - Graph showing the contact angle vs. the contact line speed for each point (U_{cl}).....190

Figure 6.13 - Flow front tracking simulation result from Spelt et al.[10] showing the shape of the flow front at different times as it progresses through the gap between two cylinders. Creeping flow simulation through a periodic square array of cylinders. The volume fraction is 0.3, the Capillary Number is large (i.e. weak surface tension

effects), the gas density is 0.1 of the liquid density, the gas viscosity is 0.01 of the liquid viscosity.....191

Figure 6.14 – Experimentally determined positions for the flow front at different times for flow between two cylinders within a hexagonal cylindrical array with a volume fraction of 58% (Superficial velocity = 0.63cm/s, $Re_{superficial}$ = 1).....192

7. SEMI INDUSTRIAL SCALE RTM

Figure 7.1 - Fabric lay-up in tool, showing the *X* and *Y* coordinates relative to the main flow direction. The fibres are parallel to the fill direction. The transverse lines are the stitching.....200

Figure 7.2 - *SMARTweave* wiring inside the mould. The *Y* coordinate wires run from right to left and *X* coordinate wires run from the front of the picture to the back. The wires were stitched into the fabric and taped at each end. One layer of fabric was used to separate the *X,Y* coordinate wires.....201

Figure 7.3 - Voltage history for run 1 at X_1 and increasing *Y*. The voltage rises sharply from 0V to 9.8V when liquid contact is made at each node.....202

Figure 7.4 - Voltage histories for run 1 at constant Y_3 and all values of *X*. A variation in the nodal contact time is observed indicating that the flow front profile is not flat.....203

Figure 7.5 – Schematic diagram showing nodal positions within the mould. The symbols, ♦, on the left-hand side of the mould denote nodes that are reflections of the ones indicated by ■ on the right-hand side. The length scale is dimensionless and can thus be applied to the corresponding fabric dimensions (360mm or 330mm).....204

Figure 7.6 - Position-time data for run 1. Parallel flow with a fibre volume fraction of 43% and 3 sensing planes.....205

Figure 7.7 - Position Y versus flow front arrival time at each node in each plane for X_2 in Run 1. Parallel flow with a fibre volume fraction of 43%.....206

Figure 7.8 - Flow front profile for run 1. Interpolated times i) 70s, ii) 150s, iii) 250s, iv) 400s and v) 550s. Parallel flow with a fibre volume fraction of 43%. Vertical filling.....207

Figure 7.9 - Flow front profile for run 2. Interpolated times i) 65s, ii) 140s, iii) 230s, iv) 330s and v) 450s. Parallel flow with a fibre volume fraction of 49%. Vertical filling.....208

Figure 7.10 - Flow front profile for run 3. Interpolated times i) 60s, ii) 150s, iii) 250s, iv) 450s and v) 600s. Parallel flow with a fibre volume fraction of 55%. Vertical filling.....209

Figure 7.11 - Flow front profile for run 4. Interpolated times i) 80s, ii) 150s, iii) 220s, iv) 280s and v) 320s. Transverse flow with a fibre volume fraction of 43%. Vertical filling.....210

Figure 7.12 - Flow front profile for run 5. Interpolated times i) 150s, ii) 330s, iii) 610s and iv) 900s and v)1340s. Transverse flow with a fibre volume fraction of 43%. Vertical filling.....212

Figure 7.13 - Flow front profile for run 6. Interpolated times i) 160s, ii) 600s, iii) 1000s, iv) 1400s and v) 1800s. Transverse flow with a fibre volume fraction of 55%. Vertical filling. The symmetric nodes at time (v) are indicated by open symbols O for clarity.....213

Figure 7.14 - Flow front profile for run 7. Interpolated times i) 90s, ii) 190s, iii) 290s, iv) 400s and v) 500s. Transverse flow with a fibre volume fraction of 43%. Horizontal filling.....214

Figure 7.15 – Schematic diagram showing nodal positions within the mould for runs 8 and 9.....215

Figure 7.16 - Flow front profile for run 8. Interpolated times i) 85s, ii) 165s and iii) 255s. Fibre lay-up sequence of [0°, 0°, 90°] with a volume fraction of 43%. Vertical filling.....216

Figure 7.17 - Through-thickness front profile for run 8 at X_2, Y_2. Fibre lay-up sequence of [0°, 0°, 90°] with a volume fraction of 43%. Vertical filling.....217

Figure 7.18 - Through-thickness front profile for run 8 at X_2, Y_1. Fibre lay-up sequence of [0°, 0°, 90°] with a volume fraction of 43%. Vertical filling.....218

Figure 7.19 - Flow front profile for run 9. Interpolated times i) 60s, ii) 115s and iii) 175s. Fibre lay-up sequence of [0°, 90°, 0°] with a volume fraction of 43%. Vertical filling.....219

Figure 7.20 - Through-thickness front profile for run 9 at X_2, Y_1. Fibre lay-up sequence of [0°, 90°, 0°] with a volume fraction of 43%. Vertical filling.....220

Figure 7.21 - Through-thickness front profile for run 9 at X_2, Y_2. Fibre lay-up sequence of [0°, 90°, 0°] with a volume fraction of 43%. Vertical filling.....221

Figure 7.22 - Through-thickness front profile for run 9 at X_3, Y_1. Fibre lay-up sequence of [0°, 90°, 0°] with a volume fraction of 43%. Vertical filling.....222

Figure 7.23 - Flow front profile for run 2 showing calculated permeability values along different lengths of the mould at X_3 in plane 2. Darcy's law was used in calculating the permeability. The Carman-Kozeny estimate of the permeability in this case is $2.2\times10^{-10}m^2$ with a Kozeny constant of 0.4. Parallel flow with a fibre volume fraction of 49%. Vertical filling.....225

Figure 7.24 - Flow front profile for run 5 showing calculated permeability values along different lengths of the mould at X_3 in plane 2. Darcy's law was used in calculating the permeability. The Carman-Kozeny estimate of the permeability in this case is $2.6\times10^{-10}m^2$ with a Kozeny constant of 0.6. Transverse flow with a fibre volume fraction of 43%. Vertical filling.....226

Figure 7.25 – Graph of $\Delta P/u\eta$ vs. Δx the filled length for run 2 for data at position X_3 in the mould and plane 2. ΔP is the measured pressure drop, u is the local velocity, η is the viscosity and Δx is the filled length. The slope of curve is equal to $1/2k$ where k is the permeability (refer to [7.2]).....227

Figure 7.26 - Graph of $\Delta P/u\eta$ vs. Δx the filled length for run 5 for data at position X_3 in the mould and plane 2. ΔP is the measured pressure drop, u is the local velocity, η is the viscosity and Δx is the filled length. The slope of curve is equal to $1/2k$ where k is the permeability (refer to [7.2]).....228

Figure 7.27 – (a) Flow front profile for run 1. Parallel flow with vertical filling at 43% fibre volume fraction. (b) Flow front profile for run 3. Parallel flow with vertical filling at 55% fibre volume fraction.....229

Figure 7.28 – (a) Flow front profile for run 1. Parallel flow with vertical filling at 43% fibre volume fraction. (b) Flow front profile for run 5. Transverse flow with vertical filling at 43% fibre volume fraction.....230

Figure 7.29 – (a) Flow front profile for run 3. Parallel flow with vertical filling at 55% fibre volume fraction. (b) Flow front profile for run 6. Transverse flow with vertical filling at 55% fibre volume fraction.....230

Figure 7.30 – (a) Flow front profile for run 1. Parallel flow with vertical filling at 43% fibre volume fraction. (b) Flow front profile for run 7. Parallel flow with horizontal filling at 43% fibre volume fraction.....232

Figure 7.31 - Dielectric cure monitoring results obtained from the RTM experimental run showing the temperature and log ionviscosity curves. The green shaded area shows the duration of the mould filling stage. Each log ionviscosity curve corresponds to a different frequency (1Hz, 10Hz, 100Hz, 1kHz, 10kHz).....233

Figure 7.32 - Cure monitoring results showing the changes in resin Conductivity during the experiment at various frequencies (1Hz, 10Hz, 100Hz, 1kHz, 10kHz)...235

8. CONCLUSIONS AND RECOMMENDATIONS FOR FUTURE WORK

Figure 8.1 - 1,3,3-trimethylindoline-6-nitrobenzospiropyran (spiropyran).....242

LIST OF TABLES

2. BACKGROUND

Table 2.1 – Details of the resin transfer moulded sample shown in Figure 2.1.....44

Table 2.2 – Experimental values for the Kozeny constant for flow parallel to the direction of fibre alignment.....46

Table 2.3 – Details of the resin transfer moulded sample with woven fabric in Figure 2.4.....48

3. EXPERIMENTAL DESIGN

Table 3.1 - Resin Properties.....91

Table 3.2 - Immersion liquid 5040 typical characteristics.....100

Table 3.3 – Aluminium tracer particle properties.....100

Table 3.4 – Properties of the Glycerine/Water solution used in the flow front tracking experiments.....101

4. RHEOLOGY AND CURE MODELLING OF RESIN SYSTEMS

Table 4.1 - Model parameters for different resin systems.....134

5. ANALYSIS OF FLOW IN FULLY SATURATED MEDIA

Table 5.1 – Summary table of velocity field results.....159

6. FLOW FRONT TRACKING

Table 6.1 – Contact angle of glycerine on a Perspex surface.....179

Table 6.2 – Average equilibrium contact angles.....180

Table 6.3 - Surface free energy of typical reinforcing fibres[a]:.....182

Table 6.4 - Surface tension results.....182

Table 6.5 – Summary table of flow rates and Reynolds number.....184

Table 6.6 – Listing of the contact angles between the progressing flow front and the cylinder surface.....188

7. SEMI INDUSTRIAL SCALE RTM

Table 7.1 – Summary table of all the experiments performed.....198

Table 7.2 – Comparison of experimentally determined permeability versus Carman-Kozeny prediction. Experimental permeability values are for the length of the mould along wire X_2.....224

NOMENCLATURE

Roman

Symbol	Denotes	Dimensions
a	Rod spacing	mm
b	Rod length	mm
c	Entry length	mm
C_s	Rod centre spacing	mm
D	Diameter	m
dQ/dt	Heat generated	W
E	Activation energy	kJ/kgK
g	Gravity	9.8 m/s^2
G'	Elastic modulus	Pa
G''	Viscous modulus	Pa
h	Height	m
k_x	Kozeny constant	
k	Permeability Tensor	m^2
K	Reaction rate constant	1/s
L	Length	m
M_f	Fibre mass fraction	
N	Number of cylinders	
P	Pressure	Bar
P_c	Capillary pressure	Bar
Q	Volumetric flow rate	m^3/s
r	Radius	mm

R	Universal gas constant	8.3143 J/kgK
R_f	Rod radius	mm
t	Time	s
T	Temperature	K
T_r	Reference temperature	K
T_g	Glass transition temperature	K
T_{g0}	Glass transition temperature of uncured resin	K
$T_{g\infty}$	Glass transition temperature of fully cured resin	K
T_{rxn}	Reaction Temperature	K
$\hat{u}$	Superficial Velocity	m/s
u_x	x-component of velocity	m/s
u_y	y-component of velocity	m/s
U	Velocity	m/s
V	Voltage	V
V_f	Volume fraction of fibres	
V_a	Available fibre volume fraction	
V_m	Volume fraction of matrix	
w	Channel width	m

Greek

Symbol	Denotes	Dimensions
α	Degree of cure	
ΔP	Pressure drop	Bar
$\Delta\rho$	Density difference	kg/m^3
ε	Fractional free volume	
Φ	Porosity	
$\dot{\gamma}$	Shear rate ε	1/s
η	Viscosity	Pa.s
η_∞	Reference viscosity	Pa.s
η_0	Initial Viscosity	Pa.s
θ	Angle	°
ρ	Density	kg/m^3

σ	Surface Tension	mN/m
ω	Angular frequency	Hz

Dimensionless Numbers

Symbol	Denotes
Bo	Bond Number
Ca	Capillary Number
C_d	Drag coefficient
Fr	Viscous Froude Number
Re	Reynolds Number

1. INTRODUCTION

Resin transfer moulding (RTM) has been studied extensively over the last 10 years and its advantages are well established. It is considered a versatile process, able to efficiently produce fibre-reinforced polymeric composites of different shapes and high structural performance for intermediate volume production runs[1]. As a result, RTM has many current and potential applications in a variety of markets, such as the automotive, aerospace and sports industries. The use of fibre reinforced plastic components is expanding rapidly due to their good mechanical performance coupled with their light weight.

In recent years, RTM has gained significant popularity as a fabrication process for the manufacture of composite structures in the aerospace industry, motor industry and other industrial applications. Of the wide range of methods available for manufacturing these components (such as sheet moulding compound, bulk moulding compound, reinforced reaction injection moulding, etc.), RTM is unique in that it permits the manufacture of high performance composite parts of essentially unrestricted geometry with fast turnaround times[2]. Additionally, the low injection pressure range used in the RTM process reduces the cost and complexity of the required tooling[3].

The main steps in the RTM process are shown in Figure 1.1. The process consists of the following basic steps: - (i) place the reinforcement material (or preform) into the mould, (ii) close the mould and draw or force the resin into the mould, (iii) saturate the preform, (iv) cure and (v) then de-mould the part.

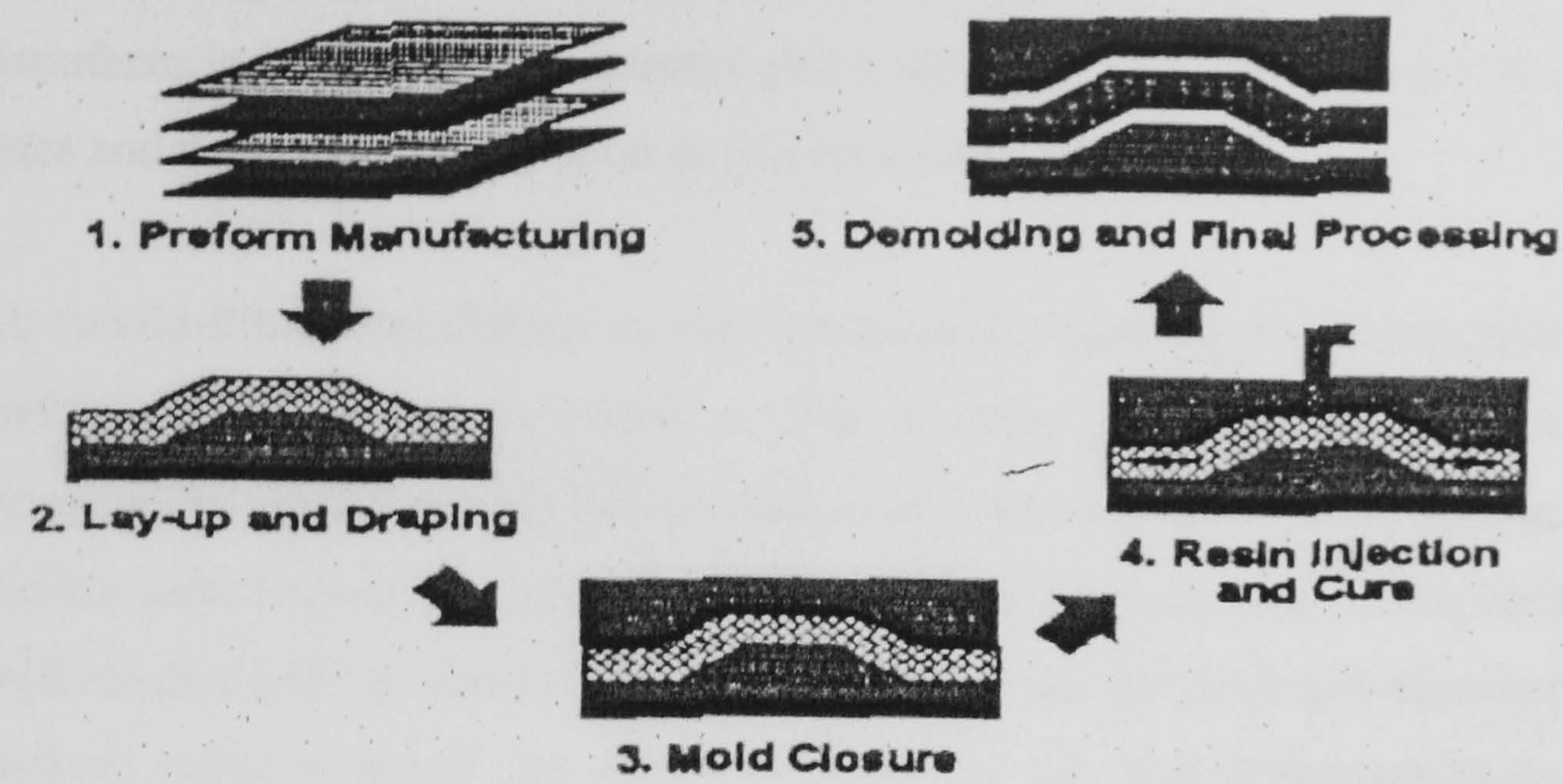


Figure 1.1 – Schematic diagram showing the principal steps of the RTM process[4]

For complicated mould shapes, the manufacturing engineer has to make decisions about injection pressure, flow rate, location of gates and vents, etc. to achieve a high quality composite part which is free of dry spots and takes a minimum amount of time for the resin impregnation process.

Although RTM does offer faster turnaround times than most other composites manufacturing processes, a lot of effort continues to be put into trying to reduce the cycle time due to the economic pressures in commercial applications. Documented methods of reducing the duration of the cure phase are based upon the use of heated moulds and additional heat sources[5]. Also the use of phased catalyst injection has been proposed by Blanchard and Rudd[6], which involves increasing the reactivity of the resin during the impregnation phase. The results show that the cure phase may be controlled to promote simultaneous cure throughout the laminate.

There are significant gains to be made in terms of reduced production costs and improved product quality through simulation of RTM. By having robust mould filling simulation codes available to manufacturing and design engineers, prototype development which usually involves many trial and error iterations of the mould configuration and boundary conditions can be speeded up providing considerable cost savings. During prototype development, the engineers can combine their

manufacturing experience with simulation results to decide if RTM is a viable manufacturing option for the selected part and to select the locations for the injection gates and vents to avoid dry spots and to minimise fill time.

All mould-filling simulations require information regarding the permeability of the preform, which is the resistance to flow at every spatial location in the mould. Permeability depends on the fabric architecture, type of preform, fibre volume fraction and the deformation that the preform undergoes during placement[7,8]. The variability in preform permeability due to compaction, deformation and improper placement of the preform inside a mould can significantly change the flow impregnation patterns as compared with simulations that do not account for these effects.

Most of the efforts in simulating composite processing have been based on the application of Darcy's law[9] to describe flow of viscous resin through the fibre reinforcement. However, industrial experience has shown that the impregnation process, cure characteristics, void formation and growth, and ultimately the shape of the final product in the processing of thick composite components are all substantially different from predictions based on Darcy's law.

Darcy's law can be expressed as:

$$U_i = -\frac{K_{ij}}{\eta}\frac{\partial P}{\partial x_j} \qquad [1.1]$$

where U_i is the superficial velocity, K_{ij} is the Darcy permeability tensor of the porous medium, η is the dynamic viscosity of the fluid and P is the pressure.

The application of Darcy's law to the processing of thick composite parts has its limitations. Firstly, Darcy's law requires knowledge of the permeability coefficient and this can be difficult to quantify for complex geometries and flow fields. Experimental studies have been carried out which illustrate that the flow behaviour in both unsaturated and saturated reinforcements deviates from Darcy's law, with permeability being represented as a function of the porosity, the superficial velocity of the permeating fluid and the pressure drop[10,11,12]. Secondly, Darcy's law is valid only under very strict restrictions[13]. Darcy's law describes the saturated laminar flow of a Newtonian fluid through a homogenous porous medium on a macroscopic scale.

During processing of thick structures, heat transfer can become non-uniform. Non-uniformity in heat transfer will result in a highly non-uniform temperature distribution that can violate the assumptions in the derivation of Darcy's law. Also, almost all polymers and thermoset resins used in composite materials are non-Newtonian during at least part of the cure cycle.

The work presented in this thesis forms part of a larger study involving other researchers. The overall aim of this study is to accurately model, simulate and therefore produce recommendations for the design and production of composite elements using the resin transfer moulding (RTM) process. This thesis presents the results of an experimental investigation into some of the key flow parameters in the RTM process. The flow parameters studied are; the resin viscosity, its curing behaviour, the progression of the flow front and micro scale flow filling properties. The thesis is structured in the following manner: - Chapter 2 presents an overview of the research in some of the key areas of RTM studies. Chapter 3 describes the equipment, materials and procedures used in the current experimental investigation. Chapter 4 presents the results of the rheology and cure monitoring studies of typical RTM resin systems. A model is proposed for the advancement of the rheology during cure. In Chapter 5, the results of an investigation of the micro-scale velocity field in a saturated model porous medium are discussed. A qualitative comparison is made of these experimental results with those from a numerical simulation model proposed by Spelt et al.[14]. Chapter 6 highlights the results of a micro-scale investigation of the propagation of the liquid flow front. Again a comparison is shown of the experimental result to a model simulation result proposed by Spelt et al.[14]. Semi-industrial scale RTM experiments were performed to investigate the propagation of the flow front using the *SMARTweave* flow front monitoring device. The results of this series of experiments are presented in Chapter 7. Additionally, dielectric cure monitoring studies are presented in this Chapter. And finally Chapter 8 provides a summary of the work presented in this thesis together with recommendations for future work.

References

[1] Parnas, R.S., Salem, A.J., Sadiq, T.A.K., Wang, H.P., Advani, S.G., "The Interaction between Micro and Macroscopic Flow in RTM Preforms", Composite Structures, **27**(1-2), 93-107, (1994).

[2] Wilks, C.E., Crosky, A., "Fabrication of Fibre Reinforced Plastics using Resin Transfer Moulding", Materials Forum, **20**, 207-218, (1996).

[3] Parnas, R.S., Salem, A.J., "A Comparison of the Unidirectional and Radial In-Plane Flow of Fluids Through Woven Composite Reinforcements", Polymer Composites, **14**(5), 383-394, (1993).

[4] Sozer, E.M., Bickerton, S., Advani, S.G., "On-line Strategic Control of Liquid Composite Mould Filling Process", Composites Part A: Appl. Sci. Manu., **31**, 1383-1394, (2000).

[5] Johnson, M.S., Rudd, C.D., Hill, D.J., "Cycle Time Reductions in Resin Transfer Moulding Using Microwave Preheating", Proc. Inst. Mech. Eng. Part B: J. Eng. Manufacture, **209**, 443-453, (1995).

[6] Blanchard, P.J., Rudd, C.D., "Cycle Time Reduction in Resin Transfer Moulding by Phased Catalyst Injection", Comp. Sci. Tech., **56**, 123-133, (1996).

[7] Bickerton, S., Simacek, P., Gulielmi, S.E., Advani, S.G., "Investigation of Draping and its Effects on the Mould Filling Process During Manufacturing of a Compound Curved Composite Part", Composites Part A: Appl. Sci. Manu, **28**, 801-816, (1997).

[8] Long, A.C., Rudd, C.D., "Simulation of Reinforcement Deformation During the Production of Preforms for Liquid Moulding Processes", Proc. Inst. Mech. Eng. Part B: J. Eng. Manufacture, **208**(4), 269-278, (1994).

[9] Darcy, H., "Les Fontaines Publiques de la Ville de Dijon", Dalmont, Paris, (1856).

[10] Chan, A.W., Larive, D.E., Morgan, R.J., "Anisotropic Permeability of Fibre Preforms: Constant Flow Rate Measurement", J. Comp. Mat., **27**(10), 996-1008, (1993).

[11] Lekakou, C., Johari, M.A.K., Norman, D., Bader, M.G., "Measurement Techniques and Effects on In-plane Permeability of Woven Cloths in Resin Transfer Moulding", Composites Part A: Appl. Sci. Manu, **27A**, 401-408, (1996).

[12] Trevino, L., Rupel, K., Young, W.B., Liou, M.J., Lee, L.J., "Analysis of Resin Injection Moulding in Moulds with Pre-placed Fibre Mats: Permeability and Compressibility Measurements", Polym. Composites, **12**(1), 20-29, (1991).

[13] Bear, J., Bachmat, Y., "Introduction to Modelling of Transport Phenomena in Porous Media", Kluwer Academic Publishers, Dordrecht, ISBN 0-7923-0557-4, (1991).

[14] Spelt, P.D.M., Selerland, T., Lawrence, C.J., Lee, P.D., "Flow of Inelastic Non-Newtonian Fluids Through Arrays of Aligned Cylinders. Part 1. Creeping Flow", Submitted to Journal of Fluid Mechanics (2003).

2. BACKGROUND

This chapter presents reviews of some of the key work carried out in the areas of research relevant to RTM simulation. Permeability characterisation studies are presented highlighting the main experimental and analytical methods. Preform compression and deformation studies are described. The main flow phenomena are discussed and the computational simulation methods presented.

2.1. Permeability Measurement

This section outlines the permeability characterisation for different types of fibrous preforms, namely, aligned fibre bundles or tows, woven or cross-ply structures and random fibre mats. Permeability is an important parameter in the modelling and design of RTM. This permeability combined with the resin viscosity determines the flow characteristics of the mould filling process.

The fibres in reinforcements are often gathered in bundles or fibre tows. Three scales can be distinguished; (i) a micro-scale with the fibre radius as a typical length as shown in Figure 2.1, (ii) an intermediate scale where the diameter of the fibre bundles gives the typical length as shown in Figure 2.2, (iii) a macro-scale where the typical length is chosen much larger than the diameter of the fibre bundles which makes it possible to treat the reinforcement as a continuous porous medium.

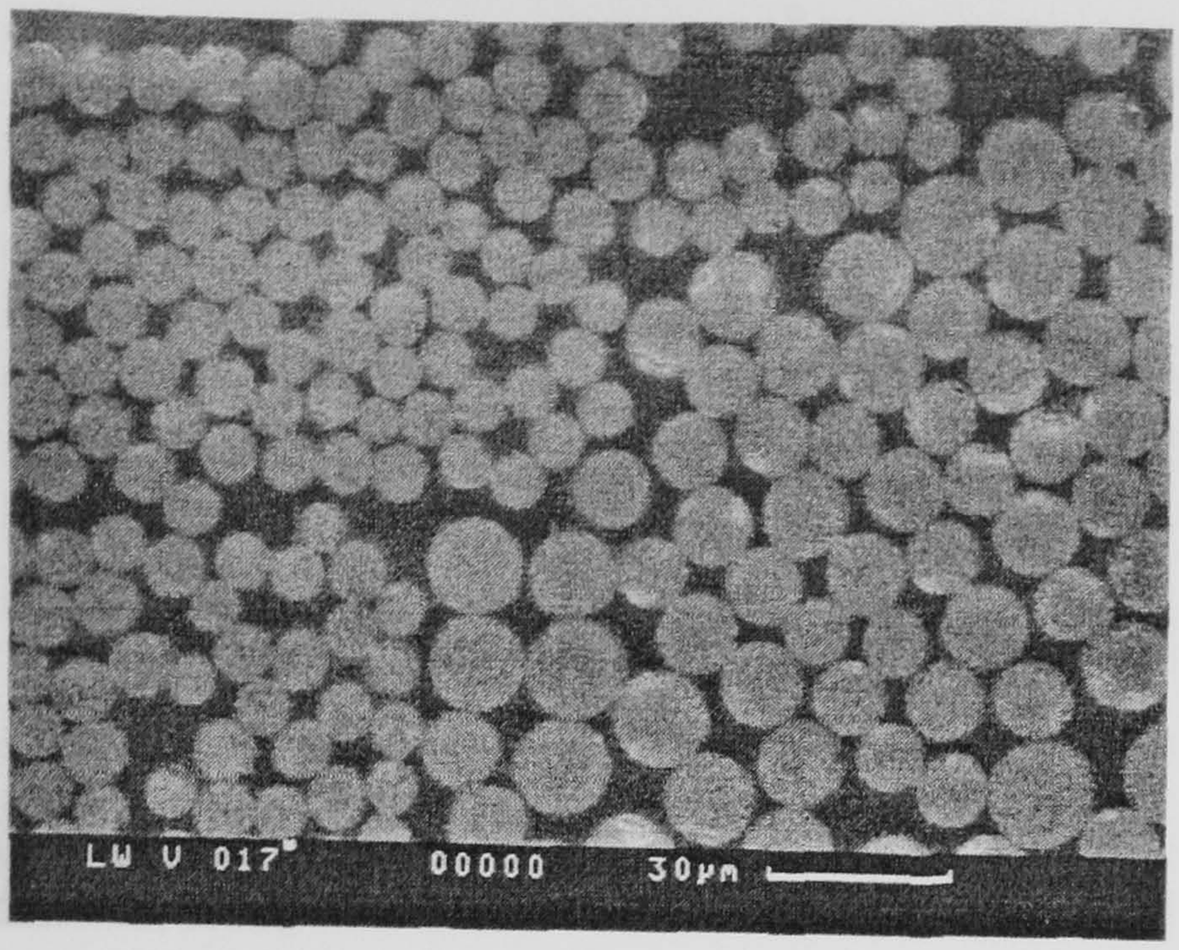


Figure 2.1 – Cross-section of a unidirectional laminate on a micro-scale showing the variation in fibre diameter[1].

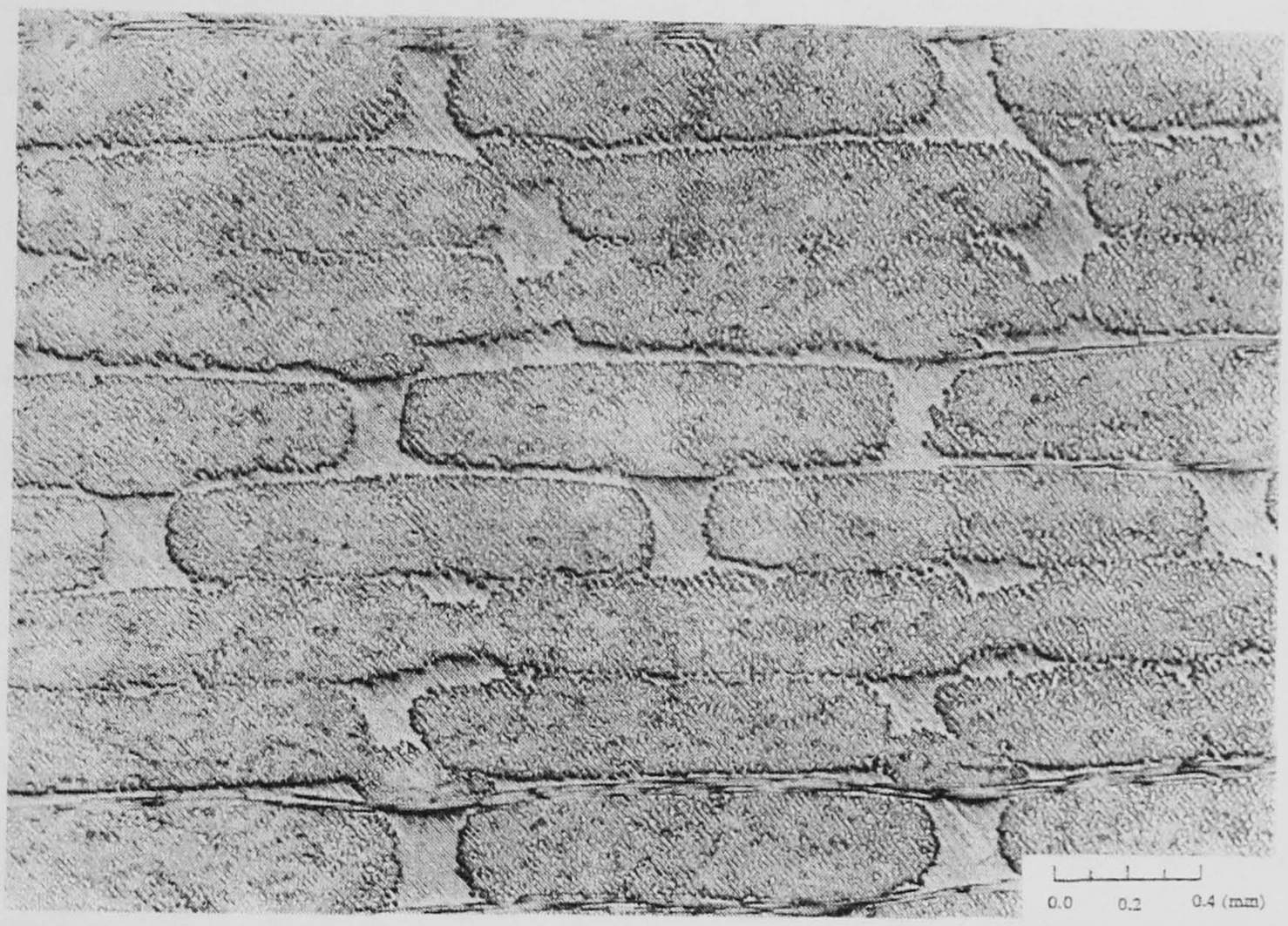


Figure 2.2 – Cross-section of a unidirectional laminate on an intermediate scale[1].

One of the first relationships derived that describes fluid flow through permeable material is Darcy's Law[2], which for on-axis flow (flow along the axis of the fibre tows) through an anisotropic material has the form:

$$U = -\frac{K}{\mu}\frac{\Delta P}{L} \qquad [2.1]$$

where U is the mean flow velocity, μ is the viscosity of the fluid, ΔP is the change in pressure over the length L in the direction of the fluid flow and K is the permeability of the medium.

Darcy's Law has proved to be a reliable model for flow through porous media. In 1927 Kozeny developed a relationship that was an extension of this model. This was modified by Carman in 1937 to form the Kozeny-Carman equation, which describes the flow rate Q as a function of pressure gradient ΔP over a bed of length L[3]

$$Q = \varepsilon \frac{Am^2}{k\mu} \frac{\Delta P}{L} \qquad [2.2]$$

where ε is the fractional free volume of the bed (porosity), A is the cross-sectional area of the bed, k is the Kozeny constant, μ is the viscosity and m is the mean hydraulic radius of the pores in the bed[4]. The mean hydraulic radius is related to the fibre radius, r:

$$m = \frac{r}{2} \frac{\varepsilon}{(1-\varepsilon)} = \frac{rV_m}{2V_f} \qquad [2.3]$$

where V_m and V_f are the volume fractions of the matrix and fibres respectively[15].

The Kozeny-Carman equation can be developed into a relationship between the permeability of the material, K and the porosity, ε[5]

$$K = \frac{r^2}{2k} \frac{\varepsilon^3}{(1-\varepsilon^2)} \qquad [2.4]$$

The Kozeny-Carman relationship is a relatively good approximation for many porous media although it is not so effective in modelling fibrous media. This is due to the assumptions that are made in deriving this relationship; for example, it is assumed that the medium is isotropic but fibre media are frequently anisotropic.

Other models use drag theory, the capillary flow approximation or ad hoc approaches. The validity of Darcy's law and the Carman-Kozeny equation has been questioned by many researchers. Visconti et al.[6] identified differences in the measured permeability brought about by changes in injection pressure. Gauvin et al.[7] suggested that the flow rate, pressure and the nature of the fluid are among factors that could strongly influence the permeability measurements. Griffin et al.[8] and Steenkamer et al.[9] found different permeability values depending on the infiltrating fluid. Chan et al.[10] and

Dave[11] observed an increase in permeability with flow rate. Despite these and other findings, Darcy's law is still by far the most widely used flow model and, as mentioned by Parnas et al.[12], many of these discrepancies may be due to neglect of the effects of microscopic flow phenomena in the interpretation of the macroscopic flow. Originally, Kozeny[13] related the pressure drop to velocity by assuming flow through an idealised isotropic porous medium consisting of tortuous capillaries. Carman[14] later modified the Kozeny equation by incorporating the specific pore surface area.

2.1.1. Aligned and Continuous Fibre Bundles

Figure 2.3 displays an optical microscope image of a resin transfer moulded sample with unidirectional layers. Carbon fibre material is used with an average fibre diameter of 7μm. Each tow consists of between 3 to 6 thousand fibres. The resin system used is RTM6. Details are listed in Table 2.1.

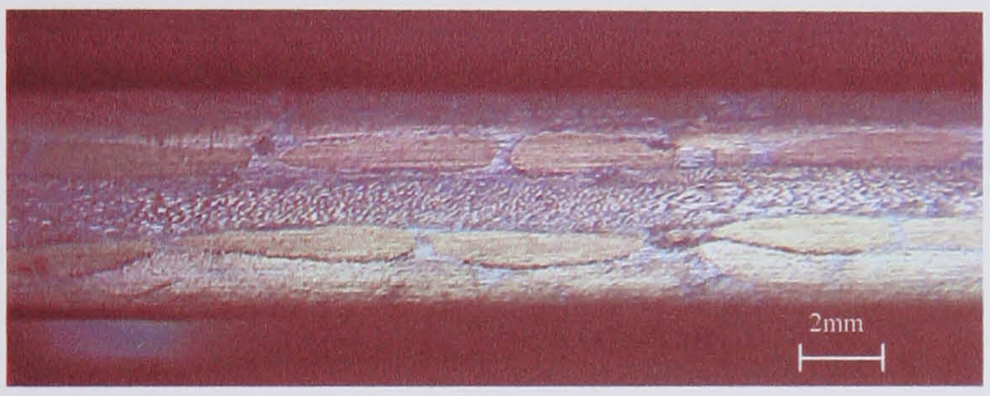


Figure 2.3 - Optical microscope image of a resin transfer moulded sample with unidirectional layers[a].

Table 2.1 – Details of the resin transfer moulded sample shown in Figure 2.1

	Unidirectional ply sample
Carbon fibre cloth manufactured by	BTI Europe
Fabric Serial number	0, 90 plies are unidirectional (Ct300); +/- plies are +45/-45 non-crimp (CBX602)
Fibre	T300 (7μm diameter)
Tow	3*k* or 6*k*
Ply orientation	[+/-, 0, 90, +/-, 0, 90]
Resin	RTM6 produced by Hexcel, Duxford

[a] Courtesy of *QinetiQ*, Cody Technology Park, Farnborough, Hampshire, GU14 OLX, UK

The geometrical parameters of aligned fibre bundles are more certain making them relatively easier to handle. Williams et al.[15] presented a permeability model for flow along the fibre direction based on the Kozeny-Carman equation which has become the most cited work in this field. This model was studied further and improved by Gutowski et al.[16], Kardos and coworkers[17,18] and others[19,20]. For flow transverse to the fibre direction the approach is different. Some studies have applied the same approach but use different values for the Kozeny constant[17]. However, others consider the fact that in the transverse direction the flow can be stopped at the maximum packing capacity which is less than 1. For ideal packing the maximum packing capacity is 0.79 for a square array and 0.91 for a hexagonal array. For a bundle of fibres under practical conditions, the real value of fibre packing is somewhere between these two ideal values. The resistance to the transverse flow also increases dramatically once the fibre volume fraction approaches its maximum value because of the tortuous flow paths and the large flow resistance in the narrow gaps. This consideration leads to a modified set of equations[16,19].

The Kozeny-Carman equation (for flow along the fibre direction) can be written as:

$$K_x = \frac{r_f^2}{4k_x}\frac{(1-V_f)^3}{V_f^2} \qquad [2.5]$$

where K_x is the permeability in the fibre direction, r_f is the fibre radius, k_x is the Kozeny constant determined experimentally, and V_f is the fibre volume fraction. The permeability has the units of length squared. The values of the Kozeny constant are different in various experiments. Table 2.2 displays values for the Kozeny constant determined in different studies.

Table 2.2 – Experimental values for the Kozeny constant for flow parallel to the direction of fibre alignment

Reference	k_x	Experimental Conditions
15	0.38 (initial water flow) 0.45 (water displaced by alcohol) 0.35 (initial alcohol flow) 0.39 (alcohol displaced by water)	Pre-wet fibre beds $V_f = 0.514$
16	0.7	AS4 fibres (graphite) Corn oil or silicone fluid $V_f = 0.4$-0.8
17	0.57 (suggested) 0.35 (silicone oil) 0.68 (water)	Graphite fibres $V_f = 0.57$-0.75

For flow transverse to the fibre bundle, Lam and Kardos[17] use the same expression as [2.5] but change the Kozeny constant to k_z to match with the experimental measurements. However, one major drawback of using the same expression for both transverse and parallel flow, as mentioned earlier, is that it cannot represent the blockage of flow in the transverse direction when the fibre volume fraction reaches the maximum packing. Modifications have been proposed for the Kozeny-Carman equation to take account of this effect, such as the one proposed by Gutowski et al.[16];

$$K_z = \frac{r_f^2}{4k_z}\frac{(\sqrt{V_a/V_f}-1)^3}{(V_a/V_f+1)} \qquad [2.6]$$

where V_a is the so-called available fibre volume fraction (maximum packing fraction) at which the transverse flow stops. The constant k_z was measured experimentally and found to be 0.2.

In contrast, Gebart[19] proposed the following expression:

$$K_z = \frac{r_f^2}{4k_z}\left(\sqrt{(V_f)_{\max}/V_f}-1\right)^{5/2} \qquad [2.7]$$

where $(V_f)_{max}$ is chosen as 0.7854 and 0.9069 for square and hexagonal packing respectively.

There are other studies on the permeability of periodic arrays outside the composite processing field. An early study was reported by Happel and Brenner[21] using the cell method. Numerical results on square and hexagonal packings have been presented by Sangani and Acrivos[22]. The results of these periodic structures and the available experimental data in the composite processing field[15,16,17,18] are not close in the case of longitudinal flow. This shows that disturbances of the fibre bundle status have a strong effect on the longitudinal permeability[23].

2.1.2. Woven and Cross-Ply Fibrous Structures

Figure 2.4 displays an optical microscope image of a resin transfer moulded sample with carbon fibre woven fabric. The area density of the fabric is 285g/m^2. Each tow consists of approximately 3000 fibres with an average fibre diameter of 7μm. A fibre volume fraction of 55% was used. The resin system used is *PR*500. Details are listed in Table 2.3.

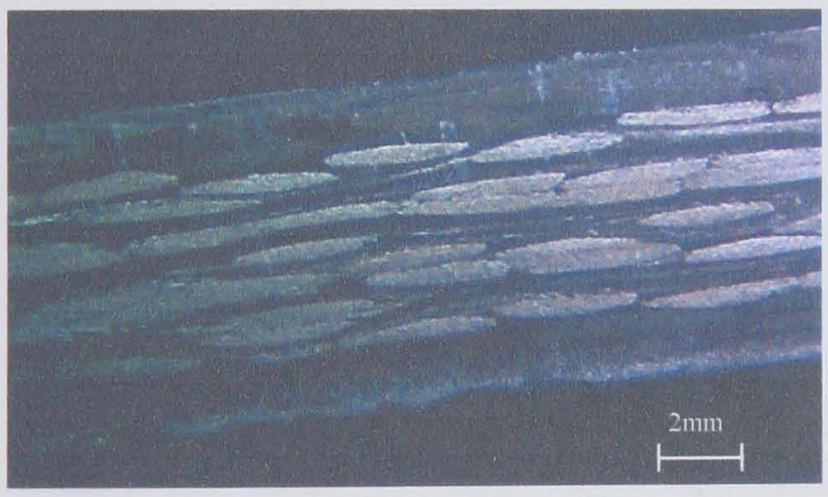


Figure 2.4 – Optical microscope image of resin transfer moulded sample with woven fabric[b].

[b] Courtesy of *BAE Systems*, Sowerby Research Centre, Filton, Bristol, UK

Table 2.3 – Details of the resin transfer moulded sample with woven fabric in Figure 2.4

	Woven fabric sample
Carbon fibre cloth manufactured by	Tech Textiles
Fabric Serial number	285 gsm 5 satin harness weave (Hexcel *G*933)
Fibre	T300 (7μm diameter)
Tow	3*k*
V_f	Approx. 55 %
Ply orientation	45, 0, 45, 0, 0, 0, 45, 0, 0, 0, 45, 0, 45 (laid up from weft face towards neutral axis)
Resin	*PR*500 produced by 3*M*

Woven types of preform are more widely used in structural composite applications because of their superior performance with respect to damage tolerance. The fibres in these preforms are placed with a prescribed pattern. In woven preforms, the 0/90° arrangement is common.

Lam and Kardos[17] assume that the Kozeny-Carman equation is valid but apply different values for the Kozeny constant for different lay-up angles. The unidirectional and the 0/90 cross-woven are considered as two extreme structures. The proposed expression for the Kozeny constant is:

$$(k_x)_{0/\theta} = (k_x)_{uni}\, cos^2\theta + (k_x)_{0/90}\, sin^2\theta \qquad [2.8]$$

$$(k_z)_{0/\theta} = (k_z)_{uni}\, cos^2\theta + (k_z)_{0/90}\, sin^2\theta \qquad [2.9]$$

where θ is the angle between fibres in successive plies, subscript x refers to in-plane flow, z refers to transverse flow, $(k_x)_{uni}$ and $(k_z)_{uni}$ are the Kozeny constants for a unidirectional fibre bed in the parallel and transverse directions respectively, and $(k_x)_{0/90}$ and $(k_z)_{0/90}$ are the Kozeny constants for a 0/90 bed of fibres.

There are also reported experimental measurement data on woven fabrics[24,25,26]. A proposed method and instruments[27] have been developed for obtaining the in-plane permeability data on woven fabrics.

Braided preforms are now widely used in RTM. Fibre placement angles are more in the thickness direction in a braided structure than in woven preforms. However, the flow paths in different directions are still close to those in the woven structure, where tortuous flow paths are observed, especially at high fibre volume fractions.

2.1.3. Random and Stitched Fibre Mats

This is the earliest type of preform and still quite commonly used in RTM and other composite fabrication processes. Usually the fibre volume fraction is relatively low. The permeability characteristics of the mats can be very different from those of the aligned and cross-ply preforms.

Lee, Trevino and coworkers[28,29] have made extensive studies on the permeability of fibre mats. Experimental data suggested that the relationship between the permeability and the porosity is close to linear on a log-log plot:

$$\boldsymbol{LogK = a\ log\Phi + b} \qquad \textbf{[2.10]}$$

where Φ is the porosity, a and b are two constants to be determined by curve-fitting methods. Fibre mats were studied in all three directions (x, y and z), the permeability being about the same in the x and y directions (in-plane) but lower in the z direction (transverse). A set of explicit formulae was given for random fibre mats and bi-directional mats[30,31].

A similar approach was adopted by Rudd et al.[32]. Instead of using porosity, the fibre mass fraction was used:

$$\boldsymbol{K = a(M_f)^b} \qquad \textbf{[2.11]}$$

where M_f is the fibre mass fraction, a and b are constants determined experimentally.

Gauvin et al.[33] found that the permeability is a function of the porosity, pore size and geometry, fibre shape and fibre treatment. However, to simplify the problem, they

suggested that the permeability can be treated as a function of the porosity alone. In their study of non-Newtonian fluid using the generalized Darcy's law, they proposed an empirical function for the permeability factor K_1 as:

$$K_1 = a\Phi^b \qquad [2.12]$$

where a and b are constants, which is essentially the same as

[2.10].

Gauvin and Chibani[34] also developed a model which considers both shear flow losses and drag forces on fibre rovings. Their experimental data showed that in the porosity range of about 0.8 to 0.9, their model gives more accurate predictions than the Kozeny-Carman equation.

2.1.4. Capillary Pressure

Under certain processing conditions such as low injection pressure and high fibre volume fraction, the microscopic flow of resin within the fibre tow can considerably influence the overall flow. This process is referred to as fibre wet-out. The capillary pressure, P_c, presents a significant driving force for resin impregnation and should therefore be taken into account[35] to optimise the use of RTM, reducing, for example, the presence of dry spots and micro and macro voids[36].

A liquid can be spontaneously transported (wicking) through the inter-fibre pores of the fibre preform by capillary action. This dynamic interaction process involves wetting, liquid uptake in the porous structure and, for some fibres, liquid absorption within the fibres, making wetting measurements of fibrous assemblies more difficult to analyse[37].

Capillary pressure, P_c, has been theoretically estimated using the Young-Laplace equation, which was first applied to idealised capillary tubes. A larger capillary pressure is predicted for fluid/fabric systems with a small contact angle. Furthermore, small pores should be filled first when the fabric is brought into contact with the wetting liquid. As saturation proceeds, larger pores becomes filled and the capillary pressure decreases, becoming equal to zero for a completely saturated medium[38].

In a reinforcing fibrous preform there is a distribution of pore sizes and shapes and distinct pore path directions, hence a dimensionless shape or form factor, F, which depends on flow direction, was used by Ahn et al.[39] to allow for all different anisotropic/geometric configurations of fibrous media. For one-dimensional flow, the relationship can be expressed as:

$$P_c = \frac{F}{D_f}\frac{(1-\varepsilon)}{\varepsilon}\sigma\cos\theta \qquad [2.13]$$

where σ is the surface tension of the wetting fluid, θ is the contact angle between the liquid and the solid, ε is the void fraction and D_f is the fibre diameter. In the case of a unidirectional fibrous preform, F is considered to be 4 for axial flow and 2 for transverse flow[40]. For complex fibre alignment such as a woven fabric, F can only be determined experimentally.

Different methods can be used to measure capillary pressure of a fibrous preform[38,41], but perhaps the most widely used are experiments based on the Wilhelmy plate method[37,42]. Ahn[39] designed such an apparatus to measure the factor F, the capillary pressure, P_c, and the transverse permeability of an assembly of plain-weave carbon-fibre fabrics.

2.1.5. Summary

For all three groups of fibrous preform, the Kozeny-Carman equation is approximately valid within an intermediate porosity or fibre volume fraction range. There are deviations and scatter in all the experiments, especially in the two extreme cases when either the porosity or fibre volume fraction is large. Revisions of the Kozeny-Carman equation have been proposed by numerous researchers. The main advantage of the Kozeny-Carman equation is its ease of use since there is only one dimensionless parameter which needs to be determined experimentally. However, the limitations of the Kozeny-Carman equation can be summarised as follows; (i) For flow transverse to aligned cylinders the Kozeny-Carman equation predicts the transverse permeability to be equal to zero only when the packing arrangement reaches a porosity value of 0. However, the porosity of a packing of aligned cylinders will never reach this value. For ideal packing the maximum packing capacity is 0.7854 for a square array and 0.9069 for a hexagonal array. (ii) The Kozeny-Carman

equation accounts for shear straining of the fluid. However, the permeating fluid will experience elongational straining due to the expansion and contraction in flow through the porous media. This can be very significant in non-Newtonian fluids. (iii) The Kozeny-Carman equation assumes a constant capillary diameter. For a non-uniform pore size distribution this assumption may lead to significant errors. Another approach is to assume the porous medium as consisting of aligned groups of wide and narrow capillaries connected in parallel or series[43]. (iv) The Kozeny approach becomes inappropriate theoretically when flow paths become blocked. This will occur naturally in a random heterogeneous porous structure.

Despite these limitations the Kozeny-Carman equation has been shown to be valid for Newtonian Stokes flow through porous media over a limited porosity range.

2.2. Permeability Experiments

There are essentially two types of experimental techniques used to determine the in-plane permeability of a fibre reinforcement. Figure 2.5 displays a schematic diagram of the two methods, namely, parallel and radial flow experiments.

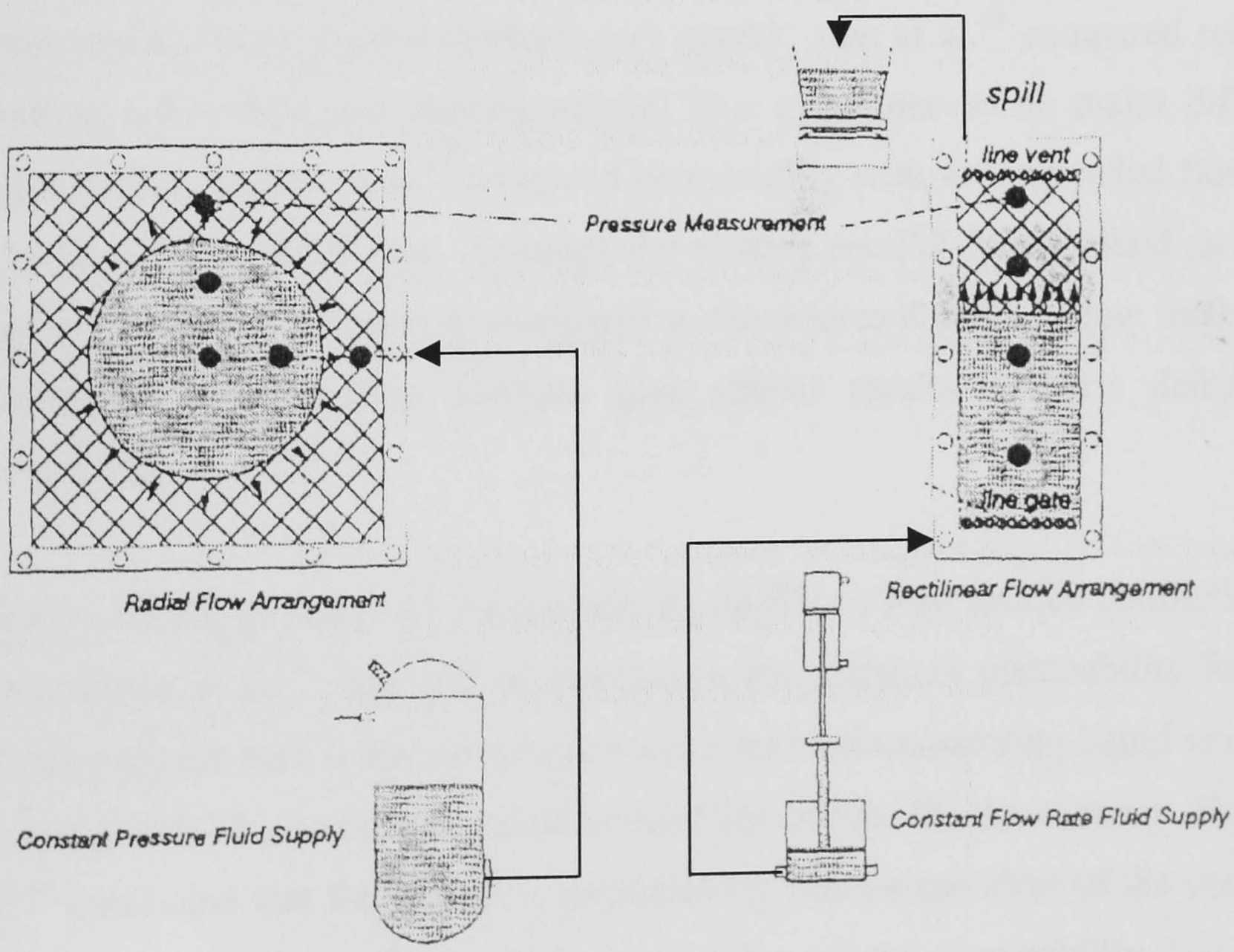


Figure 2.5 – Schematic diagram of Radial flow (on the left) and Parallel flow (on the right) experiments used to determine the permeability of fibre preform (for process description see sections 2.2.1 and 2.2.2)[44].

The permeability values may be obtained for a saturating (transient) or saturated (steady-state) filling condition at constant pressure or constant flow rate injection. The saturating permeability includes the resistance to flow due to free surface energies. The saturated experiment allows the resin to fill the mould completely and pressure measurements are taken only when the flow stabilizes to a steady-state. Parnas et al.[35] compared wetting radial flow, wetting parallel flow and saturated parallel flow. The permeability measured from the wetting technique is higher than the saturated permeability for a random mat. This is due to the effects of capillary pressure at the flow front. For a weave, the wetting technique results in a lower apparent permeability, showing that inclusion of air at the liquid flow front is the dominating flow front phenomenon in this case. Diallo et al.[45] used the parallel flow technique to measure the permeability in both the wetting and saturated regions in one measurement. It was found that the permeability did not reach an equilibrium value until the liquid had flowed out of the reinforcement for a long time. Lekakou et al.[46] explained the differences in permeability obtained in the wetting radial flow and the wetting parallel flow techniques by differences in the flow front speed. However, other studies have yielded contradictory results. Ahn et al.[47] compared results from wetting radial flow and wetting parallel flow and observed no major difference in permeability. Gebart et al.[48] measured permeability with wetting radial flow, wetting and saturated parallel flow. Although the wetting parallel flow method gave slightly higher permeability values as compared to the saturated parallel flow method, it was concluded that the three methods give similar results if fabric deformation is minimised.

Studies on the influence of the permeating fluid have also yielded conflicting results. Steenkamer et al.[36] observed an increase in the measured permeability for different fluids from the case when syrup/water was used as the measuring liquid via vinylester to motor oil. This trend was traced to capillary effects. On the contrary, Hammond et al.[49] concluded that the measured permeability was independent of the contact angle and the Capillary number and that the value of the permeability was the same regardless of the liquid used.

2.2.1. Parallel Flow Experiments

The parallel flow experiment involves injecting the resin at constant pressure or constant flow rate into a rectangular mould filled with a porous medium and venting at the opposite end.

The pressure gradient is measured by strategically placing pressure transducers along the length of the mould. The saturating (transient) permeability is obtained by measuring the flow rate of resin out of the vent immediately after mould filling and before steady-state conditions are reached. The saturated (steady-state) permeability, however, is obtained by measuring the flow rate of resin out of the vent once steady-state conditions have been attained. The in-plane permeability is then obtained by applying Darcy's law.

Depending on the orientation of the fibres relative to the filling direction, the in-plane permeability components K_{xx} and K_{yy} can be obtained. When filling is performed with the fibres aligned in a direction other than 0° or 90° relative to the main flow direction, then it is possible to define an effective permeability K^{θ}_{e}.

One advantage of the parallel flow experiment is that it is easy to set-up and the principle permeability components of the reinforcement material can be determined directly from measurements. However, race-tracking of the resin along the edges of the mould can occur. This is caused by the preform not fitting the mould dimensions exactly thus creating a cavity or channel along which the resin flows preferentially. Injecting a small amount of sealant into the cavity region can reduce this effect[44].

Lidström[50] proposed a modified parallel flow experiment called the multi-cavity parallel flow cell. The mould was comprised of four separate cavities, three of which were loaded with samples of fabric, orientated in three different directions (0°, 45° and 90°). The fourth cavity contained a reference fabric with known permeability. The experiments were conducted under steady-state conditions with each cavity supplied with fluid at the same constant pressure. The flow rate was measured from each of the four cavity vents to obtain the ratios of the effective permeability between the samples.

2.2.2. Radial Flow Experiments

In the radial flow experiment, the resin is injected into a centre gate to produce a divergent flow front which is vented at the perimeter (see Figure 2.5). The pressure gradient is measured by placing pressure transducers along the 0° and 90° axes.

The radial flow experiment can be used to measure the two principal in-plane permeability components, K_{xx} and K_{yy}, simultaneously. Filling from the centre of the mould eliminates the need for accurate reinforcement trimming and placement, as there is no edge for race-tracking to occur.

The following expression may be used to obtain the radial permeability, K_{rr}, from experimental measurements at constant inlet pressure,

$$\frac{1}{2}\left(\frac{R}{r}\right)^2\left[\ln\left(\frac{R}{r}\right)-\frac{1}{2}\right]=\frac{K_{rr}t}{\mu r^2}\left(P_i-P_f\right)-\frac{1}{4} \qquad \textbf{[2.14]}$$

In anisotropic media [2.14] can still be used; however, the radius R must be replaced by the geometrical mean of the major and minor axes of an elliptical flow front. The permeability K_{rr} must also be replaced by the geometric mean of the principal components of the permeability tensor.

2.2.3. Permeability Measurement Through Several Layers

Most applications involve multiple layers of fabric arranged in different orientations. An effective or averaged in-plane permeability value based on an arithmetical mean of the individual in-plane permeability components for each layer can then be used. This is expressed as,

$$\overline{K}_{ij}=\frac{1}{H}\sum_{l=0}^{n}h^l K^l{}_{ij} \qquad \textbf{[2.15]}$$

where $\overline{K}_{ij}$ represents the components of the gapwise averaged permeability tensor, H is the total thickness, n is the number of layers each of thickness h^l with permeability components in the local mould coordinate frame $K^l{}_{ij}$.

Verheus et al.[51] conducted experiments in a vacuum injection mould using 12 layers of unidirectional Injectex 21091 with different stacking sequences. Results obtained

suggested that [2.15] may not be appropriate for alternating stack sequences when the permeability difference between adjacent layers is large.

Luce et al.[52] reported that the averaging scheme is only accurate for fully saturated, creeping, steady-state flow under which Darcy's law was originally defined. In particular, the averaging scheme neglects the effects of fibre nesting that can occur between adjacent layers during mould closure.

2.3. Numerical Methods

The permeability of a fibrous medium may also be obtained by considering the geometry to consist of an array of regularly spaced cylinders (fibres) and solving for the drag force on the cylinders. This section discusses the solutions for both circular cylinders and elliptical shaped cylinders.

2.3.1. Circular Cylinders

The permeability of a material is an important factor in the modelling of flow through porous media. Equivalently, one may use the drag force. A relationship between permeability and the coefficient of drag can be derived by considering the forces acting in a unit cell of the material with length of side L containing N cylinders. A pressure difference of ΔP is applied over the cell and a fluid with a viscosity μ flows at a mean velocity U. The force acting on each cylinder in the cell is equal to the force experienced by the fluid:

$$C_D U \mu N = (\Delta P) L \ . \qquad \textbf{[2.16]}$$

Rearranging [2.16] gives the drag coefficient

$$C_D = \frac{(\Delta P) L}{U \mu N} \ , \qquad \textbf{[2.17]}$$

where N can be related to the solid area fraction of the cell,

$$\phi = \frac{N a^2 \pi}{L^2} \ , \qquad \textbf{[2.18]}$$

which rearranges to give:

$$N = \frac{\phi L^2}{\pi a^2} \ . \qquad \textbf{[2.19]}$$

Substituting this equation for N and Darcy's Law [2.1] into the equation for the coefficient of drag gives:

$$C_D = \frac{\pi a^2}{\phi K} \quad . \qquad \textbf{[2.20]}$$

The assumptions generally made for analytical calculations to find the drag coefficient are that the fluid is incompressible, behaves in a Newtonian manner and that the Reynolds number for the flow is small compared to unity. The cylinders are assumed to be in fixed positions.

In 1982 Sangani and Acrivos[53] derived an expression for the drag coefficient at low volume fractions for a square array of cylinders. The analytical expression for a square array they derived to calculate the coefficient of drag for this condition was:

$$C_D = \frac{F}{\mu U} = \frac{4\pi}{\ln \phi^{-\frac{1}{2}} - 0.738 + \phi - 0.887\phi^2 + 2.038\phi^3 + 0(\phi^4)} \quad , \qquad \textbf{[2.21]}$$

where F is the force per unit length on a cylinder, μ is the viscosity of the fluid and U is the mean flow velocity of the fluid. For a hexagonal array, the equation for the drag coefficient is of the same form as [2.21] but the parameter values and the equation for ϕ are different.

At high volume fractions, the lubrication approximation[c] is much more appropriate since most of the pressure drop occurs as the fluid flows through the narrow gap between adjacent cylinders. The expression for this approximation is:

$$\frac{F}{\mu U} \sim \frac{9\pi}{2\sqrt{2}} \left\{ 1 - \left(\frac{\phi}{\phi_{\max}} \right)^{\frac{1}{2}} \right\}^{-\frac{5}{2}} \quad , \quad (\phi_{max} - \phi << 1) \, , \qquad \textbf{[2.22]}$$

where $\phi_{\max}$ is the maximum fibre volume fraction, i.e. when the cylinders are touching one another. Values obtained computationally showed good agreement with values obtained from these two asymptotic expressions (see Figure 2.6).

---

[c] Schlichtings Boundary Layer Theory (McGraw-Hill, 1968).

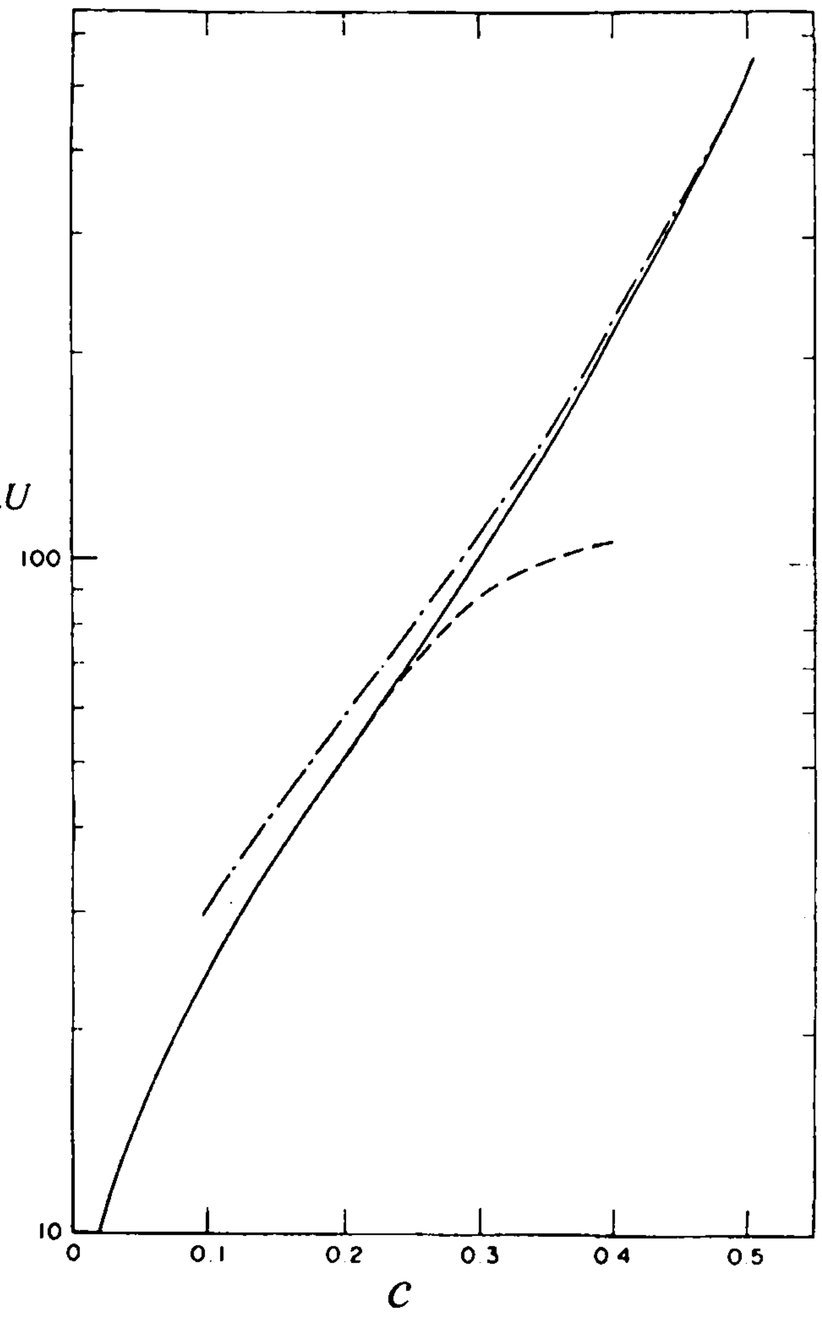


Figure 2.6 - Computed results (shown by solid line) of Sangani et al.[53] compared with numerical results from [2.21] (dashed line) and [2.22] (dashed/dotted line).

Koch and Ladd[54] extended [2.21] and [2.22] to account for finite Reynolds number in flows of Newtonian fluids.

Bruschke and Advani[3] developed a cell model and lubrication approximation into a closed form solution. The cell model is based on a single cylinder that is not surrounded by other cylinders but by a boundary at which the viscous stress is zero. They used the lubrication approximation, the cell model and a hybrid model to obtain mobility values (velocity over pressure gradient) for Newtonian and power-law fluids. Mobility, M, can be described using the following relationship:

$$M = \frac{UL}{\Delta P} = -\frac{K}{\mu} \qquad [2.23]$$

where U is the average velocity, L is the length over which the pressure gradient, ΔP, is acting. This value of mobility can be made dimensionless,

$$M' = \frac{\chi M}{(UL)^{1-n} a^{2n}} \ , \qquad [2.24]$$

where χ is the power-law coefficient, U is the average velocity, n is the power-law exponent and a is the radius of the cylinders.

Solutions for non-Newtonian fluids were found for power-law exponents of 0.5 and 0.8. The results were compared with computationally simulated results and this showed that the lubrication approximation and cell model could not be used separately to obtain mobility values over the whole range of porosities. The hybrid model showed good agreement with numerical results for both Newtonian and power-law fluids (see Figure 2.7). This meant that the mobility of non-Newtonian fluids could now be modelled analytically. The computer simulations that Bruschke et al.[3] carried out are reviewed in section 2.7.1.

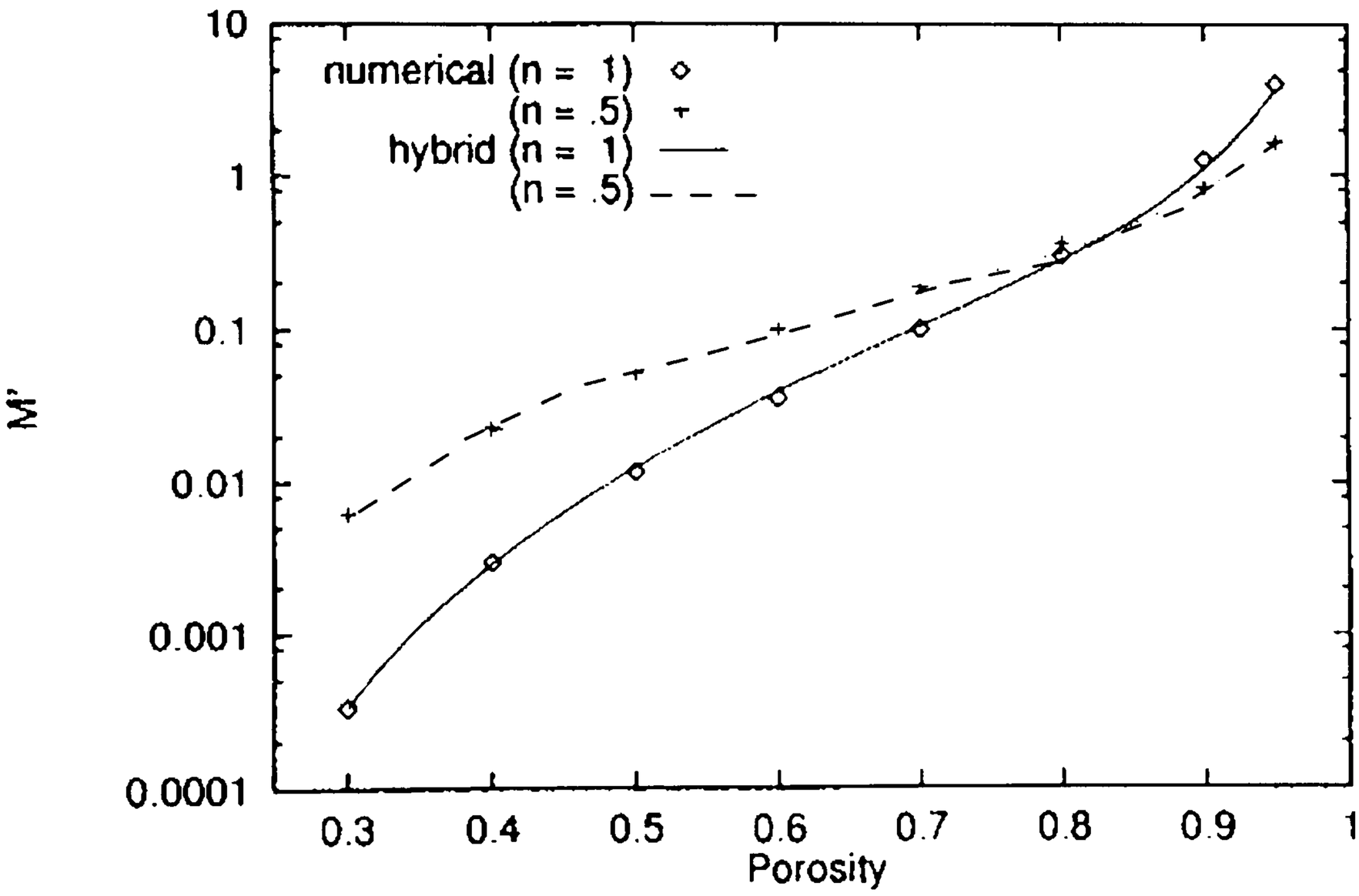


Figure 2.7 - Comparison of hybrid model results and computationally simulated results obtained by Bruschke et al.[3] for Newtonian (n=1) and power-law (n=0.5) fluids.

Generally more conventional mathematical analyses of fluid flow have been used. Stokes equations are commonly used to solve transverse fluid flow through arrays of cylinders, for example this is what Sangani et al.[53] used to analyse flow through a random array of cylinders which were periodically reproduced. They obtained permeability values that were averaged over several configurations of random arrays. In the case of RTM, these may be seen as physically more relevant results than values obtained for periodic arrays as tows become randomly arranged in processing.

Gebart[55] derived an analytical solution for transverse fluid flow between fibres in hexagonal and square arrays during the resin transfer moulding process which was in the same form as that of [2.22]. The solution to this equation is similar to the Kozeny-Carmen equation but it predicts that flow will stop when the maximum volume fraction is reached, i.e. when the gap size is zero. The geometry used to obtain the analytical solutions is shown in Figure 2.8. The solutions that Gebart[55] obtained from these analytical expressions showed good agreement with computational solutions and experimental results.

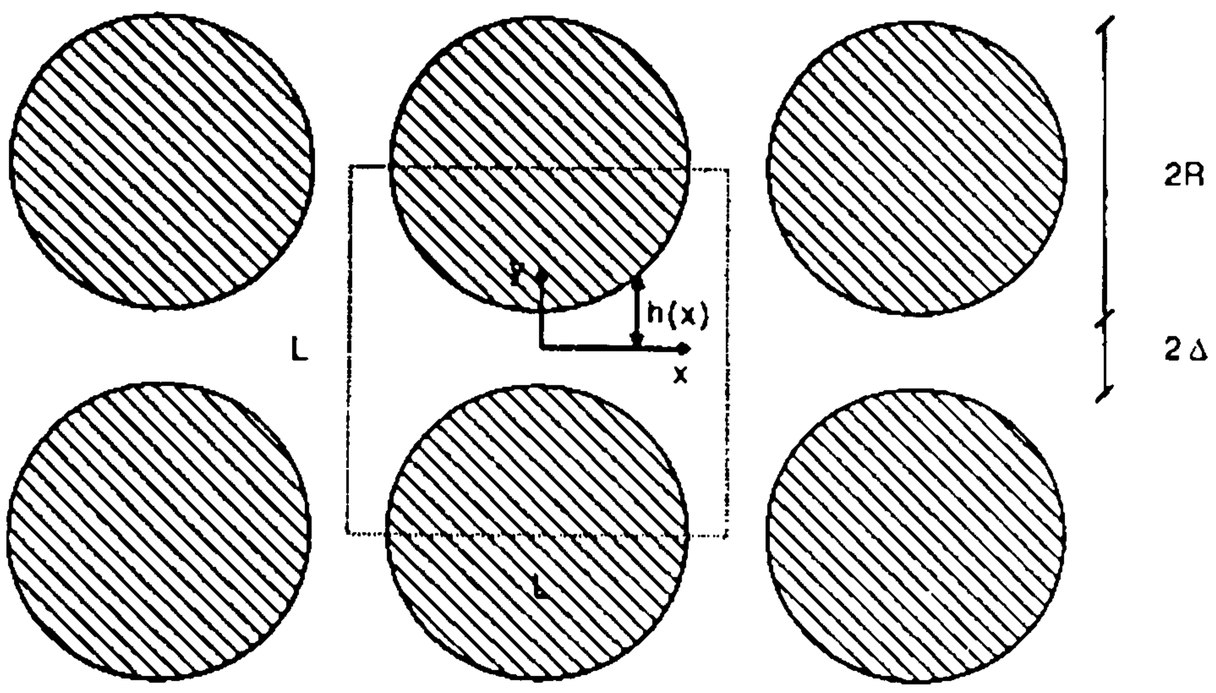


Figure 2.8 - Sketch of square fibre array in a unidirectional reinforcement where *R* is the rod radius, Δ is the rod spacing and *L* is the length/width of the unit cell[55].

2.3.2. Ellipsoid Shaped Tows

Circular cylinders are a common approximation to the shape of fibres and tows in RTM, but tows are not likely to be this shape inside the mould. Reinforcement plies undergo compression when the mould is closed and this causes the cross-sections of the tows to form elliptical rather than circular shapes. Saunders et al.[56] investigated the effect of compression on the microstructure of plain-woven fibre cloths. Their studies showed that the tows approximated an elliptical shape. The width of these ellipses increased with increasing pressure and the height decreased, i.e. the ellipses became more elongated.

To improve the accuracy of the computer simulations it is important to obtain the aspect ratios of the ellipses that the tows formed in order to produce realistic meshes. Image analysis can be used to extract this information from optical microscope

images of composite specimens. Pearce et al.[57] examined the possibility of automating image analysis of fabric architecture. From this they aimed to obtain a relationship between permeability and microstructure. They digitised images of fabric microstructures and then carried out fractal analysis on them. Fractal images of different weaves of fabric were produced and experimental permeabilities were obtained for each. It was found that variations in permeability and mechanical properties could be related to variations in microstructure.

Bhat et al.[58] digitised images of dendrites that form in Columnar-Dendritic alloys and then created meshes on these images. These were used for computer simulations of fluid flow around dendrites during casting. The investigation carried out by Bhat et al. is reviewed in section 2.7.2.

Very few investigations have been carried out into the analytical solutions of fluid flow perpendicular to ellipsoid shaped tows. Kuwabara[59] used a method proposed by Imai to calculate the drag force experienced by a lattice of equidistant elliptical cylinders. These elliptical cylinders were placed parallel to each other at a tilt angle β to uniform flow at small Reynolds number, as shown in Figure 2.9. He calculated the drag and lift coefficients for three Reynolds numbers and six different values of tilt angle, β, for $\alpha = 90\,°$ and $h = 10$, where

$$h = \frac{d}{(1+\sigma^2)}, \qquad [2.25]$$

d is the distance between ellipses and $(1+\sigma^2)$ is the semi-major axis for an aspect ratio of t.

The drag and lift coefficients were calculated for four different aspect ratios of elliptic cylinders: $t = 0$ (flat plates), $t = 0.1$, $t = 0.5$ and $t = 1.0$ (circles). The results from Kuwabara's[59] calculations are shown in Figure 2.10.

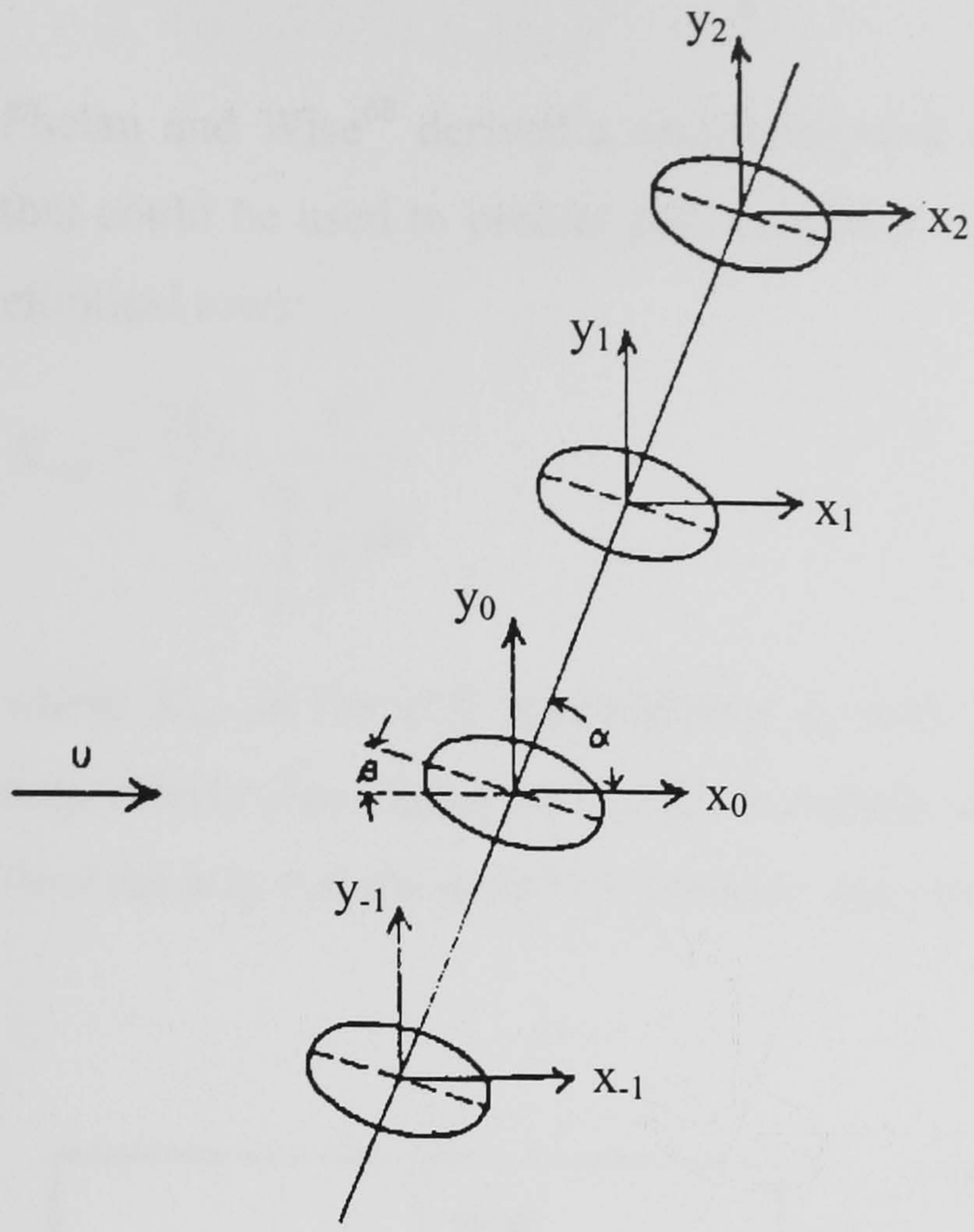


Figure 2.9 - The general configuration of a grating of elliptic cylinders used by Kuwabara[59] to calculate drag and lift coefficients.

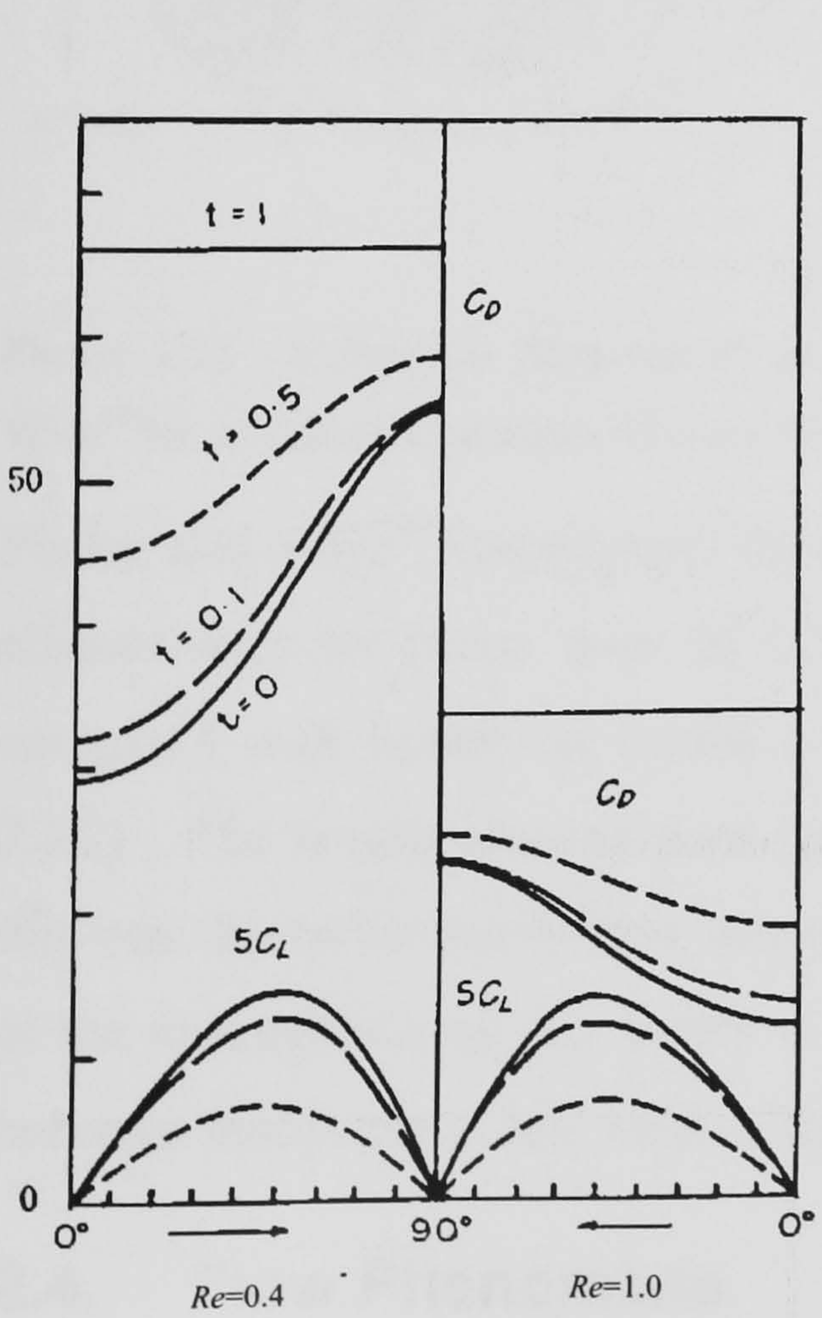


Figure 2.10 - Variation of C_D (drag coefficient) and C_L (lift coefficient) with β when h=10, α=π/2 and Re=0.4 and 1.0 obtained by Kuwabara[59] using a method proposed by Imai.

Phelan and Wise[60] derived a semi-analytical expression from the lubrication theory that could be used to predict permeabilities at high volume fraction for flow around elliptical tows:

$$K_{cell} = \frac{2L_x}{L_y} \frac{1}{\int_{-L_x}^{L_x} \frac{1}{f} dx} \qquad [2.26]$$

where K_{cell} is the cell permeability, L_x and L_y are half the cell width and depth respectively (see Figure 2.11) and f is a parameter that depends on the geometry of the flow domain and the intra-tow porosity and permeability.

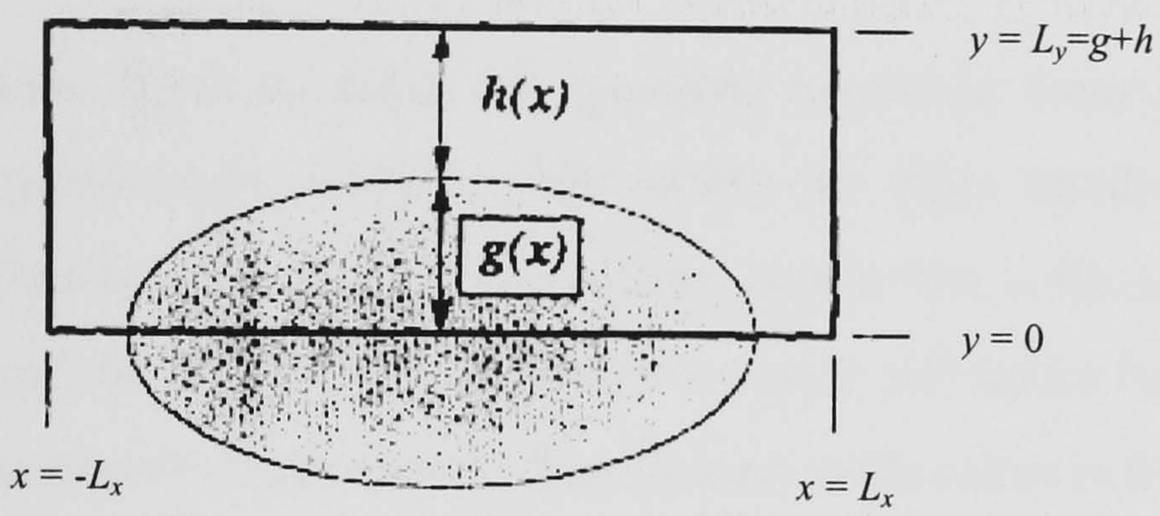


Figure 2.11 - Schematic diagram of an elliptical tow giving parameters used by Phelan and Wise[60] for lubrication analysis of cross flow.

Phelan and Wise[60] investigated the transverse permeability of a rectangular array of ellipses with an aspect ratio of 0.5. The results of the analytical solutions were compared with numerical results (also obtained by Phelan and Wise[60], see section 2.7.2). The results showed poor agreement especially at low volume fractions and this was due to the lubrication theory being used to approximate the fluid flow. One of the assumptions of this theory is that the transverse velocity is negligible, which becomes inaccurate at low volume fractions.

2.4. Flow Phenomena

Experimental studies have identified several phenomena during the processing of composite parts that influence the success of mould filling simulations. Some of the key phenomena affecting the flow of resin are presented in the following sub-sections.

2.4.1. Void Formation

Although the properties of manufactured composites are generally quite good they are often adversely affected by flaws that may occur during the manufacturing process[61]. One type of defect is voids in the matrix area. It has been suggested that the inter-laminar shear strength of fibre reinforced polymer composites (FRPC) decreases by 7% for each volume percent of voids up to at least the 4% level[62]. The transverse tensile strength, compressive strength and the flexural strength have also been proven to reduce with increasing void content[62]. Voids may also impair the surface quality of composites[63] and reduce the water resistance of the composite[64]. The presence of voids within a composite reduces its water resistance as water can occupy the void area. This can lead to structural degradation of the composite part in the event of the water freezing and hence expanding within the void.

Two types of voids are typically identified from micrographs of cured laminates: cylindrically shaped voids within the fibre bundles and spherically shaped voids between the bundles. It has been shown that voids are initiated at the resin flow front and that the preform geometry strongly influences both the formation and the possible transport of the voids[65]. The formed voids move in the direction of the resin flow front if the pressure gradient is sufficiently high to force the voids through constrictions in the reinforcement. It is shown that the cylindrical voids are more likely to be trapped in constrictions than the spherical voids[65].

The most efficient way to decrease the void content is to apply a partial vacuum at the outlet side of the mould. This decreases the size of the voids formed and makes them more mobile. Also, the mould should be airtight. Lundström[65] also considered other techniques of reducing the void content such as degassing the resin before injection, using resins and reinforcements that are compatible, using reinforcements in which voids are mobile, applying pressure during cure and continuing to fill the mould after complete filling with a high driving pressure.

Research has also revealed that the void content in a given fibre preform depends mainly on the capillary number during filling, which is defined as the ratio of viscous force to capillary force. The void contents measured with different fluids and

processing conditions were found to overlap with one another when the capillary numbers were the same[66,67]. Patel and Lee[68] proposed a model based on the unsaturated flow through a porous medium. However, their model neither accounted for the void formation at the flow front nor included the size and population of voids.

Moon et al.[69] developed a mathematical model to describe void formation resulting from a microscopically non-uniform velocity field at the resin flow front. Both the overall pressure gradient and the local capillary pressure were used to calculate the resin velocities inside and outside a tow at the flow front. Figure 2.12 shows the progression of the flow front both within and between fibre tows. The flow front is observed to progress more rapidly between the tows than within them.

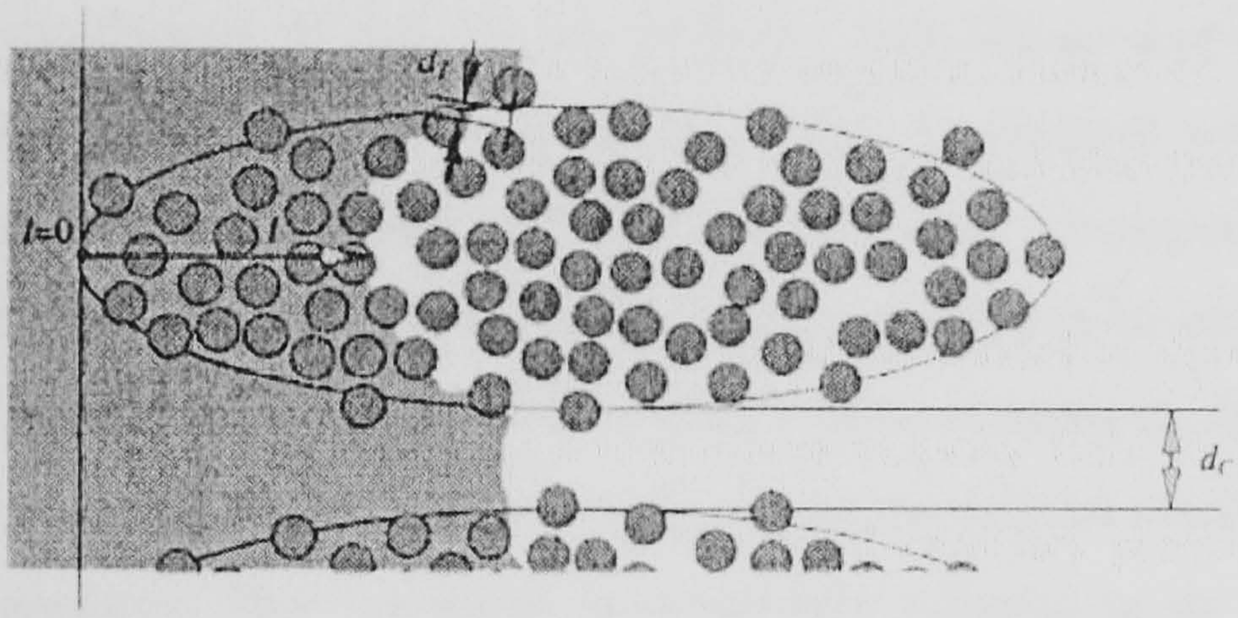


Figure 2.12 – Diagram showing the progression of the flow front both within and between fibre tows[69].

2.4.2. Race-Tracking

Air channels can be present within a mould cavity, either unintentionally formed, or intentionally placed to enhance the mould filling process. Such channels provide paths of relatively low flow resistance, and can drastically alter the flow front advancement and injection pressures, this effect being commonly referred to as 'race-tracking'. Race-tracking must therefore be considered in numerical mould-filling simulations.

Race-tracking can occur unintentionally at edges, corners and other complicated portions of a mould, as it may be difficult to fill the mould cavity consistently with the preform. This type of race-tracking may be difficult to foresee, and should be eliminated by careful mould design, as far as possible. Bickerton and Advani[70]

focussed on race-tracking through well defined air channels within a mould. Such air channels may be used intentionally, to improve and facilitate mould filling[71]. Air channels incorporated into a mould design may be used to channel resin quickly to places in a mould that may be difficult to fill. If air channels can be implemented into a mould design, they can reduce the overall flow resistance of a mould cavity, reducing the fill time for constant pressure injection or reducing the required injection pressure for constant-flow-rate injection.

Several methods have been explored in the literature to model race-tracking within existing Darcy's law-based filling simulations. Most of this work has focused on race-tracking occurring in well-defined air channels. It would be highly advantageous to find an efficient method to model non-Darcian flow in air channels, within existing simulations. If this can be achieved, then the development of simulations that must solve both Darcian, and Stokes flows in different portions of the domain may be avoided. One simple approach that has been developed, which can be easily applied within Darcy's law-based simulations, represents air channels and other high porosity regions in a mould cavity within a finite-element model by representative groups of elements. These elements are given permeabilities much greater than those of the bulk preform. This approach is commonly referred to as the 'equivalent permeability' approach. Significant work is described in the literature on the validation of this approach, and methods to predict the equivalent permeability analytically. Several variations of this approach have also been explored.

Han et al.[72] and Leek at al.[73] studied race-tracking in rectangular moulds, where well-defined regions of higher-porosity preform were set up on at least one side of the mould. The permeabilities in both the bulk preform and the high-porosity regions were measured, and did not therefore require to be modelled by equivalent permeabilities, or other methods. Fong and Advani[74] derived an analytical expression for permeabilities in mould corners where air channels exist, though race-tracking was not the main focus of this work. Bickerton and Advani[75] experimentally investigated race-tracking in air channels, by considering purely two-dimensional flow in a rectangular cavity, having a well-defined air channel along one side of the mould. Experimental flow fronts were matched with numerical predictions to measure equivalent permeabilities for continuous-strand-random-mat at three different volume

fractions, and a variety of air-channel widths. An empirical relation for equivalent permeability of rectangular-duct air channels was derived. This empirical relationship was compared with an analytical expression for rectangular-duct equivalent permeability, based on steady-state, fully developed Stokes flow. A variety of equivalent permeability solutions were presented by Ni et al.[76] for various air-channel cross-section geometries. The rectangular-duct model was extended to consider the porous interface of the preform at one of the four duct walls. This model was tested in a rectangular mould having channels at either side, experimental flow fronts and numerical predictions were visually compared for one experimental case.

Flow channels in the familiar rectangular mold configuration were studied by Sheard et al.[77], applying a novel technique to allow the use of high-volume fraction preforms not achieved by other investigators. Such preforms prove difficult in this mold configuration, as it is next to impossible to achieve an accurate, undamaged preform edge after cutting. A flow-front comparison scheme similar to that used by Bickerton and Advani[75] was used. Hammami et al.[78] derived and applied two simple models for equivalent permeability. Flow fronts were compared visually for 2D flow in a rectangular mould cavity with an air channel along one side. The effect of transverse flow from the channel into the preform was considered, and a 'transverse flow factor' was developed to characterize the amount of such flow. Hammami et al.[78] suggested a limiting value for this transverse flow factor, above which transverse flow should be considered in the equivalent permeability used.

2.5. Preform Compression

Gutowski et al.[79,80,81] performed a series of experimental and theoretical studies on the compression of unidirectional composites during manufacture. They envisaged a type of Voigt viscoelastic model in which the total applied pressure was split into two components, acting on the fibres and resin respectively. The fibre reinforcement was considered as an assembly of solid beams which behaved as a whole in a non-linear elastic manner. The resin flowed through the reinforcement under compression following Darcy's law where the permeability depended on the value of the local fibre volume fraction and hence the degree of compression. Continuity equations were applied to both fibres and resin to ensure mass balance during compression. The results of this model showed that the pressure component acting on the fibres depends

on the fibre fraction whereas the pressure component causing the resin flow depends on both the range of fibre fraction (rate of compression) and the fibre fraction value. Hence, when compression is performed at very low speeds, the effect of resin flow on the relation between pressure and change of fibre fraction may be ignored. Comparisons between predictions and experimental data were made under elastic compression conditions[80] and theoretical parametric studies were carried out under viscoelastic conditions[79], though without a corresponding comparison with experimental data.

Other studies[82,83] have modelled compression during the processing of composites as a type of viscous squeeze flow without any elastic contributions. By fitting predictions with experimental data, the model rheological parameters of the composite were determined. The viscous approach was applied[82,83] to non-stitched, unidirectional or random fibre mats in which the fibres were assumed to be able to move without severe restrictions. Any restrictions in the fibre motion were translated into extremely high theoretical viscosities for the composite.

Hamada and Ikegawa[84] simulated the compression process with simultaneous resin infiltration in a structural resin transfer moulding process following the viscous-fluid-dynamics approach, where the composite viscosity depended on permeability which, in turn, was affected by the degree of compression. No comparisons were presented between predictions and experimental data.

If a viscoelastic model is applied to studies of woven fabrics, the deformation of the fabric and the resin flow need to be considered separately. Carnaby and Pan[85] considered the possibility of a fibrous assembly behaving as a viscoelastic solid with a compression hysteresis. They attributed this to slip mechanisms at fibre contact points during compression.

Lekakou et al.[86,87] constructed a micromechanical model of the compression of dry, plain weaves assuming them to behave as a network of elastic beams. They fitted the resulting mathematical relation for pressure against fibre fraction to experimental data; it was found that in the fabric tested the value determined for the empirical constraint factor at the support points of the fibres/beams corresponded to full slip of

fibres at the contact points. Toll and Manson[88] developed a micromechanical model for the compression of fibre reinforcements in which they considered elastic deformation without inelastic fibre sliding at the contact points. However, the constraint factor at the support points of the fibre/beams can be adjusted in value to incorporate reversible fibre slip at the contact points. According to Toll and Manson[88] the applied pressure on the fibres is proportional to V_f^5 for planar fibre networks but there is some uncertainty about the power-law index when fibre bundles are present.

In experimental studies[89,90], compression data for weaves were fitted to the power-law relation, $P \alpha V_f^b$, with power-law index, b, in the range of 7-11. Summerscales and Pearce[91] fitted their experimental compression data to b=5 approximately for a single plain woven cloth and b=7-8 for assemblies of up to five layers of the same cloth. Assemblies of woven cloths[91] were subjected to relaxation cycles in which the reinforcement demonstrated pressure relaxation indicating viscoelastic behaviour for the tested dry assemblies. Saunders et al.[56] carried out compression studies on assemblies of plain woven, twill and satin fabrics. They concluded that dry compression was independent of the compression rate. Their compression curves were fitted to the power law relation with b in the range 10-10.5 for the plain weave, b=9.8 for the twill weave and b=9.1 for the satin weave.

An area of further concern is the curing resin behaving in a viscoelastic manner. Skartsis et al.[92] presented a semi-analytical, one dimensional model for viscoelastic impregnation of fibrous media. The model contains a significant number of empirical constants to be determined experimentally.

2.6. Fibre Wetting

An important parameter in the production of fibre reinforced polymer composites (FRPC) is the wetting between the polymers and the fibres. An improvement of the wettability will generally result in easier production and improved product quality.

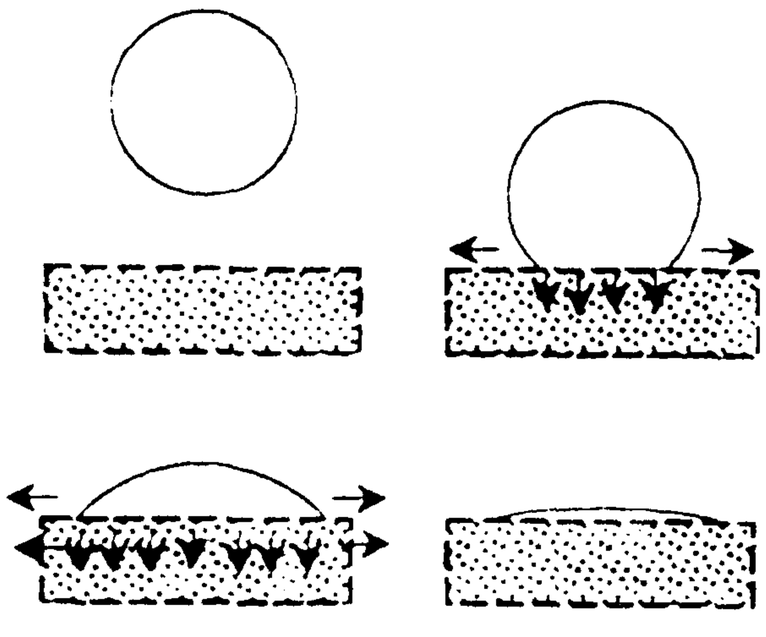


Figure 2.13 – Typical development of a liquid drop wetting a porous media[98].

Fibres used in FRPC are often gathered in bundles which can contain hundreds or even thousands of fibres. These bundles can be assembled to form fibre mats. When measuring the wetting compatibility the wetting can either be measured on single fibres, the fibre bundles or fibre mats. The Wilhemy method[93], the liquid membrane method[94] and the method of spreading of liquid droplets on cylindrical surfaces[95] all assume measurements on single fibres. However, several factors may influence this choice. Uneven distribution of surface treatment on single fibres can lead to a large deviation of the wetting measurement on individual fibres. Single fibre measurements are not suitable when the fibre bundles have been treated with coating or when the fibre mats are applied with binder. For several processes of FRPC the fibres are wetted simultaneously and not individually. Hence, wetting measurements on individual fibres do not always give a value of the wetting relevant to actual process conditions of FRPC.

The wicking method[96] and the method of wet-out time[97] measure wetting on fibre bundles and fibre mats. The drawback with the wicking method, however, is that large channels between the fibre bundles can influence the wicking. With the wet-out time method the reinforcement geometry may strongly influence the results. Dahlbäck and Lundström[98] proposed the FIBRO 1100 DAT device that dynamically measures the contact angle. Their results showed that the measured values of contact angle appear to have a strong correlation with the mechanical properties of the finished composite.

2.7. Computational Simulations

This thesis presents experimental studies on the propagation of the fluid flow front during impregnation and also the velocity field within saturated media. It is therefore useful to consider the literature on computational simulations of fluid flow around cylinders.

Computer modelling of fluid flow around cylinders and other geometries is examined in this section. The majority of investigations have been concerned with cylinders of circular cross-section and it is only recently that analysis has been extended to other cross-sectional shapes such as ellipses. Sections of resin transfer moulded components indicate that the actual cross-section of the tows during resin impregnation is elliptical rather than circular, so the modelling of fluid flow around elliptical shaped tows is important to achieve more accurate numerical solutions.

Generally for computer simulations the two-dimensional steady-state Navier-Stokes equations are used to describe the flow (Nagelhout et al.[99]):

$$\rho u\frac{\partial u}{\partial x}+\rho v\frac{\partial u}{\partial y}=-\frac{\partial p}{\partial x}+\mu\left(\frac{\partial^2 u}{\partial x^2}+\frac{\partial^2 u}{\partial y^2}\right), \qquad [2.27]$$

$$\rho u\frac{\partial v}{\partial x}+\rho v\frac{\partial v}{\partial y}=-\frac{\partial p}{\partial y}+\mu\left(\frac{\partial^2 v}{\partial x^2}+\frac{\partial^2 v}{\partial y^2}\right), \qquad [2.28]$$

subject to the continuity equation for incompressible fluid:

$$\frac{\partial u}{\partial x}+\frac{\partial v}{\partial y}=0, \qquad [2.29]$$

where ρ is the density of the fluid, u and v are components of the velocity vector, with respect to Cartesian coordinates, x and y, and μ is the viscosity.

2.7.1. Simulations of Flow Transverse to Circular Cylinders

There has been a significant amount of research into fluid flow around circular cylinders, rather than ellipsoidal or irregular shaped cylinders. The reason for this is that it simplifies the problem by reducing the number of parameters required to describe the geometry, and allows relatively easy meshing of the geometries. It is also a classical problem in fluid mechanics and has been studied for other applications

- one of the main motivations for research into fluid flow around cylinders has been for the design of heat-exchangers.

Bruschke and Advani[3] carried out computational simulations of the flow transverse to cylindrical fibres for both Newtonian and power-law fluids under a creeping flow regime (so inertial effects could be ignored). Simulations were carried out using the numerical flow simulation package POLYFLOW for porosities in the range of 0.3 to 0.95 and the results from these were related to flow on the macroscopic scale which is described by Darcy's Law, [2.1]. They applied a known pressure drop to obtain a flow rate through the fibre array that could then be used to calculate the permeability.

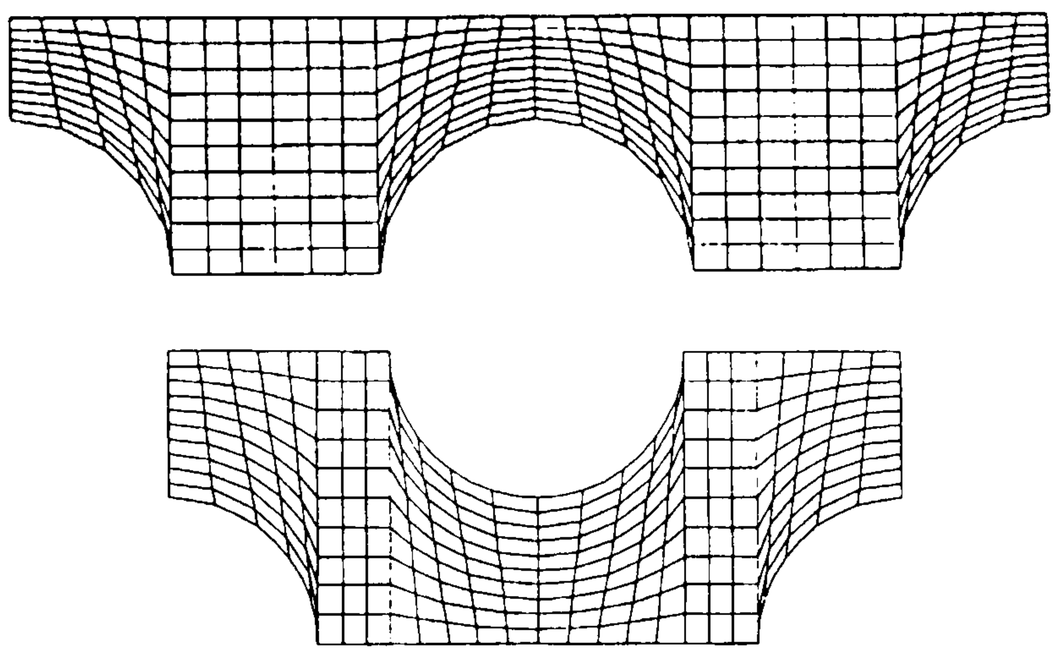


Figure 2.14 - Square (top) and hexagonal (bottom) unit cells used by Bruschke and Advani[3] in their computer simulations.

The unit cells that Bruschke and Advani[3] used are shown in Figure 2.14 and these correspond to square and hexagonal arrays of cylinders. The conditions they applied to these unit cells were:

- Constant pressure boundary conditions applied to the inlet and outlet.
- No-slip boundary conditions applied to the cylinder surface.
- Symmetry conditions applied on the remaining surfaces.

The porosity was varied by changing the fibre diameter appropriately, although the fibre packing arrangement remained unchanged. A mesh density sensitivity analysis was carried out and Bruschke and Advani[3] noticed only a 0.7 % difference in the flow rate obtained when quadrupling the mesh density. Bruschke and Advani[3] used this method for both the Newtonian and power-law fluids with a power law exponent of 0.5. As the viscosity for the power-law fluids is not fixed the results obtained could

not be presented in terms of a drag coefficient $F/\mu U$; instead, the mobility was used (see [2.23]).

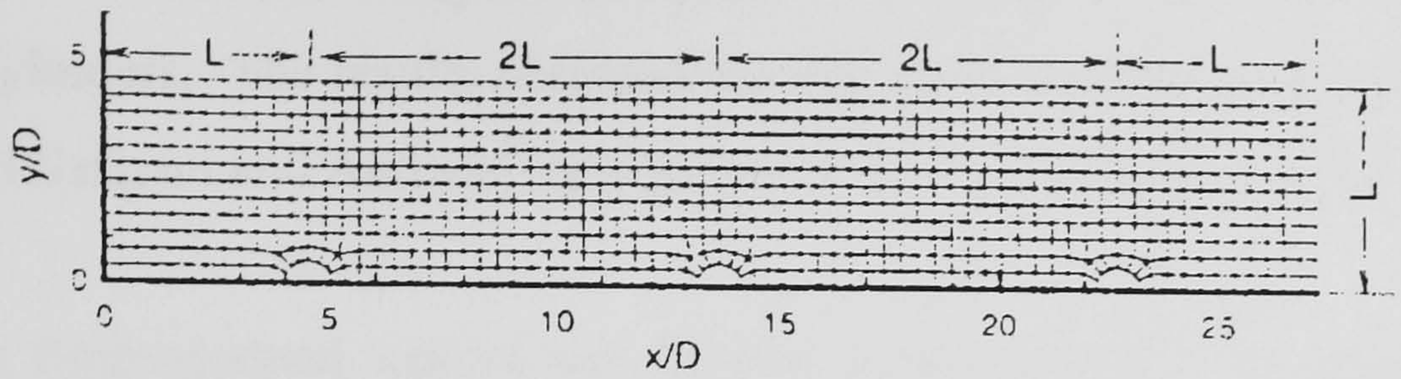


Figure 2.15 - Mesh used by Nagelhout et al.[99] to simulate fluid flow perpendicular to cylinders in sparse arrays.

Nagelhout et al.[99] also simulated the fluid flow perpendicular to cylinders, using a finite element formulation. They concentrated on sparse arrays and Reynolds numbers up to 40. Like Bruschke and Advani[3] they used the Navier-Stokes equations to solve two-dimensional flow but only for a square array of cylinders. A similar mesh geometry was used, as shown in Figure 2.15. However, a boundary condition of uniform velocity at the inlet was imposed, which is not valid for periodic arrays. A three-cylinder domain was chosen to allow a periodic flow to develop.

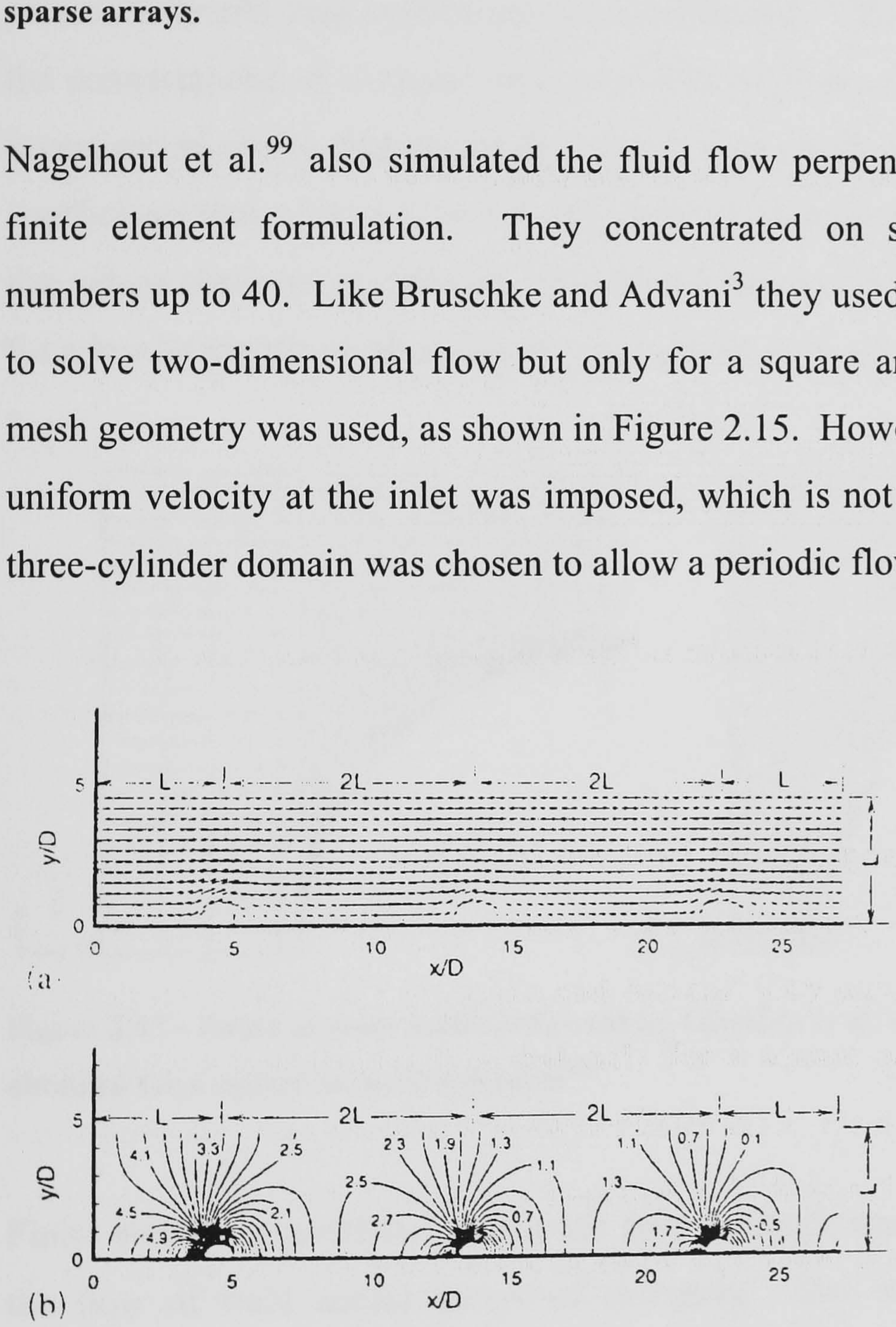


Figure 2.16 - Velocity vector diagram[99] (a) and pressure contour diagram (b) for numerical simulation of flow normal to circular cylinders in a square array where Re = 5 and $g_L = 0.99$.

Nagelhout et al.[99] calculated an average pressure gradient from the pressure gradients between the first and second cylinders and the second and third cylinders. From this

and the superficial velocity (equal to the uniform velocity specified at the inlet) they calculated the permeability. Figure 2.16 shows the velocity vector diagram and pressure contour diagram obtained for flow transverse to a square array of circular cylinders. The results obtained showed good agreement with the analytical solutions of Sangani and Acrivos[53] and the numerical computations of Edwards et al.[100].

A finite element method was used by Edwards et al.[100] to obtain numerical solutions for cross-flow through spatially periodic arrays of cylinders from which the permeability and drag coefficients were calculated. The finite element mesh used for the computations of a square array is shown in Figure 2.17. The main aim of their investigation was to find the effect of Reynolds number on the permeability. The drag coefficients they obtained for low Reynolds number showed excellent agreement with the values obtained analytically by Sangani and Acrivos[53]. A pressure contour map for a low Reynolds number simulation is shown in Figure 2.17.

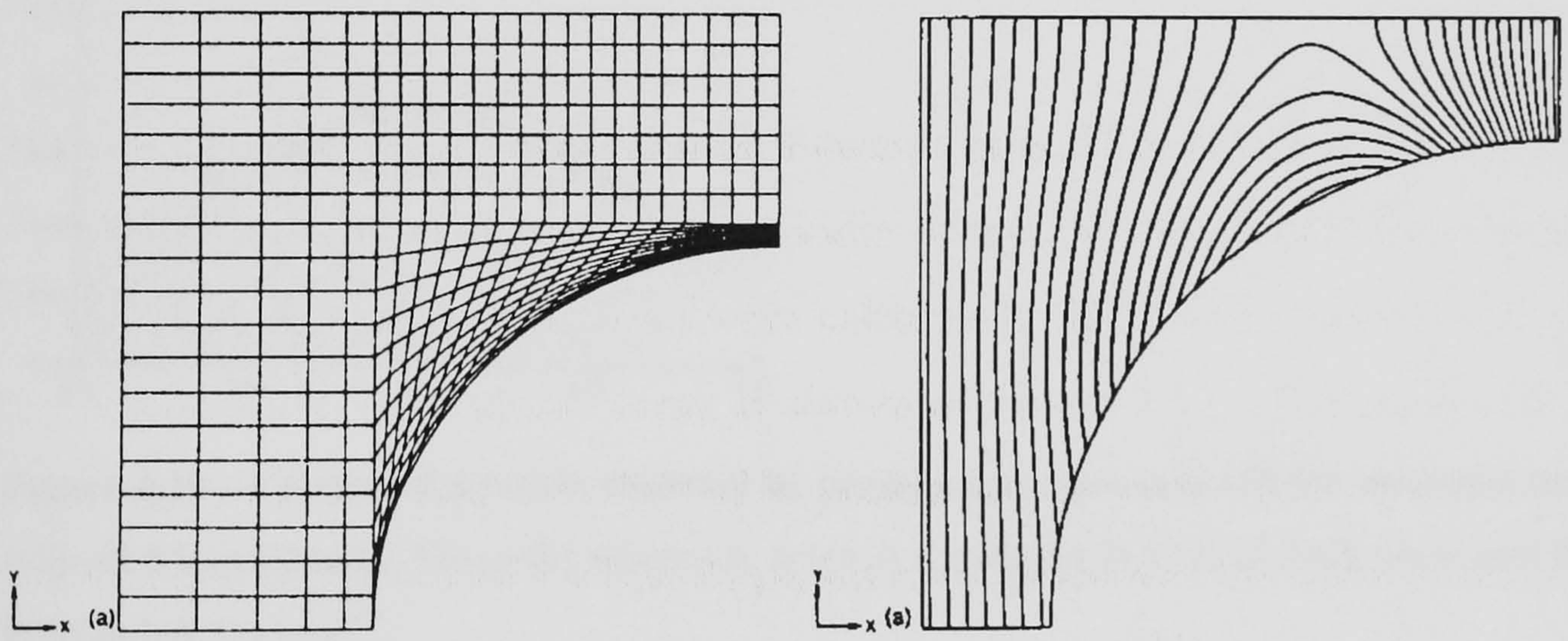


Figure 2.17 - Finite element mesh (left) used by Edwards et al. and pressure contour map (right) obtained for a square array of cylinders[100].

Finite element algorithms are not the only methods that have been used to simulate the flow of fluid across arrays of cylinders. The boundary integral method, or boundary element method (BEM), has also been used. For example Papathanasiou[101] used this method to solve the Stokes equations. This method involves the use of integral equations that are defined on the boundary of the domain rather than differential equations. The meshing of the geometry is much easier using this method as only the boundary of the flow domain has to be meshed. A post-processing technique can be used to obtain solutions in the interior of the domain if required.

Papathanasiou[101] used BEM to find the effective permeability of square arrays of unidirectional fibre tows within which individual fibres were arranged in a uniform square packing. Figure 2.18 shows both an impermeable fibre tow and a permeable tow with the fibres arranged in a square packing. In the case of the permeable tow, both inter-tow and intra-tow porosities were analysed. Papathanasiou compared some of his BEM computations with the analytical solutions of Gebart[55] reviewed in section 2.3.1 and good agreement was seen.

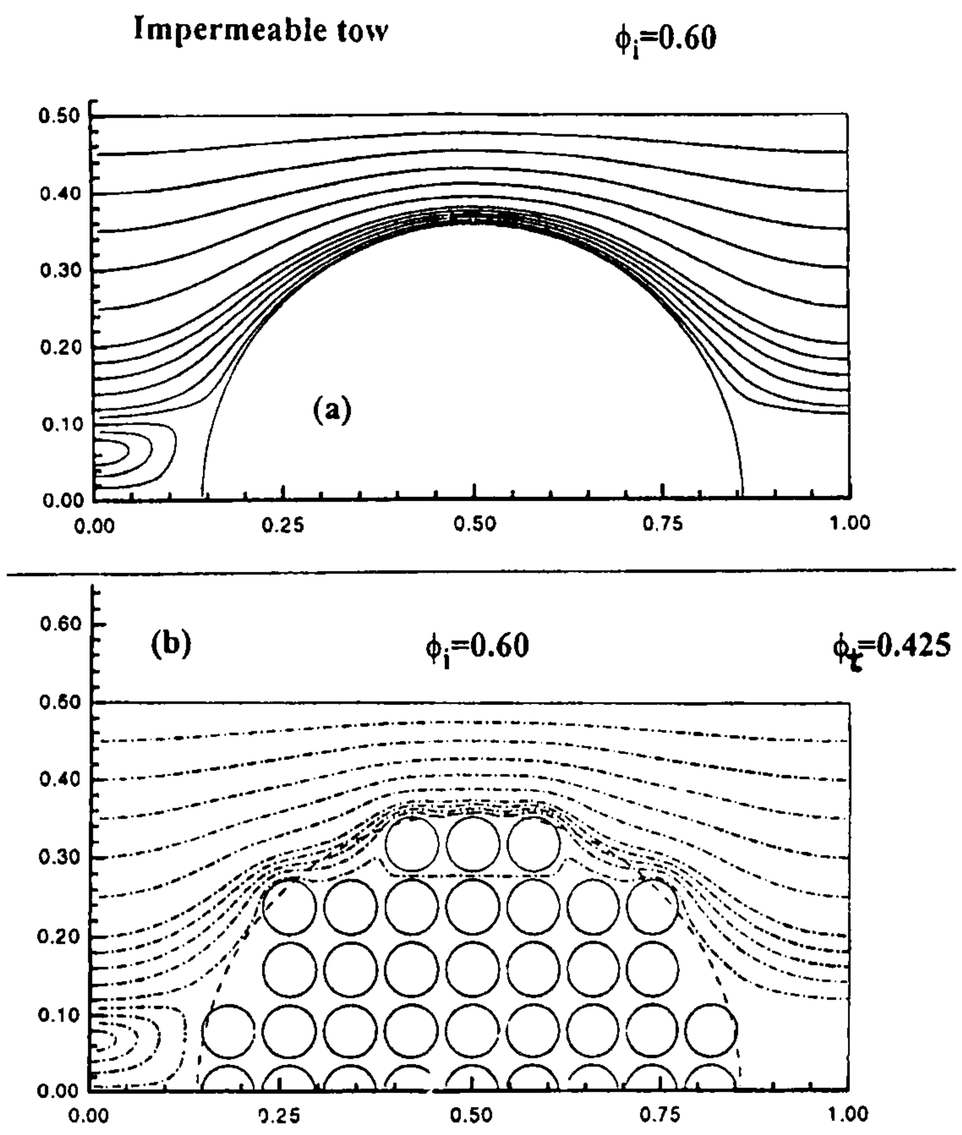


Figure 2.18 - Computed particle trajectories (streamlines) in a unit cell for an impermeable tow (a) and a bundle of 61 fibres (b) where the intra-tow porosity is 60% in both cases and fluid flow is from left to right[101].

2.7.2. Flow Simulations for Other Geometries

Although much of the current work addresses flow across cylinders it is also important to consider fluid flow transverse to elliptical shaped fibre tows. There has been very little previous work that has examined flow across geometries other than cylinders.

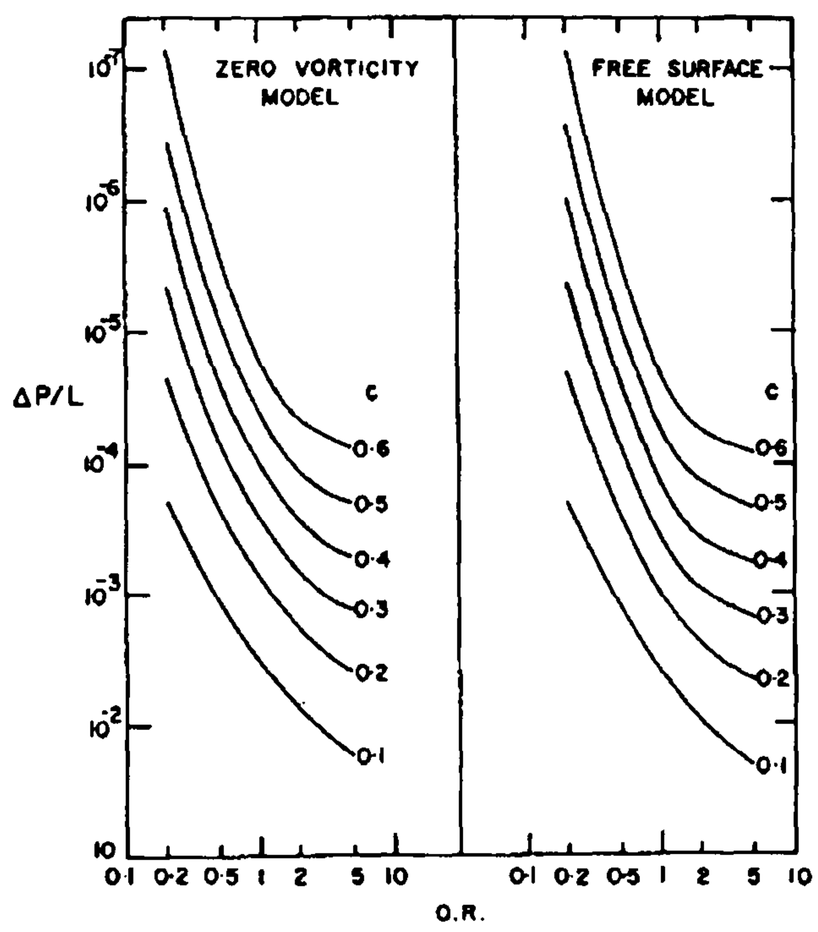


Figure 2.19 - Change in pressure per unit length ($\Delta P/L$) obtained by Epstein and Masliyah[102] at various orientation ratios (*O.R.*) for creeping flow perpendicular to elliptical cylinders with solid volume fraction *c*.

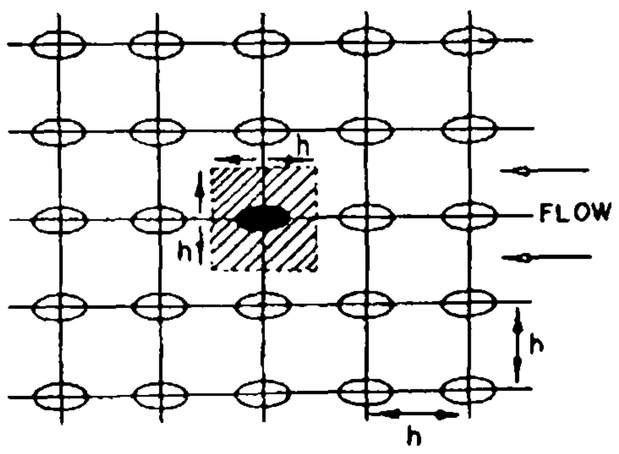


Figure 2.20 - Rows of elliptical cylinders used by Epstein and Masliyah[102] to form a square array of pitch *h*.

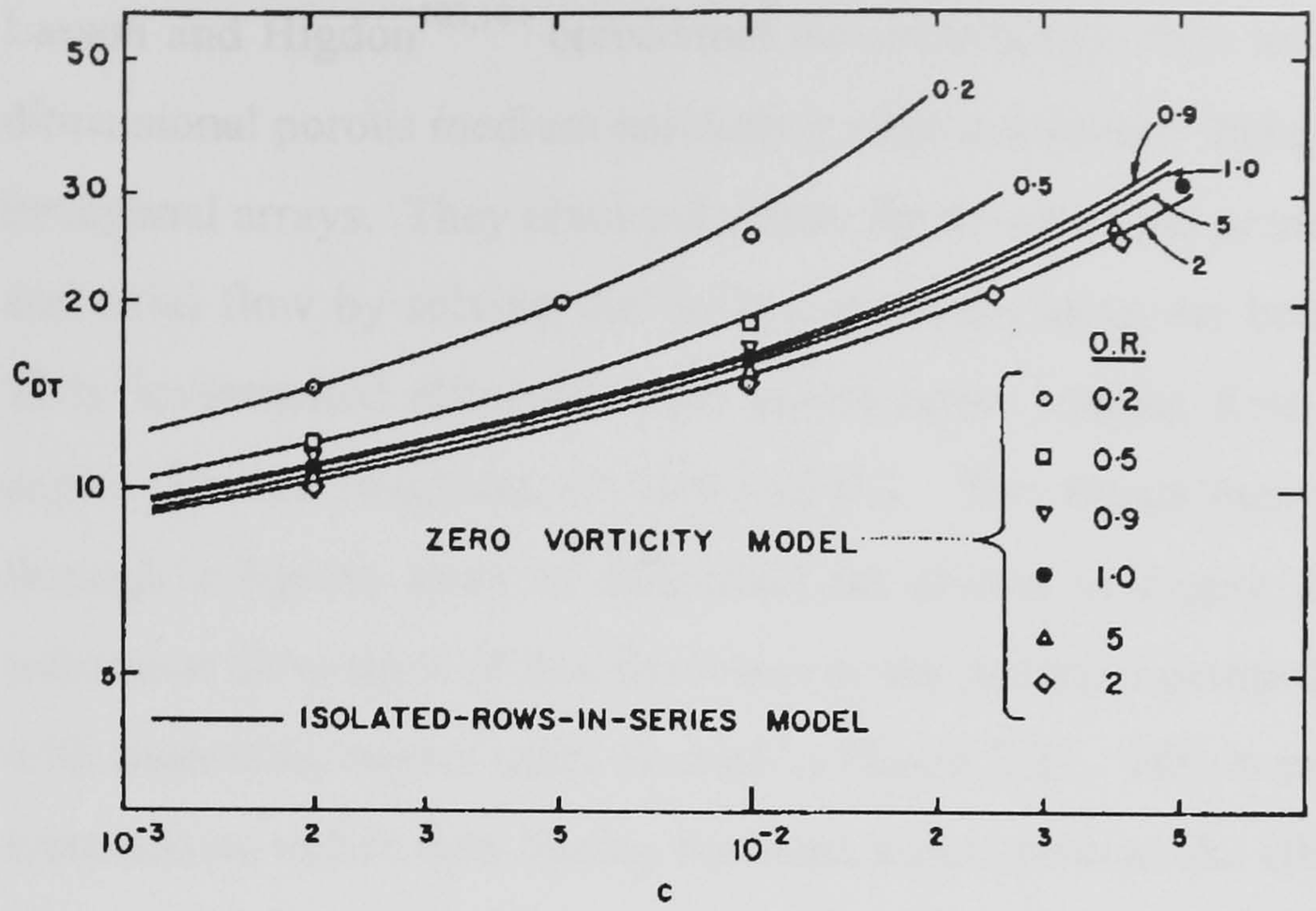


Figure 2.21 - Comparison of total drag coefficient, C_{DT}, calculated for elliptical cylinders by the zero vorticity cell model and by the isolated-rows-in-series model for creeping flow[102]. *O.R.* is the orientation ratio and *c* is the solid concentration.

Epstein and Masliyah[102] investigated creeping flow around elliptical cylinders in rows. They used the Navier-Stokes equations with both the Happel free surface and the Kuwabara zero vorticity cell models to calculate the change in pressure per unit length for transverse flow through a square array. This was carried out for various orientation ratios of fluid flow with respect to the major axis of the ellipsoids (see Figure 2.19). From the results of the zero vorticity cell model they calculated the total drag coefficients and compared them with values for the isolated rows-in-series model (see Figure 2.20). As seen in Figure 2.21 the two models showed excellent agreement at low values of concentration *c*.

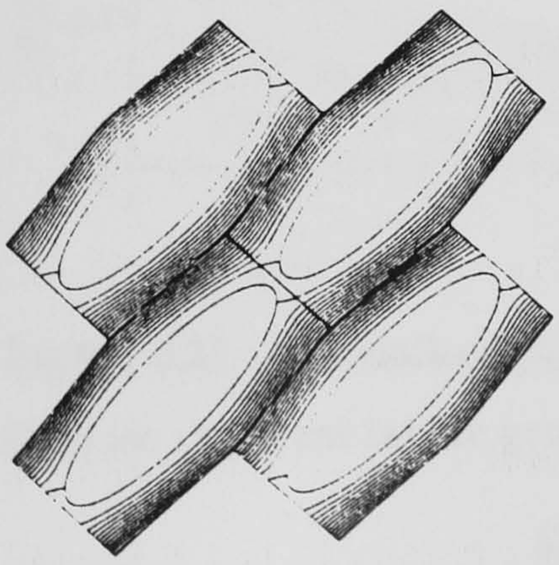


Figure 2.22 - Streamlines obtained by Larson and Higdon[103] for flow through a square array of elliptical cylinders with area fraction 0.3.

Larson and Higdon[103,104] considered the microscopic flow near the surface of a two-dimensional porous medium containing elliptical shaped inclusions in both square and hexagonal arrays. They obtained values for the principal permeabilities for transverse and axial flow by solving the Stokes equations using the boundary-integral method. They investigated ellipsoids with aspect ratios ranging from 1 to 10 at various tilt angles for area fractions of 0.05 and 0.3. The streamlines they obtained for flow through a square array of ellipsoids are shown in Figure 2.22. Their results for transverse flow showed that the lower of the principal permeabilities approaches zero with increasing aspect ratio, as seen in Figure 2.23. This is expected as the unit cells were square rather than having the same aspect ratio as the ellipsoids. So an increase in area fraction leads to a more significant change in permeability in one direction than the other (see Figure 2.23).

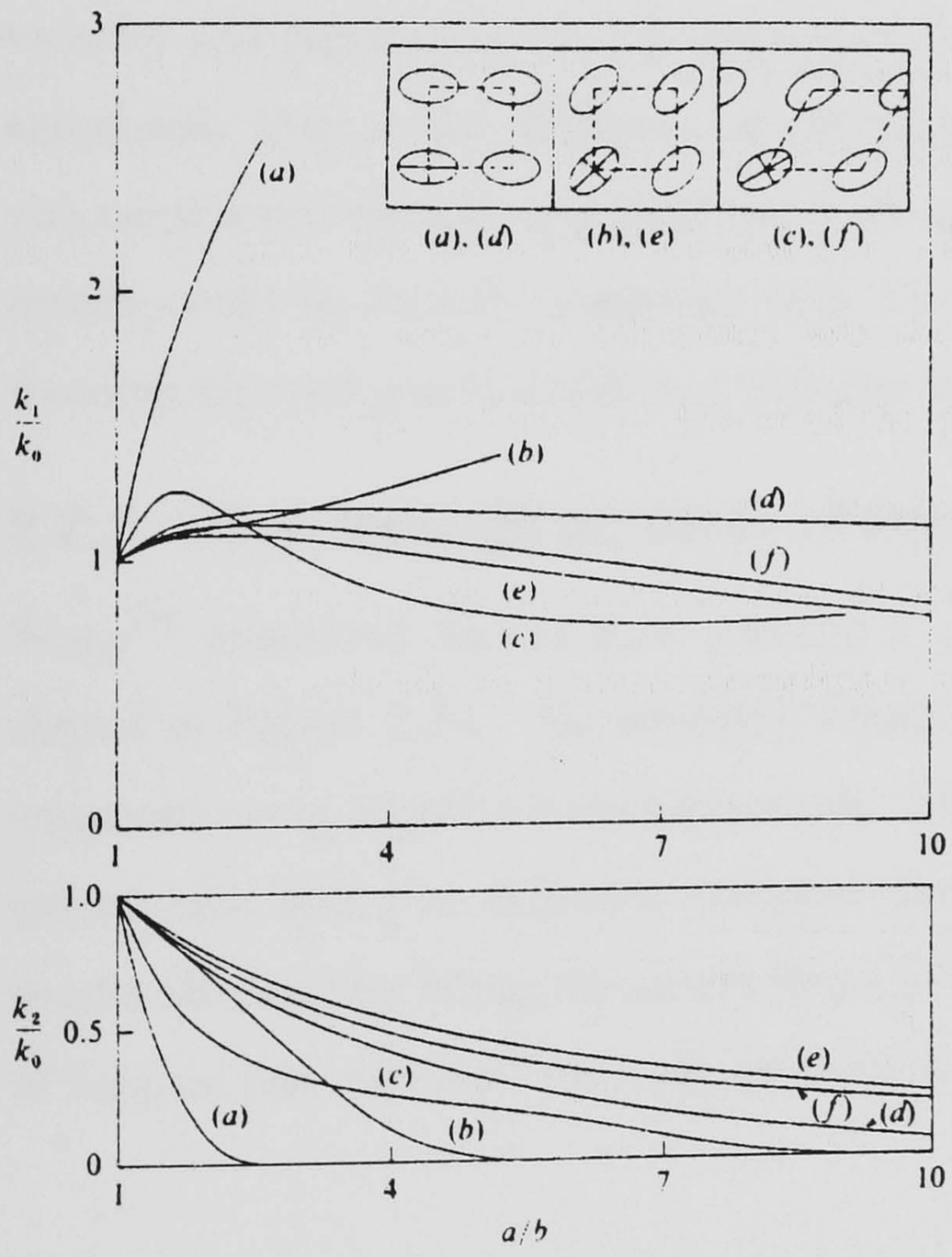


Figure 2.23 - Normalised principal permeabilities k_1 and k_2 for elliptical inclusions of aspect ratio (*a/b*) for different lattice geometries at two concentrations, c. From Larson and Higdon[103,104].

Square lattice, $\phi = 0°$ (a) c = 0.3 (d) c = 0.05

Square lattice, $\phi = 45°$ (b) c = 0.3 (e) c = 0.05

Hexagonal lattice, $\phi = 30°$ (c) c = 0.3 (f) c = 0.05

Phelan and Wise[60] analysed transverse flow across both solid and porous elliptical and circular cross-sections arranged in rectangular arrays using the computational fluid dynamics package FIDAP. The elliptical cross-sections had aspect ratios of 0.5 and 0.25, where the fluid flowed in the direction of the major axis. Phelan and Wise[60] used the Stokes equations to model flow between tows and the Brinkman equation for the microscopic flow between fibres in the tows. As explained in section 2.3.2 these numerical results were compared with analytical results also obtained by Phelan and Wise[60] and showed good agreement, but only at very high values of volume fraction where the lubrication theory is more accurate. Bhat et al.[105] have also investigated cross flow for non-circular shapes. Their work examined this situation in Columnar-Dendritic alloys, although it can also be applied to fluid flow around tows in the RTM process. They solved the Navier-Stokes equations using a finite element method for velocity and pressure at the microstructural level and from this the permeability was calculated. Due to the difficulty of obtaining permeability measurements for high volume fraction through experimental work there was no experimental data that these results could be directly compared with, but the results calculated for high volume fractions showed good consistency with empirical data at lower volume fractions.

2.7.3. Flow through an Array of Rectangular Fibres

Wang[106] examined Stokes flow through a periodic array of rectangular fibres, as shown in Figure 2.24. He obtained values of permeability by solving the Stokes equations using eigenfunction expansions. This was carried out for fibres of different aspect ratio and also different distances from each other. Figure 2.25 shows the results obtained by Wang for square fibres in a square array compared with the results of Sangani and Acrivos[53] for a square array of circular cylinders.

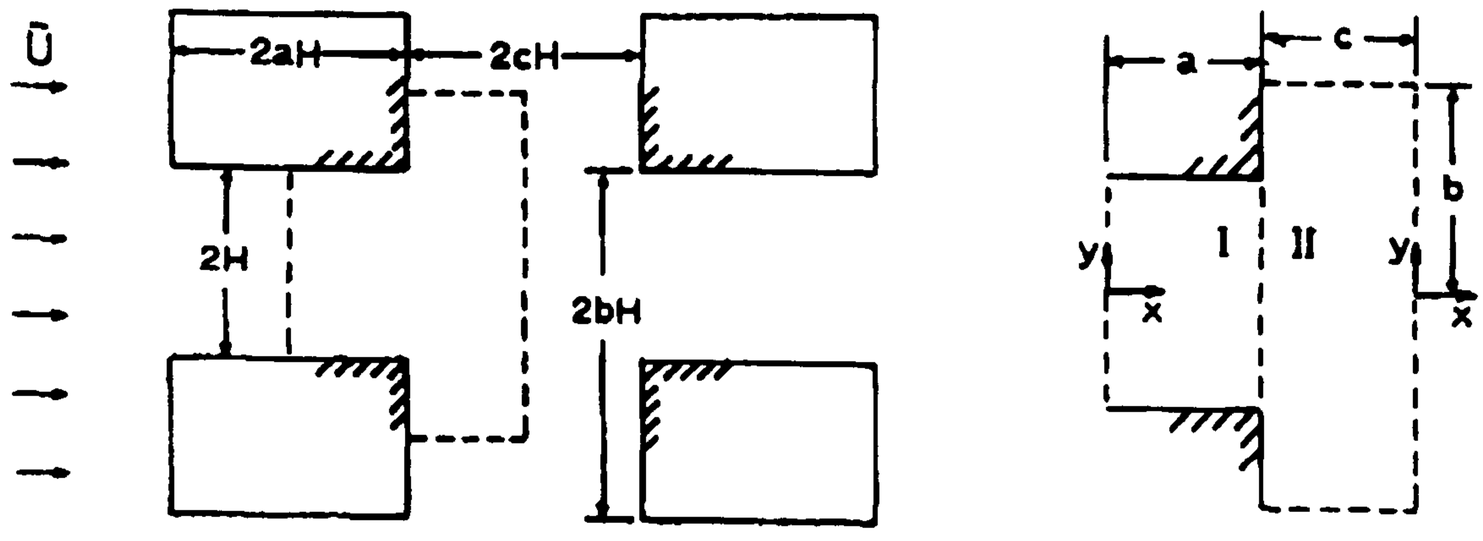


Figure 2.24 - Geometry (left) and partition into two regions (right) used by Wang[106] to examine Stokes flow through an array of rectangular fibres.

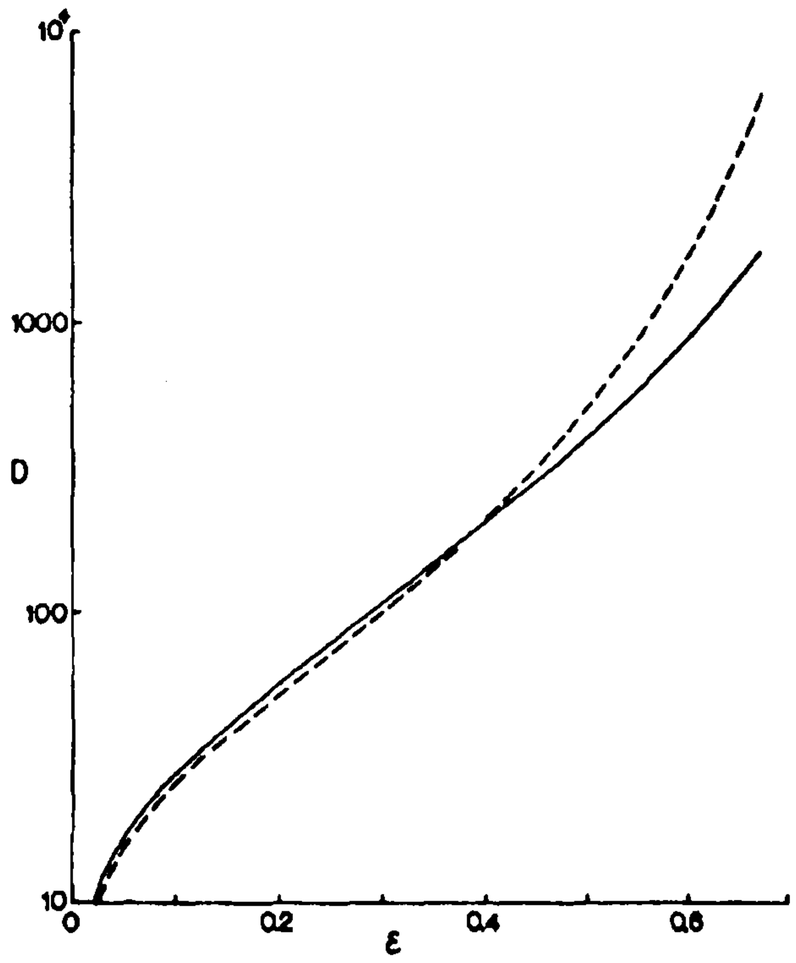


Figure 2.25 - Normalized drag D as a function of solid fraction ε for square fibres in a square array obtained by Wang[106] (solid line) compared with values obtained by Sangani and Acrivos[53] for circular cylinders in a square array (dashed line).

2.8. Summary

In this chapter a review has been made on the areas of research relevant to RTM simulation. A review of the factors affecting permeability measurements in different types of fibrous preform, namely, aligned, woven and random fabric structures, has been highlighted. Additionally, a review has been made of the parallel and radial flow experiments for determining the permeability experimentally. Also presented are the numerical methods of determining permeability by considering the geometry to consist of an array of regularly spaced cylinders (fibres) and solving for the drag force on the cylinders. Results are presented for both circular and elliptical shaped cylinders.

The main flow phenomena in RTM processing are presented, namely, void formation and race-tracking. Preform compression is also discussed introducing some of the models used to account for it. Another important parameter presented in this review is the wetting between the polymers and the fibres. An improvement of the wettability will generally result in easier production and improved product quality.

The final section considers the literature on computational simulations of fluid flow around cylinders. Presented in this thesis are experimental studies on the propagation of the fluid flow front during impregnation and also the velocity field within saturated media. Thus a review of the computational simulations of fluid flow around cylinders is important.

2.9. References

[1] Lundström, T.S., Gebart, B.R., "Effect of Perturbation of Fibre Architecture on Permeability Inside Fibre Tows", J. Composite Materials, **29**(4), (1995).

[2] Darcy, H., "Les Fontaines Publiques de la Ville de Dijon", Dalmont, Paris, (1856).

[3] Bruschke, M.V., Advani, S.G., "Flow of Generalised Newtonian Fluids Across a Periodic Array of Cylinders", J. Rheology, **37**(3), (1993).

[4] Blake, F.C., "The Resistance of Packing to Fluid Flow", Trans. Inst. Chem. Engs., **15**, 150-166, (1937).

[5] Lekakou, C., Bader, M.G., "Mathematical Modelling of Macro- and Micro-Infiltration in Resin Transfer Moulding (RTM)", Composites Part A, **29A**, 29-37, (1998).

[6] Visconti, I.C., Langella, A., Durante, M., "The Influence of Injection Pressure on the Permeability of Unidirectional Fibre Preforms in RTM", ECCM-8, 737-743, (1998).

[7] Gauvin, R., Trochu, F., Lemenn, Y., Diallo, L., "Permeability Measurement and Flow Simulation through Fibre Reinforcement", Polymer Composites, **17**(1), 34-42, (1996).

[8] Griffin, P.R., Grove, S.M., Russell, P., Short, D., Summerscales, J., Guild, F.J., Taylor, E., "The Effect of Reinforcement Architecture on Long-Range Flow in Porous Reinforcement", Composites Manufacturing, **6**(3-4), 221-235, (1995).

[9] Steenkamer, D.A., Wilkins, D.J., Karbhari, V.M., "Influence of Test Fluid on Fabric Permeability Measurements and Implications for Processing of Liquid Moulded Composites", J. Materials Sci. Letters, **12**(13), 971-973, (1993).

[10] Chan, A.W., Larive, D.E., Morgan, R.J., "Anisotropic Permeability of Fibre Preforms: Constant Flow Rate Measurement", J. Comp. Mater., **27**(10), 996-1008, (1993).

[11] Dave, R., "A Unified Approach to Modelling Resin Flow During Composite Processing", J. Comp. Mater., **24**(1), 22-41, (1990).

[12] Parnas, R.S., Salem, A.J., Sadiq, T.A.K., Wang, H-P, Advani, S.G., "The Interaction between Micro and Macroscopic Flow in RTM Preforms", Composite Structures, **27**(1-2), 93-107, (1994).

[13] Kozeny, J., "Uber Kapillare Leitung des Wassers im Boden", Sitzung Akademie der Wissenschaft, **136**, 271-306, (1927).

[14] Carman, P.C., "Fluid Flow Through Granular Beds", Transactions, Inst. Chemical Eng., **15**, (1937).

[15] Williams, J.G., Morris, C.E.M., Ennis, B.C., "Liquid Flow Through Aligned Fibre Beds", Polymer Eng. Sci., **14**(6), 413-419, (1974).

[16] Gutowski, T.G., Cai, Z., Bauer, S., Boucher, D., Kingery, J., Wineman, S., "Consolidation Experiments for Laminate Composites", J. Composite Mater., **21**, 650-669, (1987).

[17] Lam, R.C., Kardos, J.L., "The Permeability of Aligned and Cross-Plied Fibre Beds During Processing of Continuous Fibre Composites", Proc. American Society for Composites, Third Tech. Conf., Seattle, WA, 3-11, (1988).

[18] Skartsis, L., Kardos, J.L., "The Newtonian Permeability and Consolidation of Oriented Carbon Fibre Beds", Proc. American Society for Composites, Fifth Tech. Conf., East Lansing, MI, 548-556, (1990).

[19] Gebart, B.R., "Permeability of Unidirectional Reinforcements for RTM", J. Composite Mater., **26**(8), 1100-1133, (1992).

[20] Kim, Y.R., McCarthy, S.P., Fanucci, J.P., Nolet, S.C., Koppernaes, C., "Resin Flow Through Fibre Reinforcements During Composite Processing", SAMPE Quarterly, **22**(3), 16-22, (1991).

[21] Happel, J., Brenner, H., "Low Reynolds Number Hydrodynamics", (Prentice-Hall, 1965), 387-399.

[22] Sangani, A.S., Acrivos, A., "Slow Flow Past Periodic Arrays of Cylinders with Application to Heat Transfer", Int. J. Multiphase Flow, **8**(3), 193-206, (1982).

[23] Berdichevsky, A.L., Cai, Z., "Preform Permeability Predictions by Self-Consistent Method and Finite Elements Simulation", Polymer Composites, **14**(2), 132-143, (1993).

[24] Miller, B., Clark, D.B., "Liquid Transport Through Fabrics: Wetting and Steady-State Flow, Part I: A New Experimental Approach", Textile Research J., 150-155, (1978).

[25] Miller, B., Clark, D.B., "Liquid Transport Through Fabrics: Wetting and Steady-State Flow, Part II: Fabric Wetting", Textile Research J., 256-260, (1978).

[26] Adams, K.L., Miller, B., Rebenfeld, L., "Forced In-Plane Flow of an Epoxy Resin in Fibrous Networks", Polymer Eng. Sci., **26**(20), 1434-1441, (1986).

[27] Rebenfeld, L., "In-Plane Liquid Flow in Fibre Networks", Proc 4th Textile Structural Composites Symp., Philadelphia, PA, (1989).

[28] Molnar, J.A., Trevino, L., Lee, L.J., "Liquid Flow in Moulds with Prelocated Fibre Mats", Polymer Composites., **10**(6), 414-423, (1989).

[29] Trevino, L., Lee, L.J., Rupel, K., Liou, M.J., "Permeability and Compressibility Measurement of Fibre Mats in Resin Transfer Moulding and Structural RIM", Proc. 45th Ann. Conf., Composite Inst., SPI, Session 9-E/1-7, (1990).

[30] Young, W.B., Rupel, K., Han, K., Lee, L.J., Liou, M.J., "Simulation and Experimental Verification of Mould Filling in Resin Transfer Moulding and Structural RIM", Proc. 45th Ann. Conf., Composite Inst., SPI, Session 9-D/1-6, (1990).

[31] Young, W.B., Rupel, K., Han, K., Lee, L.J., Liou, M.J., "Analysis of Resin Injection Moulding in Moulds with Preplaced Fibre Mats. II: Numerical Simulation and Experiments with Mould Filling", Polymer Composites, **12**(1), 30-38, (1991).

[32] Rudd, C.D., Owen, M.J., Middleton, V., "Effects of Process Variables on Cycle Time During Resin Transfer Moulding for High Volume Manufacture", Mater. Sci. Tech., **6**, 656-665, (1990).

[33] Gauvin, R., Chibani, M., Lafontaine, P., "The Modelling of Pressure Distribution in Resin Transfer Moulding", J. Reinforced Plastics and Composites, **6**, 367-377, (1987).

[34] Gauvin, R., Chibani, M., "A study of Permeability of Non-Woven Reinforcements in Composite Moulding", SAMPE Quarterly, 52-58, (1990).

[35] Parnas, R.S., Howard, J.G., Luce, T.L., Advani, S.G., "Permeability Characterisation. Part I: A Proposed Standard Reference Fabric for Permeability", Polymer Composites, **16**(6), 429-445, (1995).

[36] Steenkamer, D.A., McKnight, S.H., Wilkins, D.J., Karbhari, V.M., "Experimental Characterisation of Permeability and Fibre Wetting for Liquid Moulding", J. Mater. Sci., **30**(12), 3207-3215, (1995).

[37] Hsieh, Y.L., Yu, B., "Liquid Wetting, Transport and Retention Properties of Fibrous Assemblies. Part I: Water Wetting Properties of Woven Fabrics and Their Constituent Single Fibres", Textile Research J., **62**(11), 677-685, (1992).

[38] Ghali, K., Jones, B., Tracy, J., "Experimental Techniques for Measuring Parameters Describing Wetting and Wicking in Fabrics", Textile Research J., **64**(2), 106-111, (1994).

[39] Ahn, K.J., Seferis, J.C., Berg, J.C., "Simultaneous Measurements of Permeability and Capillary Pressure of Thermosetting Matrices in Woven Fabric Reinforcements", Polymer Composites, **12**(3), 146-152, (1991).

[40] Williams, J.G., Morris, C.E.M., Ennis, B.C., "Liquid Flow Through Aligned Fibre Beds", Polymer Eng. Sci., **14**(6), 413-419, (1974).

[41] Kotomin, S.V., Avdeev, N.N., "Wetting of Synthetic Fibres by Thermoplastic Melts During Capillary Impregnation of Filaments", Colloid J., **61**(3), 306-313, (1999).

[42] Batch, G.L., Chen, Y.T., Macosko, C.W., "Capillary Impregnation of Aligned Fibrous Beds: Experiments and Model", J. Reinforced Plastics & Composites, **15**, 1027-1051, (1996).

[43] Scheidegger, A.E., "The Physics of Flow Through Porous Media", 3rd Edition, University of Toronto Press, ISBN 0-8020-1849-1, (1974).

[44] Rudd, C.D., Long, A.C., Kendall, K.N., Mangin, C.G.E., "Liquid Moulding Technologies", Woodhead Publishing, Cambridge, (1997).

[45] Diallo, M.L., Gauvin, R., Trochu, F., "Key factors Affecting the Permeability Measurement in Continuous Fibre Reinforcements", ICCM-11, (1997).

[46] Lekakou, C., Johari, M.A.K., Norman, D., Bader, M.G., "Measurement Techniques and Effects on In-Plane Permeability of Woven Cloths in Resin Transfer Moulding", Composites Part A, **27**, 401-408, (1996).

[47] Ahn, S.H., Lee, W.I., Springer, G.S., "Measurement of the Three-Dimensional Permeability of Fibre Preforms Using Embedded Fibre Optic Sensors", J. Comp. Mat., **29**(6), 714-733, (1995).

[48] Gebart, B.R., Lidström, P., "Measurement of In-Plane Permeability of Anisotropic Fibre Reinforcements", Polymer Composites, **17**(1), 43-51, (1996).

[49] Hammond, V.H., Loos, A.C., "The Effects of Fluid Type and Viscosity on the Steady-State and Advancing Front Permeability Behaviour of Textile Preforms", J. Reinforced Plastics and Composites, **16**(1), 50-71, (1997).

[50] Lidström, P., SICOM Technical Report 92-013, Swedish Institute of Composites, (1992).

[51] Verheus, A.S., Peters, J.H.A., "The Role of Reinforcement Permeability in Resin Transfer Moulding", Composites Manufacturing, **4**(1), 33-38, (1993).

[52] Luce, T.L., Advani, S.G., Howard, J.G., Parnas, R.S., "Permeability Characterisation. Part 2: Flow Behaviour in Multiple-Layer Preforms", Polymer Composites, **16**(6), 429-445, (1995).

[53] Sangani, A.S., Acrivos, A., "Slow Flow Past Periodic Arrays of Cylinders with Application to Heat Transfer", Int. J. Multiphase Flow, **8**(3), 193-206, (1982).

[54] Koch, D.L., Ladd, A.J.C., "Moderate Reynolds Number Flows Through Periodic and Random Arrays of Aligned Cylinders", Journal of Fluid Mechanics, **349**, 31-66, (1997).

[55] Gebart, B.R., "Permeability of Unidirectional Reinforcements for RTM", Journal of Composite Materials, **26**, 1100-1133, (1992).

[56] Saunders, R.A., Lekakou, C., Bader, M.G., "Compression in the Processing of Polymer Composites. Part 1: A Mechanical and Microstructural Study for Different Glass Fabrics and Resins", Comp. Sci. Tech., **59**, 983-993, (1999).

[57] Pearce, N.R.L., Guild, F.J., Summerscales, J., "The Use of Automated Image Analysis for the Investigation of Fabric Architecture on the Processing and Properties of Fibre-Reinforced Composites Produced by RTM", Composites Part A, **29A**, 829-837, (1998).

[58] Bhat, M.S., Poirier, D.R., Heinrich, J.C., "Permeability for Cross Flow through Columnar-Dendritic Alloys", Metallurgical and Materials Transactions B, **26B**, 1049-1056, (1995).

[59] Kuwabara, S., "The Forces Experienced by a Lattice of Elliptic Cylinders in a Uniform Flow at Small Reynolds Number", J. Physical Society of Japan, **14**(4), 522-527, (1959).

[60] Phelan Jr., F.R., Wise, G., "Analysis of Transverse Flow in Aligned Fibrous Porous Media", Composites Part A, **27A**(1), 25-34, (1996).

[61] Holmberg, J.A., Lundström, T.S., Gebart, B.R., Strömbeck, L.A., "Process Induced Defects in Resin Transfer Moulding", SICOMP Technical report 94-005, Swedish Institute of Composites, (1994).

[62] Judd, N.C.W., Wright, W.W., "Voids and their Effects on the Mechanical Properties of Composites – an Appraisal", SAMPE Journal, **14**(1), 10-14, (1978).

[63] Yamada, H., Mihata, I., Tomiyama, T., Walsh, S.P., "Investigation of the Fundamental Causes of Pinholes in SMC Moldings", Proc. SPI Composite Institutes 47th Annual Conf. (1992).

[64] Harper, B.D., Chen, G.H., Chen, R.S., "A Note on the Effects of Voids Upon the Hydral and Mechanical Properties of AS4/3502 Graphite/Epoxy", J. Comp. Mat., **21**, 280-289, (1987).

[65] Lundström, T.S., "Void Formation and Transport in Manufacturing of Polymer Composites", Doctoral Thesis, Swedish Inst. Comp., (1996).

[66] Manhale, A.D., Prud'homme, R.K., Rebenfield, L., "Quantitative Measurement of Voids Formed During Liquid Impregnation of Non-woven Multifilament Glass Networks Using An Optical Visualisation Technique", Polym. Eng. Sci., **32**, 319-326, (1992).

[67] Rohatgi, V., Patel, N., Lee, L.J., "Experimental Investigation of Flow Induced Microvoids During Impregnation of Unidirectional Stitched Fibreglass Mat", Polym. Comp., **17**(2), 161-170, (1996).

[68] Patel, N., Lee, L.J., "Modelling of Void Formation and Removal In LCM. Part II: Model Development and Implementation", Polym. Comp., **17**(1), 104-114, (1996).

[69] Moon, K.K., Woo, I.L., Thomas, H., "Formation of Microvoids During RTM Process", Comp. Sci. Tech., **60**(12), 2427-2434, (2000).

[70] Bickerton, S., Advani, S.G., "Characterisation and Modelling of Race-tracking in Liquid Composite Moulding Processes", Comp. Sci. Tech., **59**(15), 2215-2229, (1999).

[71] Mohan, R., Bickerton, S., Shires, D.R., Advani, S.G., Tamma, K.K., "Analysis and Characterization of Flow Channel Effects During Manufacturing of Composites by Resin Transfer Moulding", Proc. Annual Meeting of the Society of Plastics Engineers: ANTEC, Toronto, (1997).

[72] Han, K., Wu, C.H., Lee, L.J., "Characterization and Simulation of Resin Transfer Moulding — Race-Tracking and Dry Spot Formation", Proc. Ninth Annual ASM-ESD Advanced Composite Conference, Michigan, (1993).

[73] Leek, R., Carpenter, G., Donnellan, T., Phelan, F., "Simulation of Edge Flow Effects in Resin Transfer Moulding", Proc. 25th International SAMPE Technical Conference, Philadelphia, 233–45, October, (1993).

[74] Fong, L.L., Advani, S.G., "Preforming Analysis of Thermoformable Fibre Mats: Preforming Effect on Mould Filling", J. Reinforced Plastics and Composites, **13**, 637, (1994).

[75] Bickerton, S., Advani, S.G., "Characterization of Corner and Edge Permeabilities During Mould Filling in Resin Transfer Moulding", Proc. ASME AMD-MD, **56**, 143-150, (1995).

[76] Ni, J., Zhao, Y., Lee, L.J., Nakamura, S., "Analysis of Two-Regional Flow in Liquid Composite Moulding", Polymer Composites, **18**(2), 254–269, (1997).

[77] Sheard, J., Senft, V., Mantell, S.C., Vogel, J.H., "Determination of Corner and Edge Permeability in Resin Transfer Moulding" Polymer Composites, **19**(1), 96–105, (1998).

[78] Hammami, A., Gauvin, R., Trochu, F., "Modelling The Edge Effect in Liquid Composites Moulding", Composites Part A: Applied Science and Manufacturing, **29**(5–6), 603–609, (1998).

[79] Gutowski, T.G., Morigaki, T., Cai, Z., "The Consolidation of Laminate Composites", J. Composite Mater., **21**, 172-188, (1987).

[80] Gutowski, T.G., Kingery, J., Boucher, D., "Experiments in Composites Consolidation: Fibre Deformation", Proceedings ANTEC '86, MA: SPE, 1316-1320, (1986).

[81] Gutowski, T.G., Cai, Z., Soll, W., Bohomme, L., "The Mechanics of Composites Deformation During Manufacturing Processes", Advances in Modelling of Composite Processes, Wiley Interscience, ISBN 047115301X, 154-170

[82] Kotsikos, G., Bland, J.H., Gibson, A.G., "Squeeze Flow Mechanics for Glass Mat Thermoplastics", Proc. ECCM7, Inst. of Materials, London, 213-219, May, (1996).

[83] Wang, E.L., Gutowski, T.G., "Laps and Gaps in Thermoplastic Composites Processing", Composites Manufacturing, **2**(2), 69-78, (1991).

[84] Hamada, H., Ikegawa, N., "Structural Resin Transfer Moulding With Compression Process", FPCM'96, Wales, (1996).

[85] Carnaby, G., Pan, N., "Theory of the Compression Hysteresis of Fibrous Assemblies", Tex. Res. J., 275-284, (1989).

[86] Lekakou, C., Johari, M., Bader, M.G., "Compressibility and Flow Permeability of Two-Dimensional Woven Reinforcements in the Processing of Composites", Polymer Composites, **17**(5), 666-672, (1996).

[87] Lekakou, C., Bader, M.G., Tonkin, J.D., "Modelling of Fibre Network Deformation During Processing of Continuous Fibre Reinforced Polymer Composites", Computer Aided Innovation of New Materials, **2**, 1511-1518, (1993).

[88] Toll, S., Manson, J.A.E., "An Analysis of the Compressibility of Fibre Assemblies", Proc. FRC Conf., 25, Newcastle, March, (1994).

[89] Kim, Y.R., McCarthy, S.P., Fanucci, J.P., "Compressibility and Relaxation of Fibre Reinforcements During Composite Processing", Polymer Composites, **12**(1), 13-19, (1991).

[90] Gauvin, R., Chibani, M., Proc. 43rd Annual Conf., SPI Composites Inst., Cincinnati, February, (1998).

[91] Summerscales, J., Pearce, N., "The Compressibility of a Reinforcement Fabric", Composites Manufacturing, **6**, 15-21, (1995).

[92] Skartsis, L., Khomami, B., Kardos, J.L., "A Semi-Analytical One-Dimensional Model for Viscoelastic Impregnation of Fibrous Media", J. Advanced Materials, **25**(3), 38-44, (1994).

[93] Hiemenz, P.C., "Surface Tension and Contact Angle", Principles of Colloid and Surface Chemistry, Marcel Dekker, ISBN 0824793978, 287-289, (1997).

[94] Kamath, Y.K., Dansizer, C.J., Hornby, S., Weigmann, H.D., "Surface Wettability Scanning of Long Filaments by a Liquid Membrane Method", Textile Research Inst., **57**, 205-213, (1987).

[95] Wagner, H.D., "Spreading of Liquids on Cylindrical Surfaces: Accurate Determination of Contact Angle", Journal of Applied Physics, **67**, 1352-1355, (1990).

[96] Chwastiak, S., "A Wicking Method for Measuring Wetting Properties of Carbon Yarns", Journal of Colloid and Interface Science, **42**, 298-309, (1972).

[97] ISO/TR 3717-1975

[98] Dahlbäck, L.M., Lundström, T.S., "A Method to Measure Wetting Between Resin and Reinforcement", Proc. ICCM-10, Whistler, B.C., Canada, (1995).

[99] Nagelhout, D., Bhat, M.S., Heinrich, J.C., Poirier, D.R., "Permeability for Flow Normal to a Sparse Array of Fibres", Materials Science and Engineering, **A191**, 203-208, (1995).

[100] Edwards, D.A., Shapiro, M., Bar-Yoseph, P., Shapira, M., "The Influence of Reynolds Number upon the Apparent Permeability of Spatially Periodic Arrays of Cylinders", Physics of Fluids A, **2**(1), 45-55, (1990).

[101] Papathanasiou, T.D., "A Structure Orientated Micromechanical Model for Viscous Flow through Square Arrays of Fibre Clusters", Composites Science and Technology, **56**, 1055-1069, (1996).

[102] Epstein, N., Masliyah, J.H., "Creeping Flow through Clusters of Spheroids and Elliptical Cylinders", Chemical Engineering Journal, **3**, 169-175, (1972).

[103] Larson, R.E., Higdon, J.J.L., "Microscopic Flow Near The Surface of Two-Dimensional Porous Media. Part 1. Axial flow", J. Fluid Mechanics, **166**, 449-472, (1986).

[104] Larson, R.E., Higdon, J.J.L., "Microscopic Flow Near The Surface of Two-Dimensional Porous Media. Part 2. Transverse Flow", J. Fluid Mechanics, **178**, 119-136, (1987).

[105] Bhat, M.S., Poirier, D.R., Heinrich, J.C., "Permeability for Cross Flow Through Columnar-Dendritic Alloys", Metallurgical and Materials Transactions B, **26B**, 1049-1056, (1995).

[106] Wang, C.Y., "Stokes Flow through an Array of Rectangular Fibres", International Journal of Multiphase Flow, **22**(1), 185-194, (1996).

3. EXPERIMENTAL DESIGN

This chapter describes the equipment, materials and procedures used in the experimental studies discussed in later chapters, specifically: (i) the rheology and curing behaviour of typical RTM resin systems, (ii) construction of a simulation flow cell, for the gathering of information on the velocity field in saturated media and also information on the propagation of the flow front, (iii) near-industrial-scale RTM for filling and cure studies.

3.1.1. Rheological Measurements

Rheological characterisation studies were performed on typical RTM resin systems. The results of these studies were then used to develop a model for resin viscosity during cure in RTM.

3.1.2. Resin Systems

The following resin systems were used in the various analyses performed: LY5052/HY5052[a], LY564/HY2954[a], RTM6[b], Derakane Momentum 411-C50[c] and PR500[d]. (The relevant manufacturer-supplied physical data for these resin systems are

---

[a] Manufactured by *Ciba-Geigy*, Macclesfield, Cheshire SK10 2NY, UK

[b] Manufactured by *Hexcel Composites*, Duxford, Cambridge CB2 4QD, UK

[c] Manufactured by *Dow Chemicals*, Kings Lynn, Norfolk PE30 2JD, UK

[d] Manufactured by *3M*, Bracknell, Berkshire RG12 1JU, UK

given in Table 3.1). These five resins provide examples that span the range of typical resins used in RTM processing systems.

Table 3.1 - Resin Properties

Physical Data	LY5052/HY5052	LY564/HY2954	RTM6	PR500	411-C50
Mix ratio (parts by weight)	100 : 38	100 : 35	One part	One part	One part
Viscosity (mPa s) at 25°C	600-700	1000-1400	200	400	350
Gel time (min)	2-3(@ 120°C)	16-18(@ 100°C)	30(@180°C)	13(@200°C)	N/A

LY5052/HY5052 is a two-part epoxy/amine resin from Ciba-Geigy. LY5052 is the base resin containing 1,4-butanediol diglycidylether, HY5052 is a hardener based on modified cycloaliphatic amines. LY564 is a bisphenol *A* epoxy resin containing a reactive diluent and its hardener is HY2954 a cycloaliphatic polyamine. RTM6 is a premixed epoxy system; the main components of this resin system are tetraglycidyl methylene dianiline, 2,6-diethylaniline and 2-isopropyl-6-methylaniline. PR500 is also a one-part epoxy resin which is a thick paste at room temperature, containing 35% diglycidylether of bisphenol A and 15% diglycidylether of distributed carbopolycycle. Dow Derakane Momentum 411-C50 is a bisphenol-A epoxy resin. The Dow Derakane Momentum 411-C50 used in this study is a special formulation, requiring low temperature storage (<15°C), manufactured specifically for *Vosper Thronycroft* and is different from the Dow Derakane Momentum 411-C50 mentioned in Chapter 7.

3.1.3. Rheometers

Three rheometers were used for the experiments: one for low-viscosity measurements and two for the higher viscosity readings to more closely track the viscosity changes all the way to the gelation point. The rheometer used for low-viscosity measurements, a TA 1000N (*T.A. Instruments*, Leatherhead, Surrey KT22 7UQ, UK), is a controlled stress/controlled shear rate type rheometer. All the measurements on LY5052, LY564 and Derakane 411-C50 resin systems were performed on this rheometer, which was used with a stainless steel cone and plate geometry with a cone diameter of 4cm, cone angle of 2 degrees and truncation of 45μm. The RTM6 measurements were performed on a Rheometric Scientific SR-5000 rheometer with disposable parallel plates. The

PR500 resin was measured on a Carri-Med CSR500 rheometer, also using disposable parallel plates. The RTM6 and PR500 measurements were made by Dr Quentin Fontana[e], whose contribution is gratefully acknowledged.

3.2. The Flow Cell

A series of experiments was conducted to simulate the infiltration of resin through a fibre matrix. A Perspex flow cell containing a hexagonal arrangement of cylindrical rods inside was constructed in order to conduct simulations. The primary functions of the flow cell were to gather information on the velocity field in a saturated medium and to acquire information on the propagation of the flow front.

A hexagonal arrangement was chosen as this represents a more realistic packing configuration than a square array, but is sufficiently simple to make comparisons with results from numerical simulations.

3.2.1. Velocity Profile Consideration

It was desired to construct a flow cell that could be used to determine an approximately two-dimensional flow field for comparison with numerical calculations. In order to determine the correct aspect ratio (ratio of rod length, b, divided by spacing, a) an analytical solution for a simplified geometry was used to obtain an aspect ratio sufficiently large to give a planar or near 2-D flow region in the central area. The rectangular gap of width a and height b between cylindrical rods (representing fibre bundles) is represented in Figure 3.1.

[e] British Aerospace, Sowerby Research Centre, FPC 267, P.O. Box 5, Filton, Bristol BS12 7QW

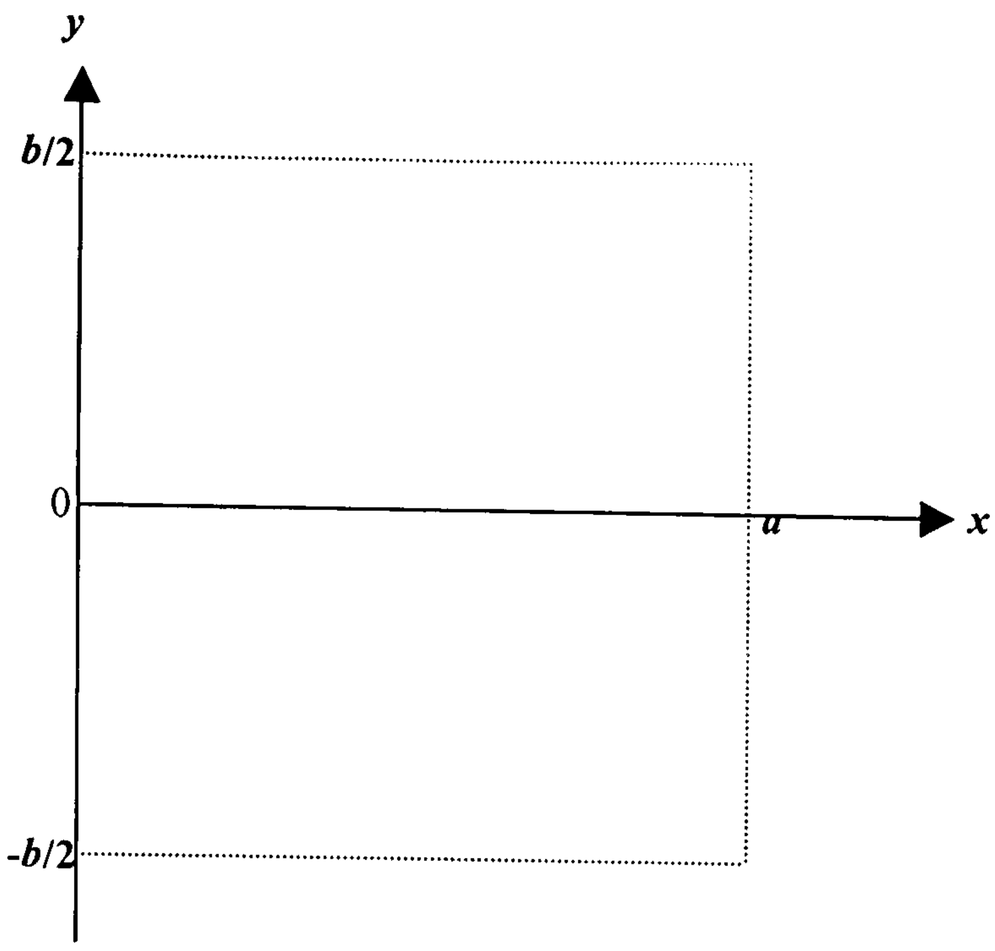


Figure 3.1 – The geometry of the gap between rods in the flow cell.

The flow is modelled as parallel flow through a straight channel using the following scaling;

$$\hat{x} = \frac{x}{a}, \qquad \hat{y} = \frac{y}{a}, \qquad \hat{u} = \frac{u}{U}.$$

Assuming low Reynolds number flow, the Stokes equation, [3.1], can be solved analytically to obtain the superficial velocity, $\hat{u}$, [3.2];

$$\frac{\partial^2 \hat{u}}{\partial \hat{x}^2} + \frac{\partial^2 \hat{u}}{\partial \hat{y}^2} = -1 \qquad \textbf{[3.1]}$$

with boundary conditions: $\hat{u} = 0$ on $\hat{x} = 0$, $\hat{x} = 1$, $\hat{y} = \pm b/2$

giving,

$$\hat{u} = \frac{1}{2}\hat{x}(1-\hat{x}) - \left[\sum_{n=1}^{\infty} \sin n\pi\hat{x} \frac{\cosh n\pi\hat{y}}{\cosh \frac{n\pi\beta}{2}} \left(\frac{2 - 2\cos n\pi}{n^3\pi^3}\right)\right] \qquad \textbf{[3.2]}$$

Figure 3.2 shows a graph of the variation of velocity with y in the mid-plane ($\hat{x} = 0.5$) for different values of the aspect ratio, b/a.

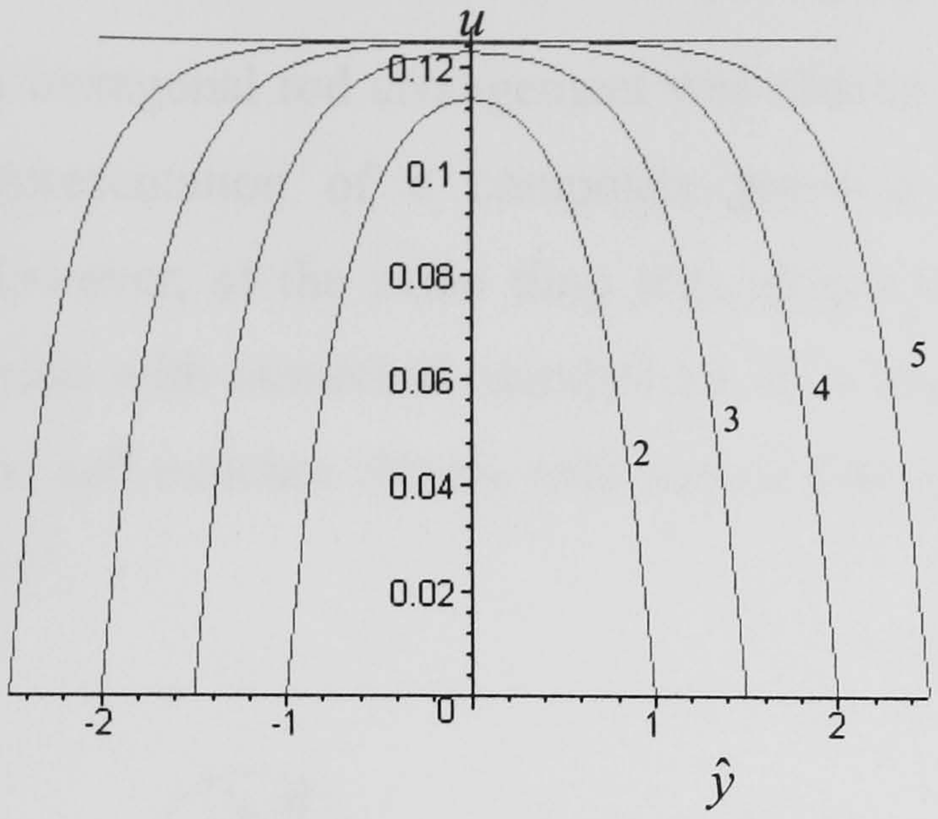


Figure 3.2 - Graph of variation of dimensionless velocity with $\hat{y}$ at constant $\hat{x} = 0.5$ for aspect ratio $b/a = 2,3,4,5$.

From Figure 3.2 it is seen that at an aspect ratio of 5 the velocity is practically constant over an appreciable intermediate range of y-values, therefore the flow in the central part of the cell approximately represents two-dimensional flow.

The actual two-dimensional velocity profile plotted in x,y coordinates is represented in Figure 3.3.

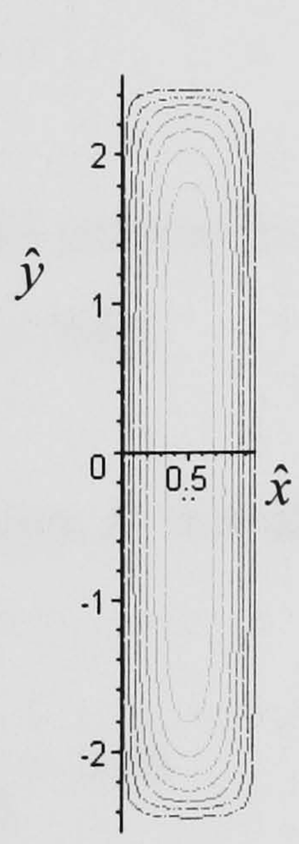


Figure 3.3 – Full velocity profile for aspect ratio $b/a = 5$.

Again, from Figure 3.3 it is evident that at an aspect ratio of 5 the velocity field is two-dimensional over an appreciable range of $\hat{y}$. Therefore an aspect ratio of 5 was chosen for the flow cell design.

3.2.2. Fibre Volume Fraction (V_f)

A hexagonal rod arrangement was chosen for the flow cell as this is a more realistic representation of a composite preform than the more simplistic square array. However, at the same time it is simple enough for meaningful comparisons to be made with numerical simulations. It is important that the volume fraction of rods in the cell matches closely with that of fibres in applications, which is in the range 0.4 – 0.6[1].

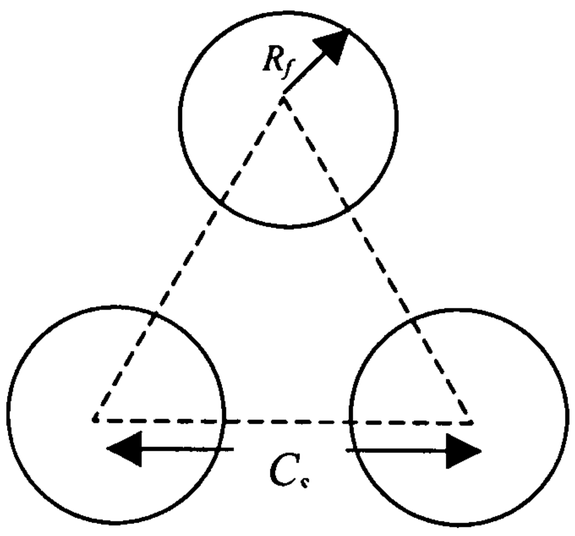


Figure 3.4 - The triangular unit cell in the hexagonal arrangement of rods.

The volume fraction is given by

$$V_f = \frac{\pi R_f^{\,2}}{C_s^{\,2} \sin 60}$$

where V_f is the solid volume fraction, R_f is the radius of the rods and C_s is the centre spacing between the rods.

In the flow cell design, R_f was chosen to be 0.008m and C_s to be 0.02m, giving a fibre volume fraction of

$$V_f = \frac{\pi \times 0.008^2}{0.02^2 \times \sin 60} = 0.58$$

This is at the upper end of the volume fraction range for typical fibre composites, 40 to 60%[1]. The resulting gap between the cylinders was $a = C_s - 2R_f = 0.004m$. With the chosen aspect ratio of $b/a = 5$, this leads to $b = 0.02m$.

3.2.3. Pressure Drop in the Flow Cell

A requirement of the flow cell design was to provide even distribution of the fluid entering the cell. To accomplish this, the pressure drop in the distributing flow perpendicular to the main flow direction in the region before the first row of rods was

estimated and compared with the pressure drop across the first row of rods. A flow distribution device such as a mesh could have been used to achieve even distribution, but was deemed unnecessary as long as the pressure drop required to distribute the flow was less than 10% of that across each row of rods. The calculations are presented below.

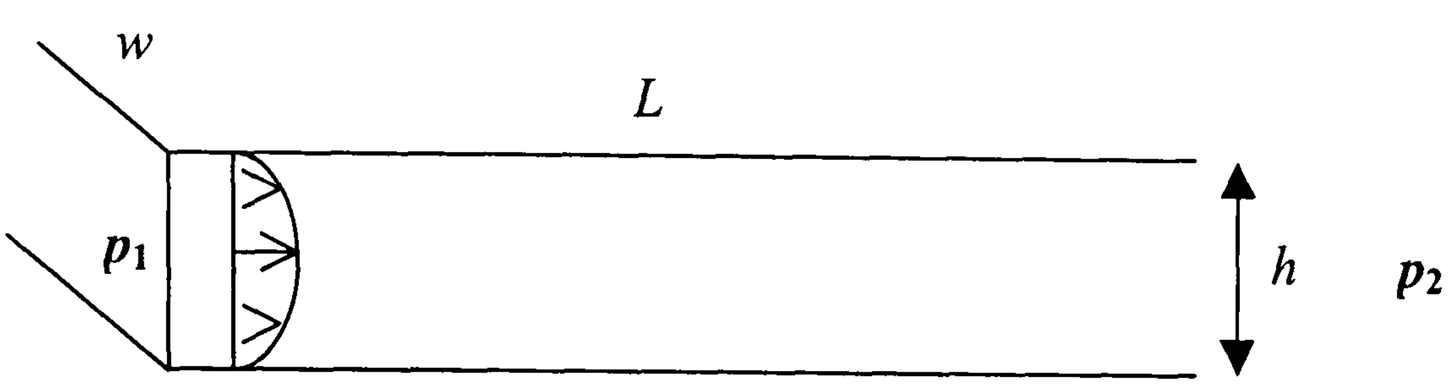


Figure 3.5 – Geometry of the flow cell used for pressure drop calculation.

The pressure drop over a length L is obtained from the 2-D approximation,

$$\Delta p = \frac{12\mu QL}{wh^3}.$$

where w is the width of the channel, h is the height of the channel, L is the length and Δp is the pressure drop over the length L.

In the first case, we consider the pressure drop across the first row of rods (Δp_{12}). It was decided to have 5 rods in each row, and 7 rows of rods, so that the flow in the central portion of the cell would be unaffected by the side walls, entrance or exit. The flow through each gap is equal to $Q_{Tot}/5$, L is equal to D the rod diameter, the width of the channel, w, is equal to b the rod length and the channel gap, h, is equal to a the rod spacing, giving

$$\Delta p_{12} = \frac{2.4\mu Q_{Tot} D}{ba^3}.$$

In the second case, we consider the pressure drop perpendicular to the flow direction before the first row of rods (Δp_{13}). The flow splits in half at the entrance, the transverse flow falls to zero near the wall, so the appropriate flow rate is now $Q_{Tot}/4$, L is equal to half the width of the cell, B, which is equal to $3s + 2.5D$, the flow width, w, is equal to c the entry length, and the channel gap, h, is equal to, b, the rod length, giving

$$\Delta p_{13} = \frac{3\mu Q_{Tot} B}{cb^3}.$$

The ratio of the two pressure drops is

$$\frac{\Delta p_{13}}{\Delta p_{12}} = \frac{3}{2}\frac{Ba^3}{Dcb^2}$$

with $B \approx 52$mm, $a \approx 4$mm, $D \approx 16$mm, $c \approx 15$mm, $b \approx 20$mm, we find that,

$$\frac{\Delta p_{13}}{\Delta p_{12}} \approx 5\%$$

Therefore we can expect the flow to be evenly distributed after the first row of rods in the flow cell. The first row of rods acts as a distributor and no additional intervention is needed.

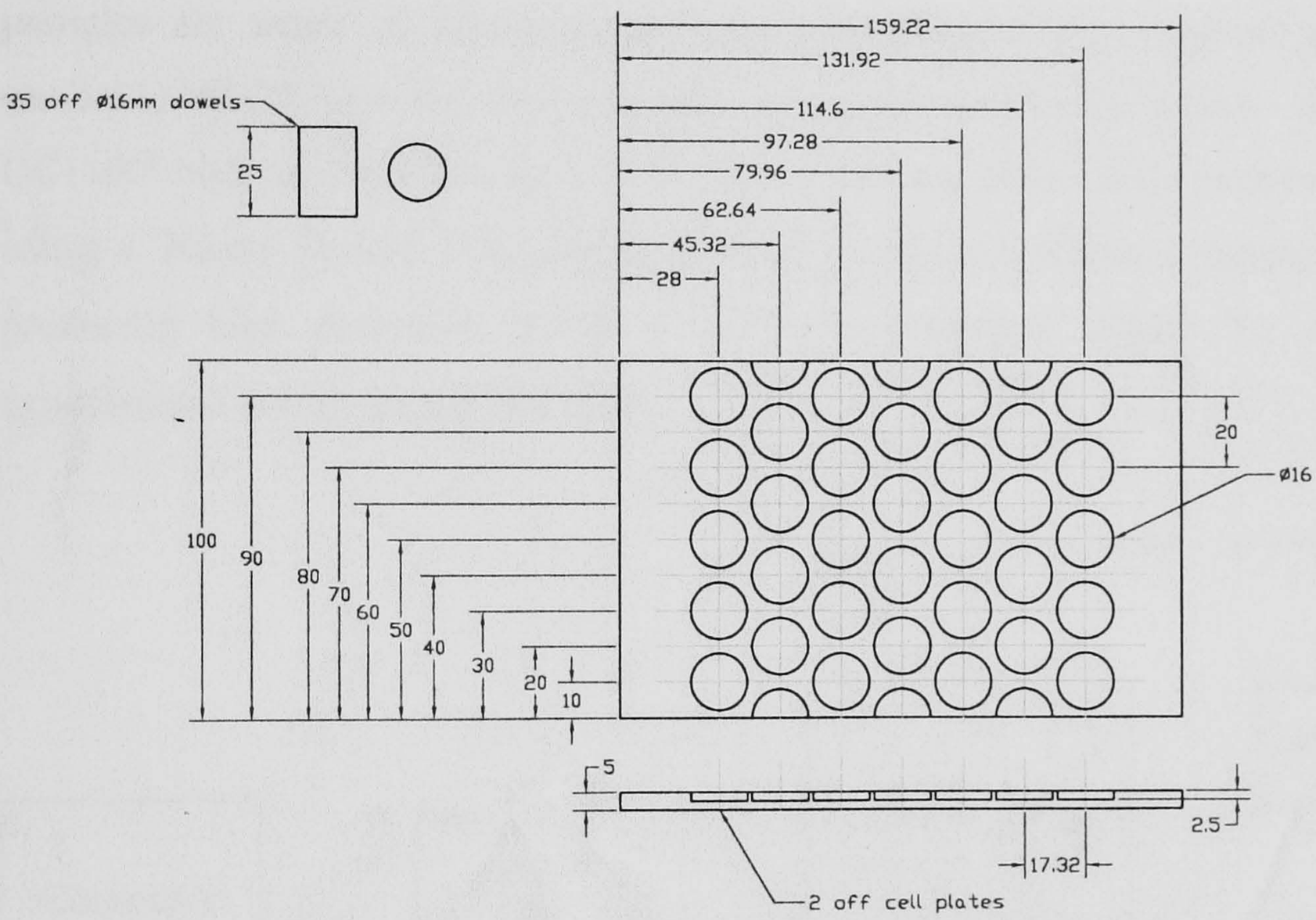


Figure 3.6 - Final design of the flow cell (dimensions in mm).

Satisfying all of the criteria discussed above with a practical size, the flow cell design was finalised and built as shown in Figure 3.6. The rod spacing is 4mm, rod length is 20mm and the arrangement of rods is a hexagonal array. The front and back faces of the cell were machined with recesses to hold the ends of the rods in place for ease of assembly.

3.2.4. Particle Image Velocimetry

One of the uses of the flow cell was to gather information on the velocity field in a saturated medium. Particle image velocimetry was used as the data acquisition technique as it is a relatively inexpensive and easy method to use. The use of a particle tracer also means that the fluid in the system needs to be changed less. A particle tracer allows multiple cycling of the fluid around the system with the flow pattern still being seen clearly. A fluid tracer would become mixed in with the liquid solution fairly quickly and so could only be cycled around the system a few times. The disadvantage, however, of both fluid and particle tracers is that they affect the fluid flow although in the case of particle tracers this should be insignificant if the particles are small. A *Micro* pump 120 series[f] magnetically coupled gear pump (model GJ-N23FFISA BI) was used to pump the fluid round the system. An Intralux DC1100[g] high quality Fibre optic DC-Light source was used. Image capture was done using a Nikon Coolpix 880 digital camera[h]. It has an effective megapixel CCD producing high definition 2,048 × 1,536 pixel images. Figure 3.7 shows the experimental set-up for the PIV study.

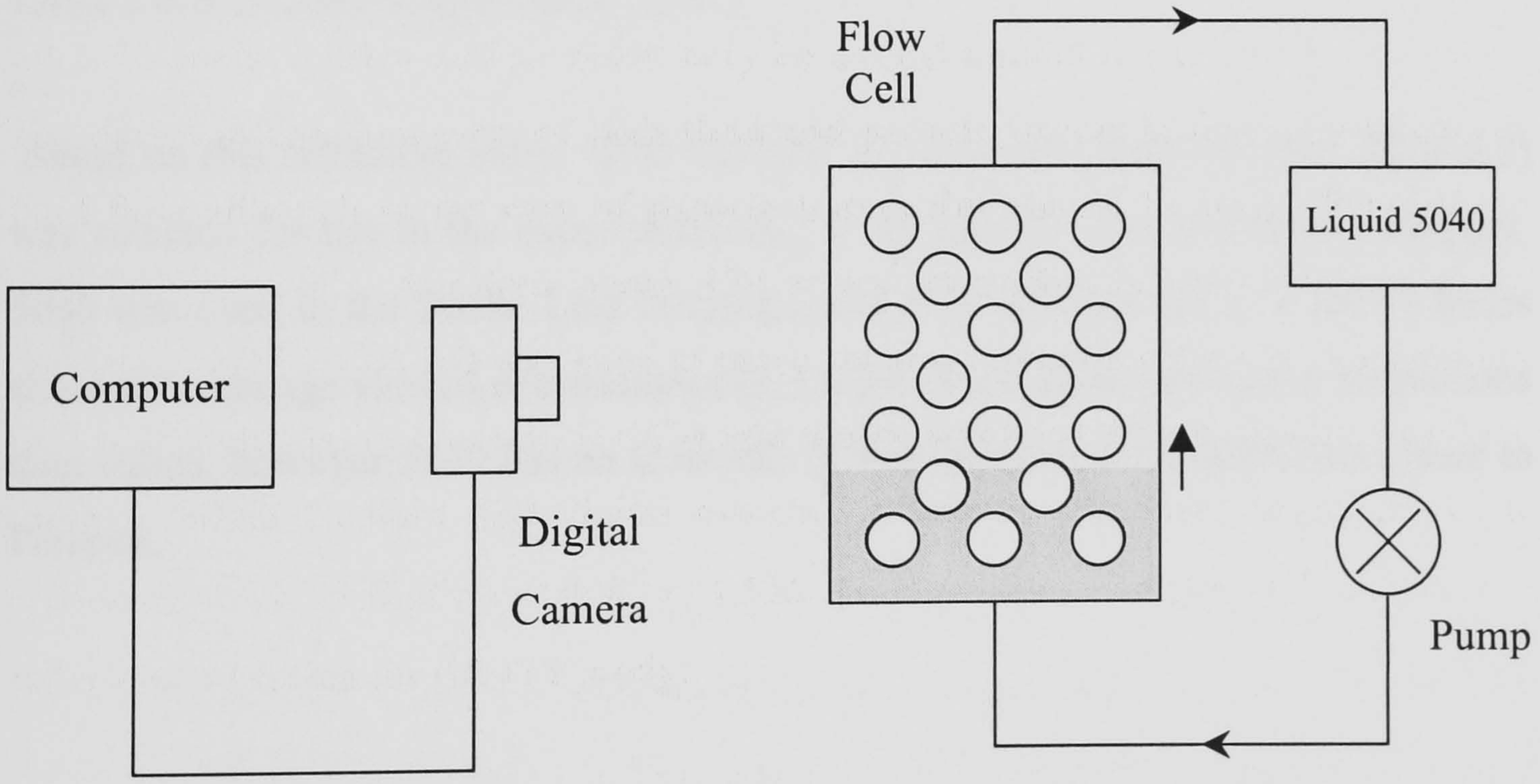


Figure 3.7 – General set-up of PIV Experiment.

---

[f] Supplied by *Orbit Pumps Ltd*, Trafford Park, Manchester, M17 1WA, UK

[g] Supplied by *Alrad Instruments Ltd.*, Newbury, RG14 2NS, UK

[h] *Nikon UK Limited*, Nikon House, Kingston upon Thames, Surrey, KT2 5PR.

When glycerol was used as the test fluid, diffraction problems in the flow cell due to differing refractive indices of the glycerol and Perspex made data acquisition impossible. Consequently, a refractive index-matched fluid was used. Details of the fluid are given below. The basis for the choice of tracer particles is described in section 3.2.4.2.

3.2.4.1. Refractive Index Matching

The Becke Line microscope technique[1] was used to determine the refractive index of the Perspex by immersing small particles in liquids of known refractive indices on microscope slides. When the slides are viewed with a microscope and the focus is raised, a faint line of light called the Becke Line will enter the medium of higher refractive index, be it the solid or the liquid. By repeating the process systematically with liquids of incrementally different refractive indices the value of the refractive index of the solid will be found to be equal to the refractive index of one liquid or to be between the values of two liquids.

The resulting refractive index of the Perspex was found to be:

1.492 ± 0.002 (5893 Angstroms at 25°C)

Based on this refractive index value Cargille[i] immersion liquid 5040 (see Table 3.2) was selected for use in the experiments due to its stability and non-toxic properties. 5040 was used in the Becke Line technique and tiny particles left in it for 24 hours showed no change viewed microscopically. Liquids have higher refractive dispersions than solids, however 5040 has an unusually low dispersion and is therefore closer to Perspex.

[i] Cargille Laboratories, Inc., 55 Commerce Rd, Cedar Grove, NJ, 07009-1289 USA

Table 3.2 - Immersion liquid 5040 typical characteristics

Cargille Immersion Liquid 5040	
Composition	Aliphatic/Alicyclic Hydrocarbons and Hydrogenated Terphenyl
Appearance	Colourless to light yellow liquid
Index change rate by evaporation	Low: -0.00002 to +0.00005 expected: exposed surface area to volume ratio of $0.2cm^2/cc$ @ 25°C for 32 days
Pour point (°C)	<-7
Boiling point (°C @ 760mm Hg)	>262
Density (g/cc @ 25°C)	0.882
Viscosity (Pa.s @ 30°C)	0.015
Surface tension (mN/m @25°C)	30

3.2.4.2. Tracer Particles

Good tracer particles must be reflective and large enough for optical detection. They should be neutrally buoyant and small enough to follow the flow without disturbing it. For this study, aluminium particles[j] were chosen, with properties listed in Table 3.3. In order to determine the suitability of the aluminium particles in Cargille immersion liquid 5040[k] the settling velocity of the particles immersed in the fluid was calculated.

Table 3.3 – Aluminium tracer particle properties

	Density (Kg/m^3)	Diameter (μm)
Standard Aluminium Powder	2.7	< 75

If the particles settle very slowly then Stokes flow may be assumed, in which case the force balance for a particle is

$$6\pi\mu a u = \frac{4}{3}\pi a^3 \Delta\rho g$$

[j] Supplied by *Fisher Scientific* UK Ltd, Loughborough, Leicestershire, LE11 5RG

[k] Cargille Laboratories, Inc., 55 Commerce Rd, Cedar Grove, NJ, 07009-1289 USA

where a is the particle radius, μ is the fluid viscosity and Δρ is the particle density minus the fluid density. The data in Tables 3.2 and 3.3 give the terminal settling velocity as,

$$u = \frac{2a^2 \Delta\rho g}{9\mu} \approx 1.7 \times 10^{-4} m/\text{s}.$$

If the measured velocity is 0.5mm/s or higher, there should be little effect on the measurements obtained. Typical measured velocities were 0.7mm/s.

3.2.5. Flow Front Tracking

The motion of flow fronts was observed using the same flow cell. A sequence of profiles for the shape of the flow front was obtained as a fluid was filled into a hexagonal array of cylinders. The experimental set-up shown in Figure 3.8 was employed to achieve this goal:

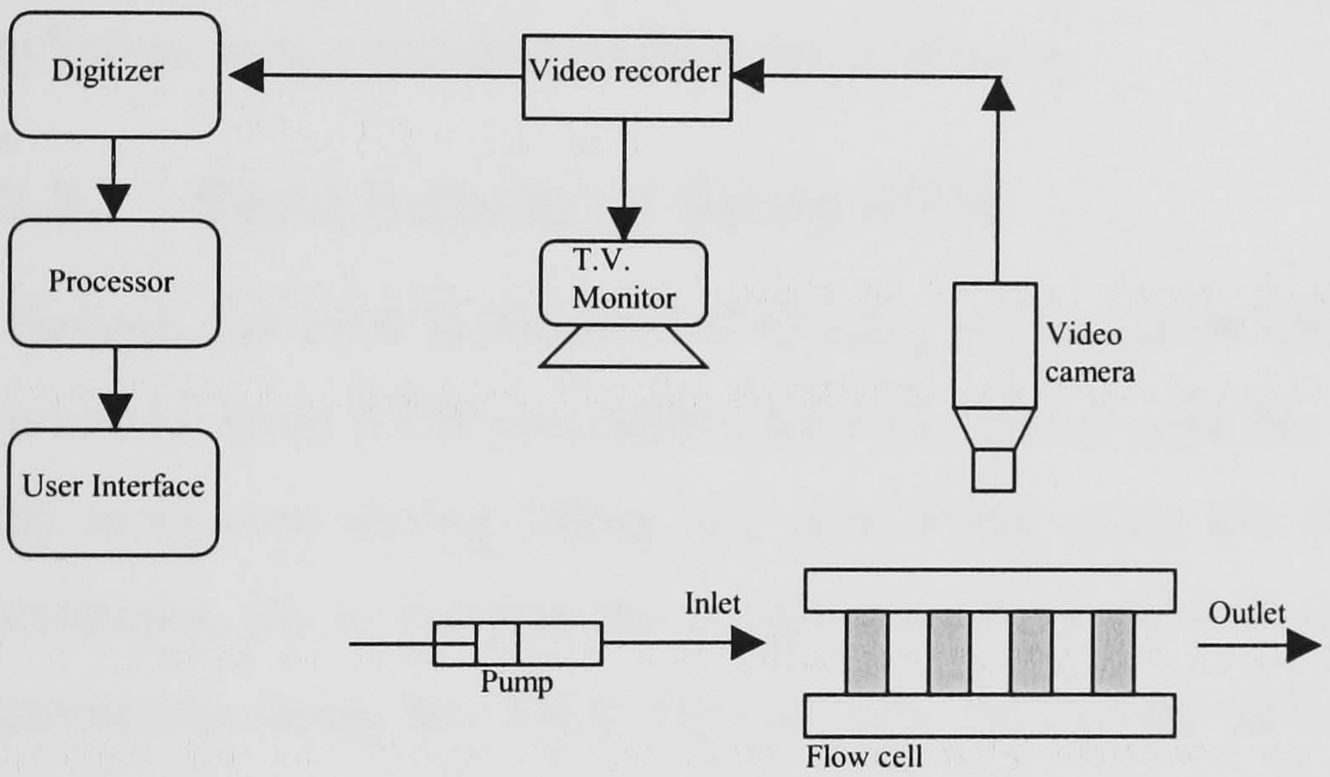


Figure 3.8 - Schematic diagram of the experimental set-up for flow front tracking.

A glycerine/water solution was used as the test fluid for the experiments.

Table 3.4 – Properties of the Glycerine/Water solution used in the flow front tracking experiments

Property	Value
Weight % Glycerine/Water/Dye	80/19.5/0.5
Surface Tension (mN/m)	59.7 @ 25°C
Viscosity (Pa.s)	0.03 @ 30°C
Density (kg/m^3)	1202 @ 30°C

A small amount of black ink was used to dye the fluid in order to provide better contrast in the resulting images. A normal table lamp (11w halogen bulb) with a sheet of tracing paper acting as a diffusing filter was used as the light source. The image capture was conducted using a CCD camera with a normal camera lens connected to a personal computer in order to acquire a series of images (saved as a stack of TIFF files) as the flow front progressed through the flow cell. A software package called '*ImageTool*', produced by UTHSCSA, provided the required functions for later analysis of the results. The time gap between each image taken (frame rate) was 0.2s which was the limit of the hardware/software combination.

Stacks of images at three superficial velocities of 0.28cm/s, 0.45cm/s and 0.63cm/s were acquired. The contact angle between the cylinders and the progressing flow front was evaluated by using '*ImageTool*' to quantify the position of the flow fronts and cylinders in x, y coordinates for detailed analysis.

3.3. Semi Industrial Scale RTM

Through the kind facilitation of Qinetiq, an industrial affiliate of the project, near industrial scale RTM simulations were conducted with two main aims; (i) to monitor the resin cure during filling and post filling using the dielectric cure monitoring technique, (ii) to monitor the progression of the flow front at different fibre lay-up geometries using the *SMARTweave* flow monitoring device. Mr Stuart McCallum[1] participated in this series of experiments. His contribution to the work is gratefully acknowledged.

3.3.1. RTM Moulds

Two different RTM moulds were used in the near-industrial-scale RTM simulations. A 4mm thick mould was used in the dielectric cure monitoring studies, and a thicker 30mm mould was used in the *SMARTweave* flow front tracking experiments. It was necessary to use a thicker mould in the *SMARTweave* experiments to enable through-thickness variation in the filling behaviour to be monitored. The whole project was targeted at thick composite sections.

---

[1] *Imperial College*, Department of Materials, London, SW7 2BY, UK

3.3.1.1. Dielectric Cure Monitoring Studies

A 4mm thick stainless steel mould manufactured from *P*20 tool steel was used for the cure studies. The flat mould dimensions were 300mm × 300mm (as shown in Figure 3.9). The volume fraction (V_f) of unidirectional glass fabric placed in the tool was 60%. The fibres were placed perpendicular (90°) to the resin flow direction.

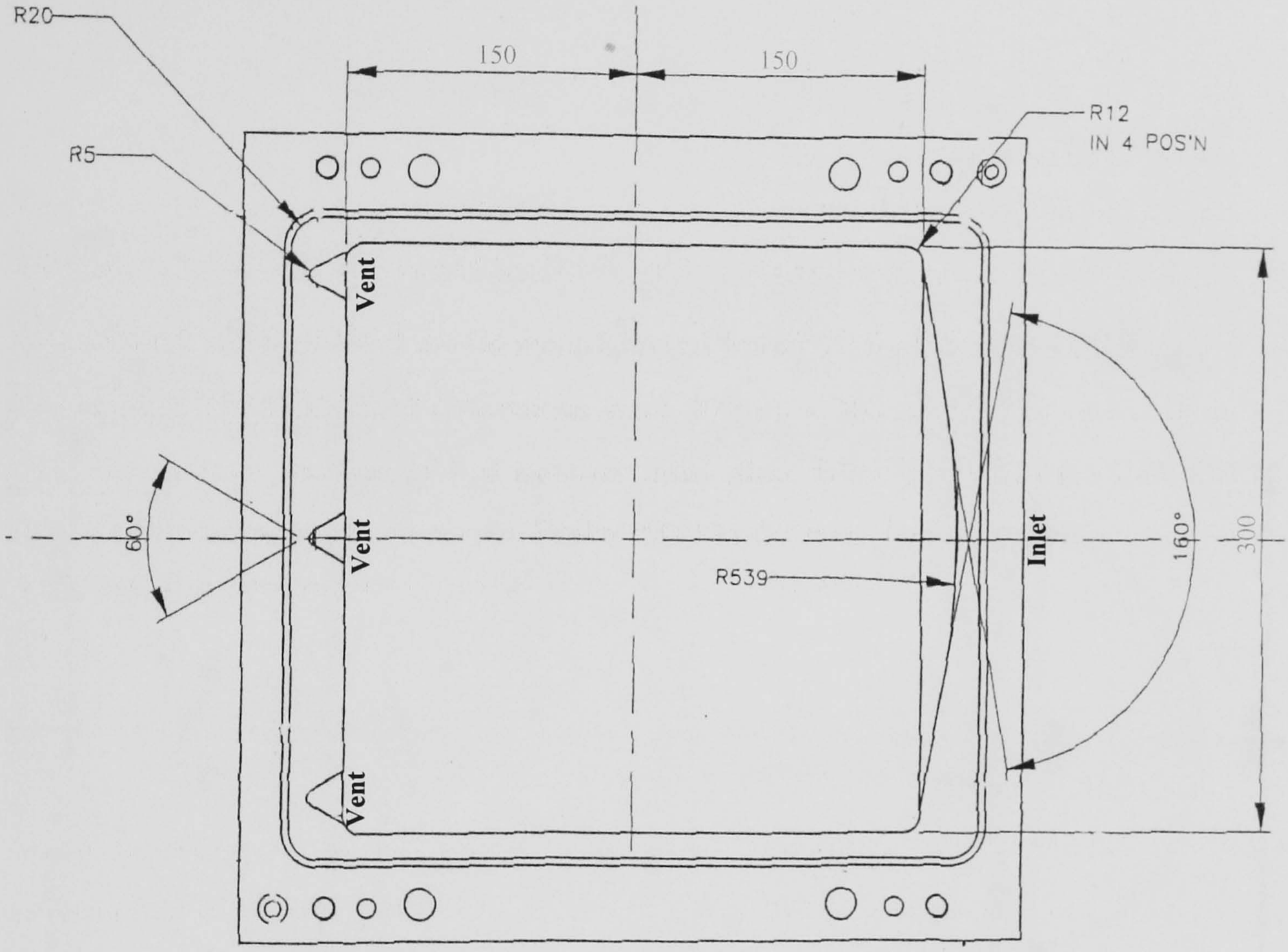


Figure 3.9 - Detailed drawing of the RTM mould used in the dielectric cure monitoring studies. The mould thickness is 4mm and has a length and width of 300mm. The single injection port is seen on the right-hand side of the drawing and the three vent ports are on the left-hand side.

An *IDEX* dielectric sensor[m] and J-type thermocouple were placed in the centre of the mould with equal layers of glass fabric above and below the sensors.

[m] Supplied by *Micromet Instruments*, 25 Wiggins Avenue, Bedford, MA 01730 USA

3.3.1.2. *SMARTweave* Studies

A 30mm thick stainless steel mould manufactured from *P*20 tool steel was used for this investigation. The flat mould dimensions were 400mm × 400mm. In order to accommodate the wiring for the sensing system, aluminium spacers were placed around the edge of the mould sizing it down to 360mm × 360mm.

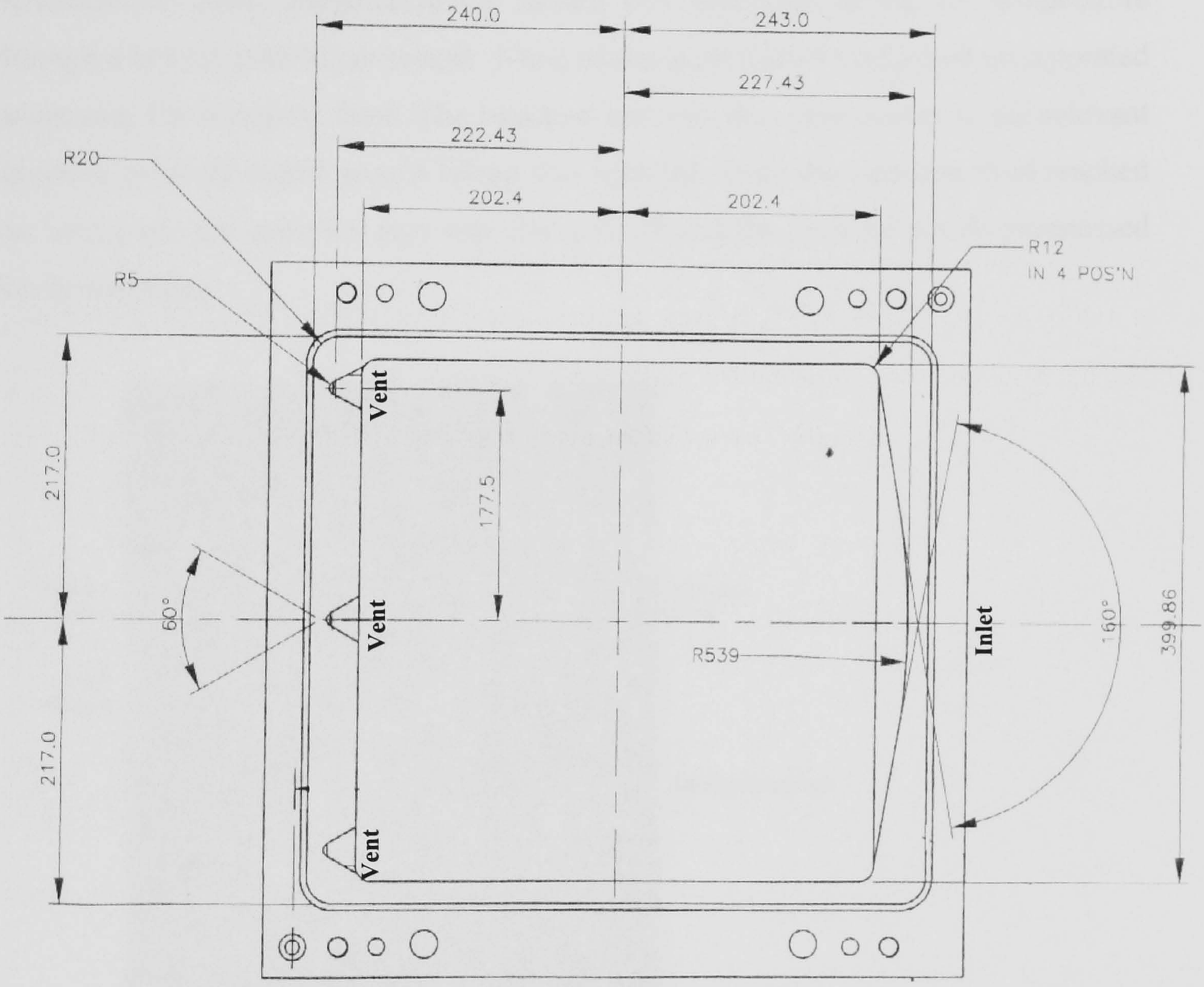


Figure 3.10 – Detailed drawing of the RTM mould used in the *SMARTweave* studies. The mould thickness is 30mm and has a length and width of 400mm. The single injection port is seen on the right-hand side of the drawing and the three vent ports are on the left-hand side.

3.3.2. Processing of Liquid and Injection Process

The injection process was carried out using an *Isojet*[n] RTM injection machine which had a maximum capacity of 15 litres, 10Bar max pressure and 175°C max temperature.

The injection liquid was placed in the pressure pot shown in Figure 3.11 and left to stand for at least half an hour to give it time to degas. For experiments that were not performed at room temperature the mould was preheated to the set temperature through a hot oil circulation system. None of the experiments performed incorporated preheating the injection fluid. The injection pot was then pressurised to the relevant injection pressure before mould filling was initiated. Once the injection fluid reached the vent ports the injection port was clamped off and the pressure pot de-pressurised for de-moulding.



Figure 3.11 – The *Isojet* RTM injection pot used to pump the liquid into the mould.

Figure 3.11 displays the *Isojet* injection pot used.

---

[n] *ISOJET Equipements*, 2 Chemin du genie 69200, Venissieux, France

3.3.3. Fabric Material

Glass fibre fabric was used in both the dielectric cure and *SMARTweave* studies. The two main reasons for choosing this fabric system were; (i) its non-conductive nature which was important for both studies and (ii) the relatively low cost. For comparability of the experimental data with numerical simulations, unidirectional glass fibre was used as this represents the simplest filling material.

The fibre used was 724g/m^2 unidirectional E-glass^o ET-760 style number D624. This was stitched with 6 gauge 76 D-Tex polyester stitching with 1200 tex per bundle. Figures 3.12 and 3.13 show the spool stack and the weaving machine used to manufacture the fabric. Figure 3.14 shows an image of the uni-directional glass fibre mat.

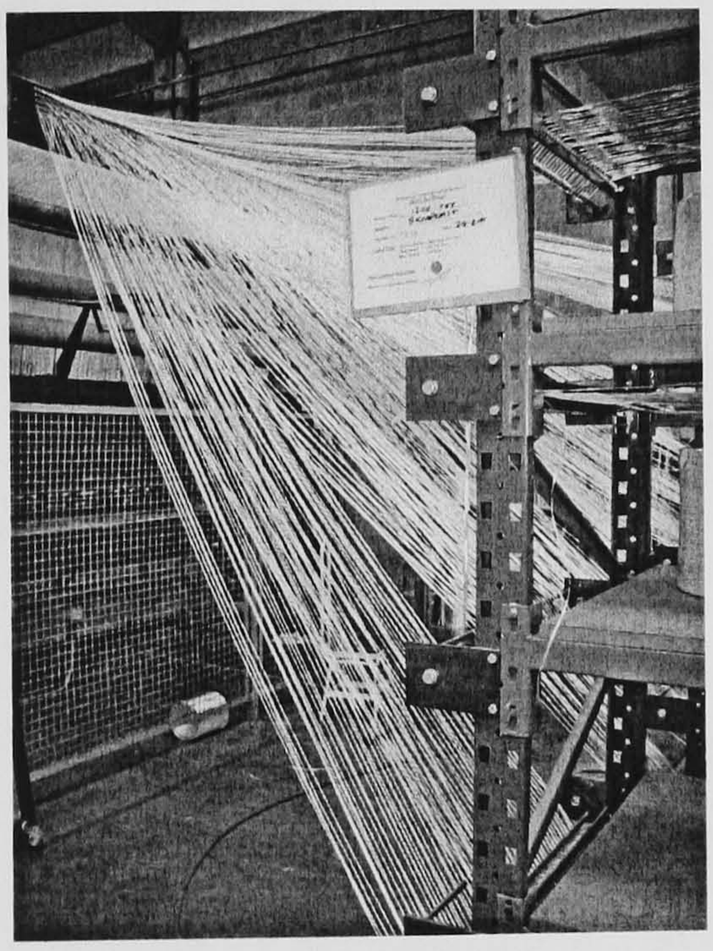


Figure 3.12 - Glass fibre spool stack.

^{o} Manufactured by *Saint-Gobain BTI UK Ltd*, Andover, Hants SP10 5LU



Figure 3.13 - Liba weaving machine used in the manufacture of the unidirectional glass fabric used in the experiments.

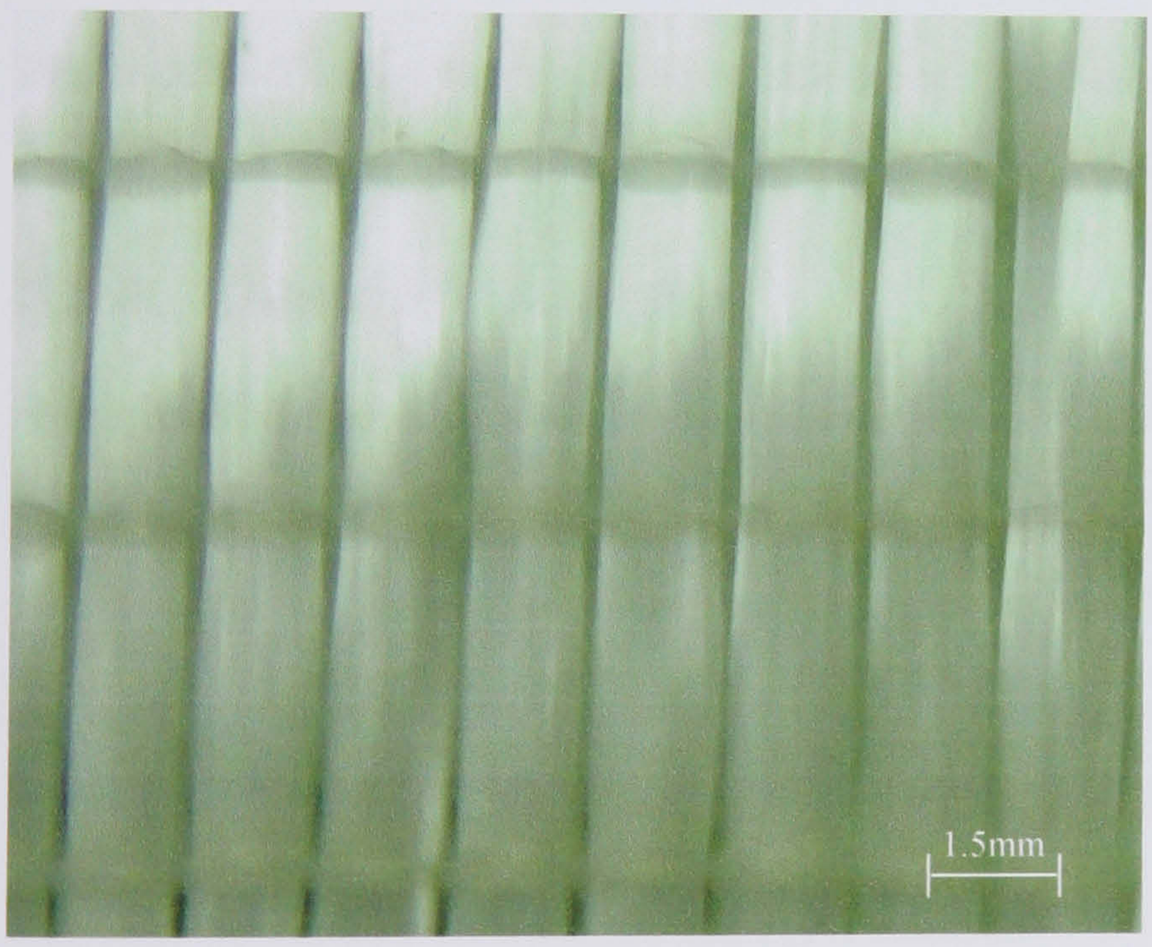


Figure 3.14 – Image of the unidirectional glass fabric material (724g/m^2 ET-760)^o.

A 1250mm wide automatic fabric-cutting machine was used to cut the glass fibre to mould size. This was kindly made available by *Dowty Aerospace Propellers*, Gloucester, GL2 9QL, UK and is shown in Figure 3.15.

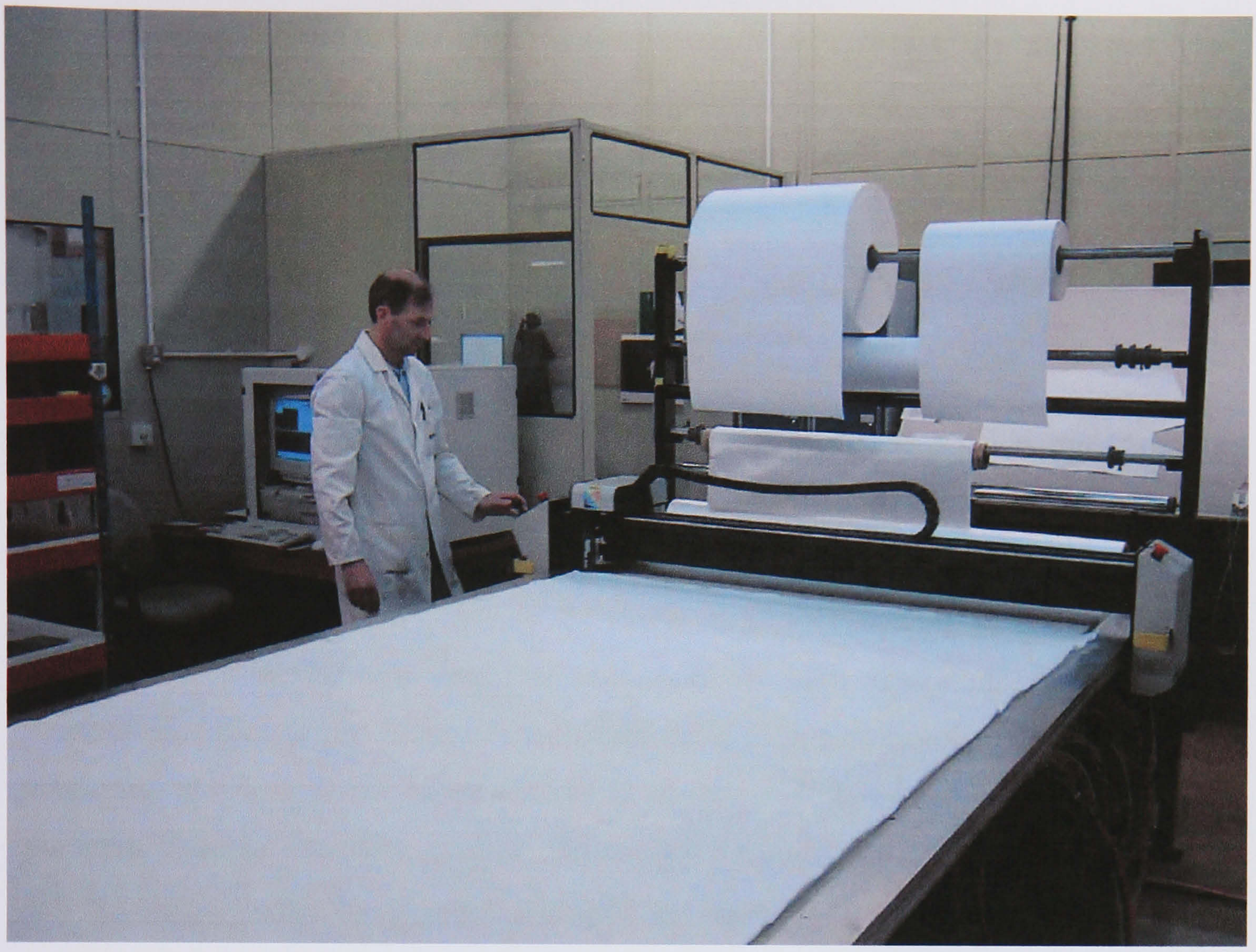


Figure 3.15 - Cutting table used to cut the glass fabric sheet to the mould dimensions of 400mm by 400mm. This was performed at *Dowty Aerospace Propellers*, Gloucester, GL2 9QL, UK.

3.3.4. Dielectric Analysis

A dielectric cure monitor[m] was used to determine the cure profile for the commercial resin system Dow Derakane 411-C50 during processing in the resin transfer moulding (RTM) process. The following literature is supplied by *Micromet Intruments*[m].

Dielectric analysis relates molecular motions to the following polymeric properties:-

- viscosity / rigidity
- rate and extent of reaction
- cure time
- diffusion coefficient
- glass transition temperature
- electrical properties

The fundamental properties measured by DEA are the voltage and current between a pair of electrodes in order to determine the conductance and capacitance between

those electrodes. From these values the permittivity and loss factor are calculated. The final parameters are the conductivity, and its reciprocal, the ion viscosity, μ_{IV}. The permittivity is a measure of the alignment and number of dipoles in the fluid (it is also referred to as the dielectric constant):-

$$\varepsilon' = \frac{C}{\varepsilon_0} . \frac{1}{A/D} \qquad [3.3]$$

where C is the capacitance, A is the electrode surface area, D is the distance between the electrodes and ε_0 is the permittivity of free space (8.854×10^{-14}Fcm^{-1}).

The loss factor is a measurement of the energy expended moving ions and aligning dipoles. The loss factor is therefore influenced by both dipole motion and ionic conduction. Since dipole motion is relatively small throughout typical polymerisation processes, the loss factor is essentially a measure of the mobility of ions in the material. If the loss factor is measured at several frequencies, it is possible to confirm that the measurement being made is largely ion mobility with little contribution from dipole relaxation since the contributions are related by,

$$\varepsilon'' = \frac{\sigma}{\omega\varepsilon_0} + \varepsilon''_{dipole} \qquad [3.4]$$

where σ is the conductivity and ω is the angular frequency ($2\pi f$).

The ion mobility, also termed the ionic conductivity, is inversely related to the viscosity prior to gelation and to the rigidity after gelation. The measurement of ion conductivity assumes that the ion concentration is constant and is dominated by ion mobility:-

$$\sigma = \varepsilon'' \times \omega \times \varepsilon_0 \qquad [3.5]$$

The ion viscosity, μ_{IV}, is routinely used to characterize the cure of thermoset materials. The reciprocal of ionic conductivity is the resistivity of the material. Since resistivity has been established to be strongly correlated to mechanical viscosity it is referred to as the Ion Viscosity:-

$$\mu_{IV} = 1/\sigma \qquad [3.6]$$

An *IDEX* sensor supplied by *Micromet Instruments*[m] was used. It is composed of two planar interdigitated comb electrodes on a Kapton film.

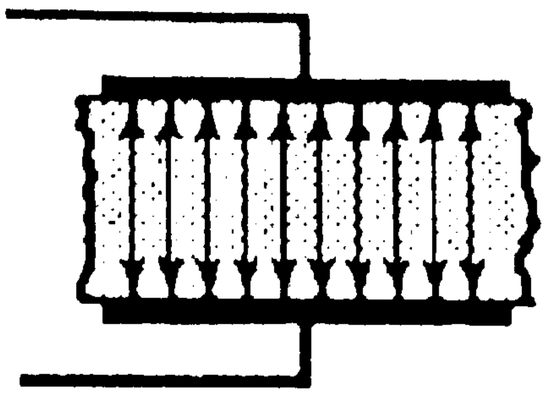


Figure 3.16 – An *IDEX* dielectric sensor.

However, the use of these sensors was not very successful as on many occasions the sensors failed to operate during the experiments. The main reason behind their failure to operate efficiently is believed to be due to an inherently poor design on the solder joints. Out of 7 experiments attempted only two yielded results.

3.3.4.1. Procedure

Dow Derakane 411-C50 was used as the fluid system using a 2-hour gel mix at 20°C (i.e. mix ratio of 1kg base resin plus 10g of M50 plus 0.8g of G-accelerator). Mould filling took place at room temperature using a fill pressure of 1.5bar. After injection, the pressure was ramped up to 3bar and the temperature was gradually ramped up to 80°C at 5°C/min. This was then held for two hours before cooling the mould to 30°C at 5°C/min. The tool was then de-moulded.

Measurements were taken using an IDEX sensor and J type thermocouple supplied by Micromet Instruments[m].

3.3.5. SMARTweave

SMARTweave[m] is Micromet's RTM resin flow front analysis system based upon a technology developed by the US Army Research Laboratory. The SMARTweave system measures the electrical properties at intersecting nodes of conductive wires or fibres (graphite fibres are often used) which are laid out in separate, electrically isolated planes to form a grid pattern in the *SMARTweave* fabric. In this case we used

conductive wires 30awg[p]. When resin reaches each node, the electrical properties of that node will change and are recorded by the system.

Karo™ corn syrup[q] was used as the matrix system in these series of experiments. The low conductivity of typical RTM resin systems made them unsuitable. The use of corn syrup also facilitated the reuse of the conductive wire since there was no cure. This allowed maximum use to be made of the available time in the Qinetiq facility.

3.3.5.1. Measurement Principle

SMARTweave monitors changes in the resistance at the gap between two grid lines (see Figure 3.17). There are two types of grid lines, sensing lines and excitation lines. The excitation lines generate a DC voltage signal. The sensing lines detect the voltage generated by the excitation lines. In practice, one excitation line is activated at a set potential and the response to the active excitation line is measured by switching along the sensing lines. By repeating the process for the other excitation lines, the voltage level is sampled over the entire grid.

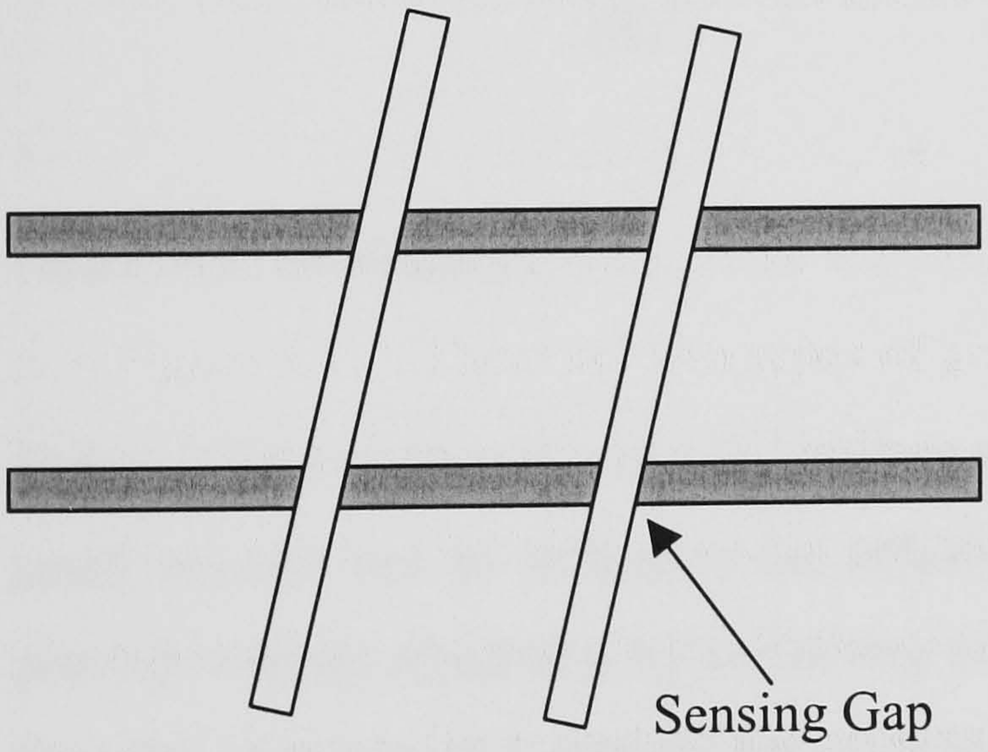


Figure 3.17 - Sensing gap between excitation and sensing lines.

---

[p] Kynar wrapping wire 30awg supplied by *RS Components*, Birchington Rd Weldon Industrial Estate Corby Northants NN17 9RS, UK.

[q] Manufactured by *Unilever BestFoods*, North America.

3.3.5.2. The Grid

The grid lines are arranged in a matrix pattern that positions sensing nodes at locations of interest. A gap between the grid lines at every node of interest is necessary to monitor the resistance at a node. This was accomplished by placing a layer of glass fabric between the sets of excitation (X) and sensing (Y) lines. Figure 3.18 shows a schematic of the 8 × 8 grid.

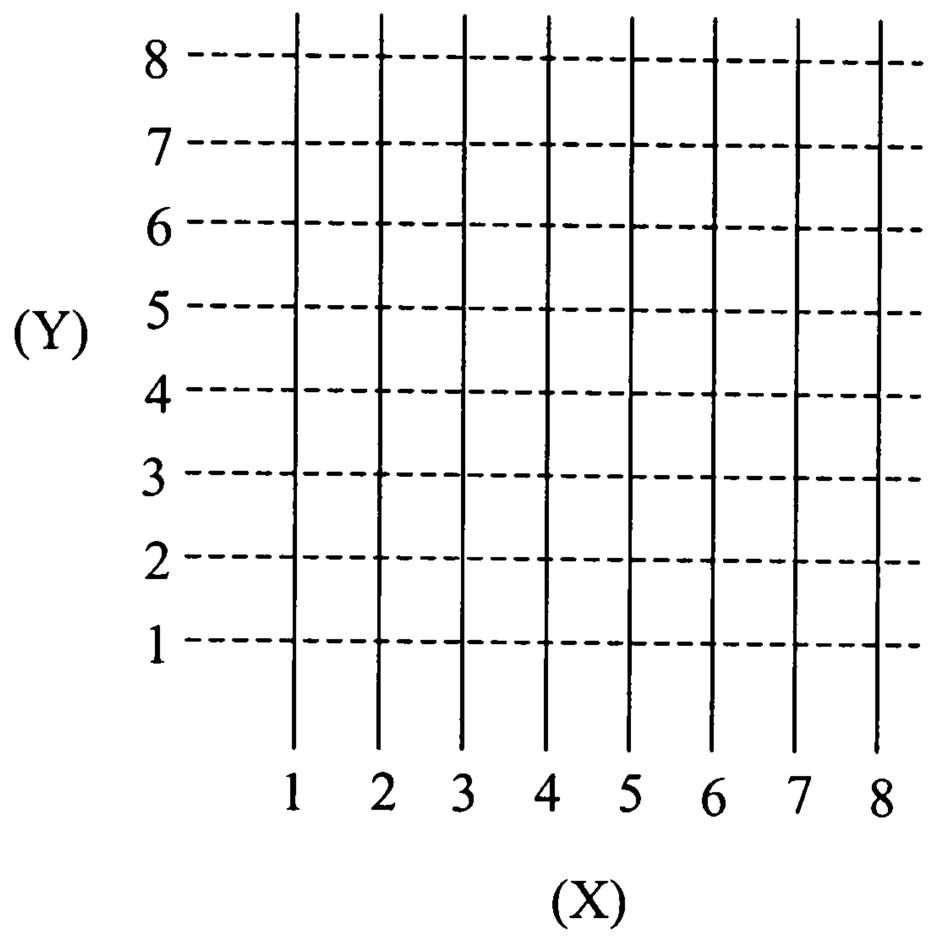


Figure 3.18 - Sensing grid.

Kynar insulated 30awg[r] wire was used as sensing and excitation lines. This wire was small enough not to influence the infusion of the resin significantly and also to provide a sharp resolution by restricting sensitivity to a smaller region. At the same time the wire was also strong enough not to break due to the stresses of closing the mould.

3.3.5.3. Sensor Positioning

In order to monitor the through-thickness variation in the progression of the flow front, the sensing elements were distributed into different planes. The *SMARTweave* system allows 15 ***X*** and 15 ***Y*** wires. This put a restriction on the number of planes and

---

[r] Supplied by *RS Components*, Corby, Northants, NN17 9RS

nodes per plane that could be achieved. Two different configurations of sensor arrangement were employed depending on the fabric lay-up:-

1. Three planes each consisting of 5***X*** and 5***Y*** cables. In order to maximise the data output, two planes were positioned in the top half of the mould and one plane in the bottom half to test for even distribution/filling.
2. Or five planes with 3***X*** and 3***Y*** cables in each plane. This configuration was only used for bi-directional fabric lay-up i.e. a section of the lay-up was parallel to the main flow direction and another transverse. The through-thickness positioning of the sensors in this case was dependant on the fabric lay-up.

Figure 3.19 shows the through-thickness sensor positioning for case 1. The mould thickness was 30mm.

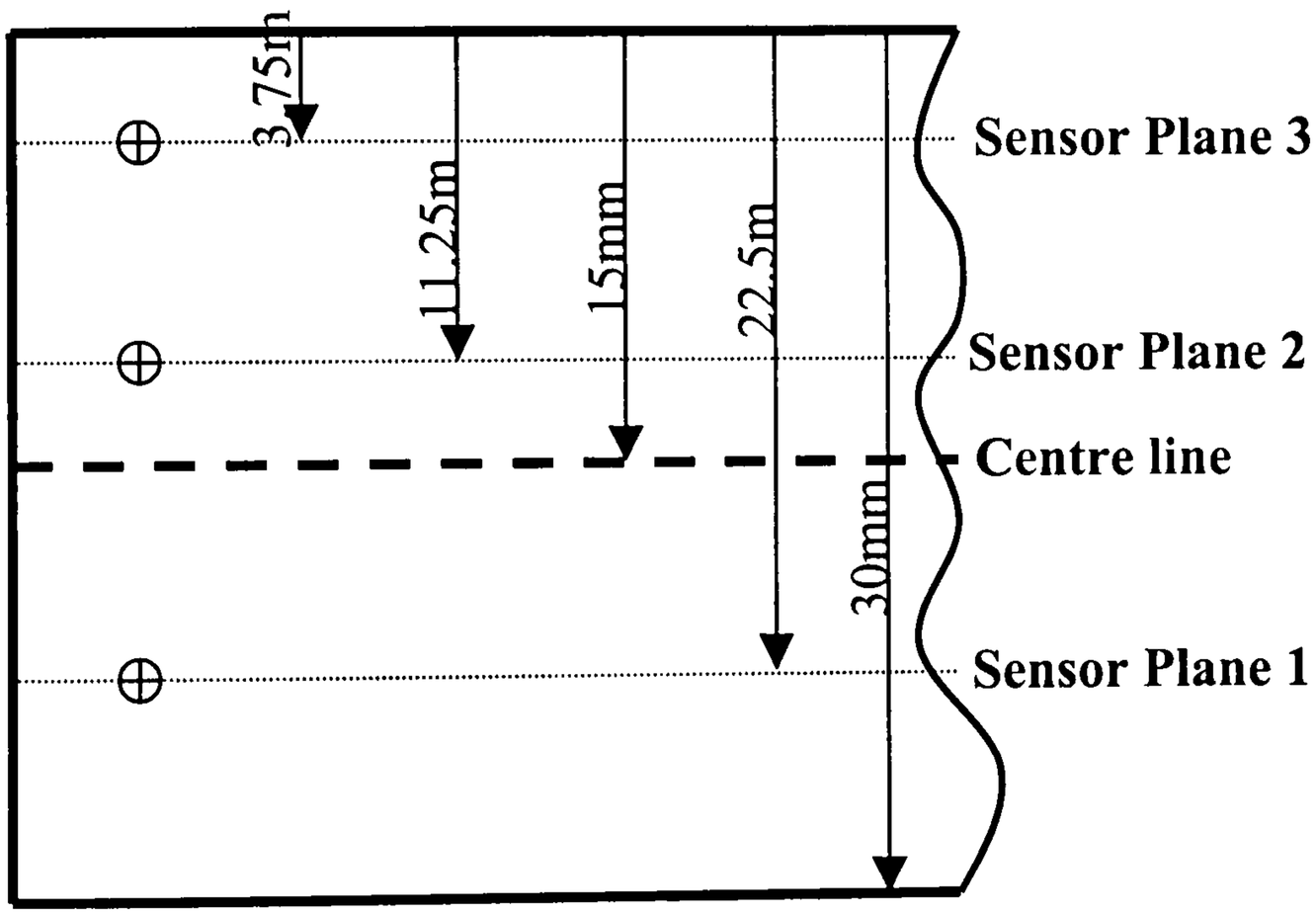


Figure 3.19 - Through-thickness sensor positioning for case 1.

The sensor positioning in each plane for case 1 is shown in Figure 3.20. Again, in order to maximize the front tracking data extracted from these few nodes, four ***X*** wires were placed in one half of the mould and one ***X*** in the other half to test for uniformity throughout the mould. The five ***Y*** wires were distributed equally along the length of the mould (see Figure 3.20).

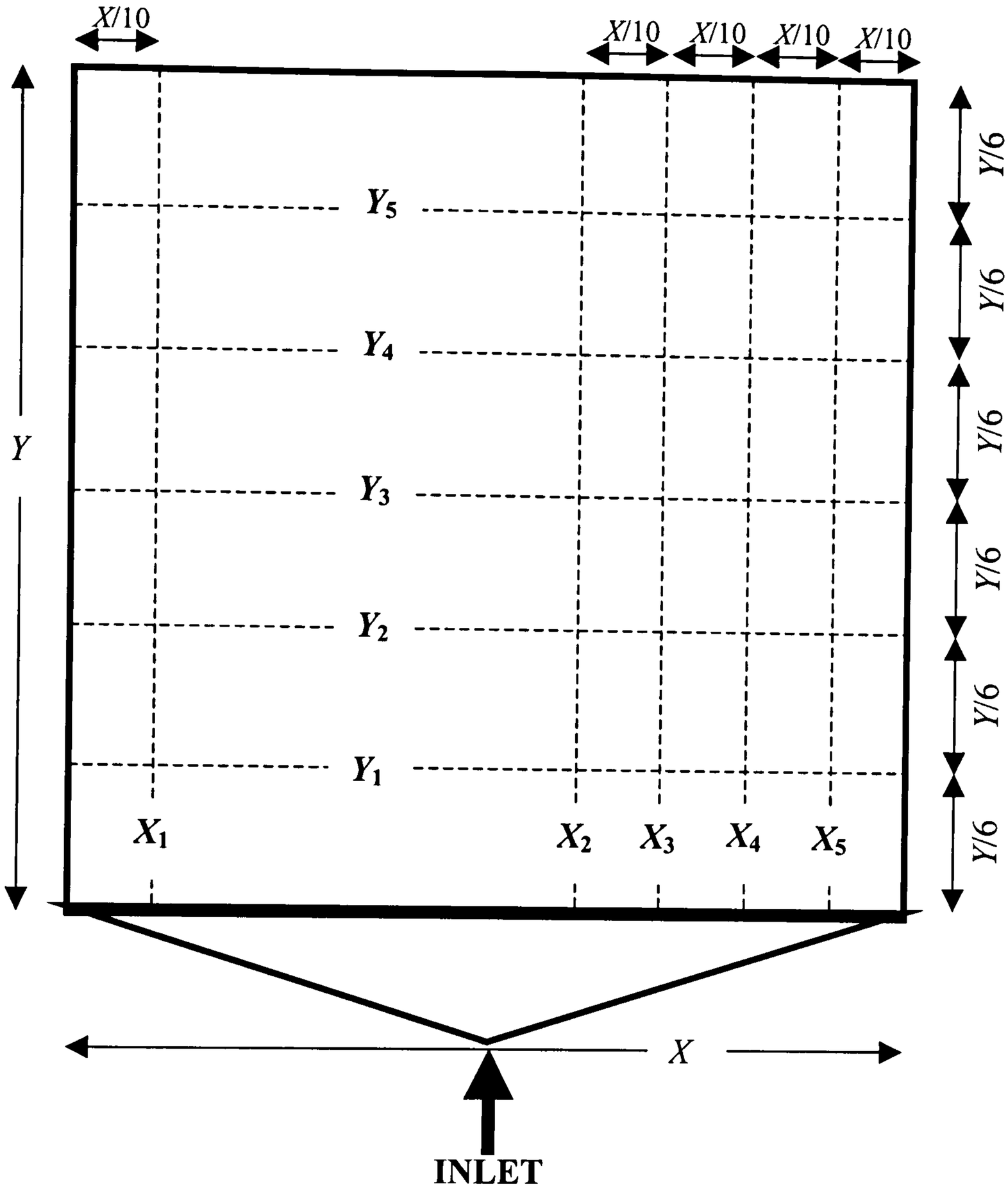


Figure 3.20 – Schematic showing the sensor positioning in each plane for experiments where three planes were used to monitor the flow. All lengths shown are dimensionless because the *X* and *Y* variables changed for different experiments depending on the dimensions of the fabric used.

Figure 3.21 shows the sensor positioning in each plane for case 2 (three ***X*** wires and three ***Y*** wires were distributed in each of the five planes).

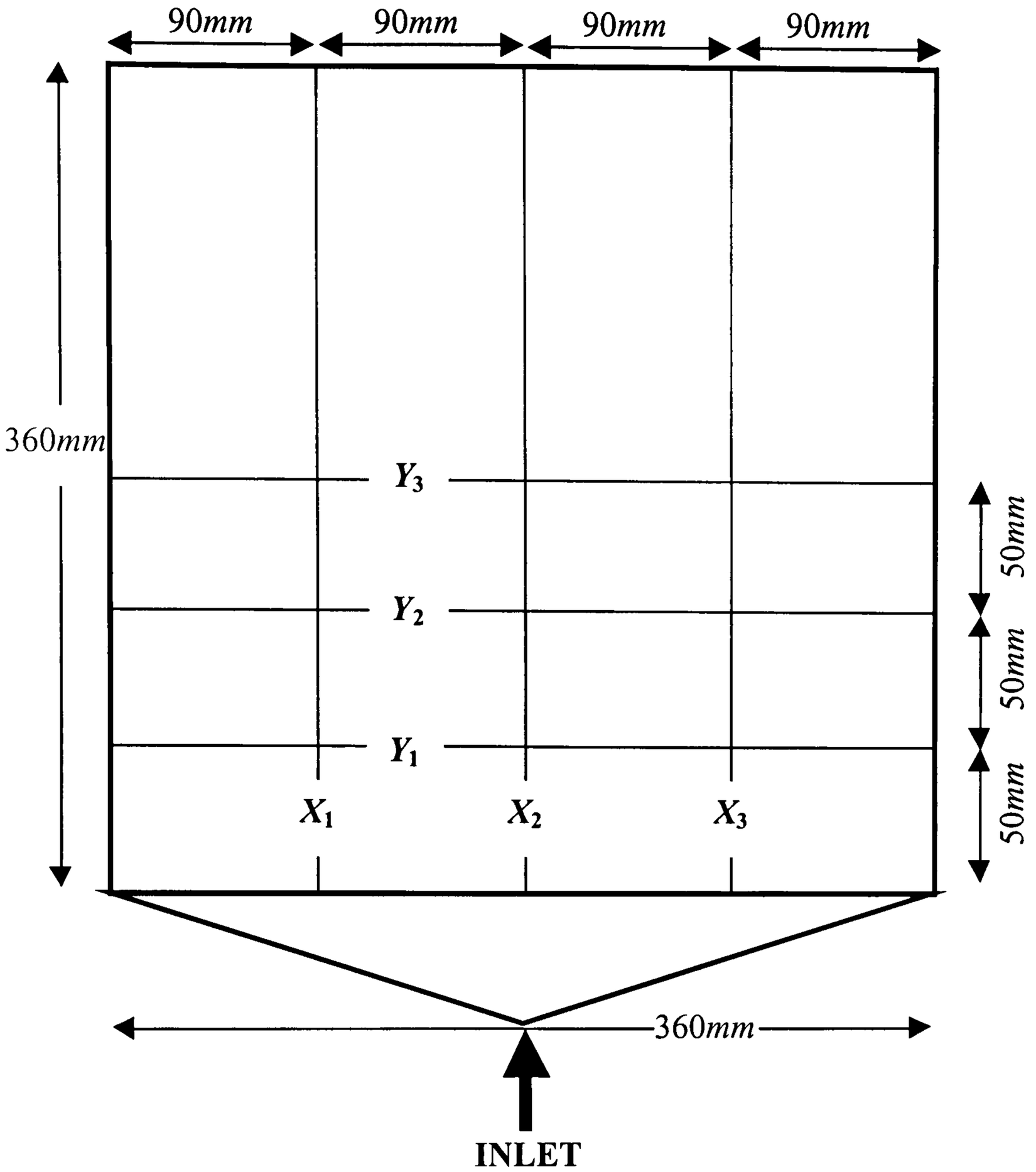


Figure 3.21 – Schematic of the sensor positioning in each plane for experiments where five planes were used to monitor the flow. All the fabric dimensions in this case were 360mm×360mm.

3.3.5.4. Preliminary Experimental Set-up

Preliminary experiments were conducted to evaluate the accuracy of the *SMARTweave* system and the conductivity of the fluid systems. Two fluids were used in the evaluation, Dow Derakane 411-C50[s] and Karo™ corn syrup[t].

---

[s] Manufactured by *Dow Chemicals*, Kings Lynn, Norfolk PE30 2JD, UK

[t] Manufactured by *Unilever BestFoods*, North America.

Dow Derakane 411-C50 is a typical RTM resin system for manufacture of thick composite parts, hence its choice for use in this study. However, it was found that the signal to noise ratio was too low. The measured voltage from this resin system at room temperature was 0.15V. This value increased to 0.6V when the resin system was heated above room temperature. However, the level of noise within this voltage range was too high to distinguish the true signal (resin contacts).

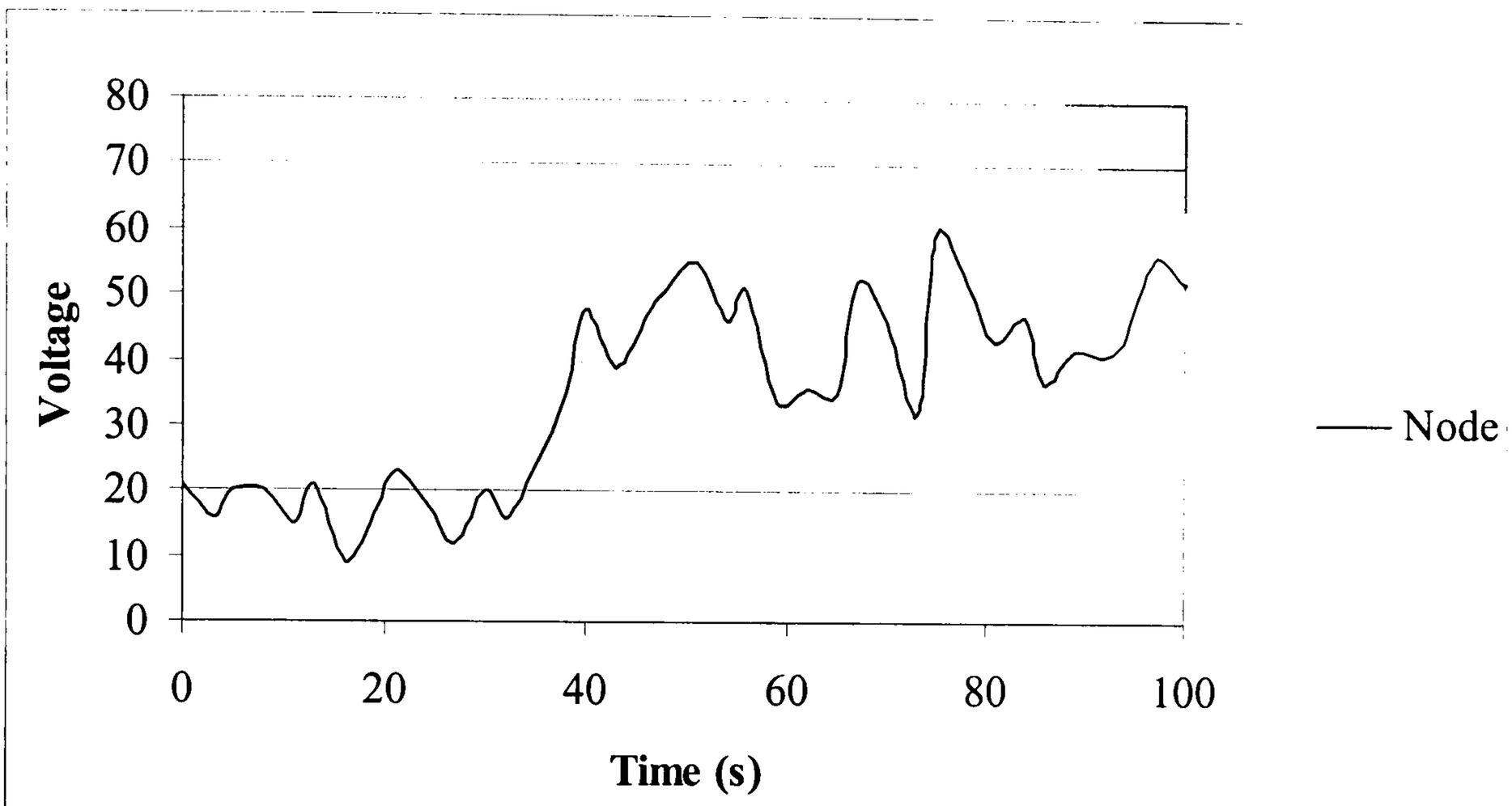


Figure 3.22 - Voltage-time history for Derakane 411-C50.

Figure 3.22 displays one of the better voltage-time history curves for Dow Derakane 411-C50 resin system. The signal to noise ratio is evidently quite low and therefore it would be difficult to determine the nodal contact time for a grid of nodes. In this case the resin made contact with the node at approximately 30 seconds. A small increase in the registered voltage is observed at this point in time. Refer to Figure 7.3 for a similar voltage-time history for Corn Syrup.

Attempts to increase the level of conductivity of this resin system proved unsuccessful enough to justify its use in the experiments. Such attempts involved the addition of graphite to resin system and the addition of processed carbon black which is the industry standard for conductive and anti-static applications.

Corn syrup, however, has a higher electrical conductivity and higher signal to noise ratio. The measured voltage from using corn syrup was approximately 9.8V. The additional advantages of using corn syrup are:

- It is cheaper
- It is safer to handle and use
- Saturation between each layer can be investigated after the test. This cannot be done using a curing resin system

The disadvantages, however, are that:

- Corn syrup is sensitive to variations in temperature (7.5% change in viscosity per °C.)
- The viscosity of the corn syrup can be matched to a typical resin system

But the surface tension and contact angle are less easily matched.

Hence it was decided to use a diluted solution of corn syrup (10% water by weight) for the investigation.

3.4. Summary

This chapter has outlined the key equipment and materials used and the procedures performed in the acquisition of data and results discussed in subsequent chapters.

Rheological characterisation experiments of typical RTM resin systems are described and the resin properties listed. Also, the design of a flow cell used to simulate the infiltration of resin through a fibre matrix is detailed. The key aspects of the flow cell are (i) it can be used to determine an approximately two-dimensional flow field, (ii) it has a hexagonal arrangement of spherical rods and (iii) it has a volume fraction of 58%. The particle image velocimetry method used to gather information on the velocity field in a saturated medium is discussed. Also described is the flow front tracking method used to obtain a sequence of profiles for the shape of the flow front as a fluid was filled into a hexagonal array of cylinders.

Near-industrial-scale RTM experiments used to monitor cure using a dielectric cure monitoring system and also to analyse the through-thickness variation in the progression of the flow front using the *SMARTweave* system are described.

3.5. References

---

[1] Lundstrom T. S., "Void Formation and Transport", Lulea University of Technology, PhD Thesis, (1996).

4. RHEOLOGY AND CURE MODELLING OF RESIN SYSTEMS

This Chapter presents results of rheological characterisation studies performed on typical RTM resin systems. A model for the resin viscosity development during cure is proposed and applied to several resin systems.

4.1. Introduction

A greater understanding of the processing of filled and unfilled thermoset polymers is of vital importance to many industries including aerospace technologies, automotive manufacturers and many other specialized as well as non-specialized applications. However, due to the complexity of the reaction systems the design and control of these processes have traditionally been undertaken by trial and error methods. In order to achieve higher efficiencies in terms of reduced design and raw material costs it is necessary to produce an accurate process model.

4.1.1. Kinetic Analysis

The many techniques used to monitor the kinetics of the cure of thermosetting resins include:

- Differential Scanning Calorimetry (DSC)
- Fourier Transform Infrared Spectroscopy (FTIR)
- Dielectric measurements

- Rheokinetic measurements

DSC is the most extensively used technique. DSC measures the rate of heat generated (dQ/dt) during a chemical reaction. The basic assumption in DSC kinetic measurements is that the heat flow is proportional to the rate of reaction and that the cumulative heat flow is proportional to the extent of reaction.

4.1.2. Chemoviscosity

Chemoviscosity involves the study of the variation in viscosity of the resin due to chemical reactions and processing conditions. In a review by Ryan[1] the chemoviscosity was expressed as a function of the pressure (P), temperature (T), time (t), shear rate ($\dot{\gamma}$) and filler properties (F):

$$\eta = \eta(T, P, \dot{\gamma}, t, F)$$

The cure effects on the chemoviscosity are two-fold, the viscosity will initially decrease due to increased temperature and will eventually increase due to formation of the cross-linked network via the curing reaction.

The effect of shear rate on the viscosity of thermosetting resins, $\eta_{sr}(\dot{\gamma})$, is important in the determination of the chemoviscosity, η. The relationship will depend on the system used. Sundstrom and Burkett[2] and Hartley and Williams[3] found that polyesters and polyurethane exhibit essentially Newtonian behaviour, whereas epoxies and phenolics show marked shear thinning. The power law model is the most extensively used viscosity-shear rate model for thermoset resins and has been used for unfilled[4,5,6] and filled[7] epoxy systems. Sundstrom and Burkett also showed a good fit of the viscosity of dialylphthalate to the Cross model[2].

The filler effects on the chemoviscosity of thermosetting resins have not been studied extensively, but are vital to understanding the rheology of filled thermosets. Ng and Manas-Zloczower[8] examined an epoxy resin with silica filler and determined that the elastic modulus of the resin can be expressed in terms of filler concentration and the modulus of the matrix and that the gel time is reduced as the filler concentration is increased due to the accelerating effect of the filler on the reaction kinetics.

4.1.3. Gel Effects

The *gel point* is defined as the time or temperature at which covalent bonds connect across the network and an infinite network is formed[9]. Curing can still proceed but the viscosity is very large and may inhibit further reaction due to low diffusion rates. The *vitrification point* of a reacting system is the point at which further reaction is prohibited due to the formation of a rigid glass. Also at the vitrification point, the glass transition temperature (T_g) equals the reaction temperature (T_{rxn}). The gelation effects of an isothermal thermoset system have been described by a Time-Temperature-Transformation (*TTT*) diagram as shown below.

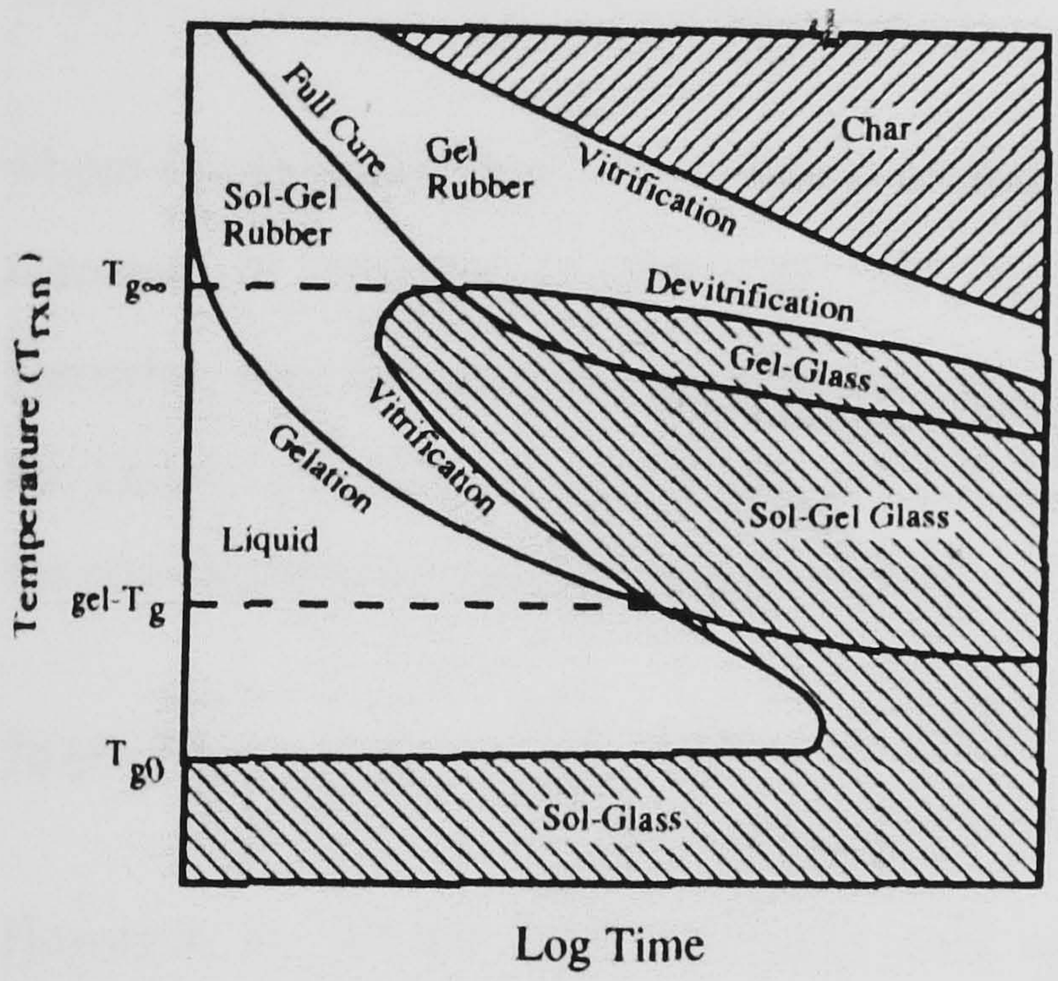


Figure 4.1 - Time temperature transformation diagram (*TTT*) (from Halley and Mackay[9]).

There are seven distinct regions on the *TTT* diagram; liquid, sol-gel rubber, gel-rubber, sol-gel glass, gel-glass, sol-glass and char. T_{g0} is the glass transition temperature of the uncured resin (if such a T_g exists) whilst gel-T_g is the temperature where gelation and vitrification coincide. $T_{g\infty}$ is the maximum T_g of the system. The full cure line represents the time required, at any reaction temperature, for T_g to equal $T_{g\infty}$ and is important for allowing comparative analysis between varied systems.

4.1.4. Cure Modelling

For a thermoplastic material, the rheological properties are determined by the shear history, temperature and flow geometry. However, for a thermosetting resin, the resin

reaction kinetics and the elapsed cure time are also important. Unsaturated polyesters (UP) are one of the most widely used thermoset resins. The reaction of a UP resin is a free-radical chain-growth crosslinking copolymerisation between the monomer and the UP molecules. The curing behaviour is complex due to the interaction between the resin chemistry and the variation of the physical properties[10]. A range of viscosity models has been presented for the viscosity of epoxy resins during the resin transfer moulding process, including empirical models[11,12], probability based models[13,14], gelation models[15,16], and models based on free volume analysis[17]. For isothermal cure, the predominant empirical model has the form[18]:

$$\ln \eta(t,T) = \ln \eta_\infty + \frac{\Delta E_\eta}{RT} + t k_\infty \exp\left(\frac{-\Delta E_k}{RT}\right), \qquad [4.1]$$

where $\eta(t,T)$ is the viscosity at absolute temperature T, t is time, η_∞ is the reference viscosity at 'infinite temperature', ΔE_η is the Arrhenius activation energy for viscosity, R is the universal gas constant, k_∞ is the kinetic analogue of η_∞ and ΔE_k is the kinetic analogue of ΔE_η. The empirical model [4.1] can be generalized to allow for non-isothermal cure conditions to give[18]

$$\ln \eta(t,T(t)) = \ln \eta_\infty + \frac{\Delta E_\eta}{RT(t)} + \int_0^t k_\infty \exp\left(\frac{-\Delta E_k}{RT(t)}\right) dt. \qquad [4.2]$$

However, by far the most commonly-used expression for the change of viscosity during non-isothermal cure is the Williams-Landel-Ferry (*WLF*) equation[19]:

$$\ln \frac{\eta(T)}{\eta(T_r)} = -\frac{C_1(T - T_r)}{C_2 + T - T_r}, \qquad [4.3]$$

where $\eta(T_r)$ is the viscosity at reference temperature T_r and C_1 and C_2 are constants independent of temperature.

Many variations of the *WLF* equation have been proposed in an attempt to improve the accuracy of the predicted viscosity. Karkanas and Partridge[20] proposed

$$\ln \frac{\eta}{\eta_g} = -\frac{C_1(T_{cure} - T_r - T_g)}{C_2 + T_{cure} - T_r - T_g}, \qquad [4.4]$$

where η_g is the fitted viscosity at the glass transition temperature, T_g, and T_r is the reference temperature, which is effectively used as an additional adjustable parameter.

Karkanas and Partridge[20] reported a successful simulation of the viscosity advancement up to gelation (identified as the point where the growth and branching of the polymer chains, caused by intermolecular reactions, causes a phase transition from the liquid state to the rubbery state).

The models introduced so far are thermal history dependent and, as highlighted by Fontana[21], there exist some critical differences between the behaviour predicted by these models and the behaviour of resins in RTM. One of the key limitations of these models is that the resin curing kinetics must be determined at temperatures significantly above the injection temperatures, which means that the real kinetics of the cross-linking of the resin during injection may be very different from the modelled kinetics.

An alternative approach was proposed by Fontana[21]. Starting from the assumption that the resin property that is most sensitive to the degree of cross-linking is the viscosity itself, a method based solely on viscosity measurements was developed. The viscosity was measured over a range of temperatures and times and interpolated look-up tables were presented. These were then incorporated directly into a modelling code. The method was shown by Fontana to be successful for isothermal cures, but proved less accurate when dealing with non-isothermal curing conditions. For the latter, Fontana proposed the normalisation of viscosity η_i at temperature T_i to viscosity η_r at reference temperature T_r:

$$\ln(\eta_r/\eta_i) = f(T_i - T_r)\,, \qquad [4.5]$$

where f is a shifting function for the normalisation of the data to the reference temperature.

This technique gives a viscosity profile that is closer to the measured behaviour than that obtained from thermal-history dependent cure models. Among the advantages of the method proposed by Fontana are that curve fitting for the viscosity *versus* time or degree of cure is not required, *i.e.* viscosity data are used directly to simulate the variations in viscosity behaviour, and determination of the cure kinetics is not required.

However, there are some drawbacks to the method proposed by Fontana, particularly in the determination of the shifting factors that are used in the simulations. These are difficult to determine and the model assumes that they are independent of temperature and cure state, limiting the applicability of the approach.

In this case the approach of Fontana[21] is adapted in a similar form to the model given in equations [4.1] and [4.2] above, but without the need for look-up tables. Furthermore, the approach is extended to deal with a non-Arrhenius temperature dependence.

4.2. Rheology

The following resin systems were used in the various analyses performed: LY5052/HY5052[i], LY564/HY2954[i], RTM6[ii], Derakane Momentum 411-C50[iii] and PR500[iv]. Further details of these resin systems and the rheological equipment used to make measurements can be found in Chapter 3. However, the experimental data for the resin systems RTM6 and PR500 was provided by Dr Q. Fontana, British Aerospace, Sowerby Research Centre, Filton Bristol. His assistance in this work is much appreciated.

In this section detailed results of the resin system LY5052 are given. In terms of applications, LY5052 can be used for: -

- Gliders / airplane parts
- Boat building
- Car bodies and fuselages
- Sports equipment
- Repairing

LY5052 comes with hardener HY5052 and the mix ratio is 100p.b.w[v] of LY5052 to 38p.b.w of HY5052.

---

[i] Manufactured by *Ciba-Geigy*, Macclesfield, Cheshire SK10 2NY, UK
[ii] Manufactured by *Hexcel Composites*, Duxford, Cambridge CB2 4QD, UK
[iii] Manufactured by *Dow Chemicals*, Kings Lynn, Norfolk PE30 2JD, UK
[iv] Manufactured by *3M*, Bracknell, Berkshire RG12 1JU, UK
[v] Parts by weight

All experiments were performed at 30°C. The different kinds of tests performed were:

- Shear stress ramp tests
- Shear rate ramp tests
- Oscillatory stress sweep
- Frequency sweep
- Strain amplitude sweep

The principal results of these tests are presented in the following sub-sections.

4.2.1. Shear Stress Ramp Results

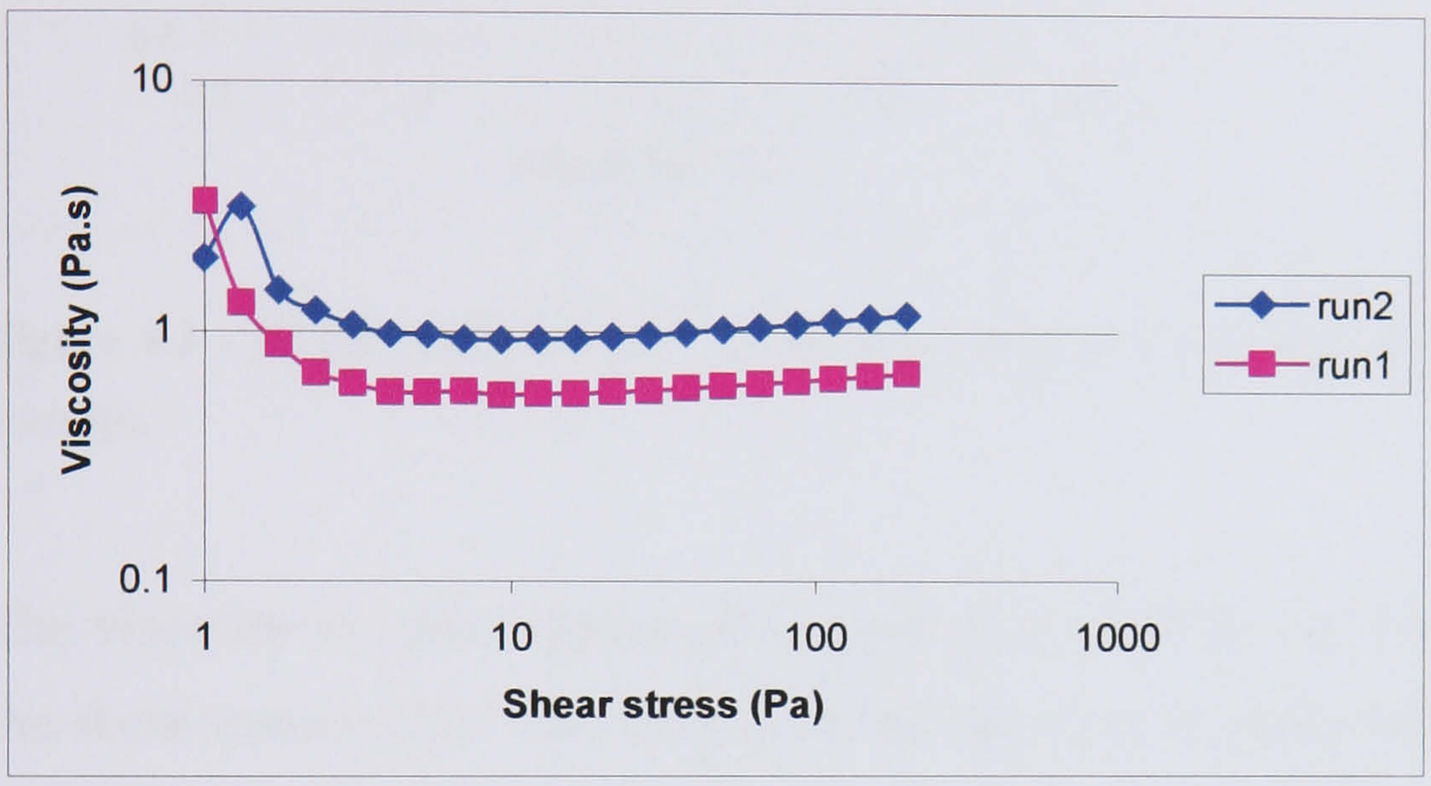


Figure 4.2 - RTMLY5052/HY5052 Shear Stress Ramp at 30°C from 1-100Pa for 20pts at 1min/pt.

From Figure 4.2 it is seen that the resin is Newtonian over an appreciable intermediate shear stress range but seems to show some yield stress behaviour at low stress and slight shear thickening behaviour at high stresses.

Notable also is that the viscosity of the resin at medium to high stress is approximately 1Pa.s. Two runs were performed and as seen the viscosity of the resin in the second run is slightly higher than in the first run due to the initiation of curing. The second run was performed immediately after the first run. This suggests that the apparent shear thickening behaviour may also be attributed to the curing process.

4.2.2. Shear Rate Ramp Results

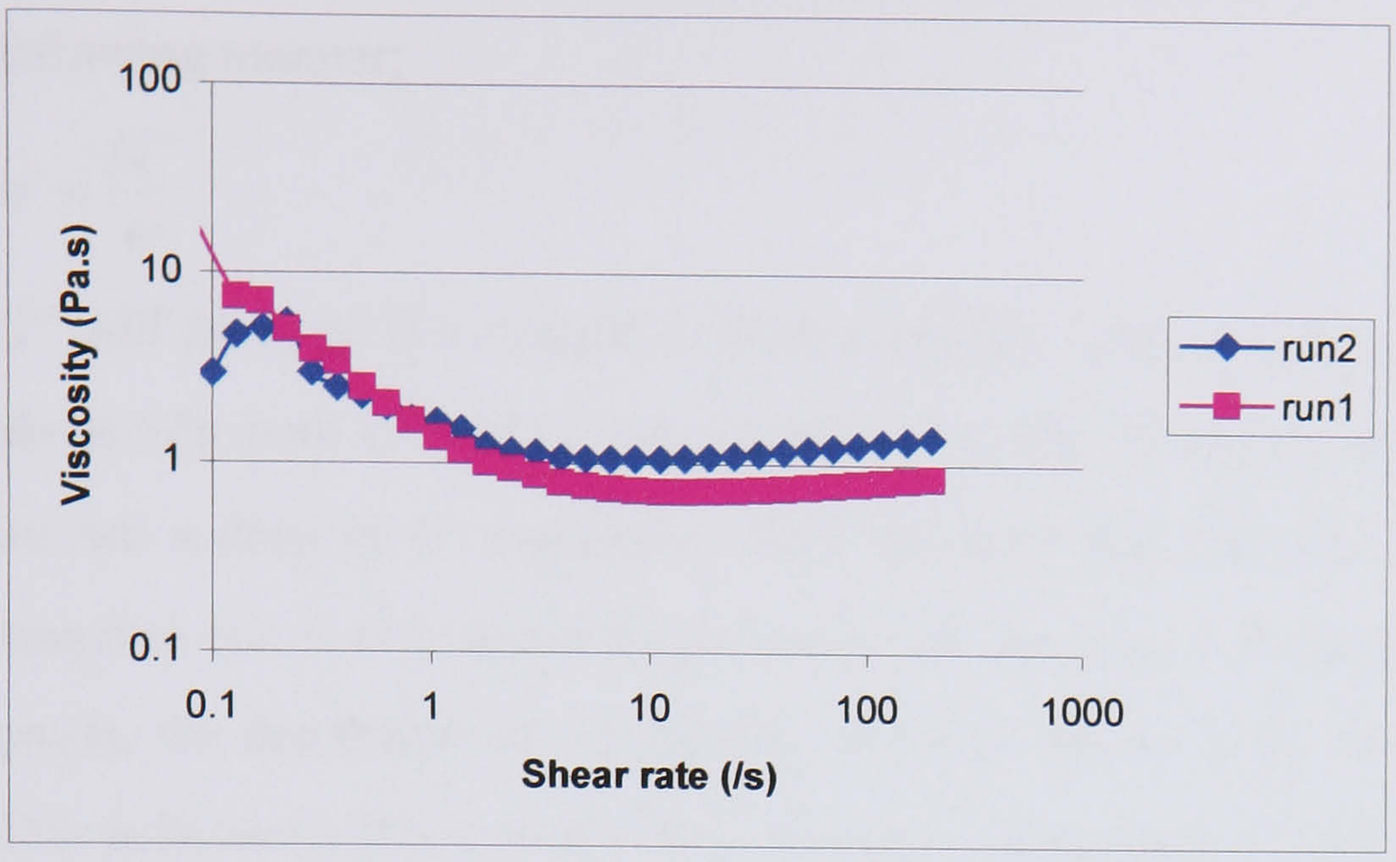


Figure 4.3 - RTMLY5052/HY5052 Shear rate ramp at 30°C from 0.1/s to 200/s for 30pts at 1min/pt.

The viscosity vs. shear rate graph (Figure 4.3) confirms the observations made from the shear stress results. The resin is Newtonian over an appreciable range but seems to show yield stress behaviour at low shear (a power law with slope –1) at about 1Pa.

4.2.3. Oscillatory Stress Sweep

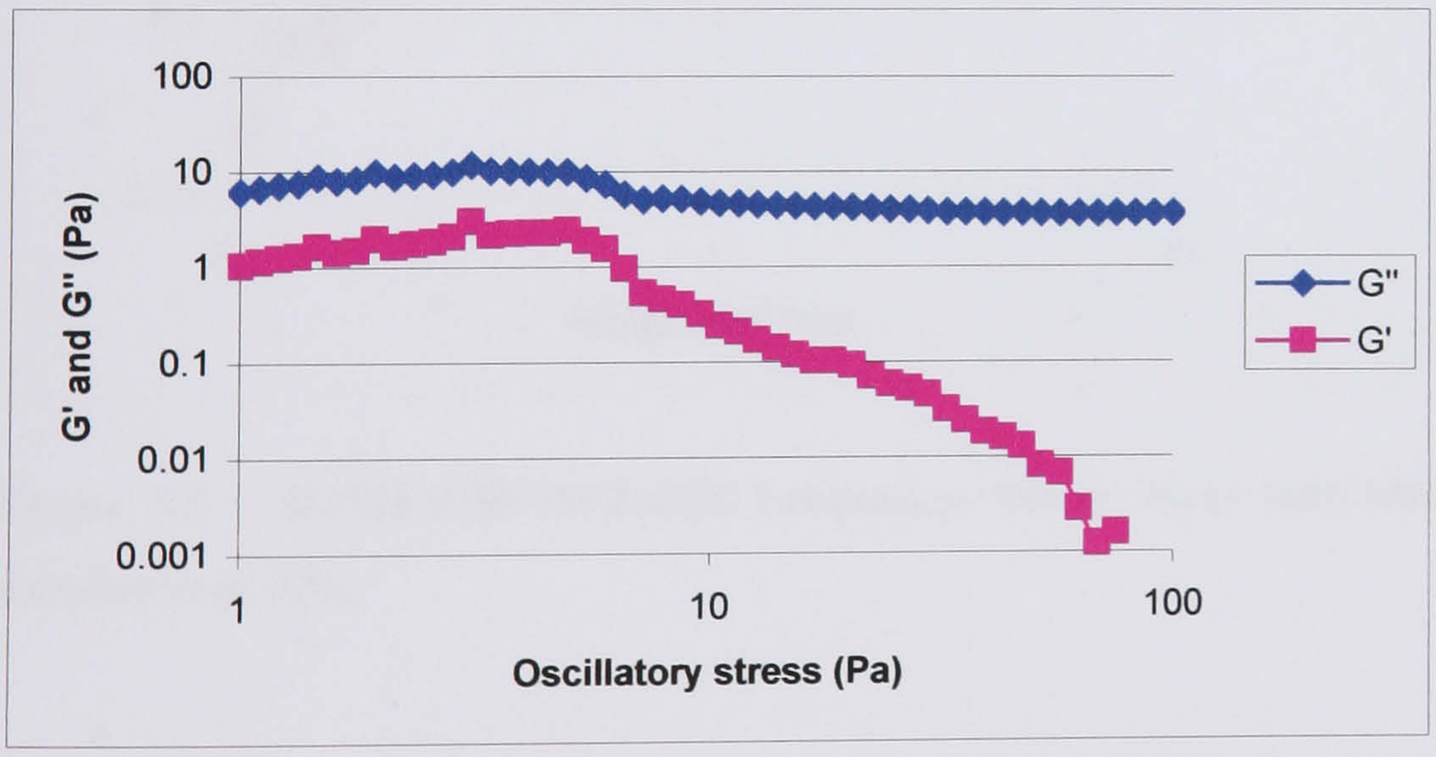


Figure 4.4 - RTMLY5052/HY5052 Oscillatory Stress Sweep, Frequency 1Hz.

Figure 4.4 shows the results of oscillatory stress sweep at a frequency of 1Hz. G' and G'' are the elastic and viscous moduli respectively. G' is a measure of how structured

a material is. It will be large if a sample is predominantly elastic or highly structured. If structure is building within a sample, G' will increase. G'' represents viscous dissipation or loss of energy and is related to the dynamic viscosity (η') in the following manner;

$$\eta' = \frac{G''}{\omega}$$

G'' will be large if a sample is predominantly viscous. Up to an oscillatory stress of about $5Pa$ both G' and G'' are roughly constant. However, at larger values of stress, we see a drop in G' especially. This indicates that the resin has a small amount of structure ($G' < G''$) which begins to break down at a stress of about 5Pa. From this graph, we determine an oscillatory stress of 3Pa to carry out the frequency sweep. This is because 3Pa is well within the range where both G' and G'' are constant.

4.2.4. Frequency Sweep

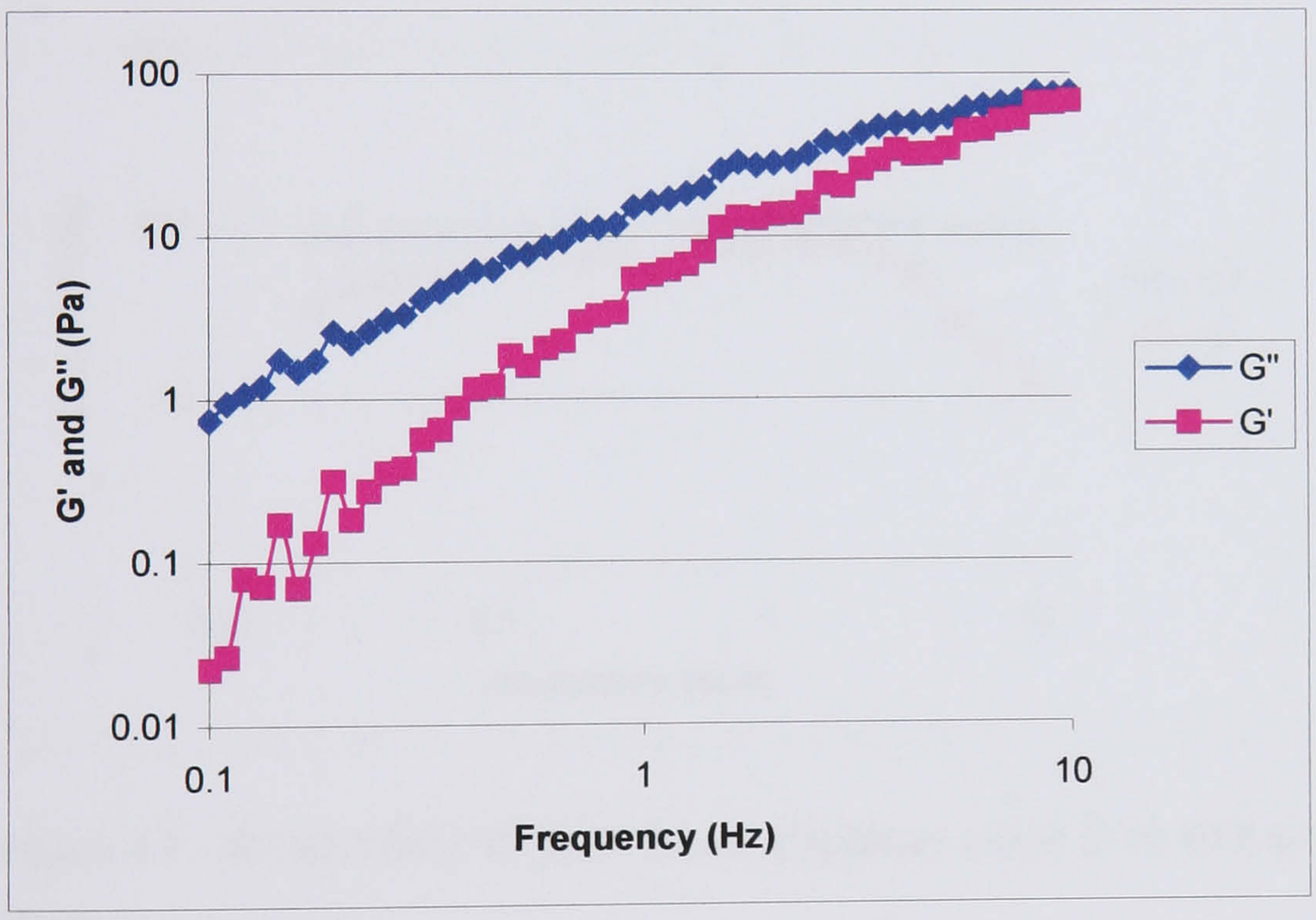


Figure 4.5 - RTMLY5052/HY5052 Frequency Sweep from 0.01-10Hz at Oscillatory Stress Amplitude of 3Pa.

A frequency sweep was carried out at constant oscillatory stress amplitude ($3Pa$) over a range of frequencies from 0.01 to 10Hz. From this it is observed that the elastic modulus is lower than the viscous modulus. Both moduli increase with increasing frequency. A crossover occurs at about 10Hz, indicating that elastic behaviour would dominate at higher frequency.

4.2.5. Strain Amplitude Sweep

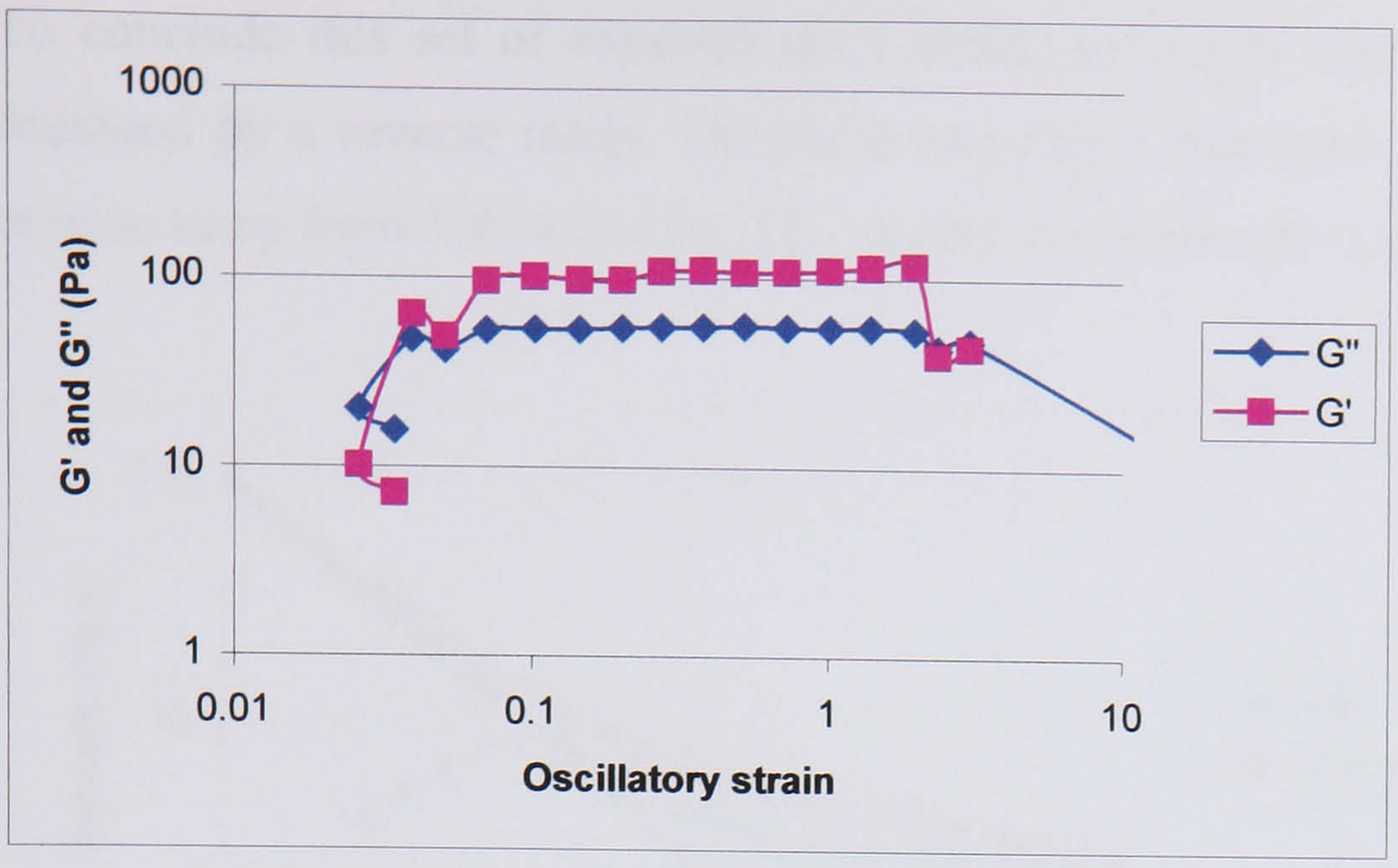


Figure 4.6 - RTMLY5052/HY5052 Strain amplitude sweep from 0.02 to 10 at 0.1Hz and 30°C for 20pts.

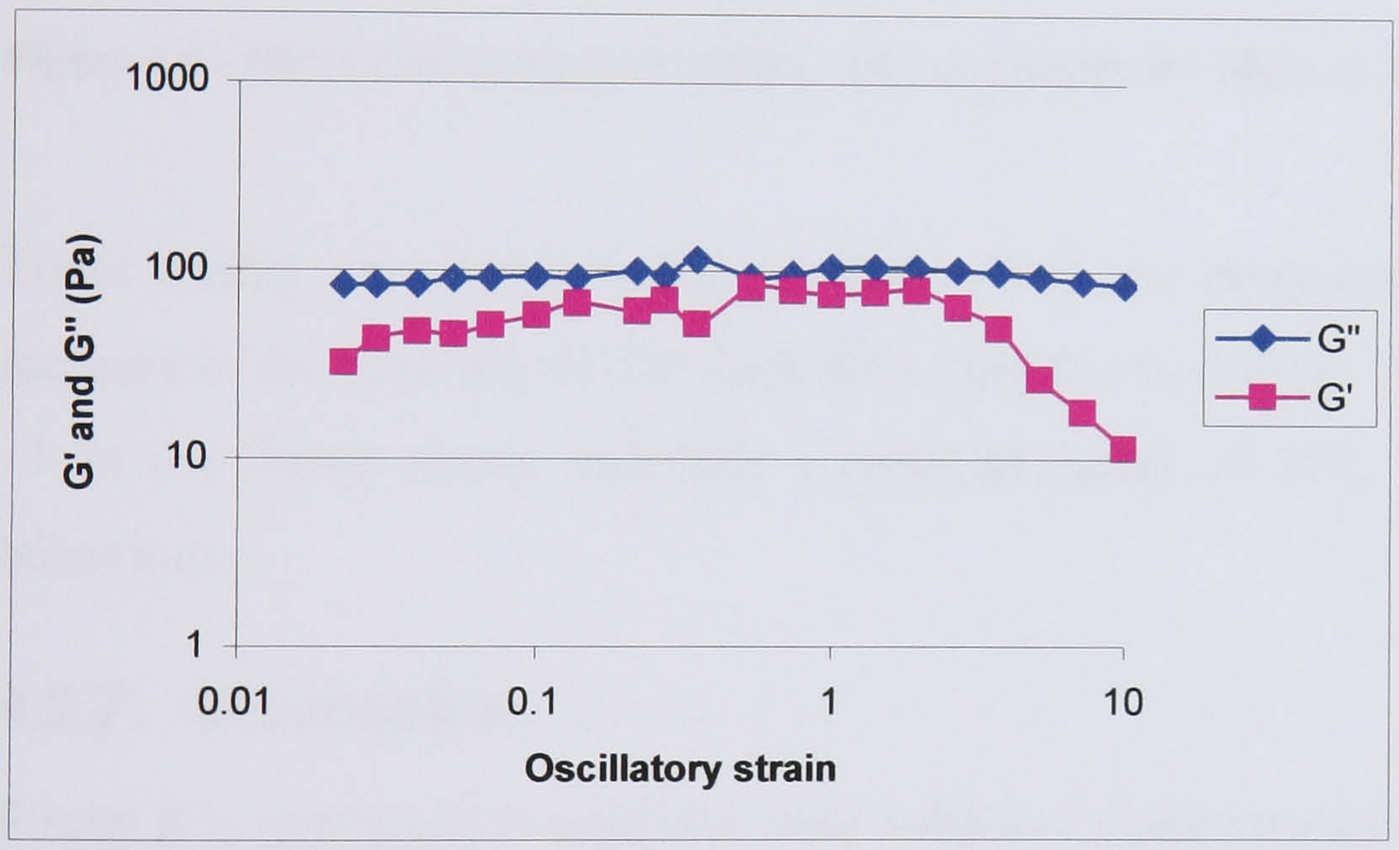


Figure 4.7 - RTMLY5052/HY5052 Strain amplitude sweep from 0.02 to 10 at 10Hz and 30°C for 20pts.

Strain amplitude sweeps were carried out (range 0.02 to 10) at low and high frequency (0.1Hz and 10Hz). It is seen that at low frequency G' is greater than G'' and at high frequency G'' is greater than G'.

4.2.6. Shear Rate Ramp – Forward and Reverse

To conclude this set of experiments 5 shear rate ramp runs were performed, each followed by a reverse ramp. The shear rate range was from 0.03/s to 10/s then the reverse ramp from 10/s to 0.03/s. The results of one run are shown in Figure 4.8.

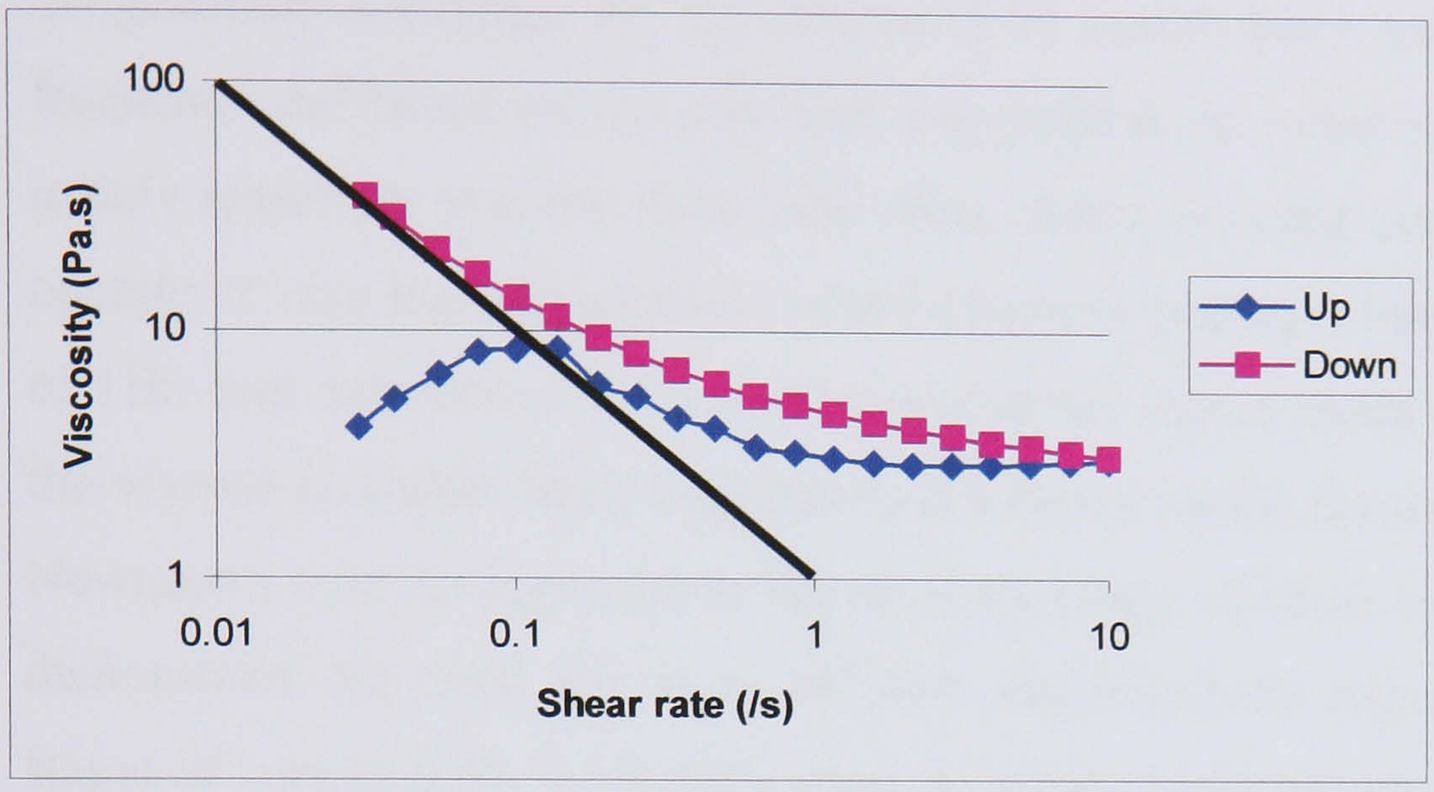


Figure 4.8 - Shear rate ramp from 0.03/s - 10/s at 1min/pt for 20pts at 30°C.

These results are similar to the previous shear rate ramp results. Again, we see an increase in the viscosity of the resin with time due to curing. The straight line of slope –1 in the figure above indicates a constant stress of 1Pa, showing a yield stress behaviour.

4.2.7. Discussion

Firstly it is important to consider what values of shear stress/shear rates are important to us in order to draw conclusions regarding RTM from the results presented above.

If we assume the following: -

Tow diameter (D) $\approx 10^{-3} m$

Resin flow velocity (U) $\approx 10^{-3}\ m/s$

Tow spacing (H) $\approx 10^{-4} m$

Then we can write the following equation for the shear rate: -

Shear rate $= 2U/H \approx 20/s$

However, for large tow spacing (H) the characteristic shear rate can be written as: -

Shear rate $= 2U/D = 2/s$

An estimate for the frequency of oscillation in the flow seen by a material element can be obtained from the time for the element to pass between tows: -

$$\text{Frequency} = \frac{s}{u} \geq \frac{D}{u} = \frac{10^{-3}}{10^{-3}} = 1Hz$$ where s is the tow centre spacing

So generally speaking, we are interested in intermediate values of shear rate and frequency and hence we can conclude that yield stress behaviour is not critical as this is only important at a low shear rate. Also, elasticity is not dominant since we do not operate at very high frequencies where elasticity becomes important. At a frequency of 1Hz (our estimate of relevant frequency) the elastic modulus is much lower than the viscous modulus. Most importantly the above results demonstrate that the resin is Newtonian over an appreciable intermediate range of shear rates. These results also demonstrate the need for us to perform viscosity-time experiments for the initial stages of cure in order to properly characterise the resin behaviour in RTM.

4.3. Proposed Viscosity Model[22]

There currently exists very little information on the rheological behaviour of typical resins used in RTM. This prompted the characterisation experiments that could later be used in developing and validating a non-parametric model. Viscosity – time measurements were carried out at a constant shear rate for five different resin systems. Measurements were performed over a range of temperatures from 30°C to 60°C on different samples. All of the measurements reported here were taken at a constant shear rate of 5/s which represents the mid-range of the actual process. However, the viscosity was not allowed to get too high as full curing of the resin could cause permanent damage to the rheometer. This was not the case for the resin systems analysed by Q. Fontana[vi] as different type of rheometer was used in those cases.

4.3.1. Model

The basic hypothesis of the proposed model is that for isothermal situations the viscosity may be represented in the dimensionless form $\alpha = f(\tau)$, where $\alpha = \ln[\eta(T)/\eta_0(T)]$ represents the change in viscosity with cure and $\tau = k(T).t$ represents the elapsed cure time; $\eta_0(T)$ is the viscosity of the uncured resin at temperature T and

---

[vi] *British Aerospace*, Sowerby Research Centre, Filton Bristol

$k(T)$ represents the rate of advance of the curing process at temperature T. Once $\eta_0(T)$, $k(T)$ and $f(\tau)$ are known, the viscosity can be determined as a function of time.

For isothermal situations, the model predicts the rate of cure in the form $\alpha = f(\tau)$. For non-isothermal situations, we first invert this basic isothermal relationship into the form $\tau = g(\alpha)$, where g is the inverse function of f. This is written subsequently in differential form $d\tau = g'(\alpha)d\alpha$, where $d\tau = k(T)dt$ represents the increment of elapsed time. The equation for non-isothermal cure can then be expressed in the simple differential form:

$$\frac{d\alpha}{dt} = \frac{k(T)}{g'(\alpha)}, \qquad [4.6]$$

which expresses the change of viscosity with time in terms of the kinetic quantity $k(T)$ and the slope of the dimensionless isothermal viscosity-time curve $g'(\alpha)$. Equation [4.6] can be expanded to give an equation for the time rate of change of viscosity:

$$\frac{d\eta}{dt} = \eta\left[\frac{k(T)}{g'(\ln(\eta/\eta_0))} + \frac{1}{\eta_0}\frac{d\eta_0}{dT}\frac{dT}{dt}\right]. \qquad [4.7]$$

The current model is also equivalent to the thermal shifting model of Fontana[21], and can be applied to non-isothermal cases. It gives the rate of change of viscosity with cure. To implement the model for a particular resin, knowledge of $k(T)$, $\eta_0(T)$ and $g'(\alpha)$ must be obtained from experimental data.

4.3.2. Isothermal Experiments

Figure 4.9 shows viscosity-time data for LY5052/HY5052 over a range of temperatures, illustrating that the rate of cure increases with increasing temperature. The initial viscosity varies inversely with temperature before commencement of curing, causing the viscosity to be initially lower at higher temperatures. As cure occurs the viscosity curves cross over due to higher cure rate at higher temperature.

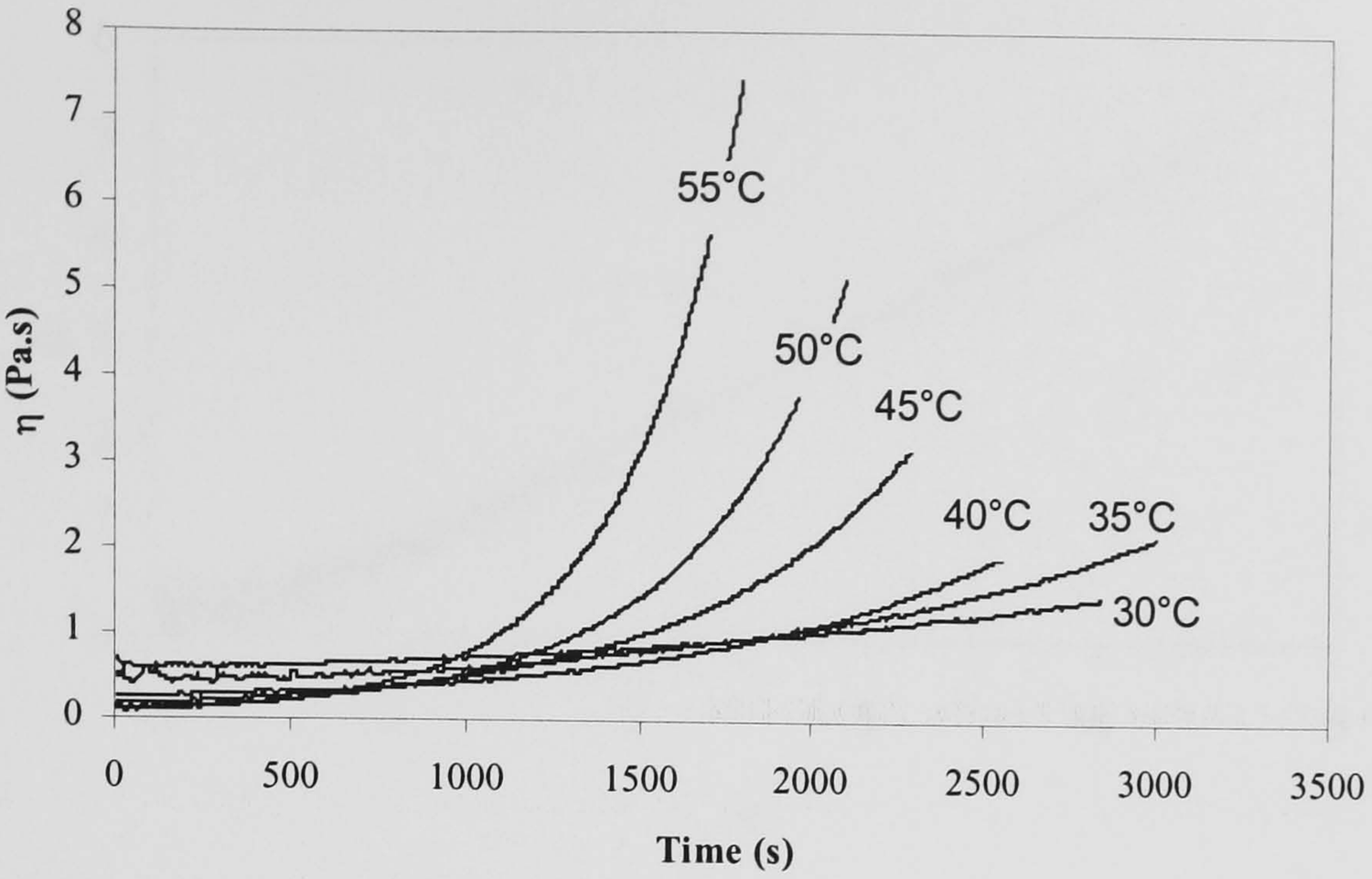


Figure 4.9 - Isothermal viscosity-time curves for LY5052/HY5052 at constant shear rate of 5/s for different temperatures.

After identifying the initial viscosity, $\eta_0(T)$, we calculate α from η and η_0. By plotting α against time, the time t_1 where $\alpha = 1$ can be identified and $k(T)$ is obtained from

$$k(T) = \frac{1}{t_1}. \qquad [4.8]$$

The dimensionless time is defined as $\tau = k(T).t$. Curves of α *versus* τ, for all temperatures, are plotted on a single graph as shown in Figure 4.10. We see that the curves for a range of fixed temperatures collapse quite well to a single (master) curve, which gives $\alpha = f(\tau)$.

Variations in the mix ratio of the resin for each experiment would account for some degree of error in the master curve. An approximate error of 3% in the mix ratio is expected. Additionally, from 10 repeatability studies a repeatability accuracy of 95% was observed in these measurements.

The approximate degree of cure in these measurements is estimated to be less than 5% based on results of an empirical model proposed by Lee and Wei[23]. Lee and Wei analysed the curing kinetics of LY564/HY2954 with DSC. An empirical model correlated the resin viscosity with temperature and the degree of cure was obtained.

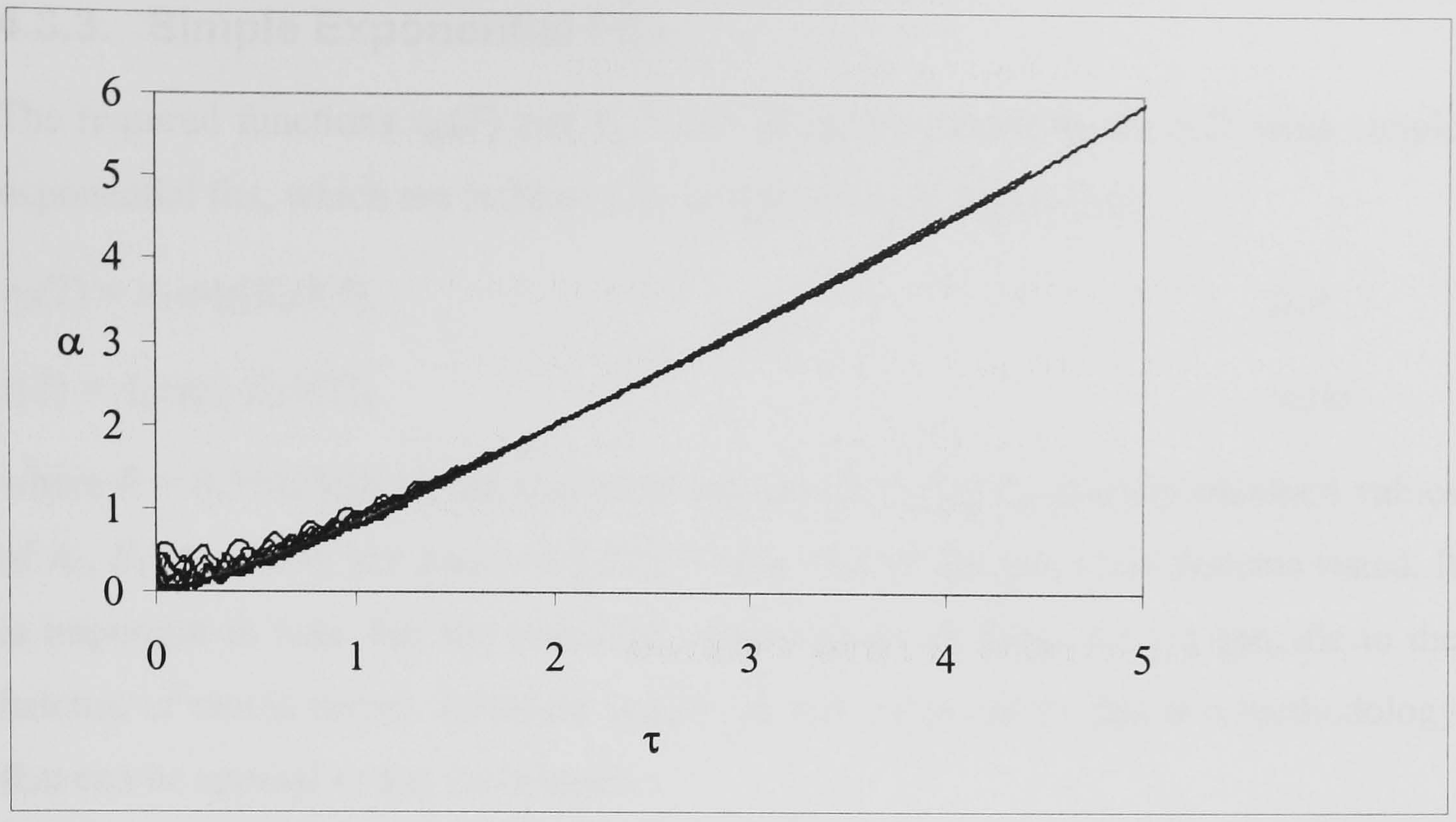


Figure 4.10 - Master Curve for LY5052/HY5052. Dimensionless viscosity against dimensionless time. Isothermal data for several temperatures in the range 20°C – 70°C are shown.

The data for $\eta_0(T)$ and $k(T)$ are also required. It is conventional to use Arrhenius plots of $\ln(\eta_0)$ *vs.* $1/T$ and $\ln(k)$ *vs.* $1/T$. Figure 4.11 displays these plots, along with corresponding least squares linear fits.

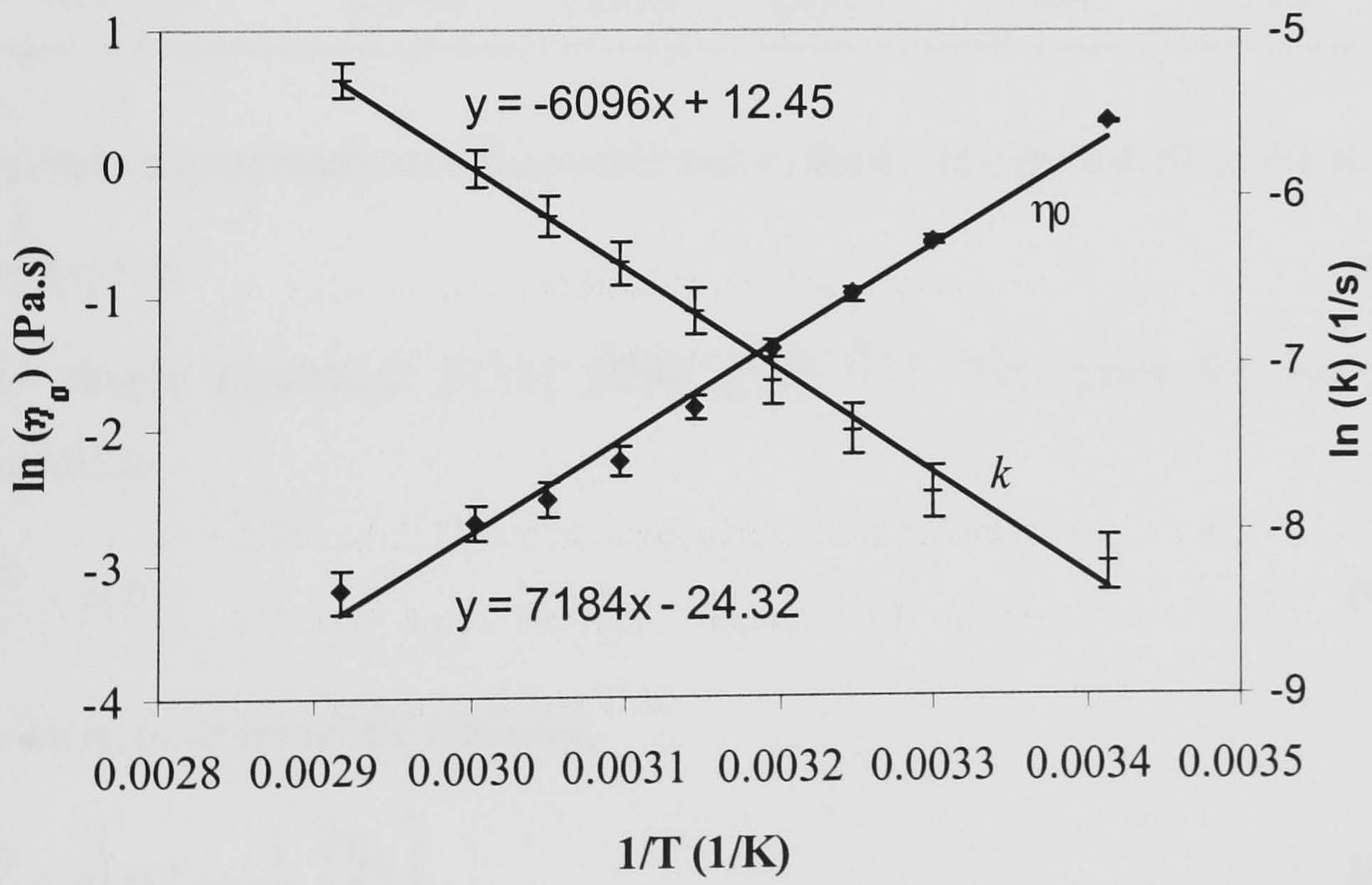


Figure 4.11 - Arrhenius plot of initial viscosity, η_0, and rate constant, *k*, for LY5052/HY5052.

4.3.3. Simple Exponential Fits

The required functions $\eta_0(T)$ and $k(T)$ can be approximated by the following simple exponential fits, which are indicated by straight lines in Figure 4.11.

$$\eta_0(T) = A_1 \exp[E_1/RT], \qquad [4.9]$$

$$k(T) = A_2 \exp[-E_2/RT], \qquad [4.10]$$

where R = 8.314J/kgK is the Universal gas constant. Experimentally obtained values of A_1, E_1, A_2 and E_2 are given in Table 4.1 for each of the five resin systems tested. It is important to note that the parameter values given in Table 4.1 are specific to the batches of resins tested. Absolute values are not important as this is a methodology that can be applied to any resin/batch.

Table 4.1 - Model parameters for different resin systems

Resin	A_1 (Pa.s)	E_1 (J/kg)	A_2 (1/s)	E_2 (J/kg)	A_3	E_3 (J/kg)
LY5052/HY5052	2.7×10^{-11}	6.0×10^{4}	2.6×10^{5}	5.1×10^{4}		
LY564/HY2954	3.7×10^{-11}	5.9×10^{4}	3.7×10^{4}	4.8×10^{4}		
RTM6	7.3×10^{-4}	1.3×10^{4}	7.4×10^{4}	6.5×10^{4}		
PR500	2.4×10^{-11}	7.6×10^{4}	7.3×10^{7}	8.9×10^{4}		
411-C50	2.5×10^{-8}	4.0×10^{4}	8.0×10^{5}	4.7×10^{4}	9.6×10^{17}	1.2×10^{5}

A simple approximation of the master curve, shown in Figure 4.10, is the straight line

$$\alpha = f(\tau) = \tau. \qquad [4.11]$$

The simple expression [4.11] yields $g'(\alpha) = 1$. This gives for non-isothermal conditions

$$\frac{d\alpha}{dt} = k(T), \qquad [4.12]$$

which is, in terms of the viscosity,

$$\frac{d\eta}{dt} = \eta\left[k(T) + \frac{1}{\eta_0}\frac{d\eta_0}{dt}\right]. \qquad [4.13]$$

This is equivalent to equation [4.2].

Results for isothermal viscosity-time profiles at two temperatures, 35°C and 40°C, are shown in Figure 4.12 together with the fits given by equations [4.9] to [4.13]. From Figure 4.12, it is seen that the viscosity increases with time as the curing reaction takes place. As expected, the increase of viscosity with time is nearly exponential. Generally the model fits the data well. At the start of the experiment there is a time lag and significant noise in the viscosity measurements. This is largely due to the time taken for the resin temperature to achieve the set point. The model can easily be refined to account for this time lag as shown below.

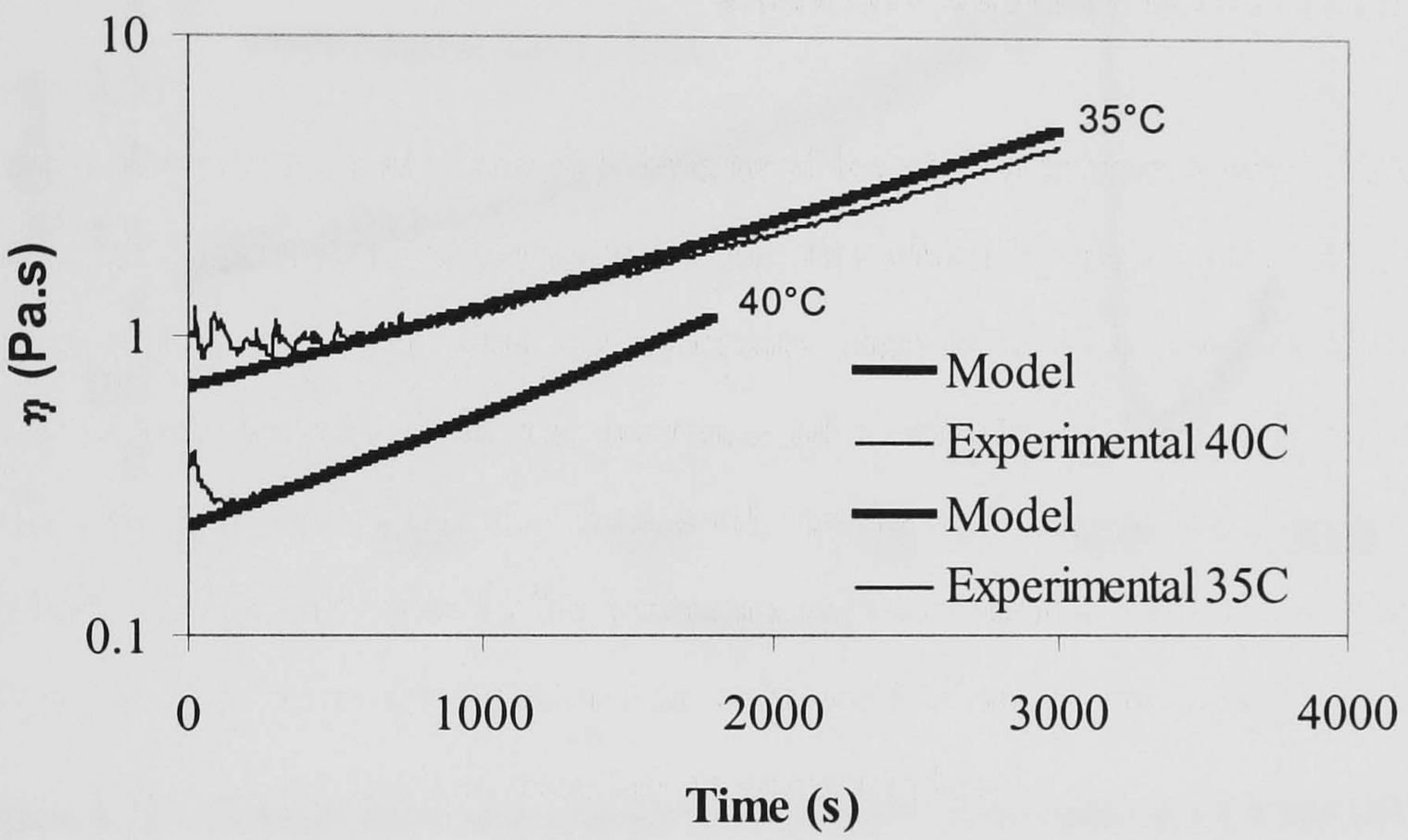


Figure 4.12 - Viscosity-time curves for LY5052/HY5052, for constant shear rate of 5/s at 35°C and 40°C.

For one of the resin systems, Derakane Momentum 411-C50, the simple exponential fit was insufficient to describe the data. A more complex fit was used and is described in section 4.3.5 below.

4.3.4. Non-isothermal Experiments

Results for experiments with a step change in the temperature are displayed in Figures 4.13 and 4.14. The results for a step increase in temperature from 20°C to 60°C (Figure 4.13) show that when the temperature increases to 60°C, a sharp decrease in the viscosity is observed, as expected. The time taken for this change in viscosity to take place is relatively small, reflecting rapid thermal equilibration of the rheometer. After a short delay we see a steep upward trend, reflecting an increase in the rate of

cure due to the increase in temperature. The results of the model are in close agreement with the experimental data. Figure 4.14 shows results for a decrease in temperature from 40°C to 30°C. As expected, the viscosity increases when the temperature is stepped down. Again the model results closely follow the experimental data.

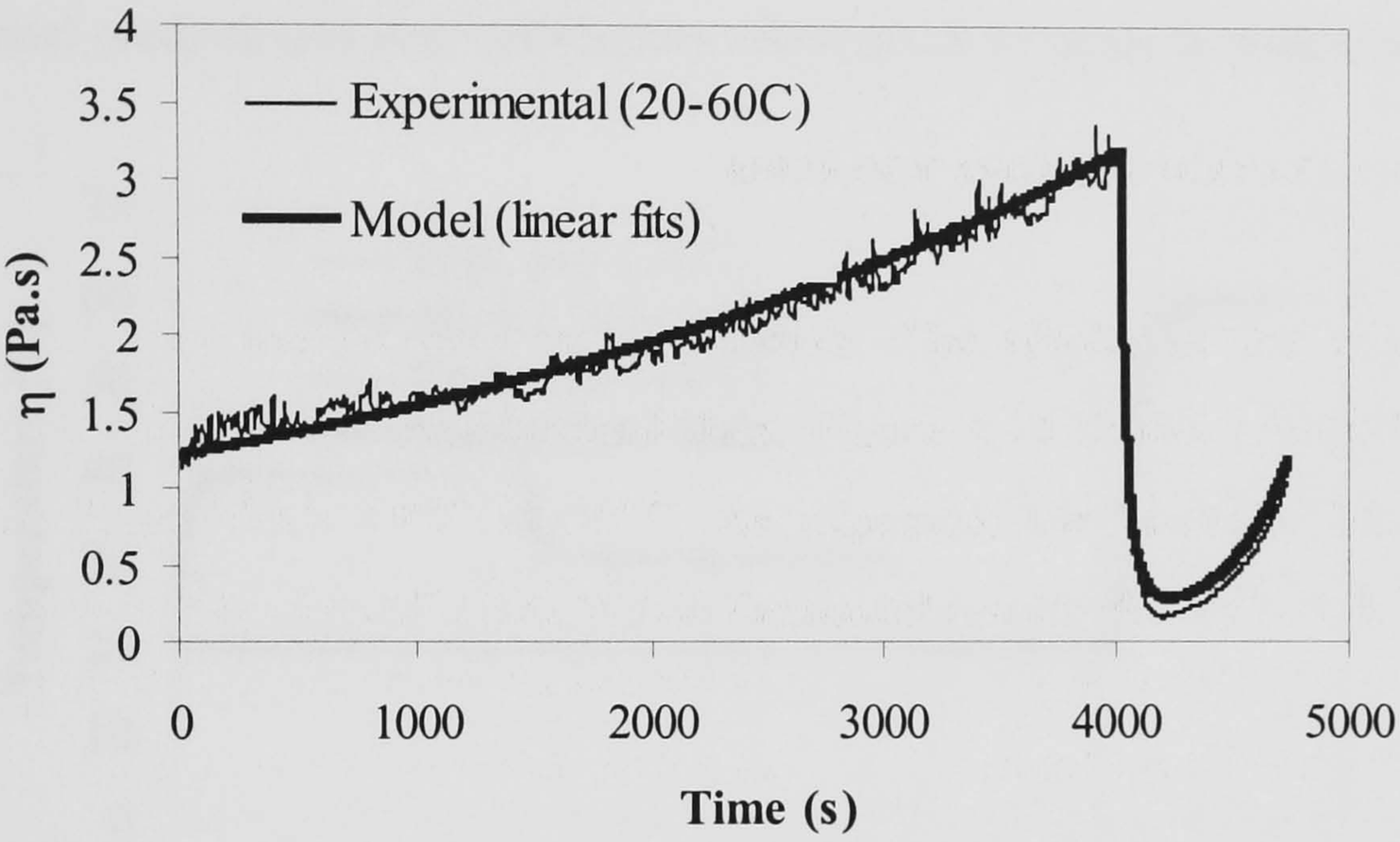


Figure 4.13 - Temperature step change from 20-60°C after 4000s for LY5052/HY5052.

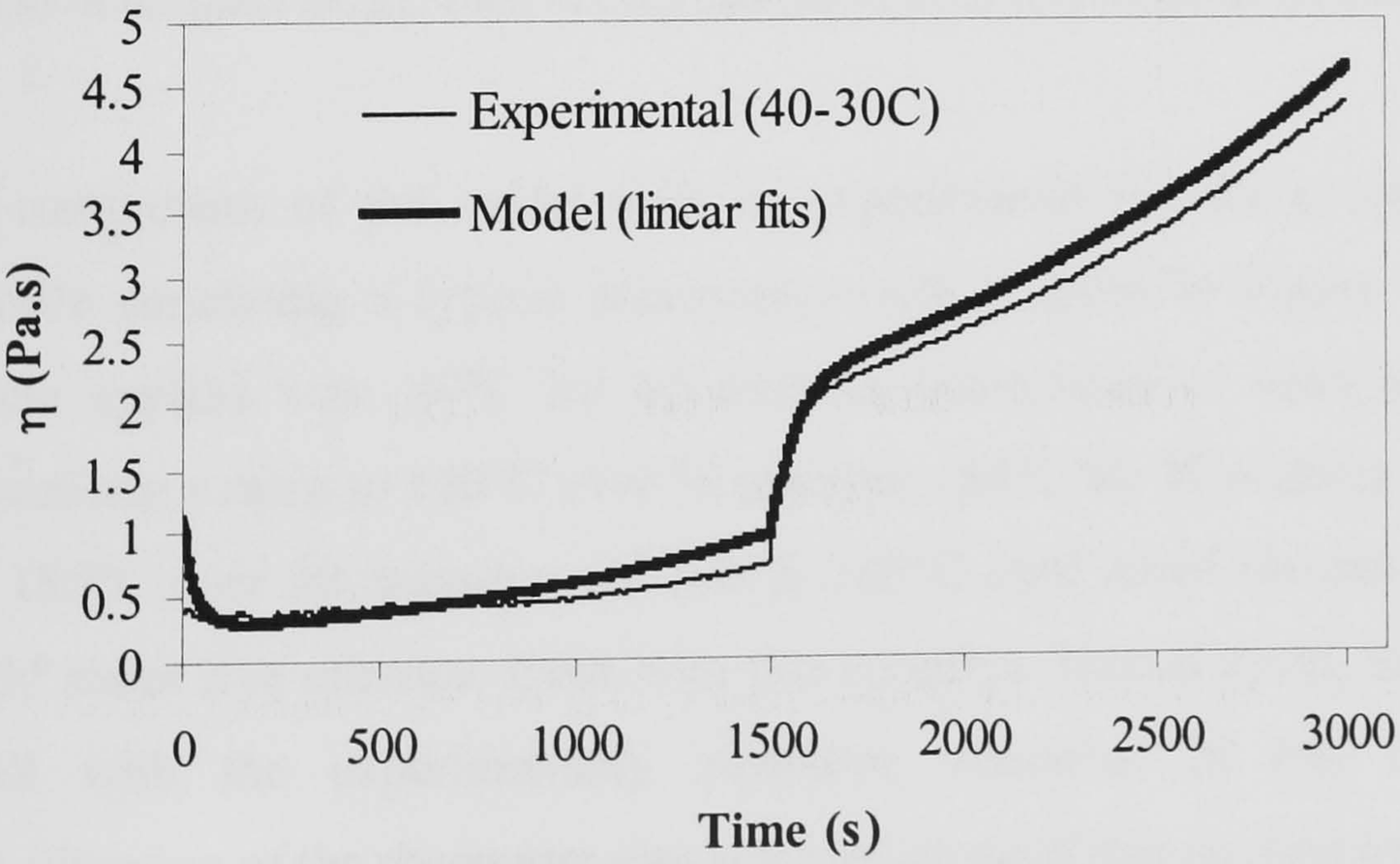


Figure 4.14 - Temperature step change from 40-30°C after 1500s for LY5052/HY5052.

Figure 4.15 shows the adjusted temperature-time profiles used in the comparisons shown in Figures 4.13 and 4.14. The adjustment accounts for the temperature delay observed in the experimental results as the resin takes time to reach the measured plate temperature of the rheometer. An exponential time delay was used and in these cases a time lag of 150s was incorporated into the model to account for the slight delay in thermal equilibration of the fluid sample (the measured temperature is that of the rheometer plate, not the fluid). From Figures 4.13 and 4.14 it can be seen that the model prediction is very satisfactory when this time delay in temperature is included.

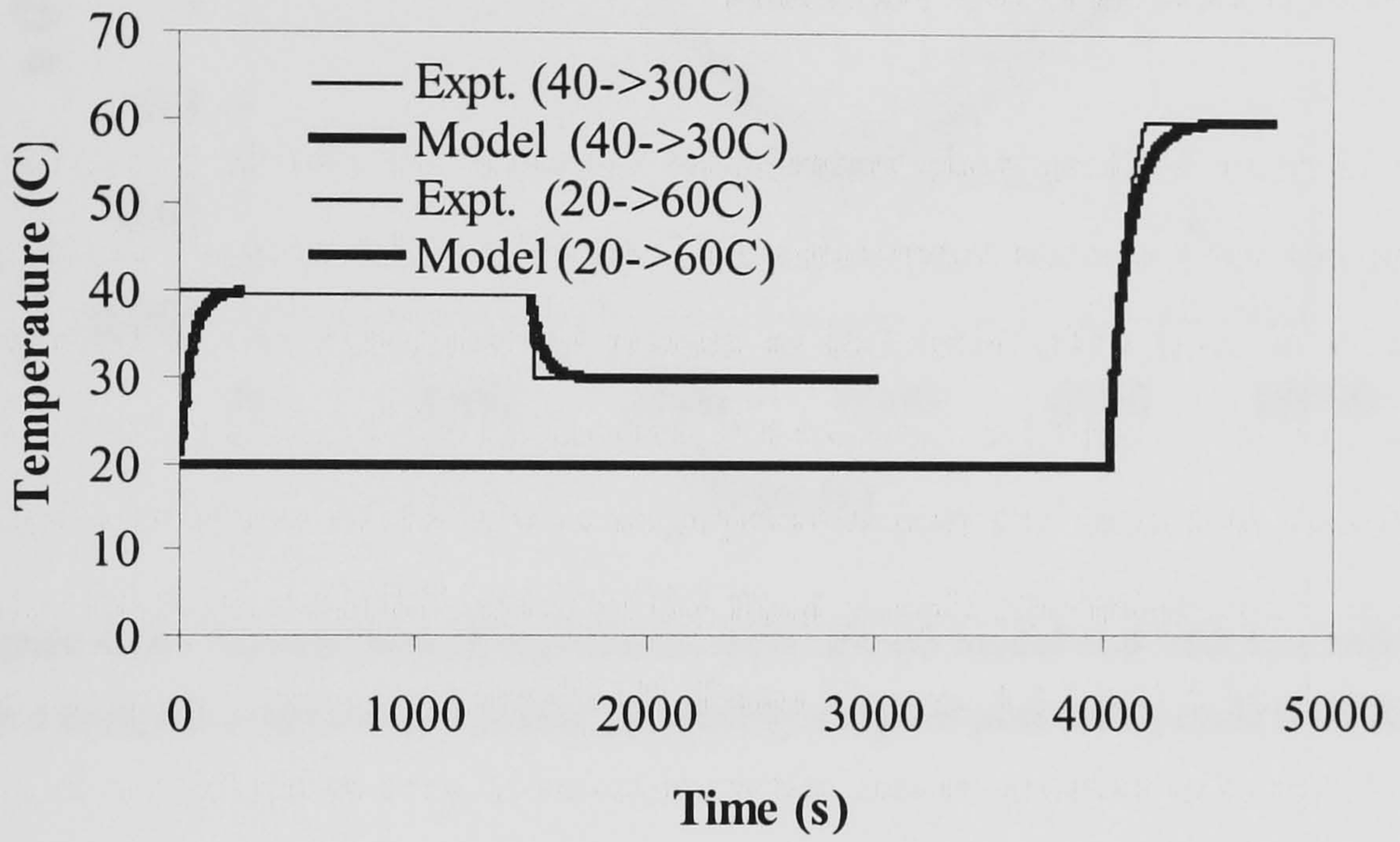


Figure 4.15 - Modified temperature profiles for Figures 4.13 and 4.14 incorporating time lags between the plate temperature (Expt.) and the fluid sample temperature (Model).

A comparison of the model with an experimental run for a complex temperature profile simulating a typical processing cycle is given in Figure 4.16. The thermal cycle applied was: 80°C for 60 minutes (simulation of hold in the pot prior to injection); a ramp to 160°C over 30 minutes; 160°C for 30 minutes (injection); a ramp to 180°C over 30 minutes; and finally 180°C until cured (in-mould cure), typically only about five minutes. Even with this complex thermal cycle, the model correlates well with the experimentally measured viscosity. In this case, the thermal equilibration of the rheometer was sufficiently rapid that no time delay was needed.

Also shown are results from the model of Lee and Hahn[24] (which is used in the software package LIMS for simulation of mould filling processes). It is clear that the

present method shows much better agreement with the experimentally measured results. The Lee and Hahn model is unable to cope effectively with the non-isothermal temperature profile.

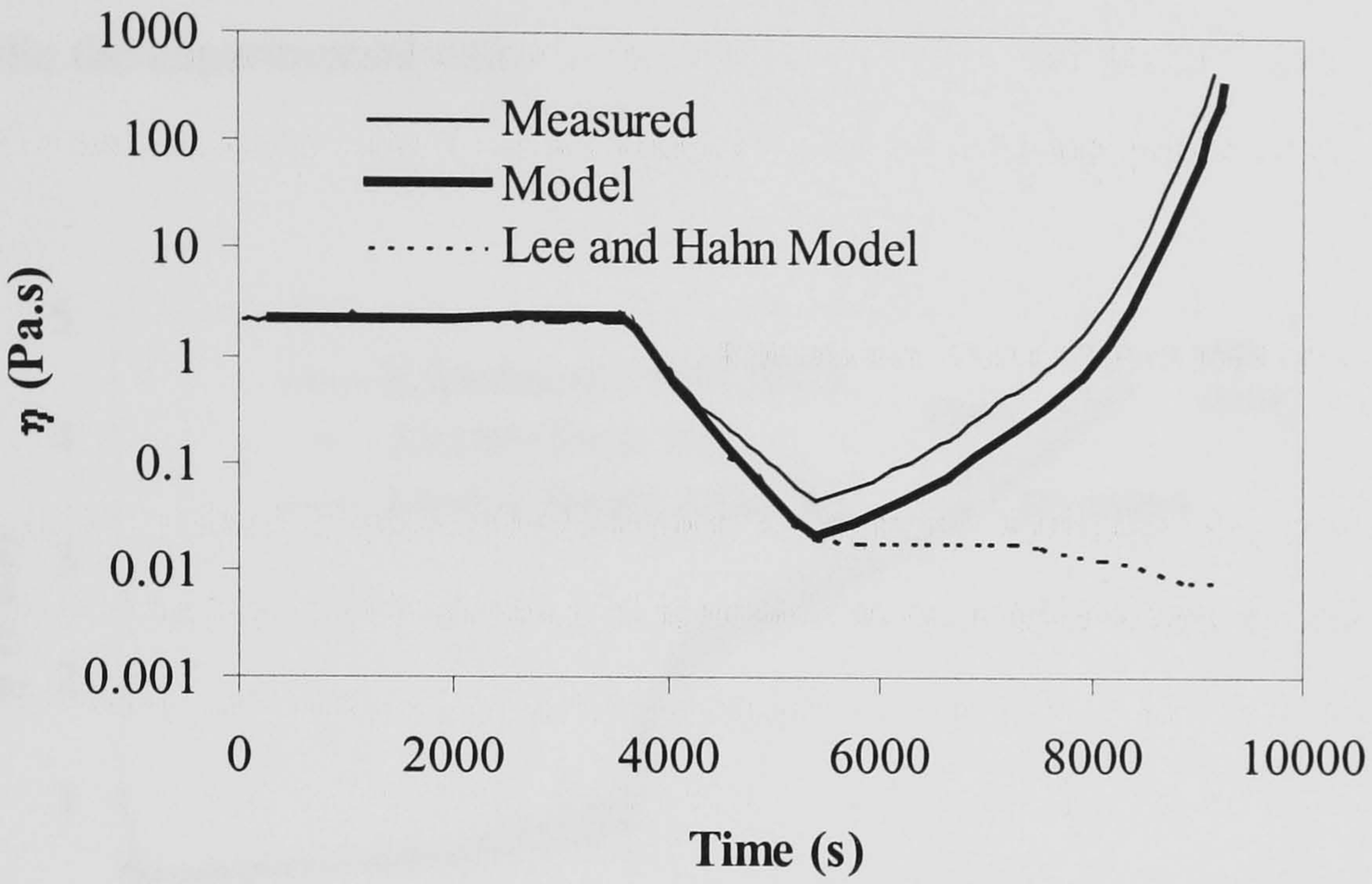


Figure 4.16 - Comparison of experiment with current model and with Lee and Hahn[24] method for a complex temperature profile simulating a typical processing cycle for PR500.

4.3.5. Higher Order Fits

Further improvements in the model can be achieved by considering higher order polynomial fits, such as:

$$\ln[\eta_0(T)] = a_1 + \frac{b_1}{T} + \frac{c_1}{T^2} + \frac{d_1}{T^3} + \ldots \quad \textbf{[4.14]}$$

$$\ln[k(T)] = a_2 + \frac{b_2}{T} + \frac{c_2}{T^2} + \frac{d_2}{T^3} + \ldots \quad \textbf{[4.15]}$$

$$f(\tau) = \tau + a_3\tau^2 + b_3\tau^3 + \ldots \quad \textbf{[4.16]}$$

$$g(\alpha) = \alpha + a_4\alpha^2 + b_4\alpha^3 + \ldots \quad \textbf{[4.17]}$$

The use of higher order fits in the model is shown in Figure 4.17. These results were obtained by fitting a third order polynomial to the curve τ *vs.* α hence giving $g(\alpha)$ from equation [4.6]. Thus α can be determined from [4.6] and the viscosity evaluated from the definition of α. As can be seen, incorporation of the higher-order terms leads to a small improvement of the model predictions, to the point where they virtually overlie the experimental data.

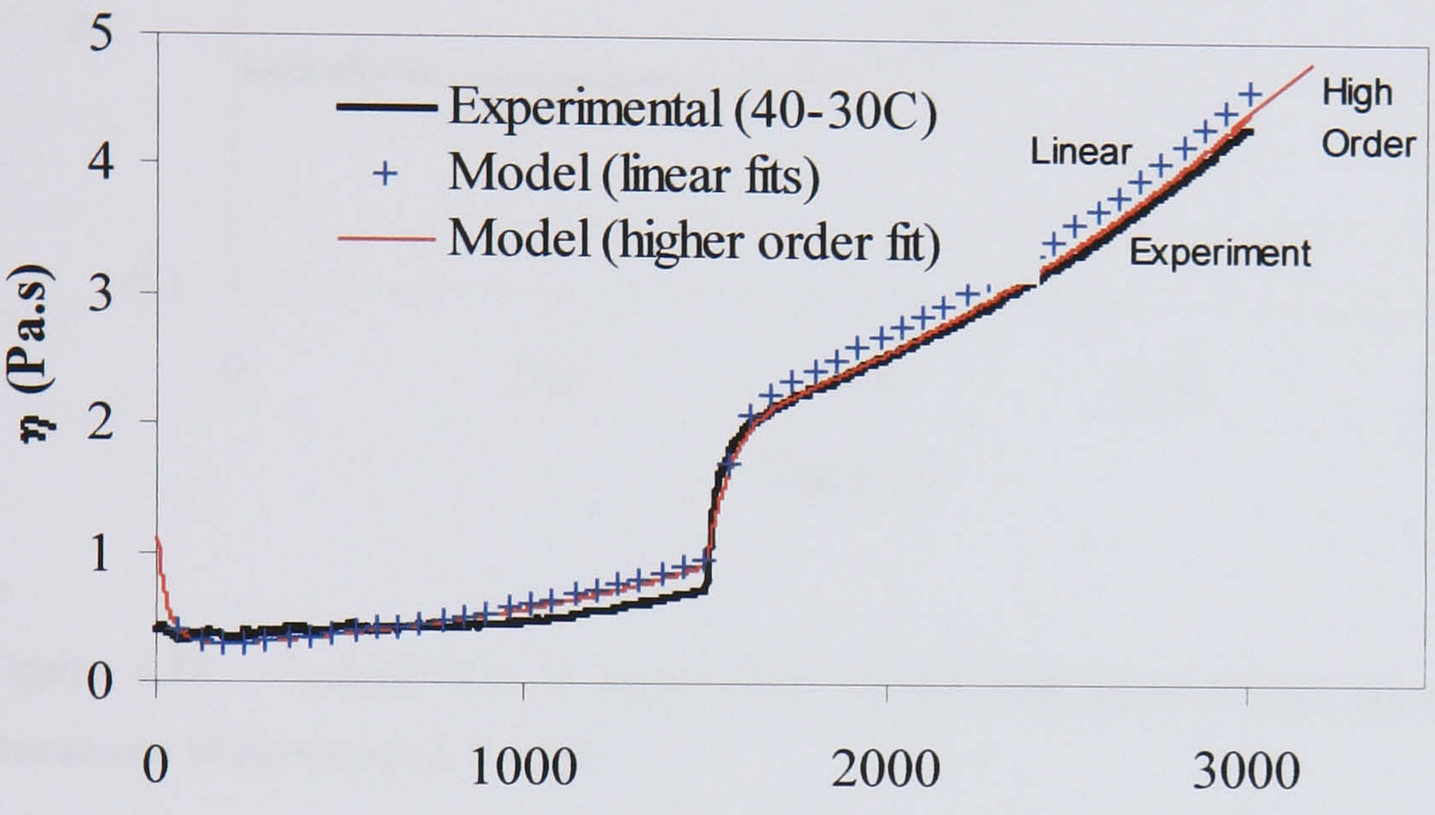


Figure 4.17 - Temperature step change from 40-30°C after 1500s comparing linear and third order fits (LY5052/HY5052).

Derakane Momentum 411-C50 exhibits very different cure kinetics from the other resins studied and hence warrants a modified cure model. A more complex type of higher order fit is required. For this resin system α is fitted in the form

$$\alpha = \alpha_0(T)\exp(\tau) \qquad [4.18]$$

Here we have a third temperature scaling function $\alpha_0(T)$, which represents a pre-factor in the curing rate curve. This factor was also found to be reasonably represented by an Arrhenius relationship of the form

$$\alpha_0(T) = A_3\exp[-E_3/RT] \qquad [4.19]$$

The experimentally determined values of A_3 and E_3 are given in Table 4.1, along with the values of A_1, A_2, E_1 and E_2 for this resin system.

A comparison of this exponential model with the linear model is shown in Figure 4.18. A significant improvement is seen in the model prediction when the exponential fit is used for this resin system.

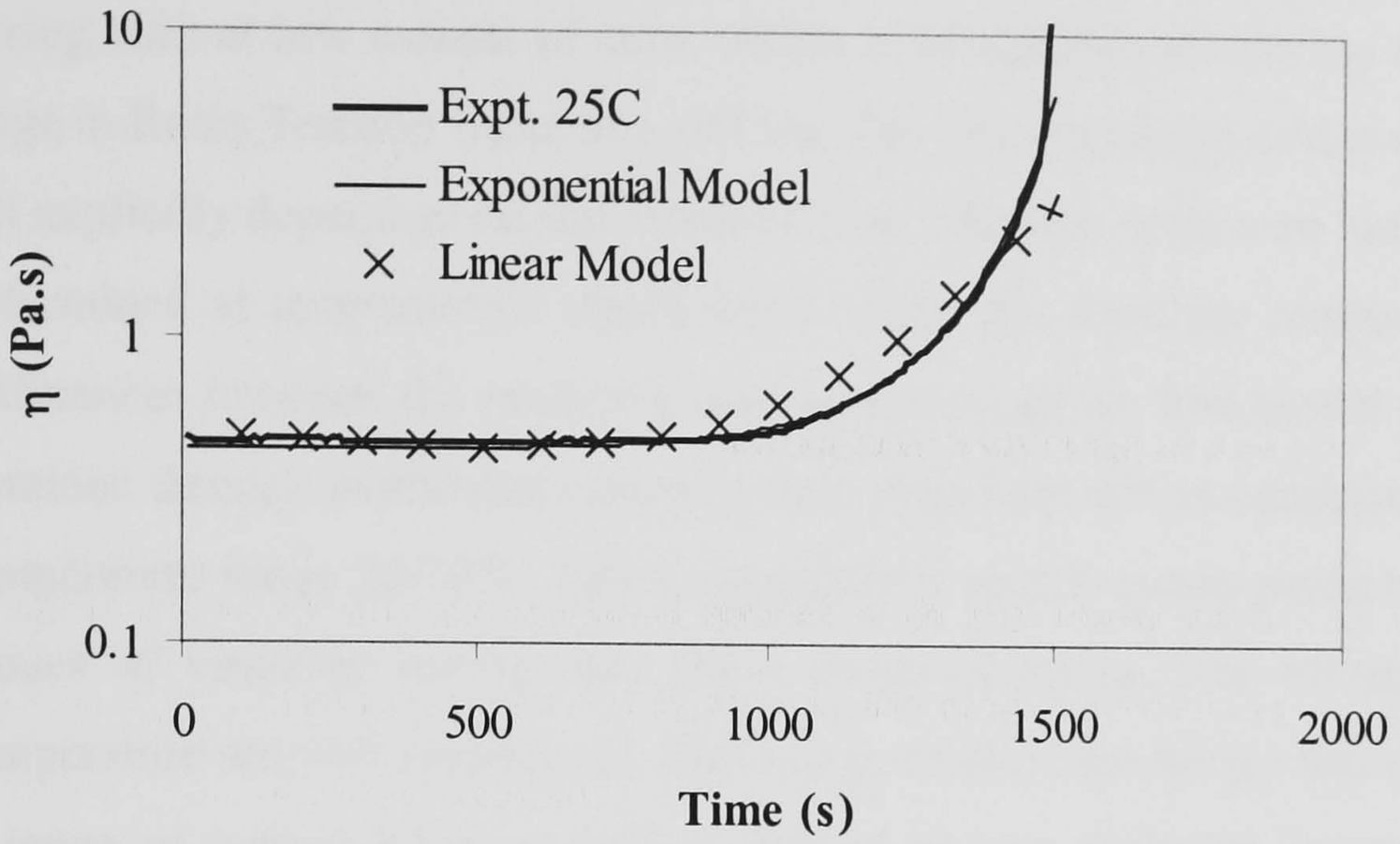


Figure 4.18 - Comparison of exponential model with linear fit for isothermal (25°C) data for Derakane Momentum 411-C50.

In the exponential model [4.18], it is clear that when $t = 0$, $\alpha = \alpha_0 \neq 0$. By the definition $\alpha = \ln[\eta/\eta_0]$, we should expect that at $t = 0$, $\eta = \eta_0$ and $\alpha = 0$. Hence, in this case, the model does not capture the exact behaviour of the viscosity for small times. Nevertheless, as seen in Figure 4.18, the model provides a good approximate representation throughout the curing curve.

4.4. Summary

Rheological characterisation studies on the resin systems LY5052/HY5052[vii], LY564/HY2954[i], RTM6[viii], Derakane Momentum 411-C50[ix] and PR500[x] have highlighted Newtonian behaviour over an appreciable intermediate shear stress range. Estimates of applicable shear stress/shear rate values during RTM processing indicate that yield stress behaviour is not critical as this is only important at much lower values

[vii] Manufactured by *Ciba-Geigy*, Macclesfield, Cheshire SK10 2NY, UK
[viii] Manufactured by *Hexcel Composites*, Duxford, Cambridge CB2 4QD, UK
[ix] Manufactured by *Dow Chemicals*, Kings Lynn, Norfolk PE30 2JD, UK
[x] Manufactured by *3M*, Bracknell, Berkshire RG12 1JU, UK

of shear rate. Also, elasticity is not dominant at relevant frequency values but is observed to become dominate at much higher frequencies.

A non-parametric model has been proposed for the advancement of the rheology during cure at low extents of cure, which is of significance during the mould-filling stage in Resin Transfer Moulding (RTM). The key advantage of this model is that it is not explicitly dependent on the extent of cure. Thus the resin cure kinetics need not be determined at temperatures significantly above the injection temperature leading to differences between the modelled and the real kinetics. The model parameters were obtained through isothermal viscosity-time measurements at constant shear rate in the temperature range 20-70°*C*. Good agreement is seen between predicted and measured values of viscosity during cure for a range of resins. The effects of changes in temperature are well reproduced. This is a general methodology that can be adapted to a range of curing kinetics, (which depend on the chemical structure of the resin system) with an accuracy that can be increased by the order of the fitting equation used. The success of the model is governed to an extent by the selection of the functional forms of $\eta_0(T)$, $k(T)$, $f(\tau)$ and of their parameters. An advantage of the methodology proposed is that it gives the flexibility to choose optimal forms for these functions (the criterion of optimality being the existence of a master curve $f(\tau)$) which can be exploited for the modelling of the viscosity of different resin systems. Indeed the form of the viscosity master curve is strongly dependent upon the chemical structure of the polymer and the associated reaction kinetics. Since the rheology of the resin is so sensitive to the extent of reaction, the proposed methodology could be used to gain insight into the reaction kinetics in the early stages of cure, well before gelation has been achieved.

4.5. References

[1] Ryan, M.E., Polym. Eng. Sci., **24**, 698, (1984).

[2] Sundstrom, D.W., Burkett, S.J, Polym. Eng. Sci., **21**, 1108, (1981).

[3] Hartley, M.D., Williams, H.L., Polym. Eng. Sci., **21**, 135, (1981).

[4] Riccardi, C.C., Vazquez, A., Polym. Eng. Sci., **29**, 120, (1989).

[5] Ryan, M.E., Kamal, M.R., Proc. VII Int. Congress on Rheology, 289, (1976).

[6] Kascaval, C.M., Musata, F., Rosu, D., Die Ange Makromol Chemie, **290**, 157, (1993).

[7] Knauder, E., Kubla, C., Poll, D., Kunstoffe German Plastics, **81**, 39, (1991).

[8] Ng, H., Manas-Zloczower, L., Polym. Eng. Sci., **33**, 211, (1993).

[9] Halley, P.J., Mackay, M.E., "Chemorheology of Thermosets – An Overview", Polym. Eng. Sci., **36**, 593, (1996).

[10] Yang, H., Lee, L.J., "Effects of Resin Chemistry on Redox Polymerisation of Unsaturated Polyester Resins", J. Appl. Polym. Sci., 84(1), 211, (2002).

[11] Ferry, J.D., "Viscoelastic Properties of Polymers", 3rd ed., J. Wiley and Sons, New York, (1980).

[12] Simon, S.L., Gillham, J.K., "Thermosetting Cure Diagrams: Calculation and Application", J. Appl. Polym. Sci., **53**, 709, (1994).

[13] Mijovic, J., Lee, C.H., "A Comparison of Chemorheological Models for Thermoset Cure", J. Appl. Polym. Sci., **38**, 2155, (1989).

[14] Lipshitz, S.D., Macosko, C.W., "Rheological Changes During a Urethane Network Polymerisation", Polym. Eng. Sci., **16**, 803, (1976).

[15] Castro, J.M., Macosko, C.W., "Kinetics and Rheology of Typical Polyurethane Reaction Injection Moulding Systems", Soc. Plast. Eng. Tech. Papers, **26**, 434, (1980).

[16] Perry, M.J., Wang, T.J., Ma, Y., Lee, L. J., "Resin Transfer Moulding of Epoxy/Graphite Composites", Proc. 24th Int. SAMPE Tech. Conf., **24**, 421, Canada, October, (1992).

[17] Bidstrup, S.A., Macosko, C.W., "Chemorheology Relations for Epoxy/Amine Cross-linking", J. Polym. Sci.: Part B: Polym. Phys., **28**, 691, (1990).

[18] Roller, M.B., "Rheology of Curing Thermosets: A Review" Polym. Eng. Sci., **26**, 432, (1986).

[19] Williams, M.L., Landel, R.F., Ferry, J.D., "The Temperature Dependence of Relaxation Mechanisms in Amorphous Polymers and Other Glass-Forming Liquids", J. Am. Chem. Soc., **77**, 3701, (1955).

[20] Karkanas, P.I., Partridge, I.K., "Cure Modelling and Monitoring of Epoxy/Amine Resin Systems. Part II: Network Formation and Chemoviscosity Modelling", J. Appl. Polym. Sci., **77**, 2178, (2000).

[21] Fontana, Q.P.V., "Viscosity: Thermal History Treatment in Resin Transfer Moulding Process Modelling", Composites Part A, **29A**, 153, (1997).

[22] Kiuna, N., Lawrence, C.J., Fontana, Q.P.V., Lee, P.D., Selerland, T., Spelt, P.D.M., "A Model for Resin Viscosity During Cure in the Resin Transfer Moulding Process", Composites Part A, **33**, 1497, (2002).

[23] Lee, C., Wei, K., "Curing Kinetics and Viscosity Change of a Two-Part Epoxy Resin During Mould Filling in Resin Transfer Moulding Process", J. Appl. Polym. Sci., **77**, 2139-2148, (2000).

[24] Lee, D.S., Hahn, C.D., "A Chemorheological Model for the Cure of Unsaturated Polyester Resin", Polym. Eng. Sci, **27**, 955, (1987).

5. ANALYSIS OF FLOW IN FULLY SATURATED MEDIA

This chapter presents results obtained from the micro-scale experimental investigation of the flow field in fully saturated media. Flow through a hexagonal matrix of cylindrical rods was observed using a particle image velocimetry (PIV) technique. A comparison of these experimental results with those of a numerical model proposed by Spelt et al.[1] is made.

5.1. Introduction

An understanding of the saturated flow of resin within a fibrous material is an important prerequisite for modelling the Resin Transfer Moulding (RTM) process. A micro-scale experimental investigation was established to determine the velocity field within a model saturated medium. This was simulated by constructing a flow cell (details given in Chapter 3) with a hexagonal arrangement of cylindrical rods, representing the fibrous material. A Newtonian fluid representing the resin matrix was pumped through the model system.

5.1.1. The Use of PIV and Other Fluid Flow Analysis Techniques

Particle Image Velocimetry (PIV) is a method by which fluid flow can be analysed (see Figure 5.1). This method involves examining the movement of tracer particles which are added to a fluid. It is a widely used technique that can be very effective

when employed to find the velocity profile of the fluid. The flow is normally illuminated with a light sheet[2] which highlights the tracer particles so they can be viewed easily. The movement of the tracer particles can be recorded with either a 35 mm camera or a CCD camera (oriented normal to the plane of the light sheet). From the images captured a measurement of the in-plane velocity vector field within a planar section of the flow can be made[3].

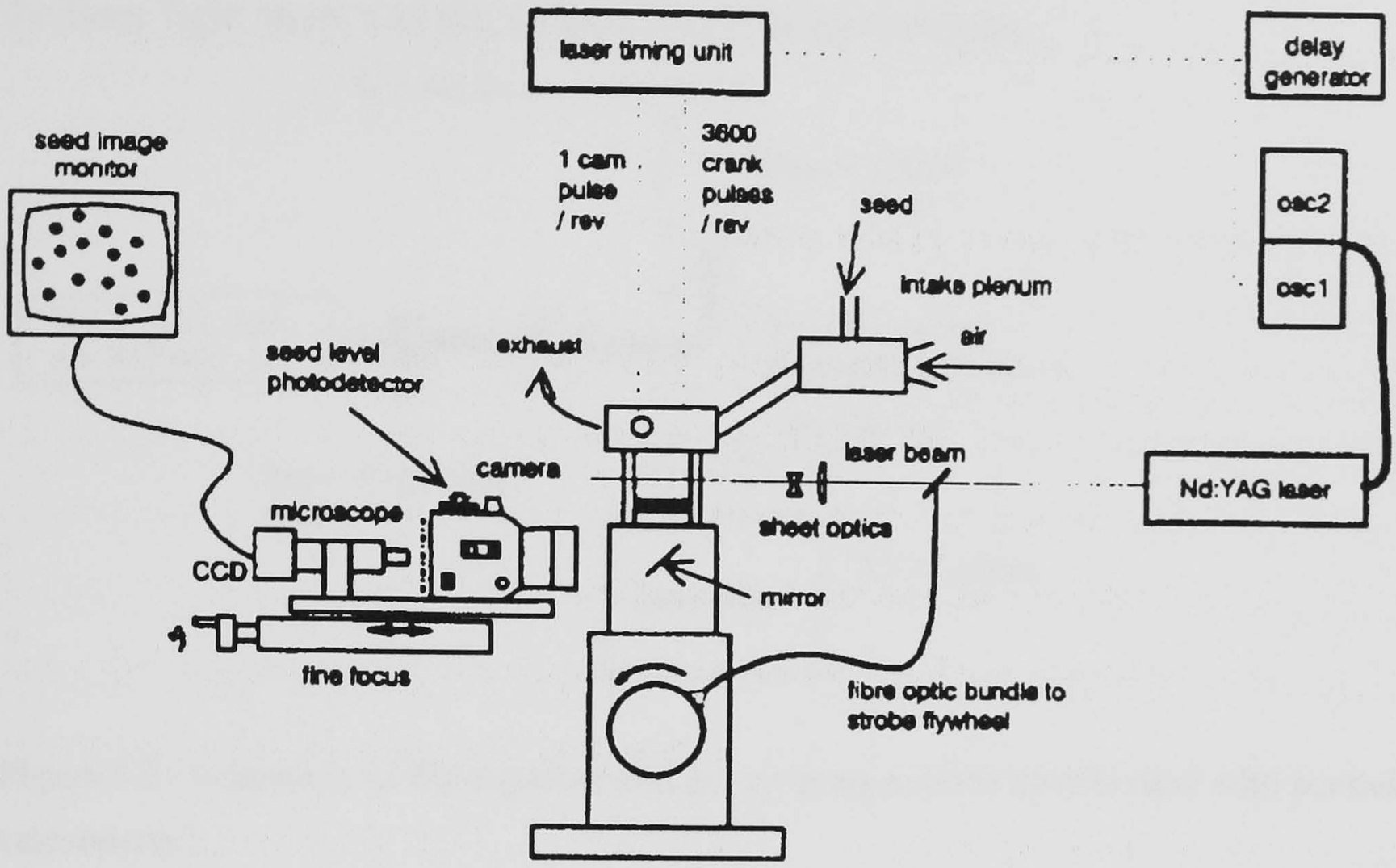


Figure 5.1 - Schematic of a typical particle image velocimetry set-up[2].

Many different types of tracer particles can be used for PIV, ranging from aluminium particles to polystyrene particles. The diameter of these particles is normally of the order of micrometers. This is large enough for the particles to be visible but small enough not to affect the fluid flow significantly. The density of the tracer particle is also important as it should be neutrally buoyant in the fluid, or at least settle very slowly.

Illumination of the particles is an important issue in PIV. There are various means such as the double-pulsed laser light sheet method (Figure 5.1), volume illumination (see Figure 5.2) or just a simple sheet illumination. The double-pulsed laser light method is one of the most common techniques for illumination. A laser is used as it provides a high level of illumination and sheets of light can be produced easily. Meinhart et al.[4] suggested the method of volume illumination of a test section rather

than using a sheet of light. They found this method advantageous for geometries that are very small and for situations where it is difficult to align the light sheet or where optical access is limited to one direction. The third method involves sheet illumination by a simple light source such as a tungsten bulb. This type of lighting does not provide as high a level of illumination as a laser, but it can still be bright enough for the tracer particles to be seen clearly. This method is less expensive than the laser light sheet and the volume illumination methods.

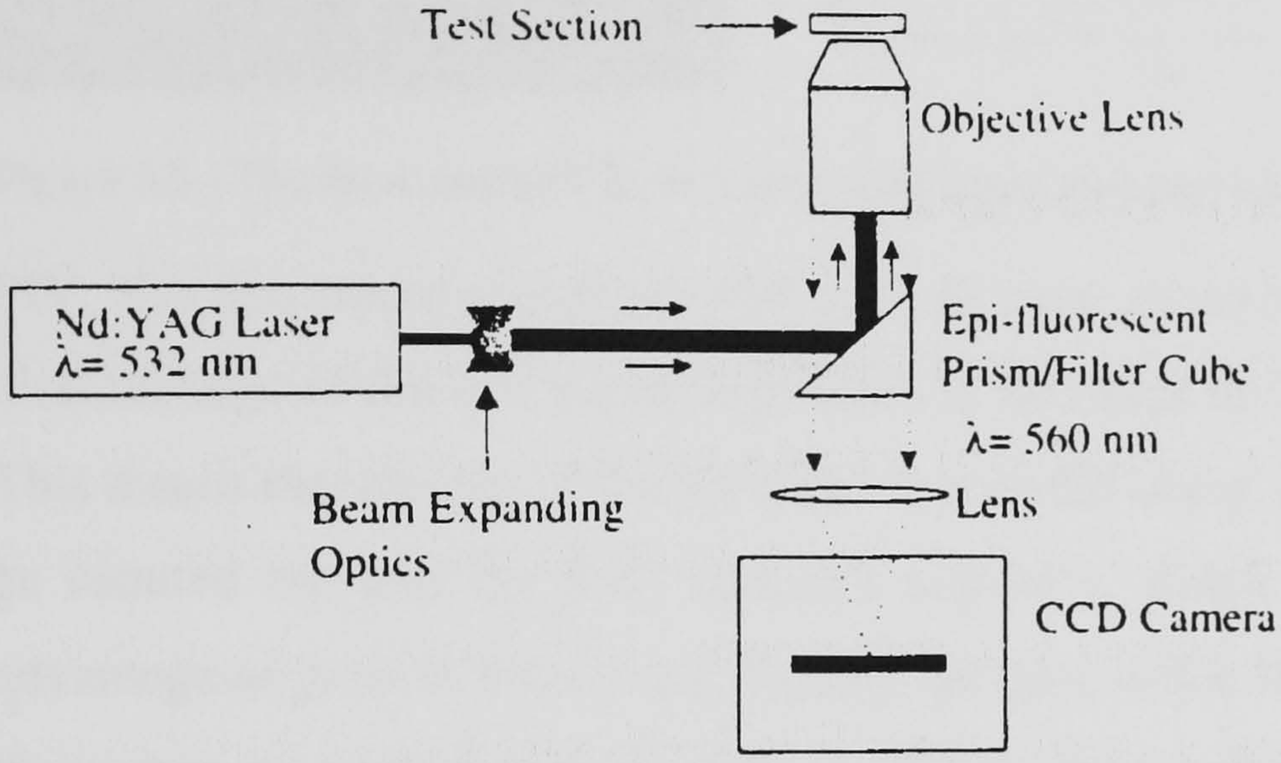


Figure 5.2 - Schematic of the experimental set-up using volume illumination with particle image velocimetry[4].

Particle Image Velocimetry is not the only method of analysing fluid flow. Another technique is to use a fluid tracer rather than particles to track the flow pattern. The tracer dye used resists break-up in regions of turbulent flow as it is a mixture of a surfactant with shear-thickening properties and high extensional viscosity fluid with a colorant[5]. This dye is added to the fluid and illuminated by one of the three illumination methods described above for PIV. Images are then captured using a 35mm camera or a CCD camera. Another similar technique is the Laser Induced Fluorescence (LIF) technique which involves the addition of a fluorescent tracer dye to the fluid (see Figure 5.3). A laser is directed at the fluid causing the dye to fluoresce and this shows the flow pattern which can then be recorded.

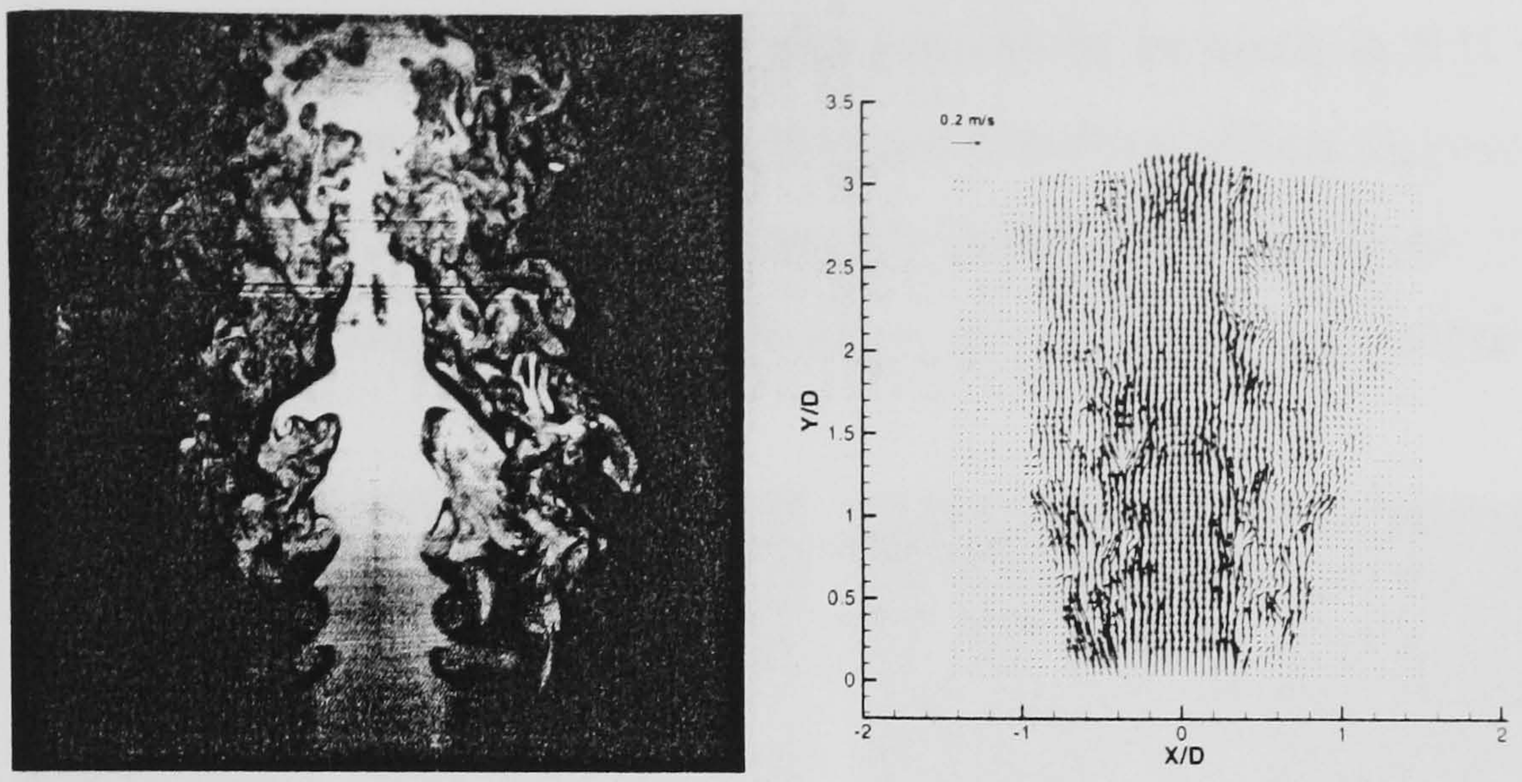


Figure 5.3 - The laser induced fluorescence technique and particle image velocimetry technique[6].

PIV, the dye tracer technique and LIF all have advantages and disadvantages. A disadvantage of the dye tracer techniques is that they involve the use of a liquid dye. This means that mixing of the fluid and dye would occur, so the system would have to be cleaned out and the fluid replaced regularly, which can be inconvenient. The advantage of particle tracers and fluorescent dyes is that they can be circulated around the system as many times as necessary and the flow patterns can still be seen clearly. The disadvantage of using particles rather than a fluid tracer is that they will have some effect on the fluid flow, although this may be sufficiently small enough to be ignored. However, with particle tracers nearly every region of the flow can be examined as a high seeding density can be used. Furthermore, PIV gives a direct quantitative estimate of the velocity field.

5.1.2. Accuracy of PIV and Image Analysis

Funes-Gallanzi[7] examined the accuracy of PIV measurements and image analysis. He stated that the sources of error could be split into two main classes, those which affect a data field and those which apply to the whole frame. He then defined the different types of frame errors and intra-frame errors; slip, scaling, rotation, translation and distortion effects are the primary types of frame errors. Figure 5.4 shows an example of image shift that leads to errors and the calibration picture that can be used to reduce the effect. When a seed does not follow the flow exactly then this is a slip error and generally these are of a low order. For example, an error of the order of 1 % can be achieved using 0.4 μm polystyrene spheres in air, even at transonic speed. Magnification errors from the recording apparatus and pulse separation errors (when using a pulsed laser) can lead to scaling errors. These types of error are slightly more

significant than those caused by slip and can be as much as 5 % for a 500 ns pulse separation. Then rotation, translation and distortion effects can occur when capturing the image, of which translation generally causes the largest error. These errors can be overcome or reduced by placing markers on the camera from which calibration can be carried out.

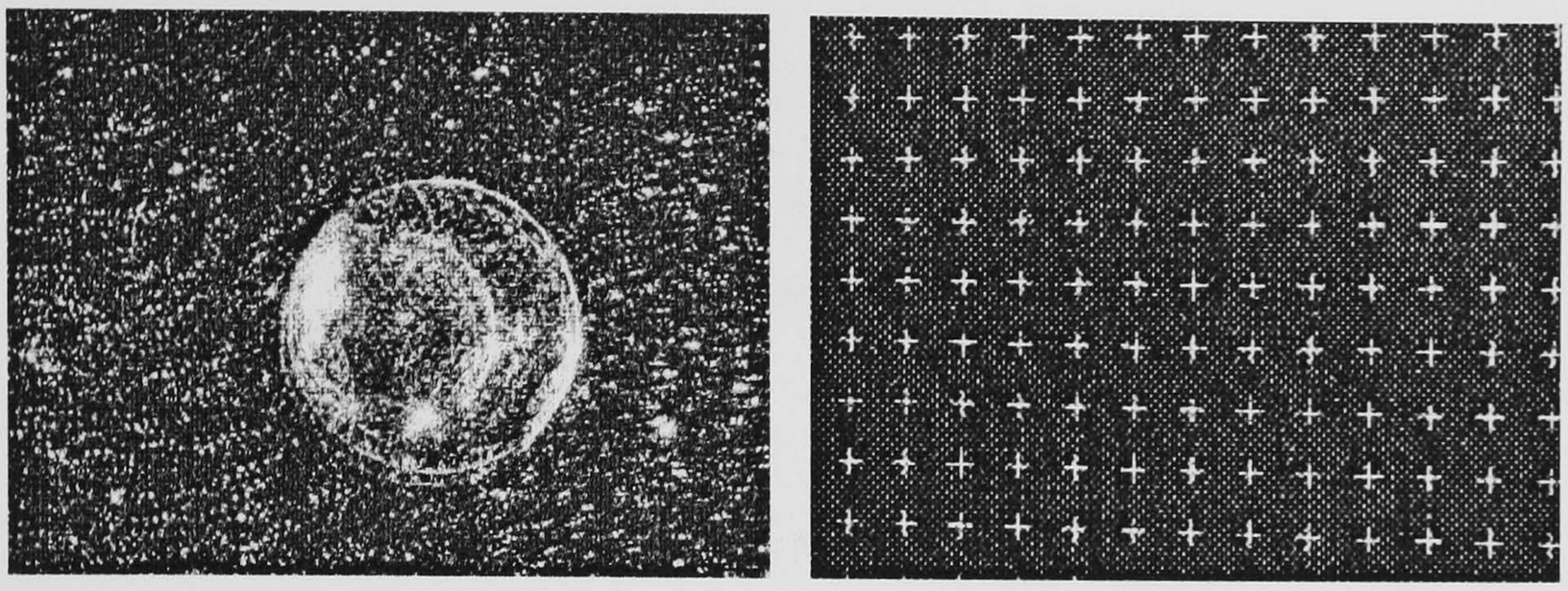


Figure 5.4 - Image shift in particle image velocimetry and calibration picture used to reduce this effect[8].

Intra-frame or data field errors occur due to estimation of the particle position or are related to the recording medium. These errors can arise from pixel sensitivity when dealing with digital cameras and image analysis software and can be overcome by calibration. Funes-Gallanzi[7] suggested that most errors could be overcome by calibration techniques and that the main source of residual errors were frame errors. He concluded though that it was possible to produce high-accuracy measurements with the PIV technique and image analysis.

5.2. Numerical Model

The numerical simulation proposed by Spelt et al.[1] is used for comparison with the experimental results. The Navier Stokes equations were solved using the finite difference method. The main assumptions of the model used for the comparison are: -

1. The (periodic) cylinder array extends to infinity
2. The fluid is Newtonian
3. Inertial effects can be neglected, so the Reynolds number is small
4. The flow is exactly perpendicular to the axes of the cylinders
5. The cylinders are infinitely long

However in other simulations Spelt et al.[1] have relaxed some of these assumptions. For example, assumption 3 has been dealt with in simulations where the Reynolds number increases. Assumption 2 has been worked on by looking at power-law and

Bingham fluids. Simulations for flow parallel to the cylinders have also been performed thus dropping assumption 4.

The general form of the Navier Stokes equation is:

$$\frac{\partial \underline{u}}{\partial t} + \nabla \cdot (\underline{u}\underline{u}) = -\frac{1}{\rho}\nabla P + \mu \nabla^2 \underline{u}\,, \qquad \textbf{[5.1]}$$

where $\underline{u}$ is the velocity field which is a function of position and time t, ρ is the density of the fluid, P is the pressure and μ is the kinematic viscosity.

This is subject to the continuity equation:

$$\nabla \cdot \underline{u} = 0\,. \qquad \textbf{[5.2]}$$

For steady flows at low Reynolds number, the terms on the left-hand side of [5.1] are zero. However, the numerical simulation procedure follows a transient towards the steady state, so the first term was retained in the model.

As the geometry being examined was two-dimensional equation [5.1] was solved for both the x and y components of $\underline{u}$, u_x and u_y respectively. There are three steps to solving the Navier Stokes equations for the three unknowns, u_x, u_y and P:

The first stage is the predictor step and this is when [5.1] is solved without the pressure term:

$$\frac{\partial \underline{u}}{\partial t} = \mu \nabla^2 \underline{u} \quad . \qquad \textbf{[5.3]}$$

Everything is known at time t=0, $\underline{u}(\underline{x},t)$ is known but $\underline{u}(\underline{x},t+dt)$ must be found. The Crank-Nicholson scheme[a] is used to find the value of the right hand side of [5.3] and this is done by calculating an average value:

$$\mu \nabla^2 \underline{u} \approx \frac{\mu}{2}(\nabla^2 \underline{u}(t) + \nabla^2 \underline{u}^*(t+dt))\,, \qquad \textbf{[5.4]}$$

$\frac{\partial \underline{u}}{\partial t}$ is approximated by taking a difference in incremental values, i.e.

---

[a] *Computational Fluid Dynamics*, John D. Anderson Jr., McGraw-Hill, 1995.

$$\frac{\partial \underline{u}}{\partial t} \approx \frac{\underline{u}^*(t+dt) - \underline{u}(t)}{dt}. \qquad [5.5]$$

The final velocity field obtained in the predictor step, $\underline{u}^*(t+dt)$, can then be used to solve the Navier Stokes equations for pressure. The pressure is obtained from the requirement that the final velocity field must be incompressible, so the same volume flows out of each computational cell as goes in. The equation used to solve for pressure is

$$\nabla^2 P = \frac{\rho}{dt} \nabla . \underline{u}^*(t+dt). \qquad [5.6]$$

Once the pressure has been determined, the last step can be carried out and this is the correction step. This gives the velocity field corrected by the pressure term:

$$\underline{u}(t+dt) = \underline{u}^*(t+dt) - \frac{dt}{\rho} \nabla P. \qquad [5.7]$$

The main result produced by the code is an average velocity value taken over the whole of the unit cell. This value is used to calculate the drag coefficient on a cylinder.

The individual velocity values at each point in the mesh were used to create images of the velocity field using a program called Tecplot 8.0[b].

5.3. Error Analysis

A detailed description of the experimental materials and methods is given in Chapter 3 (section 3.2.4.).

The main sources of error identified in these series of experiments arise from:-

- Human error in identifying the length and position of the streaks in the images. The image size is 2,048 × 1,536 pixels, but each streak is typically 30 pixels long. The estimated error in identifying the position of the streaks is ±2 pixels which equates to an error of approximately 7%.
- Additionally, parallax errors are also a major source of error as it is difficult to identify the depth of field of each of the traces in the images. These errors are estimated to be of the order of 2% in the position of each streak.

[b] Tecplot version 8.0-0-8 (Nov 15 1999) for MS-WINDOWS, Amtec Engineering Inc.

Lower orders of error would have arisen from:-

- Translation, rotation and scaling effects. However, it is believed that the method used to analyse these results would have minimised such errors (see section 5.4).
- Although a reliable gear pump was used with reinforced plastic piping to minimise peristaltic flow conditions, there is still a very small degree of error due to variation of the flow rate.
- Any inaccuracy in the timing of the exposure. Again this is believed to be a small error as a reliable digital Nikon camera[c] was used.
- Any changes in the viscosity of the fluid during the experiment due to temperature changes and shear stress. The fluid used was proved to be Newtonian so negligible changes in viscosity would occur due to shear stress. The temperature was subject to changes of ±2°C which would have a very small effect on the viscosity of the fluid. The fibre optic light used did not contribute to any heating effects.
- Slip errors caused by the tracer particles not following the flow directly. These errors are difficult to find quantitatively and should be sufficiently small to be ignored.

The total error is thus estimated to be of the order ±7%.

5.4. Results and Discussion

Images of the test fluid seeded with aluminium particles passing through the flow cell were obtained at three different global volumetric flow rates of 9.4cm^3/s, 13cm^3/s and 16cm^3/s. Figure 5.5 displays a typical image showing the particle streaks in the flow cell during the experiments.

[c] Nikon Coolpix 880 digital camera

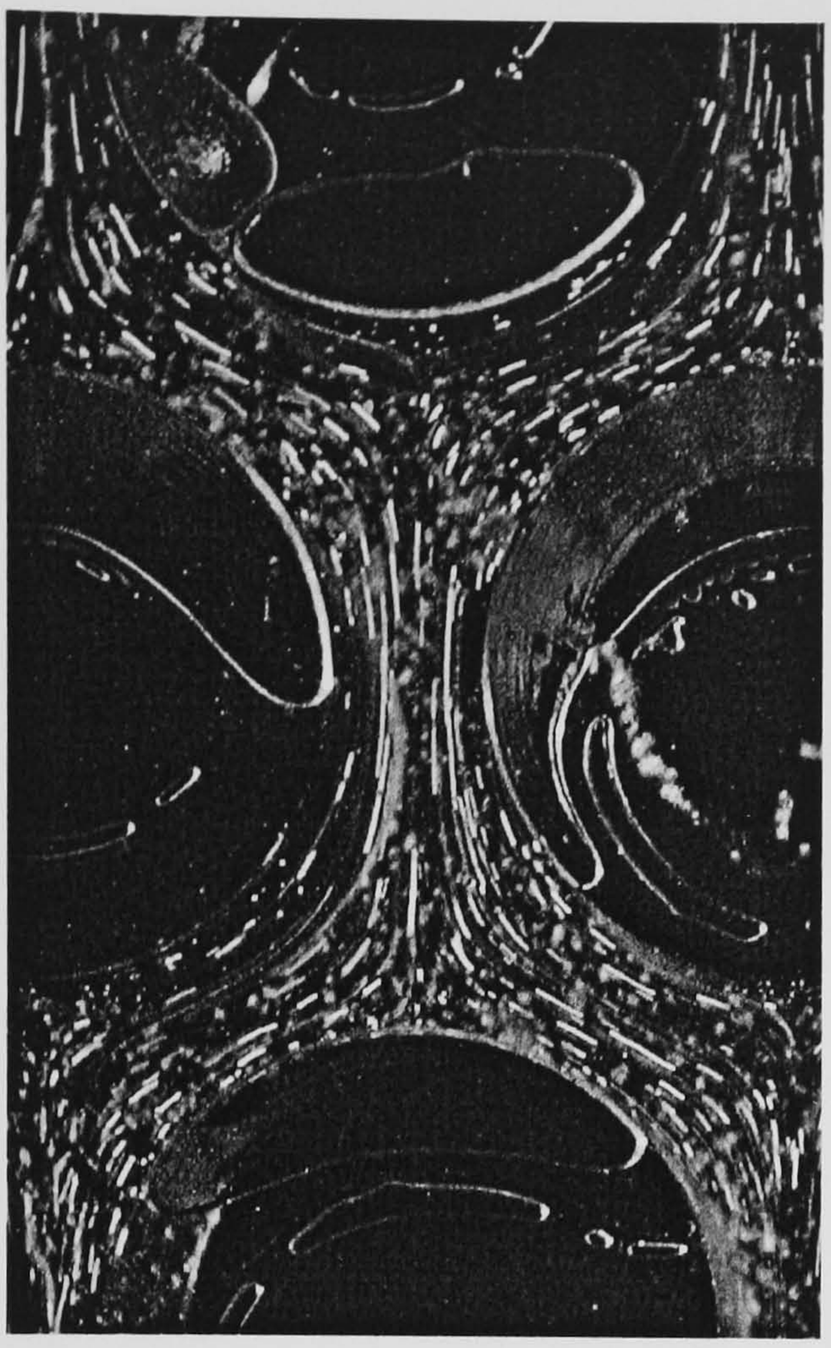


Figure 5.5 - Image of particle streaks in the flow cell for a shutter speed of 1s and fluid volumetric flow rate of 16cm^3/s (the cylinder diameter is 16mm).

The images were analysed by hand, using an image-processing package called '*ImageTool*', produced by UTHSCSA. First the end points of each streak were determined (by point and click with the mouse) from an enlarged view of the streak. The centre point of each streak was calculated as the reference point for that velocity measurement. The streak lengths were then calculated and used to determine the velocity which is proportional to the streak length. A two-dimensional scatter plot was produced showing the positions and lengths of all the streaks measured. This allowed comparison between the digitised data and the original image, and ultimately between the experimental plots and those generated from the numerical simulations (refer to section 5.2).

The raw data of length and streak position were normalised, which involved performing the following steps:- (i) rotating the image, (ii) shifting the origin of the image and (iii) rescaling the image to match the unit cell shown in Figure 5.6. To do this, several points on the periphery of each rod were digitised. A least squares error minimisation was applied (in Microsoft *Excel*) to determine the rotation, image shift and scale factor parameters. This helped to minimise any frame errors.

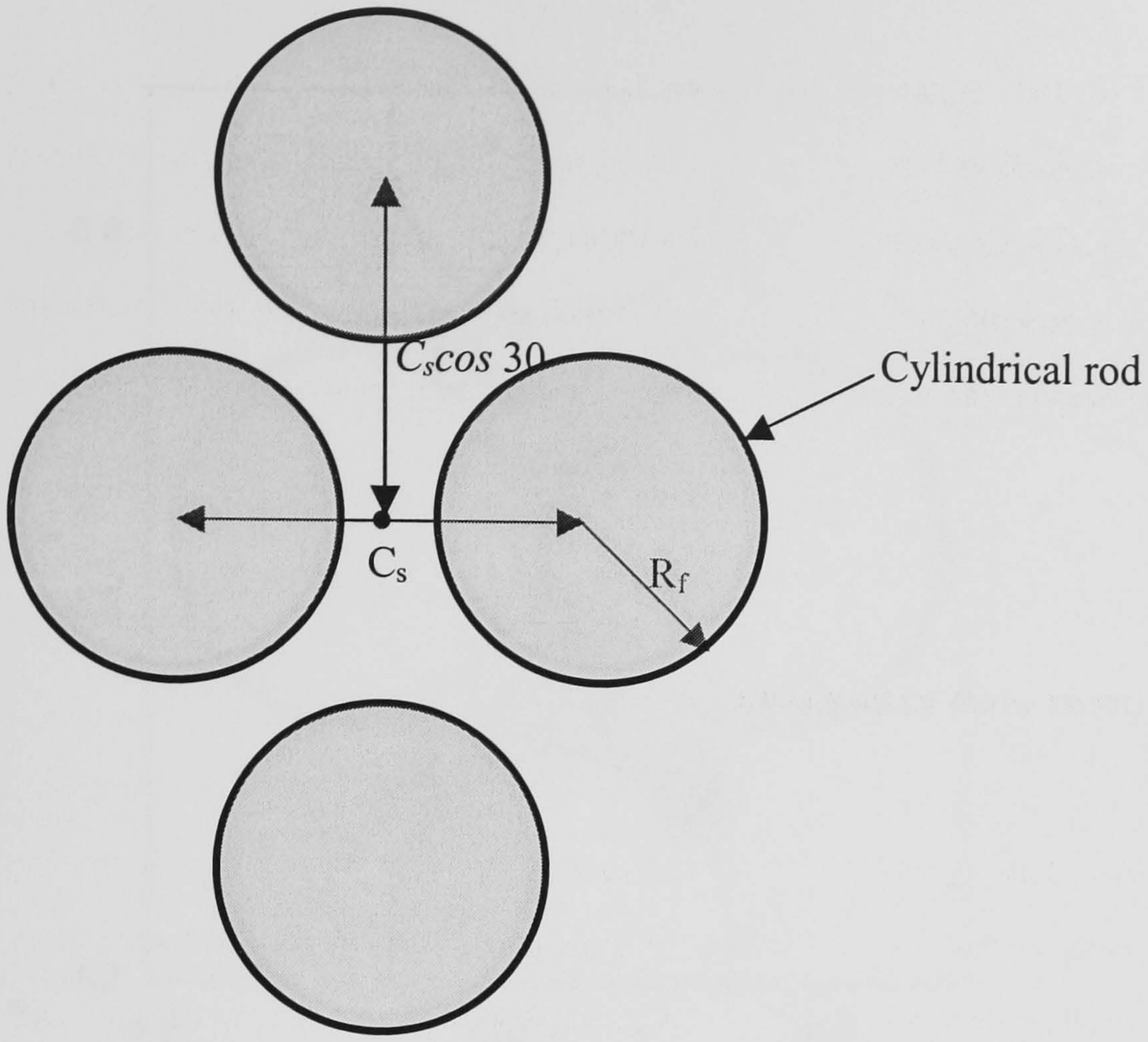


Figure 5.6 - Unit cell used to normalise the raw experimental data by rotating the original image, shifting the origin and rescaling the image size.

Details of the three functions applied to each data point during normalisation are:-

Rotating the image by angle θ;

$x_1 = x_0\cos\theta + y_0\sin\theta$

$y_1 = y_0\cos\theta - x_0\sin\theta$

Then shifting the origin of the image by coordinates x_s and y_s;

$x_2 = x_1 + x_s$

$y_2 = y_1 + y_s$

And finally re-scaling the image by scale factor L;

$x_3 = Lx_2 = L(x_s + x_0\cos\theta + y_0\sin\theta)$

$y_3 = Ly_2 = L(y_s + y_0\cos\theta - x_0\sin\theta)$

Figures 5.7 to 5.9 show the normalised particle traces at each of the respective flow rates used. An increase in the streak length is observed from Figures 5.7 to 5.9 as the global flow rate increases from 9.4cm^3/s to 13cm^3/s to 16cm^3/s respectively. Each figure includes data obtained from several photographs at the same conditions.

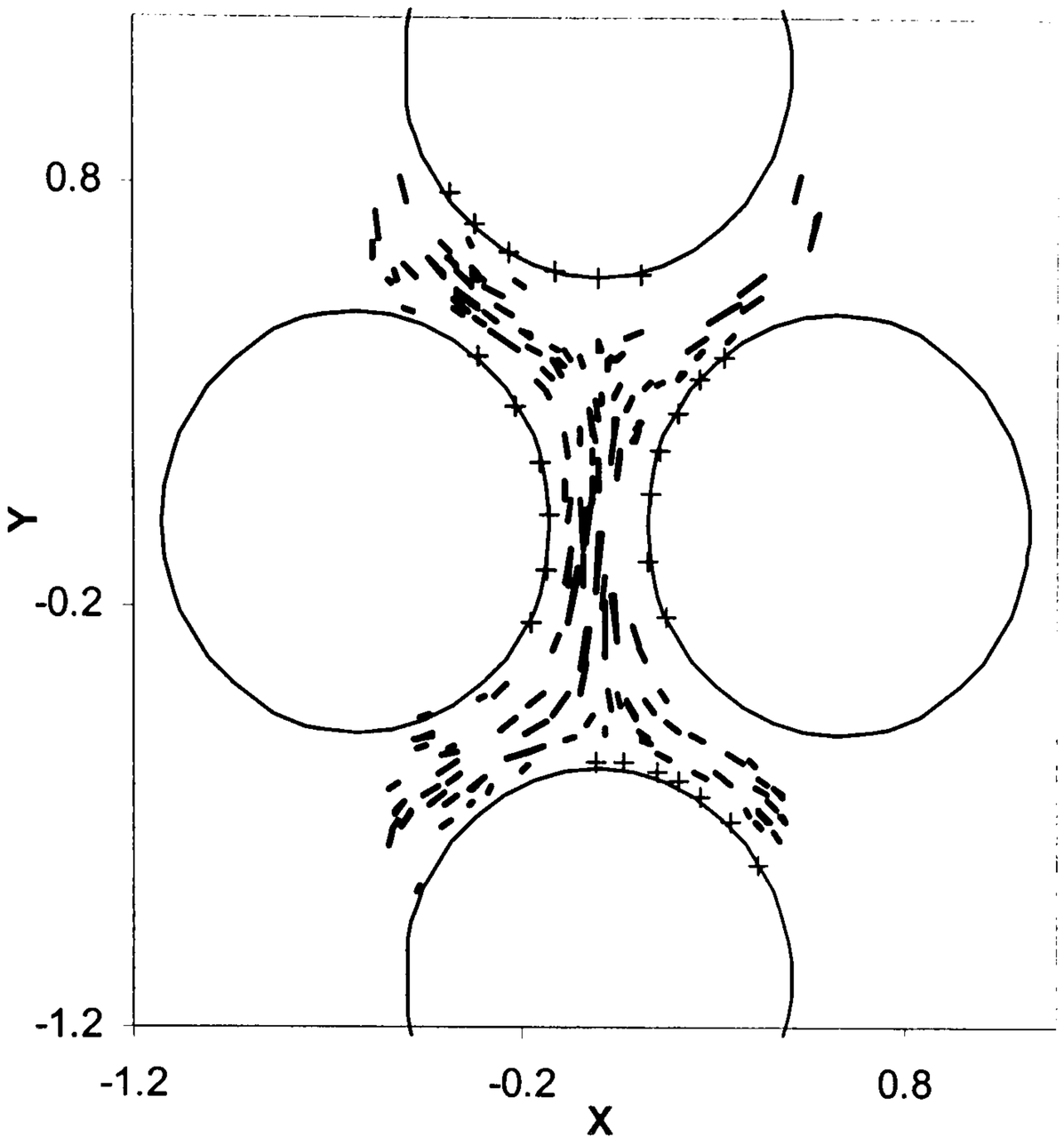


Figure 5.7 – Particle streaks of Aluminium dust showing the velocity field of the liquid flowing through a hexagonal array of cylinders (global volumetric flow rate of 9.4cm^3/s).

It can be seen from Figure 5.7 that the particle streak lengths vary depending upon their position within the unit cell. It is observed that the streak lengths are longest in the narrow channel within the central region of the unit cell, between the right and left cylinders, indicating the highest flow speed to be in this region. The shortest streak lengths and hence the lowest flow velocities are recorded around the boundary of the cylinders. Intermediate streak lengths are observed in the other channels between the cylinders.

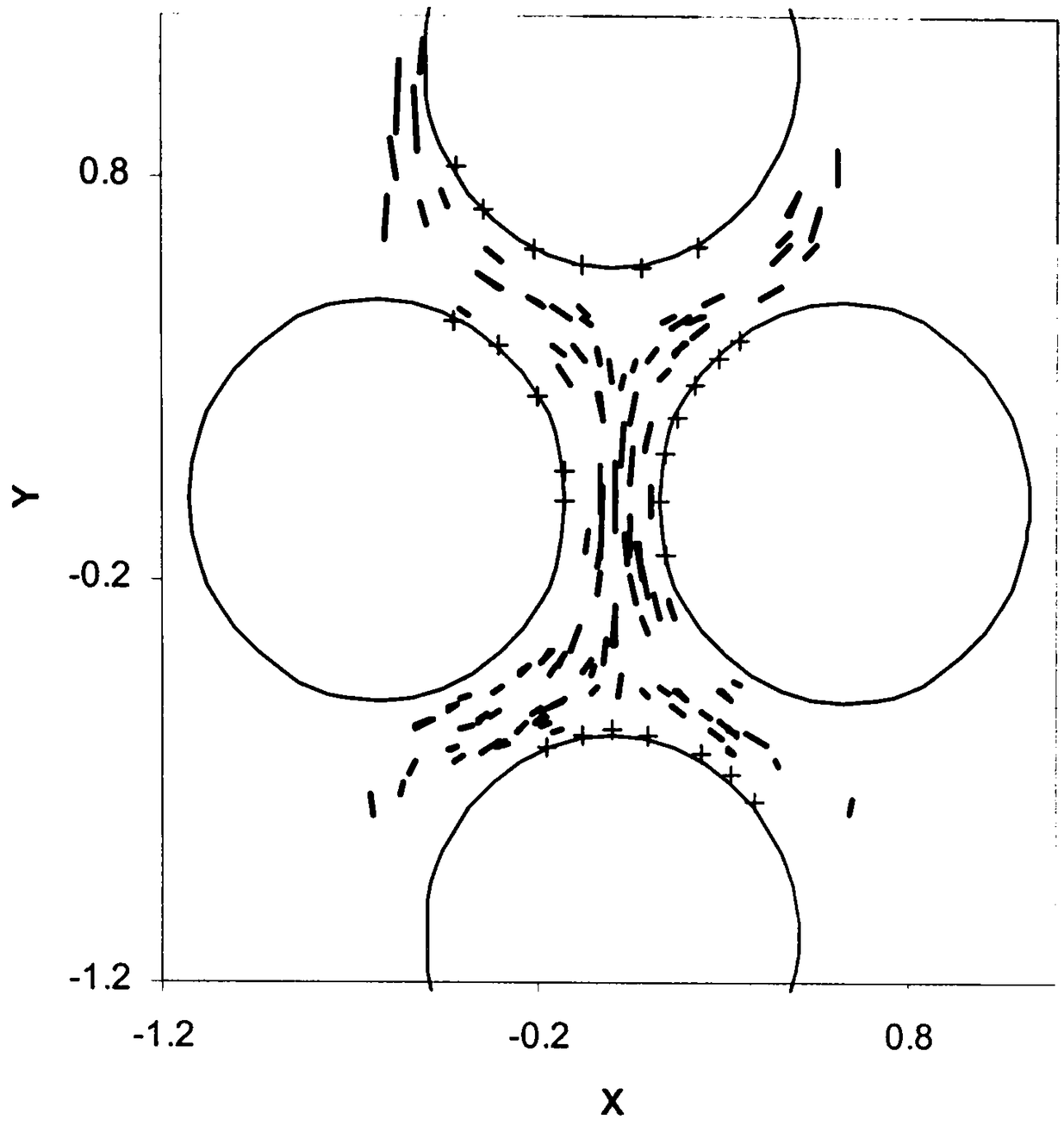


Figure 5.8 - Particle streaks of Aluminium dust showing the velocity field of the liquid flowing through a hexagonal array of cylinders (global volumetric flow rate of 13cm^3/s).

Figure 5.8 shows the same trend in particle streak length distribution within the unit cell as observed in Figure 5.7. In this case, however, the streak lengths recorded are longer corresponding to the higher global volumetric flow rate, given that the camera shutter speed remained constant.

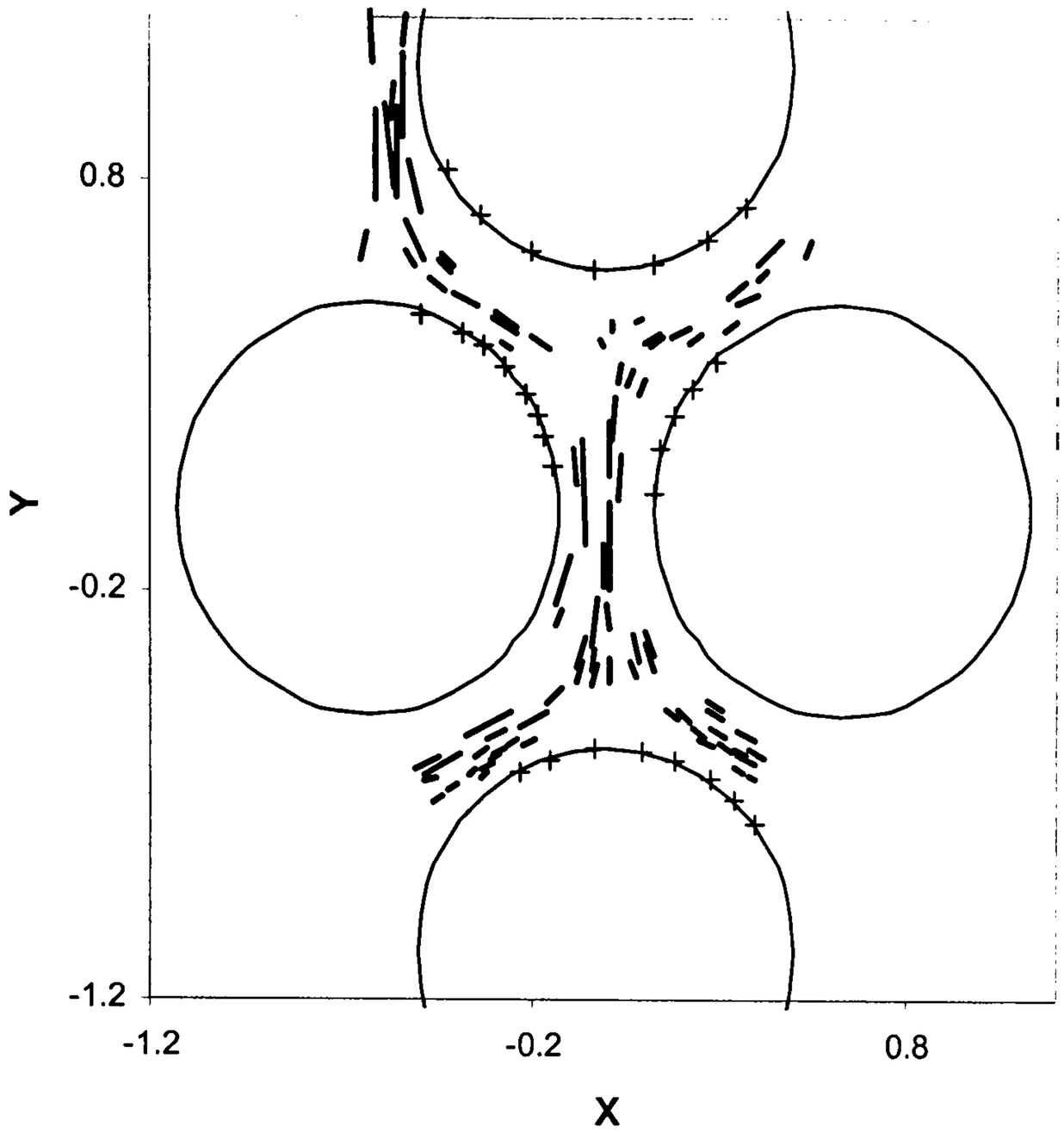


Figure 5.9 - Particle streaks of Aluminium dust showing the velocity field of the liquid flowing through a hexagonal array of cylinders (global volumetric flow rate of 16cm^3/s).

Figure 5.9 displays the results for the streak length distribution at the highest global volumetric flow rate used of 16cm^3/s. Generally it is observed that the same trend in streak length distribution is achieved as in Figures 5.7 and 5.8.

5.4.1. Redistributed Data Points

In order to obtain a more dense velocity field within the unit cell for the data points shown in Figures 5.7 to 5.9, a translation and reflection of all the data points to one quarter of the unit cell was performed. Thus each of the four quadrants shown in Figure 5.10 can be superimposed. Firstly, *C* is shifted over to *A* and *B* is shifted over to *D*. Finally *B* and *D* are reflected onto *A*. Results of this operation are shown in Figures 5.11 to 5.13 for each respective flow rate.

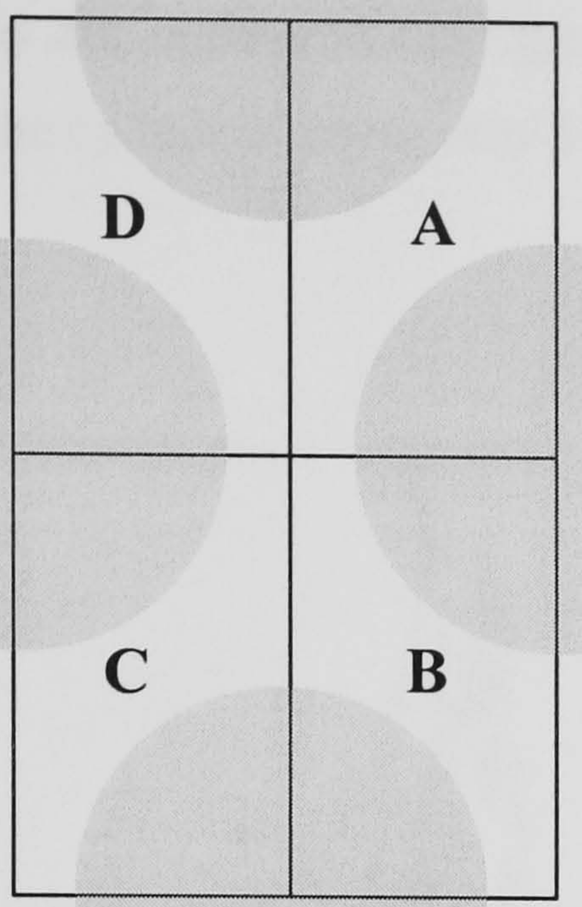


Figure 5.10 – Schematic diagram showing each of the four quadrants used in the redistribution of data points.

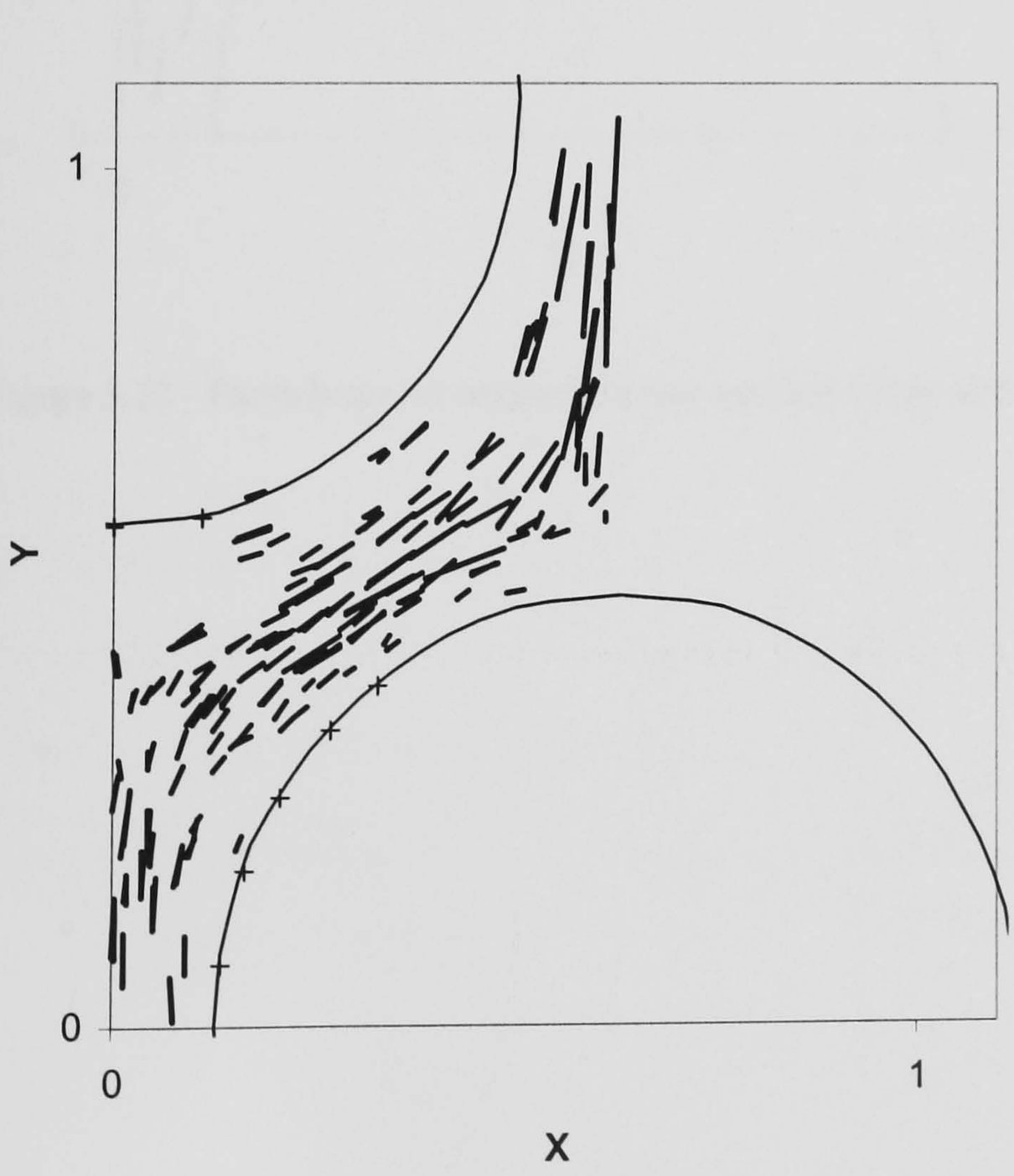


Figure 5.11 - Particle traces mapped to one-quarter of the unit cell (global flow rate of 9.4cm^3/s).

From Figure 5.11 the velocity distribution in the channel between the cylinders is much clearer when only one-quarter of the unit cell is considered. Low particle velocities are registered near the cylinder walls and there exists a boundary layer around the cylinders where very few particle velocities are registered.

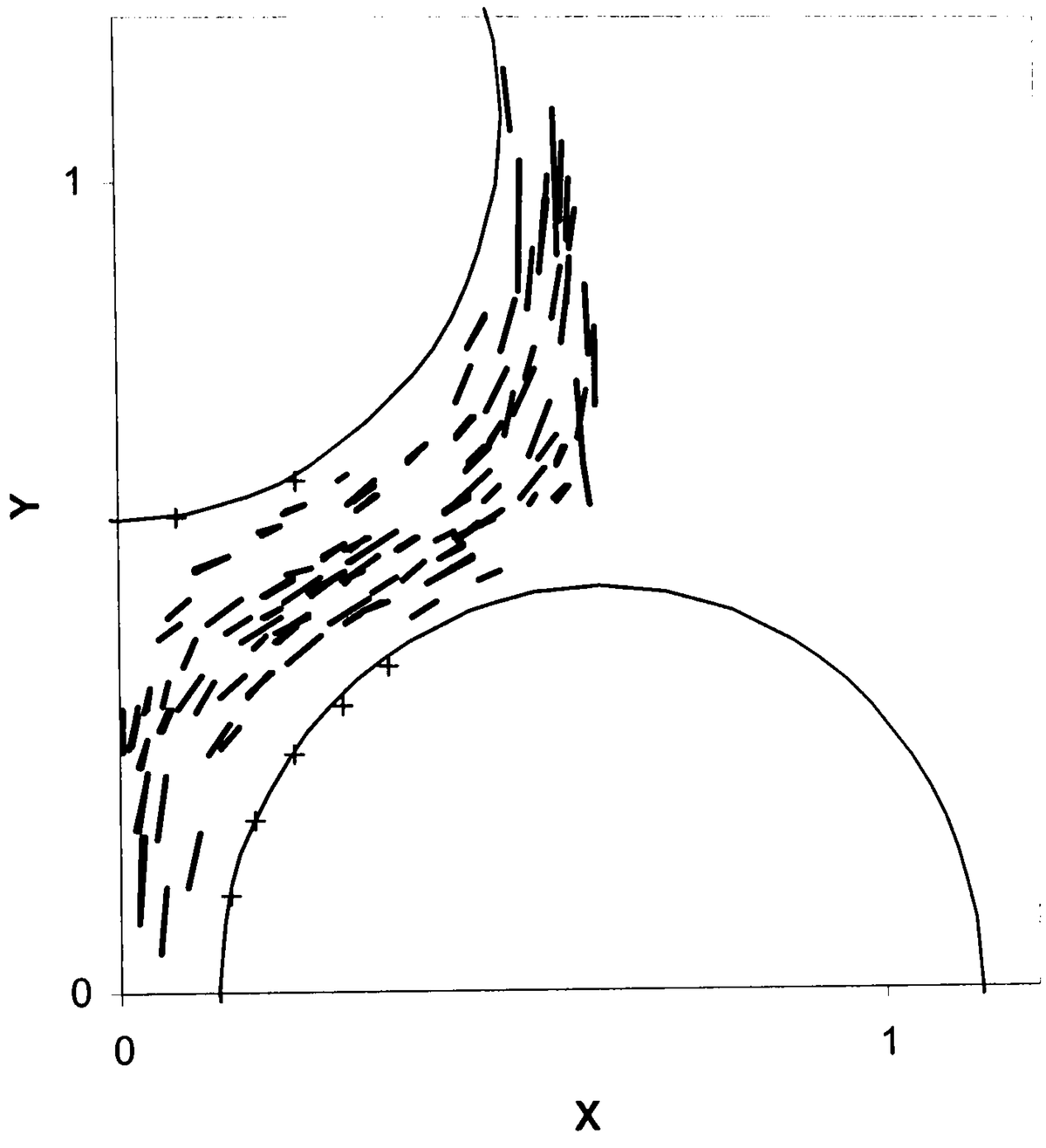


Figure 5.12 - Particle traces mapped to one-quarter of the unit cell (global flow rate of 13cm^3/s).

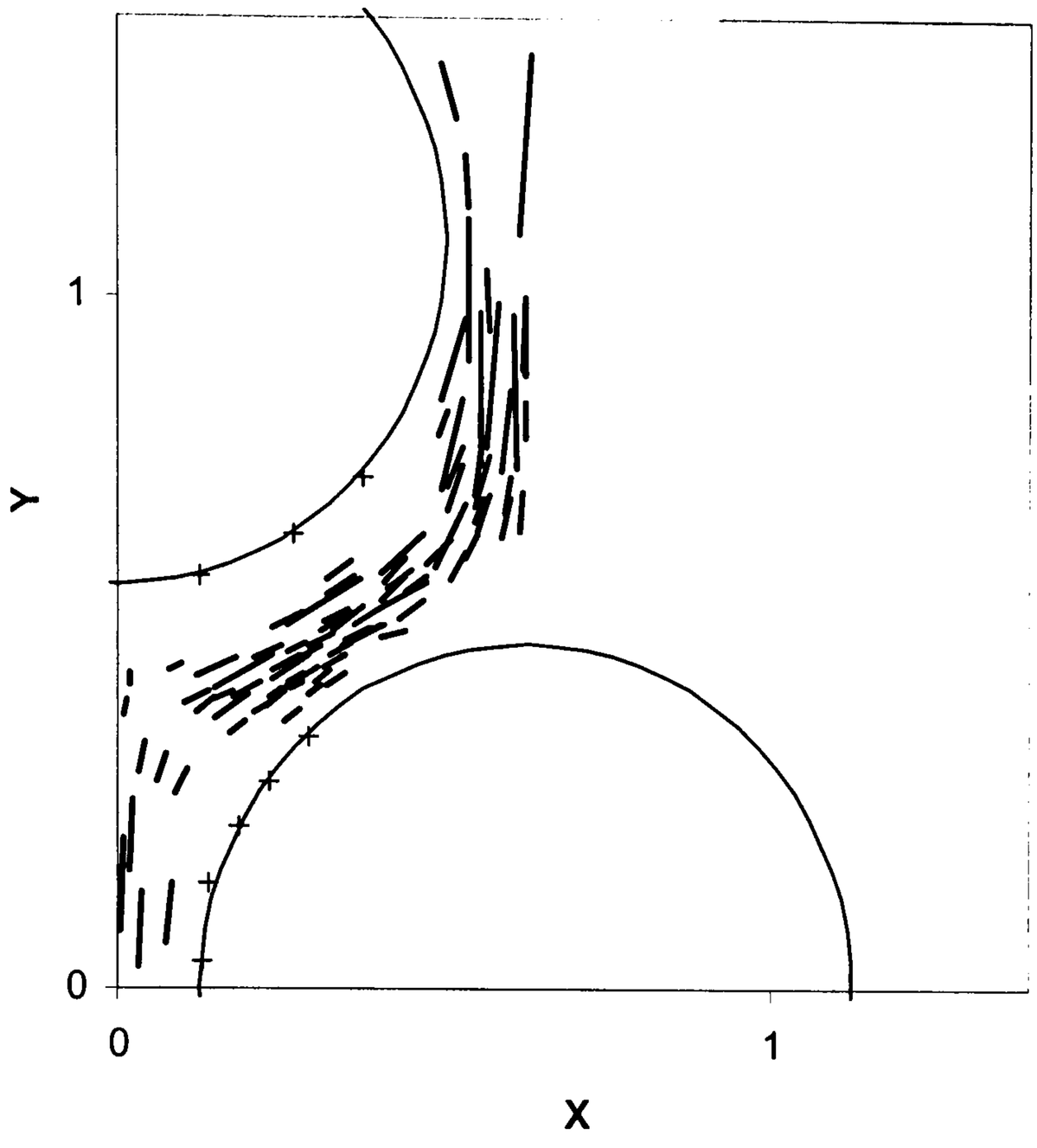


Figure 5.13 - Particle traces mapped to one-quarter of the unit cell (global flow rate of 16cm^3/s).

Table 5.1 summarises the velocity data and Reynolds number for each data set. The superficial velocity is defined as the total volumetric flow rate divided by the total cross-sectional area. The pore velocity is defined as the total volumetric flow rate divided by the average pore cross-sectional area. The maximum velocity is the velocity within the narrowest gaps and is defined as the total volumetric flow rate divided by the minimum pore cross-sectional area. The Reynolds number is based on the superficial velocity.

Table 5.1 – Summary table of velocity field results

Experiment	Flow rate (cm^3/s)	Superficial Velocity (cm/s)	Pore Velocity (cm/s)	Maximum Velocity (cm/s)	$Re_{(superficial)}$
1	9.4	0.47	1.1	11.8	1.1
2	13	0.65	1.5	16.3	1.5
3	16	0.8	1.9	20	1.9

5.4.2. Contour Plots

Contour plots of the velocity field data were generated by importing the streak coordinates and velocity vectors into Tecplot 8.0[b]. It was, however, necessary to apply the Kriging[9] algorithm to interpolate the data as it was not distributed evenly in the ***XY***-plane. Also, in order to maintain consistency with the numerical simulation results for comparative reasons, the experimental velocity data were made dimensionless by dividing by the superficial velocity (global volumetric flow rate/total cross-sectional area of the flow cell). These contour plots of the velocity field within the unit cell are displayed in Figures 5.14 to 5.16.

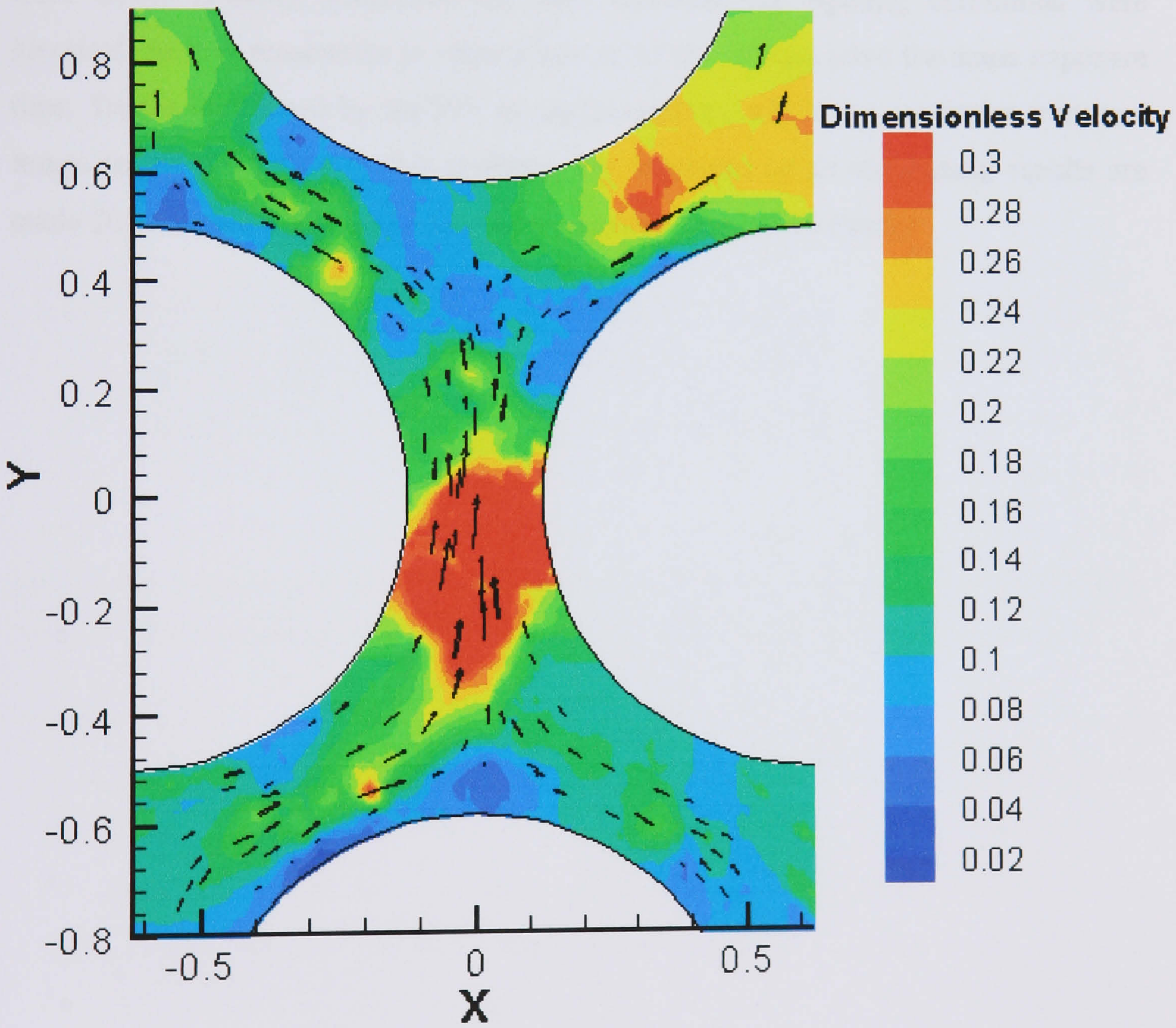


Figure 5.14 – Contour plot of the velocity field within the unit cell for a global volumetric flow rate of 9.4cm^3/s. The black arrows indicate the velocity vectors for each data point.

From Figure 5.14 it is observed that all of the dimensionless velocity values are significantly less than unity. However, the superficial velocity is an average, and one would expect some values to be greater than the average. Furthermore, the geometric constraints of the narrow gaps, should lead to velocities several times larger than the superficial value. Hence the absolute velocity measurements are in error. The most likely explanation for this discrepancy is a difference between the exposure reading on the camera and the actual exposure time of the images.. A Nikon Coolpix 880 digital camera[d] was used for the image capture. The exposure is set automatically by the camera and is not recorded on the resulting image. It is therefore difficult to ascertain what value of exposure was used. However, the images at each flow rate were taken virtually simultaneously and therefore the lighting conditions were identical, so it is reasonable to expect that all of the images have the same exposure time. This is confirmed by the PIV traces themselves, which are consistent from one image to the next. Due to this problem, the velocities in all subsequent results are made dimensionless by dividing by the maximum measured velocity.

[d] *Nikon UK Limited*, Nikon House, Kingston upon Thames, Surrey, KT2 5PR.

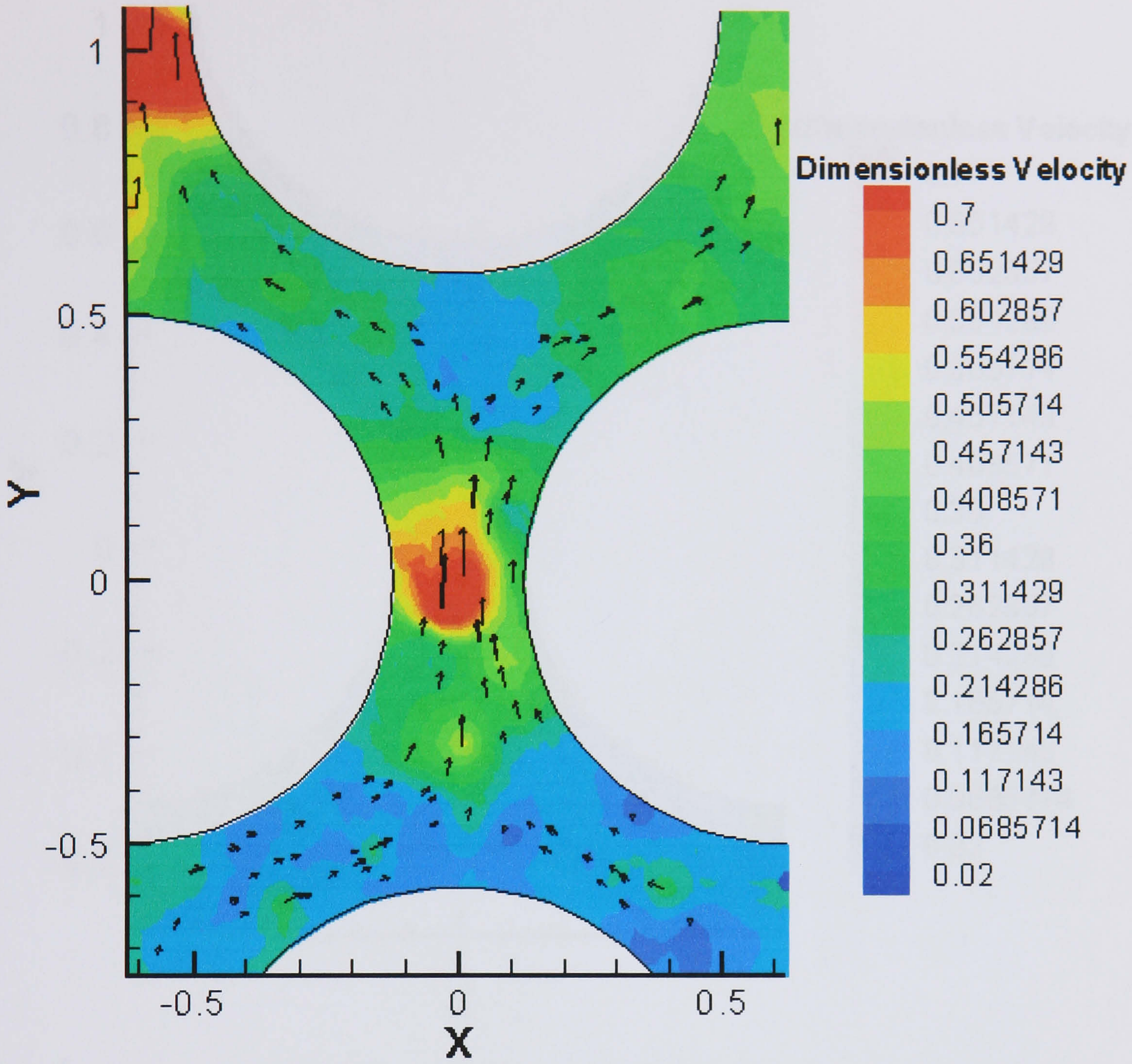


Figure 5.15 - Contour plot of the velocity field within the unit cell for a global volumetric flow rate of 13cm^3/s. The black arrows indicate the velocity vectors for each data point.

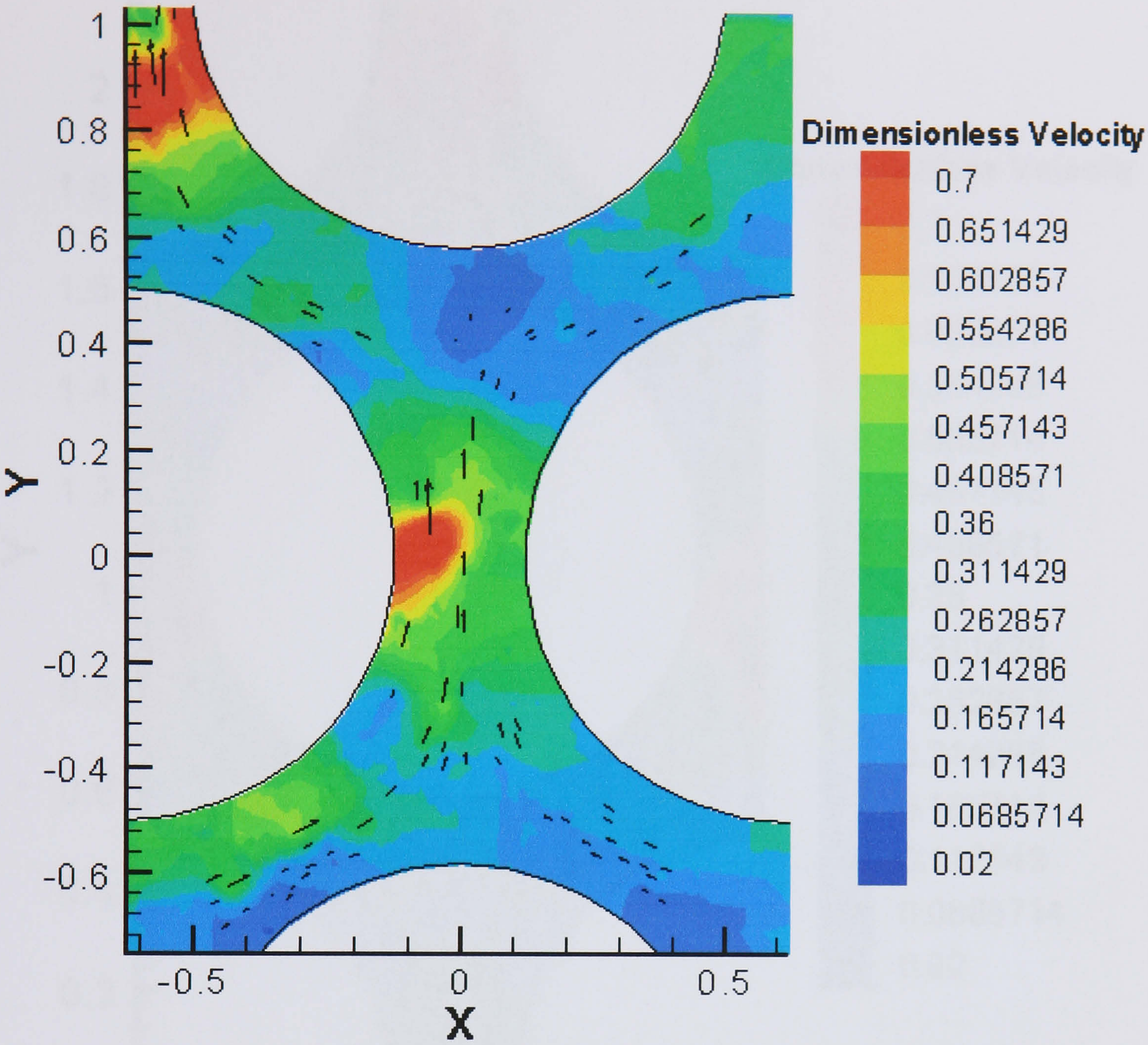


Figure 5.16 - Contour plot of the velocity field within the unit cell for a global volumetric flow rate of 16cm^3/s. The black arrows indicate the velocity vectors for each data point.

In Figures 5.14 to 5.16 the black arrows indicate the velocity vectors at each data point. The contour plots highlight the central region of the unit cell as having the highest velocity. By mapping these data onto one-quarter of the unit cell, as done previously in Figures 5.11 to 5.13, and then re-plotting these redistributed data over the entire unit cell a more dense symmetrical velocity profile distribution is achieved as shown in Figures 5.17 to 5.19. The geometry of the unit cell shown in Figures 5.17 to 5.19 is different from the unit cell presented in Figure 5.6 for comparative reasons in order to correspond with the geometry of the unit cell used in the numerical simulation.

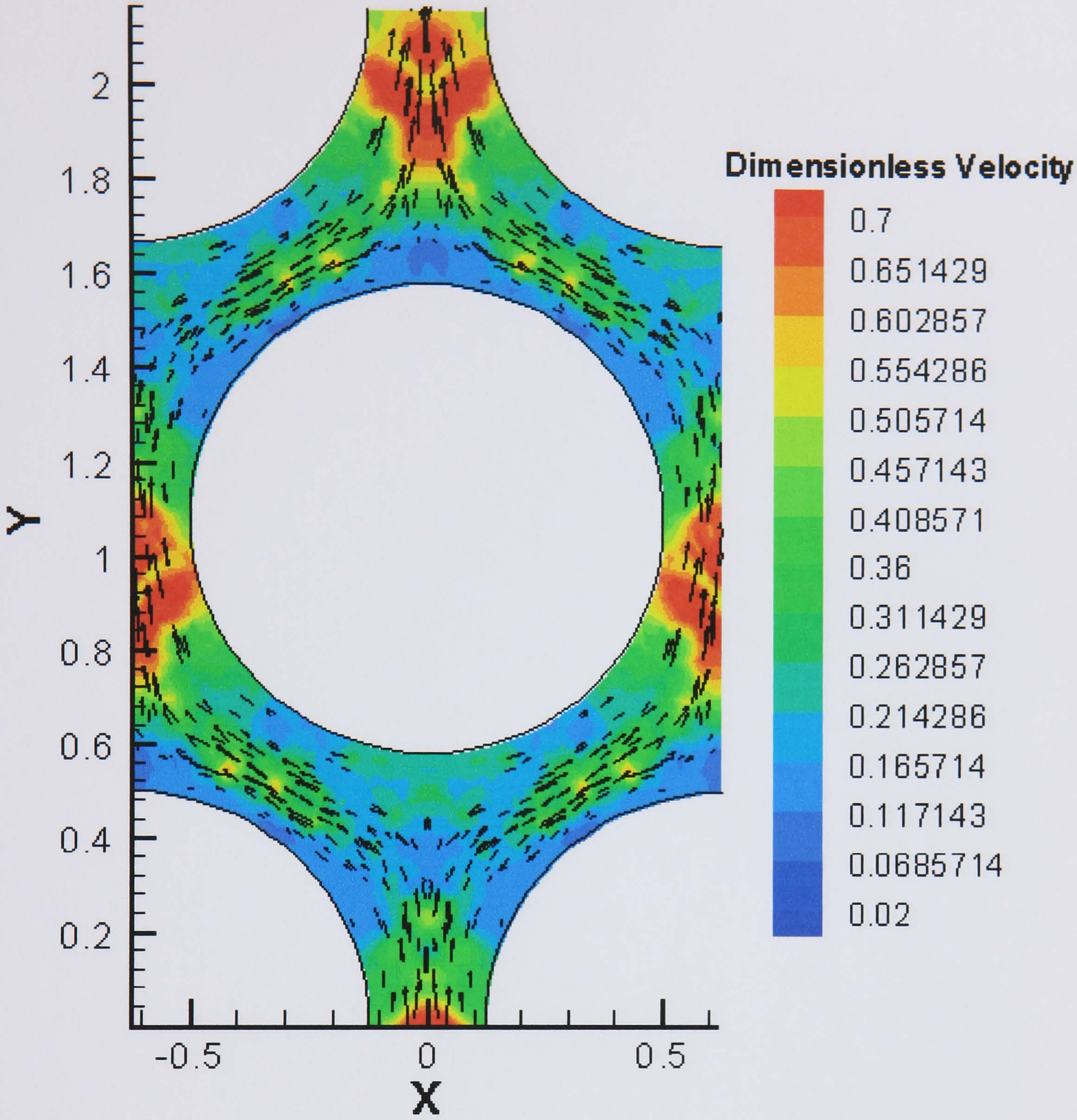


Figure 5.17 – Contour plot of the velocity field for a condensed data set at a global volumetric flow rate of 9.4cm^3/s. Each data point is plotted in all four quadrants of the unit cell.

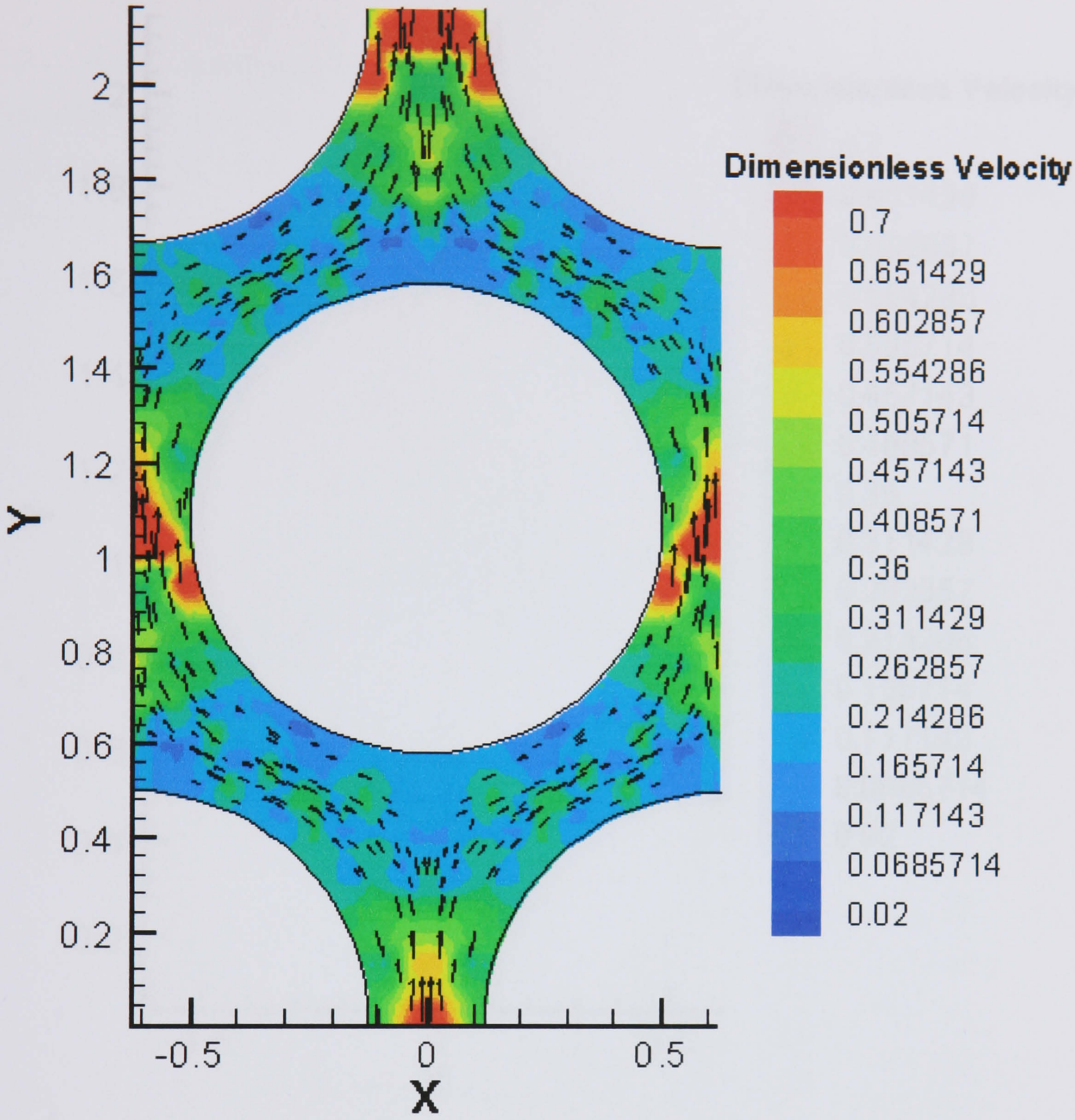


Figure 5.18 - Contour plot of the velocity field for a condensed data set at a global volumetric flow rate of 13cm^3/s. Each data point is plotted in all four quadrants of the unit cell.

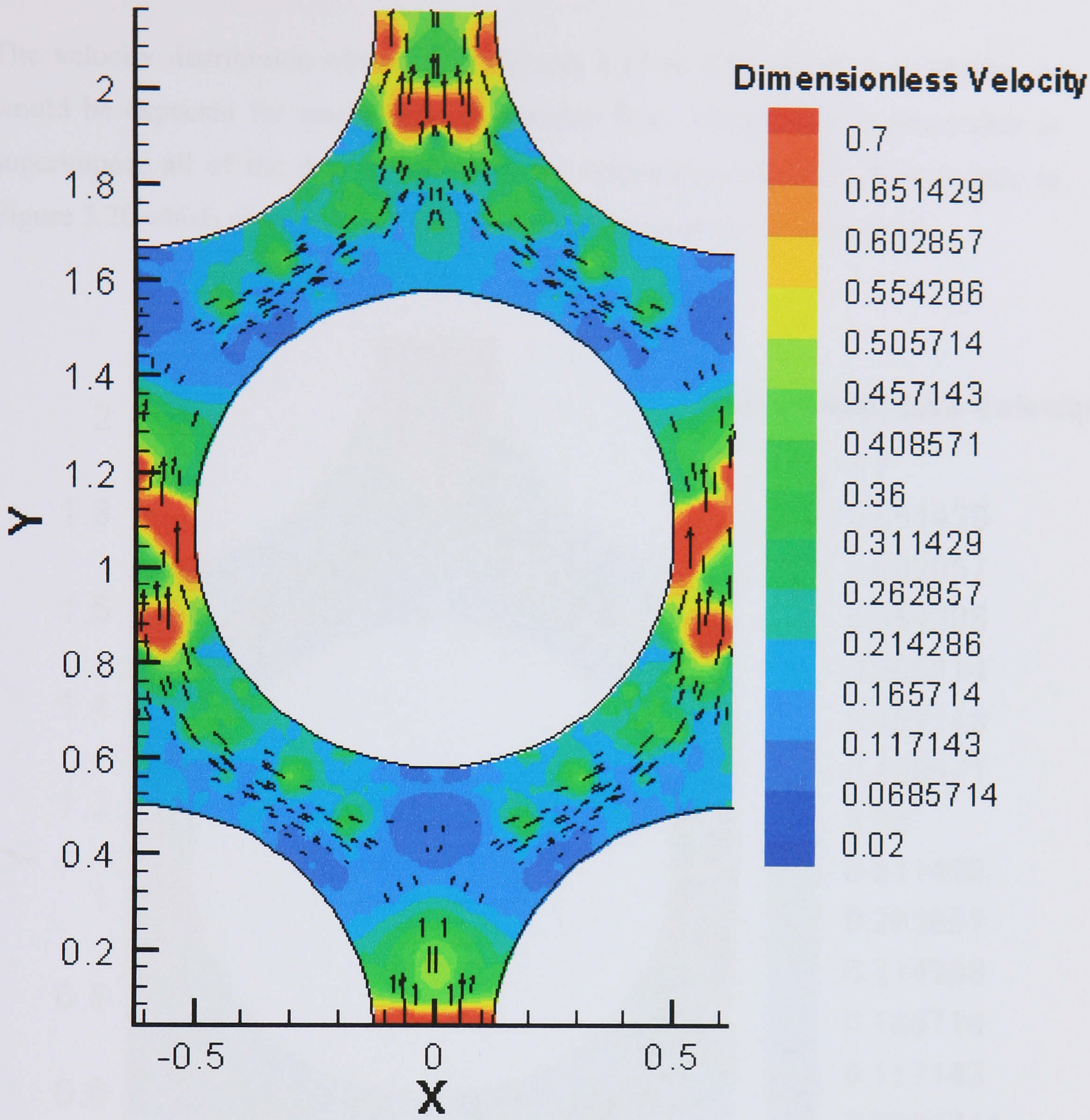


Figure 5.19 - Contour plot of the velocity field for a condensed data set at a global volumetric flow rate of 16cm^3/s. Each data point is plotted in all four quadrants of the unit cell.

Figures 5.17 to 5.19 help to emphasise more clearly the distribution of the velocity field. No velocity vectors are captured in the regions directly below the top cylinder or directly above the bottom cylinder. This means that the velocity within these regions is generally very low. Therefore, details on any re-circulation zones which might occur within these regions were not captured in this study. Experiments at a much smaller scale would be required to capture the velocity field within such regions and also within the boundary layer around the cylinders. However, on the present scale it can be concluded that the velocity within the boundary layer around the cylinders and also just below and just above the top and bottom cylinders respectively is very low.

The velocity distribution observed in Figures 5.17 to 5.19 are all very similar, as would be expected for small Reynolds number flow. Therefore it is permissible to superimpose all of the data to maximise the information obtained. This is done in Figure 5.20 which gives a more detailed representation of the velocity field.

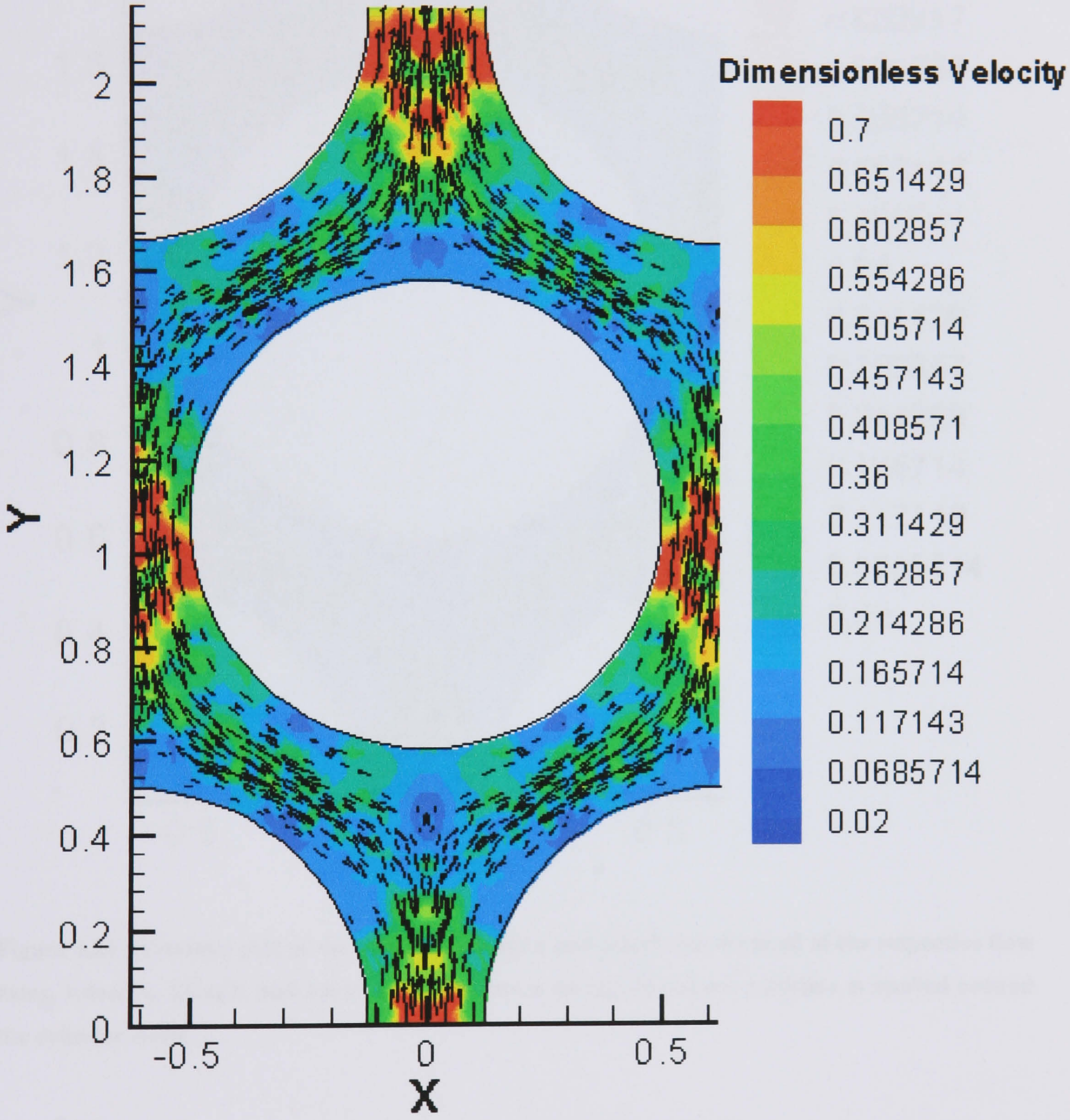


Figure 5.20 - Contour plot of the velocity field for a combined data set at all of the respective flow rates, 9.4cm^3/s, 13cm^3/s and 16cm^3/s.

Figure 5.21 shows the results of imposing a no-slip boundary condition around the cylinders in Figure 5.20. Very few particles were registered in the region near the

cylinder walls and therefore a no-slip boundary condition is legitimate. This is also consistent with the assumptions made in developing the numerical simulation code.

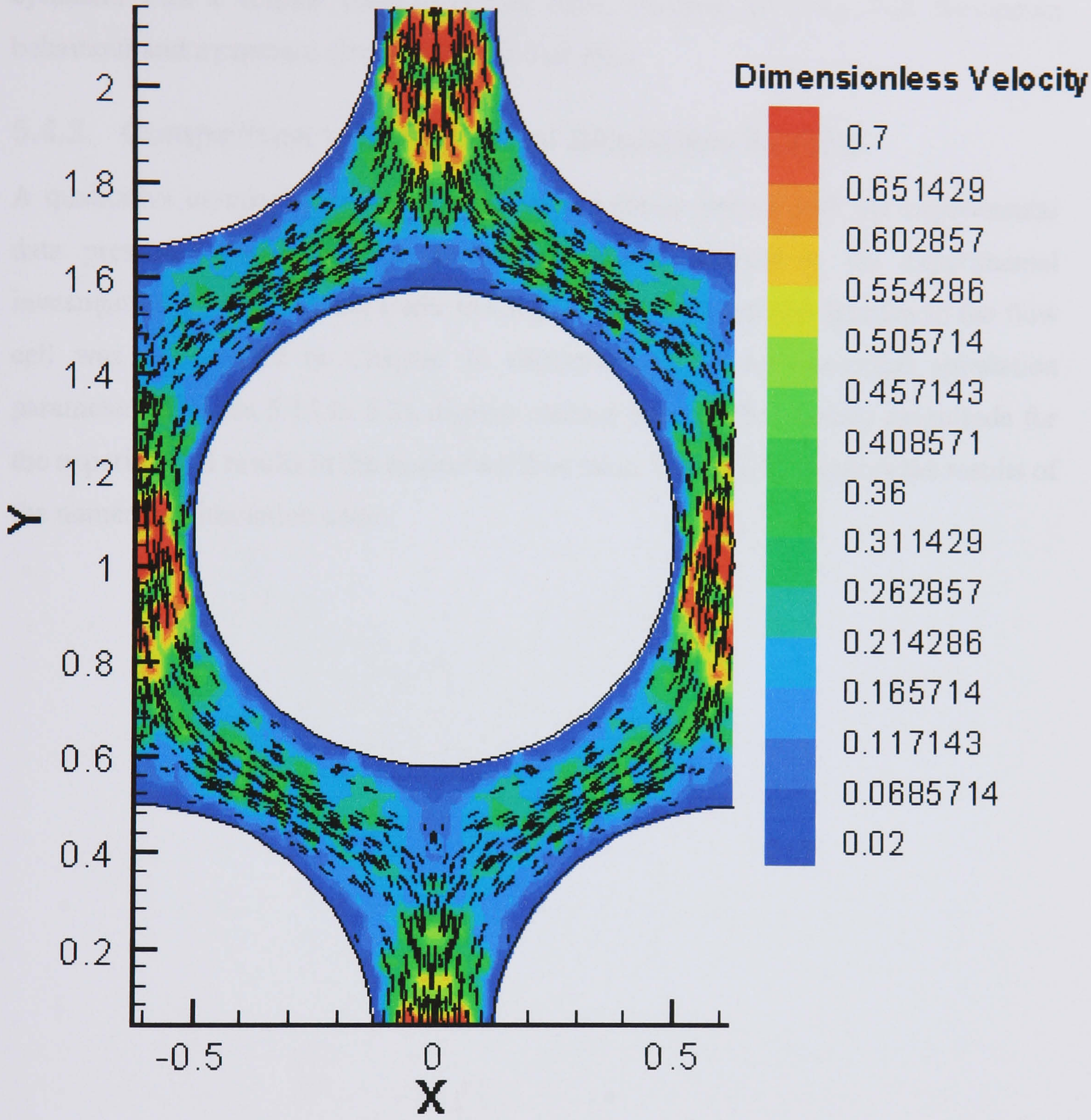


Figure 5.21 - Contour plot of the velocity field for a combined data set at all of the respective flow rates, 9.4cm^3/s, 13cm^3/s and 16cm^3/s. In this case a no-slip boundary condition is applied around the cylinder walls.

In Figure 5.21 it is observed that the low velocity boundary around the cylinders is very thin in the narrowest gap regions where the velocity field is high and widest in the areas directly above and below each cylinder where the velocity field is low.

Results obtained for the simulation code (described in section 5.2) are displayed in Figure 5.22 showing the velocity distribution for flow through a hexagonal array of cylinders with a volume fraction (V_f) of 58%, viscosity of 1Pa.s with Newtonian behaviour and a pressure drop over the cell of 1Bar.

5.4.3. Comparison with Numerical Simulation Results

A qualitative comparison of the numerical simulation results with the experimental data presented above can be made since the fluid used in the experimental investigation was Newtonian (refer to Chapter 4) and the volume fraction in the flow cell was 58% (refer to Chapter 3) corresponding to the numerical simulation parameters. Figures 5.14 to 5.21 display contour plots of the velocity magnitude for the experimental results at the respective flow rates. Figure 5.22 displays the results of the numerical simulation code.

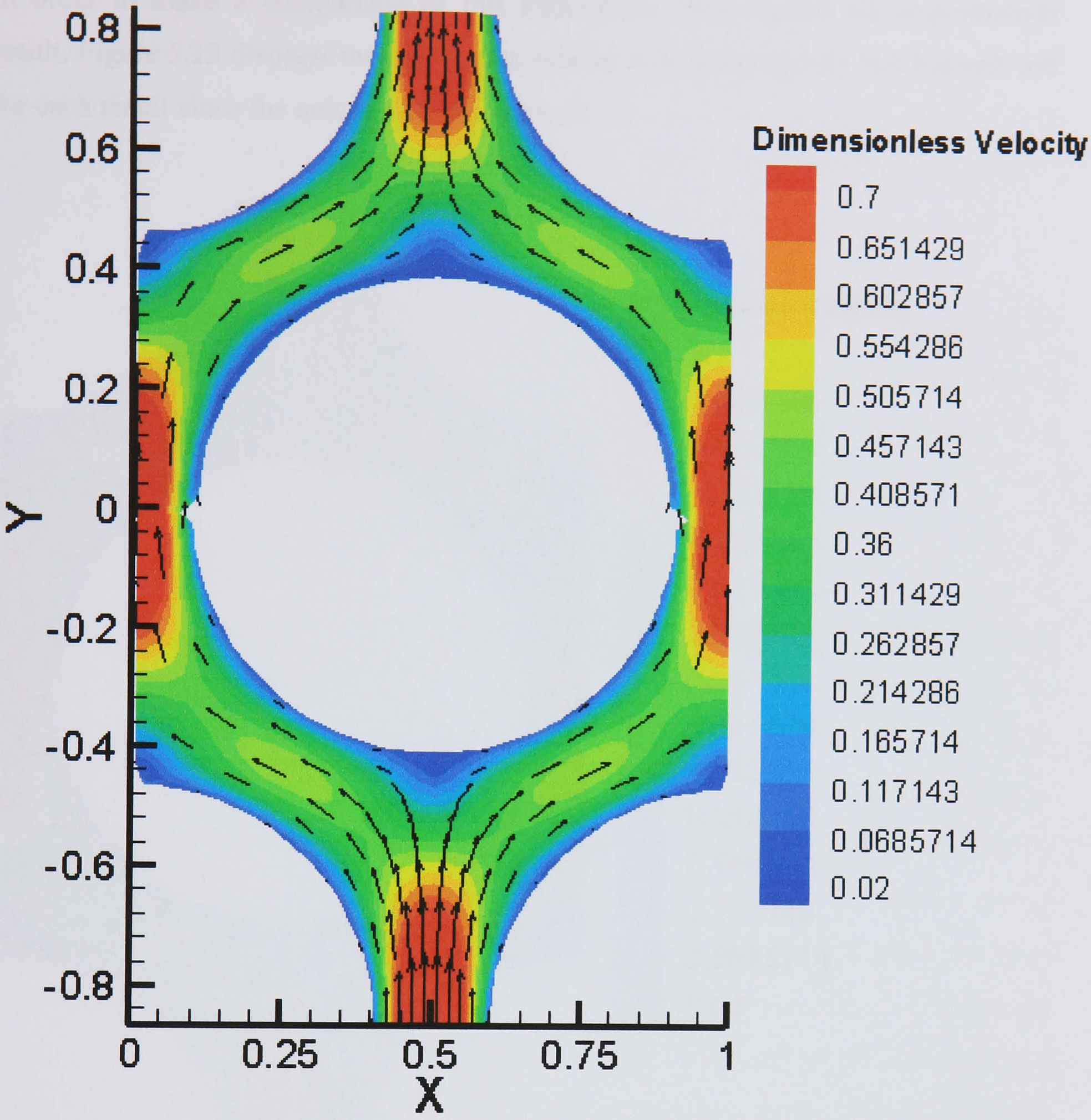


Figure 5.22 – Contour plot of the velocity field produced by the numerical simulation code[1] for the flow of a Newtonian fluid through a hexagonal array of cylinders at a volume fraction of 58%. The black arrows indicate the velocity vectors.

From Figure 5.22 it is observed that the numerical simulation code predicts the highest flow velocity in the central channel between two cylinders. Intermediate velocities are predicted within the other channels whilst very low velocity values are predicted within the boundary layers around the cylinders. Also, flow in the regions directly above and below the cylinders is estimated to be very low.

In order to make a comparison of this simulation result against the experimental result, Figure 5.23 displays the two results side by side showing only half the unit cell for each result since the unit cell is symmetrical.

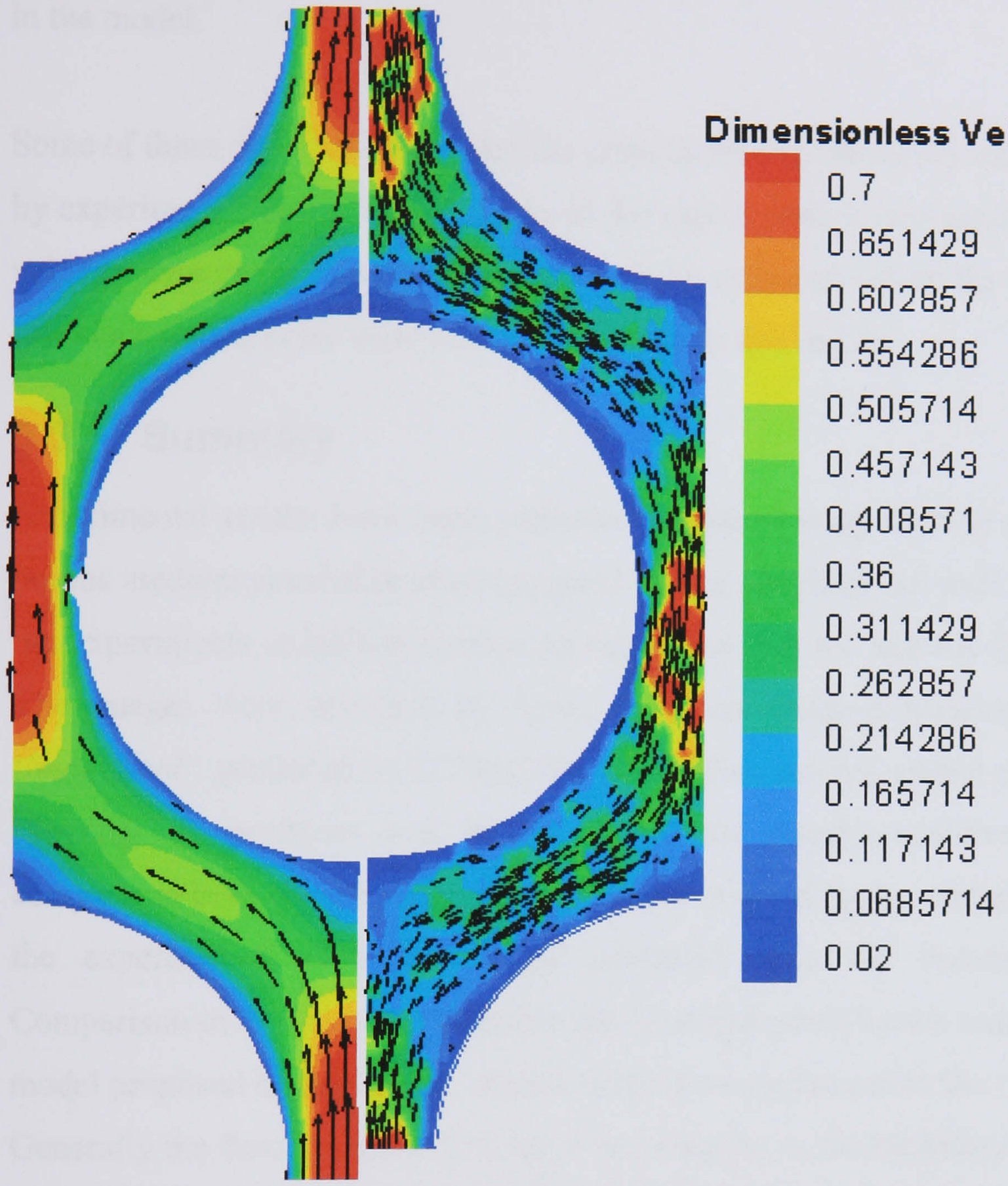


Figure 5.23 – Comparison of the contour plot of the velocity field produced by the numerical simulation code[1] on the left and the experimental result of the velocity field within the flow cell on the right.

Generally the results of the numerical simulation code agree to a large extent with the experimental results. Good agreement is seen in the regions of the highest velocity. Also, agreement is observed in predicting a very low velocity within the boundary layer around the cylinders. The general trajectory of the velocity vectors in the experimental results and model results show close agreement. However, variation between the experiments and the model is observed in the size of the highest velocity

region. Although close agreement is observed in the location of this region the model results predict this region to be much larger in length than observed in the experimental results. Also, the thickness of the low velocity boundary layer around the cylinders is observed to be slightly larger in the experimental measurements than in the model.

Some of these differences between the experiment and the model can be accounted for by experimental errors. For example, in the experiments it was very difficult to obtain velocity data in the boundary layer around the cylinders where the velocity was very low since the particles were not clearly visible in this region.

5.5. Summary

Experimental results have been presented for the velocity field in a saturated model porous medium consisting of a hexagonal matrix of cylindrical rods. The fluid used in the experiments exhibited Newtonian behaviour and the volume fraction was 58%. The images were analysed by hand, using an image-processing package called '*ImageTool*', produced by UTHSCSA. A two-dimensional scatter plot was produced showing the positions and lengths of all the streaks measured. This allowed comparison between the digitised data and the original image, and ultimately between the experimental plots and those generated from the numerical simulations. Comparison of experimental results with those generated by the numerical simulation model proposed by Spelt et al.[1] shows fairly close agreement in the velocity field data. Generally the flow is observed to be of low velocity in the boundary layer close to the cylinder surfaces and of highest magnitude in the central region of the unit cell (see Figure 5.6 for unit cell). Close agreement was also observed between the experimental and model results in the trajectory of the velocity vectors within the flow field.

However, deviations between the model and experimental measurements were observed in the size of the maximum velocity regions with the model predicting this area to be much larger in length than observed in the experimental studies. Further deviations were found in the magnitude of the velocity within the other flow channels of the unit cell. The model generally predicted the magnitude of the velocity within these channels to be much larger than observed in the experimental studies. Also, the thickness of the boundary layer around the cylinders was observed to be slightly

larger in the experimental studies than predicted by the model. Some of these deviations are believed to be due to experimental errors in obtaining the velocity field data.

5.6. References

[1] Spelt, P.D.M., Selerland, T., Lawrence, C.J., Lee, P.D., "Flow of Inelastic Non-Newtonian Fluids Through Arrays of Aligned Cylinders. Part 1. Creeping Flow", Submitted to Journal of Fluid Mechanics (2003).

[2] Reeves, M., Garner, C.P., Dent J.C., Halliwell, N.A., "Particle Image Velocimetry Analysis of IC Engine In-Cylinder Flows", Optics and Lasers in Engineering, **25**, 415-432, (1996).

[3] Soria, J., "An Investigation of the Near Wake of a Cylinder Using a Video-Based Digital Cross-Correlation Particle Image Velocimetry Technique", Experimental Thermal and Fluid Science, **12**, 221-233, (1996).

[4] Meinhart, C.D., Wereley, S.D., Gray, M.H.B., "Volume Illumination for Two-Dimensional Particle Image Velocimetry", Meas. Sci. Technol., **11**, 809-814, (2000).

[5] Hoyt, J.W., Sellin, R.H.J., "A comparison of tracer and PIV results in visualizing water flow around a cylinder close to the surface", Experiments in Fluids, **28**, 261-265, (1995).

[6] Hu, H., Saga, T., Kobayashi T., Tanguchi N., "Research on the Vortical and Turbulent Structures in the Lobed Jet Flow using Laser Induced Fluorescence and Particle Image Velocimetry Techniques", Meas Sci Technol, **11**, 698-711, (2000).

[7] Funes-Gallanzi, M., "High accuracy measurement of unsteady flows using digital particle velocimetry" Optics and Laser Technology, **30**, 349-359, (1998).

[8] Lawson, N.J., and Wu, J., "Three-Dimensional Particle Image Velocimetry: a Low Cost 35 mm Angular Stereoscopic System for Liquid Flows", Optics and Lasers in Engineering, **32**, 1-19, (1999).

[9] Davis, J.C., "Statistics and Data Analysis in Geology", 2nd Edition, John Wiley & Sons, New York, (1986).

6. FLOW FRONT TRACKING

Results for the micro-scale flow front tracking experiments are reported in this chapter. Experiments were carried out for flow through a hexagonal rod arrangement in the flow cell described in Chapter 3. Additionally, results are presented for the contact angle and surface tension of the respective liquids and surfaces.

6.1. Fundamentals of Flow Modelling

An understanding of the filling stage of the resin into the fibre preform is an important aspect of RTM simulations. The modelling approach that is extensively used for this assumes that the flow of resin through a fibrous preform is equivalent to that of an incompressible fluid through a porous medium. Therefore the physics of the fill phase during RTM is based on in-plane incompressible mass conservation and uses Darcy's law[1] as a momentum balance. The equation of mass conservation for the fluid phase can be written as:

$$\nabla.\vec{u} = 0 \qquad [6.1]$$

where $\vec{u}$ is the superficial fluid velocity vector. The general form of Darcy's law can be stated as follows,

$$\vec{u} = -\frac{1}{\mu}[K].\nabla P \qquad [6.2]$$

where *[K]* is the permeability tensor and *P* is the pressure. This equation relates the components of superficial fluid velocity vector to the associated pressure gradients parallel to the coordinate axes and can be applied to Newtonian fluids, given that inertia and gravity effects are ignored. A combination of Darcy's law with the equation for mass conservation forms the basis for flow simulation of RTM and leads to the governing partial differential equation for the pressure field in the resin saturated domain and can be solved either numerically or explicitly, depending on the complexity of the mould geometry and injection strategy. The pressure field is then differentiated and Darcy's law is applied to obtain the fluid velocities from which the flow front position can be determined at any time during the injection phase.

However, Amico and Lekakou[2] stated that over the years the validity and applicability of Darcy's law has been questioned by many authors. For example Visconti et al.[3] identified differences in the measured permeability brought about by changes in injection pressure. Gauvin et al.[4] suggested that the flow rate, pressure and the nature of the fluid are among the factors that could strongly influence the permeability measurements. Griffin et al.[5] and Steenkamer et al.[6] found different permeability values depending on the infiltrating fluid. Despite these and other findings, Darcy's Law is still by far the most widely used flow model and, as mentioned by Parnas et al.[7], many of these discrepancies may be due to neglecting the effects of microscopic flow phenomena on the interpretation of the macroscopic flow. Since then various alternative governing equations or modified methods have been used to improve on Darcy's Law. But there are also other factors such as surface tension of the fluid, surface effects and wetting of the porous medium that would have a significant contribution to the flow behaviour and finally affect the accuracy of the permeability measurement. The following section looks into these factors in more depth.

6.1.1. Surface Tension and Contact Angle

One of the limitations of liquid moulding processes is the relatively short length of time between the macroscopic impregnation of the preform and the rapid viscosity rise which accompanies the curing reaction. As a consequence, the time available for fibre wetting and development of a strong fibre-matrix interface is limited, making the understanding of the wetting process important to prevent a reduction of the mechanical performance of the composite. However, it is important to note that the

relatively short length of time available for impregnation would have a more significant effect on the porosity.

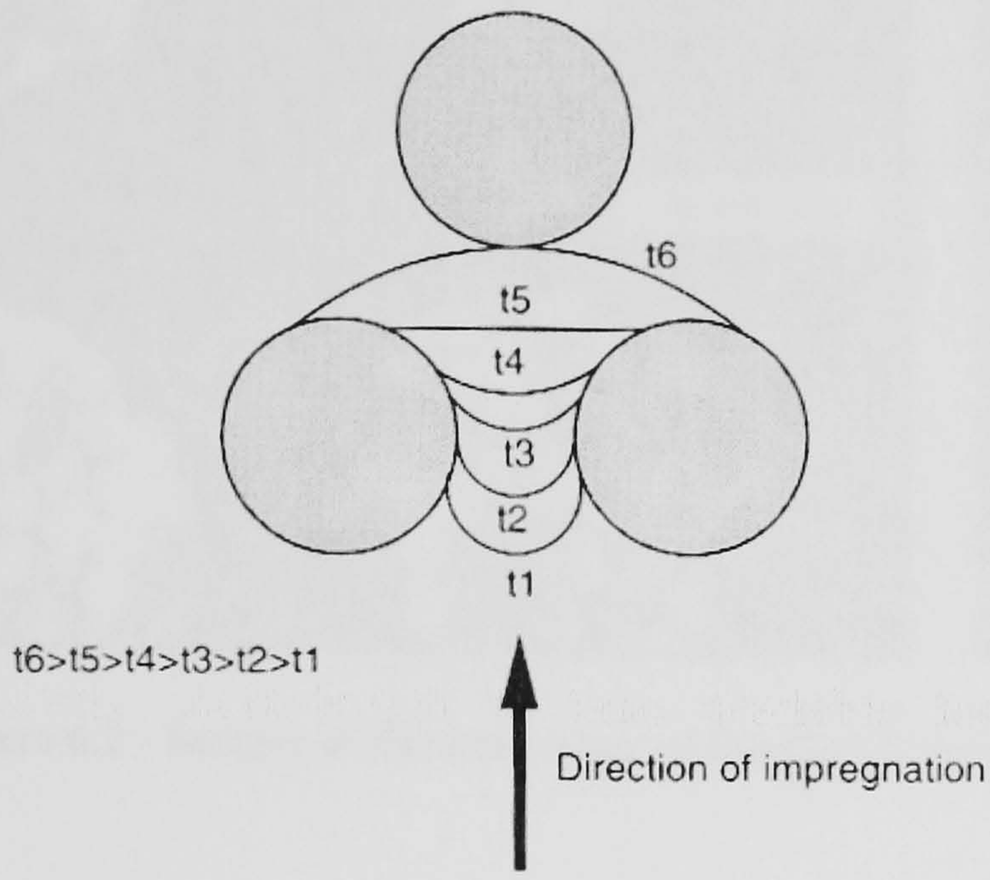


Figure 6.1 – Stages in the wetting-out of an array of cylinders by capillary flow due to surface tension[8] (*t* is time).

The wetting of the individual fibres is influenced by the surface energy of resins and fibres and is particularly important in high fibre volume fraction structures where capillary flow is an important impregnation mechanism. A useful indication of the degree of wettability of the fibres is provided by the contact angle. As the liquid wets the fibres, a concave meniscus is formed and the wetting front starts to move inwards to minimize surface energy. Under the influence of surface tension the resin continues to move inwards until the meniscus is flat and no pressure differential exists across the liquid surface, this is demonstrated in Figure 6.1.

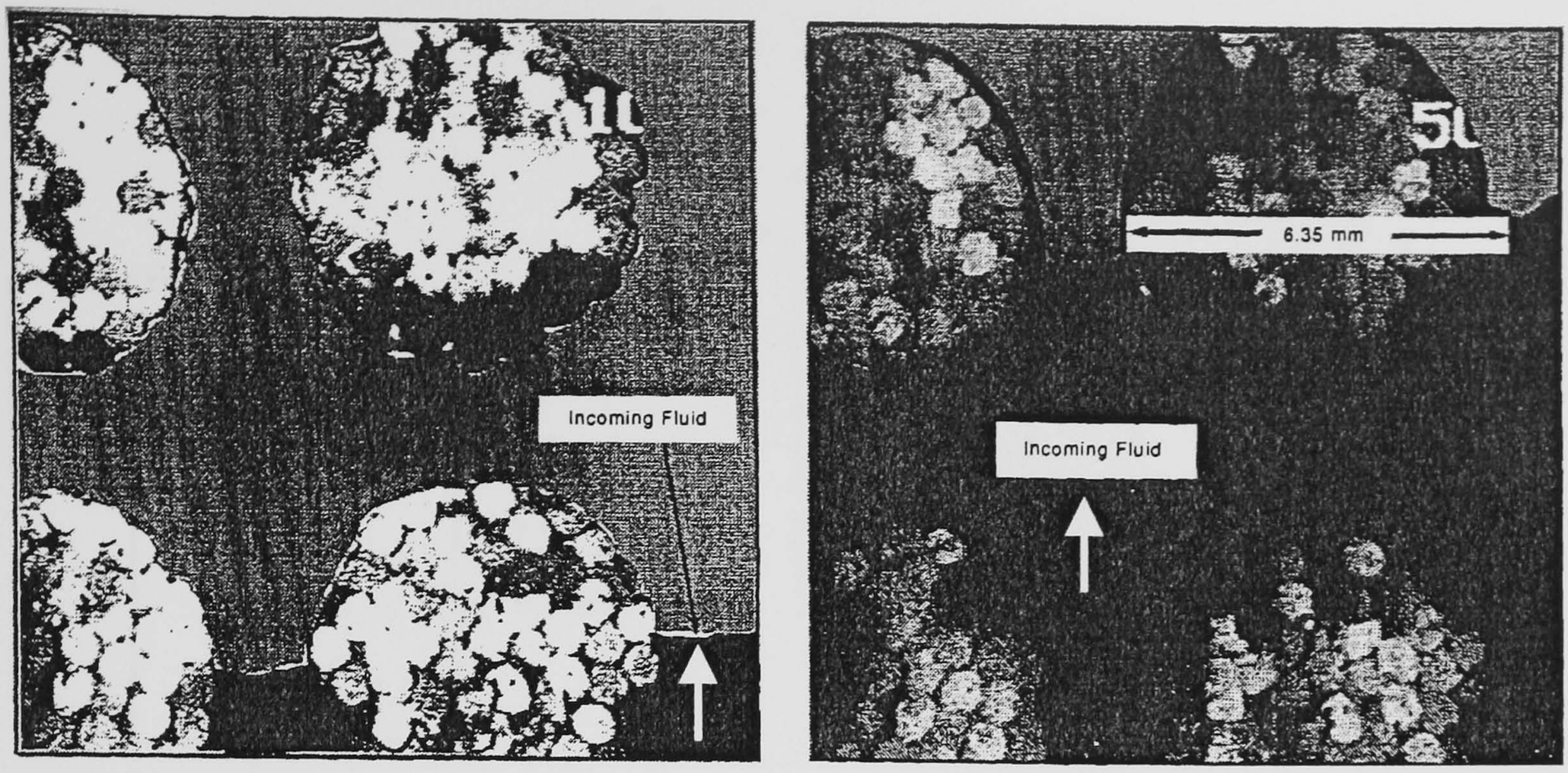


Figure 6.2 - Images of the behaviour of the flow front during filling[9].

Very limited previous work has been done in looking at the behaviour of the flow front but Sadiq et al.[9] have constructed a flow cell with a square array of fibre bundles, which consisted of numerous 0.07cm diameter nylon fibres, to capture a series of images of the flow front. As shown in Figure 6.2, the quality of the images is low and few quantitative results were extracted from them to discuss in the paper, since the emphasis was more on the void formation phenomena inside the fibre bundle. Therefore further investigations are necessary to understand the behaviour of the flow front and quantify the effect of contact angle as the front progresses through the array.

Figure 6.3 shows a schematic diagram of the experimental set-up used to obtain the results. Further details of the experimental procedure are given in Chapter 3.

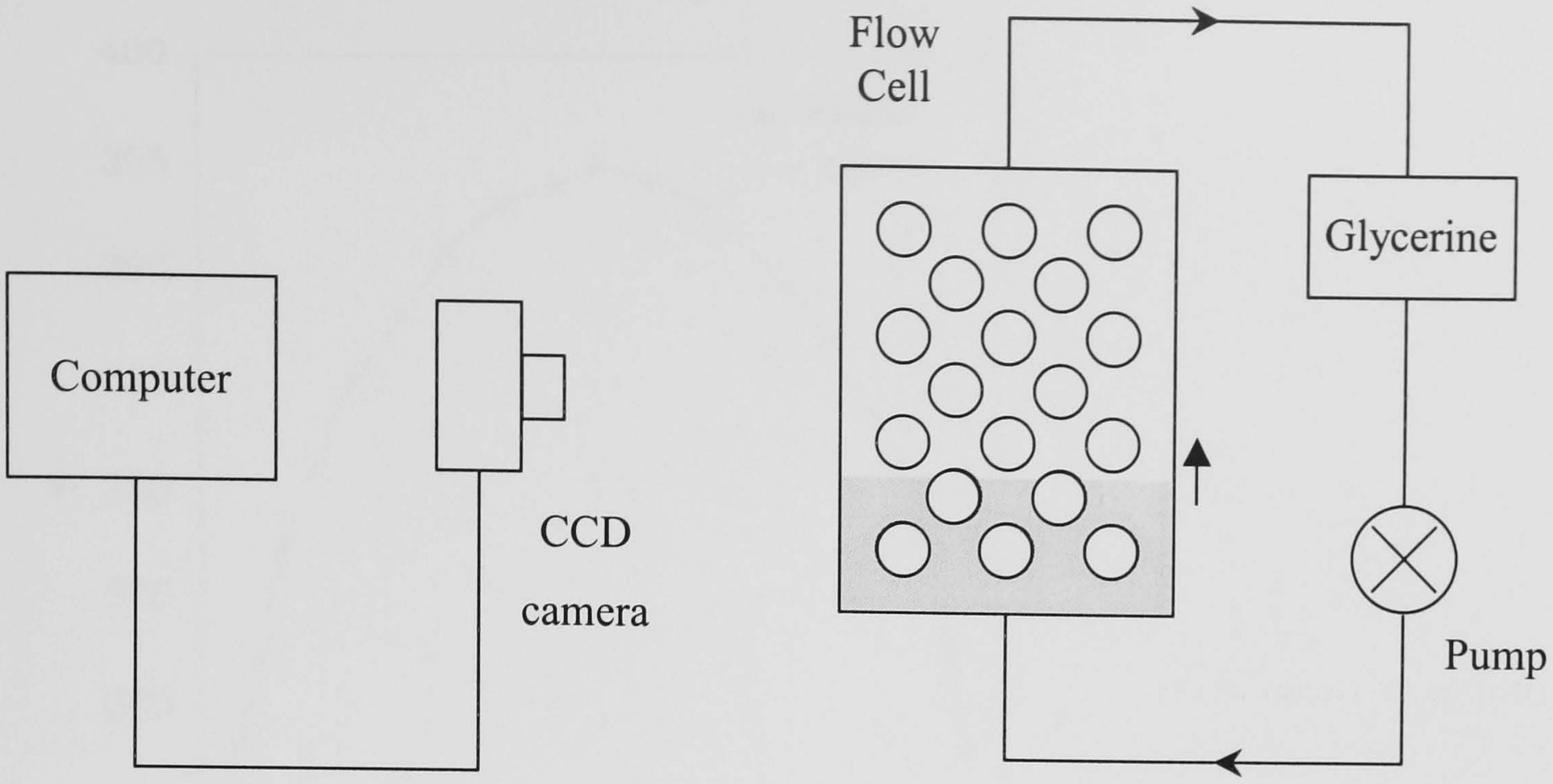


Figure 6.3 - Schematic diagram of flow front tracking set-up.

6.2. Contact Angle Measurement

Because the surfaces and fluids used in the micro-scale experimental investigation were different from those in industrial scale RTM, it was necessary to quantify the differences in contact angle and surface tension of the different systems. In these micro-scale flow front tracking experiments, glycerine fluid was observed flowing in a Perspex flow cell. However, in the near industrial scale *SMARTweave* front tracking simulations (presented in Chapter 7), a model fluid (corn syrup) was observed flowing through a glass fibre preform. In real RTM applications however, a resin (in this case Derakane 411-C50) flows through a glass/carbon fibre preform. The respective results are presented in this and the following section.

The positions of the droplet and surface were quantified in *x*-*y* coordinates, as shown in Figure 6.4, and the points fitted with polynomials to evaluate the contact angle. The results for the average contact angle of glycerine fluid on a Perspex surface are listed in Table 6.1 and demonstrated in Figures 6.5a and 6.5b. These results are averaged from a series of 10 experiments. The equilibrium contact angle and the advancing/receding contact angles were measured on horizontal and inclined surfaces respectively.

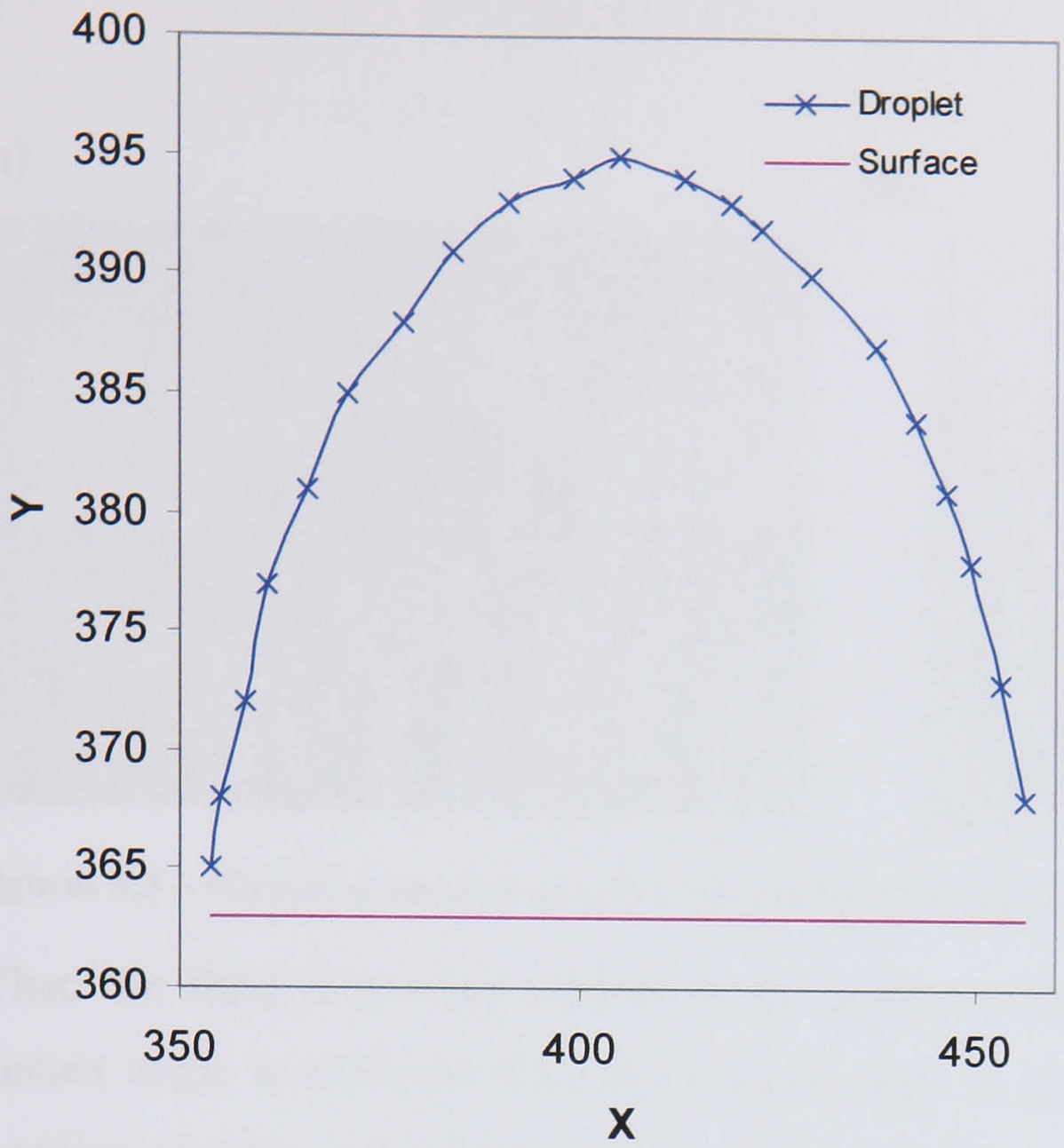
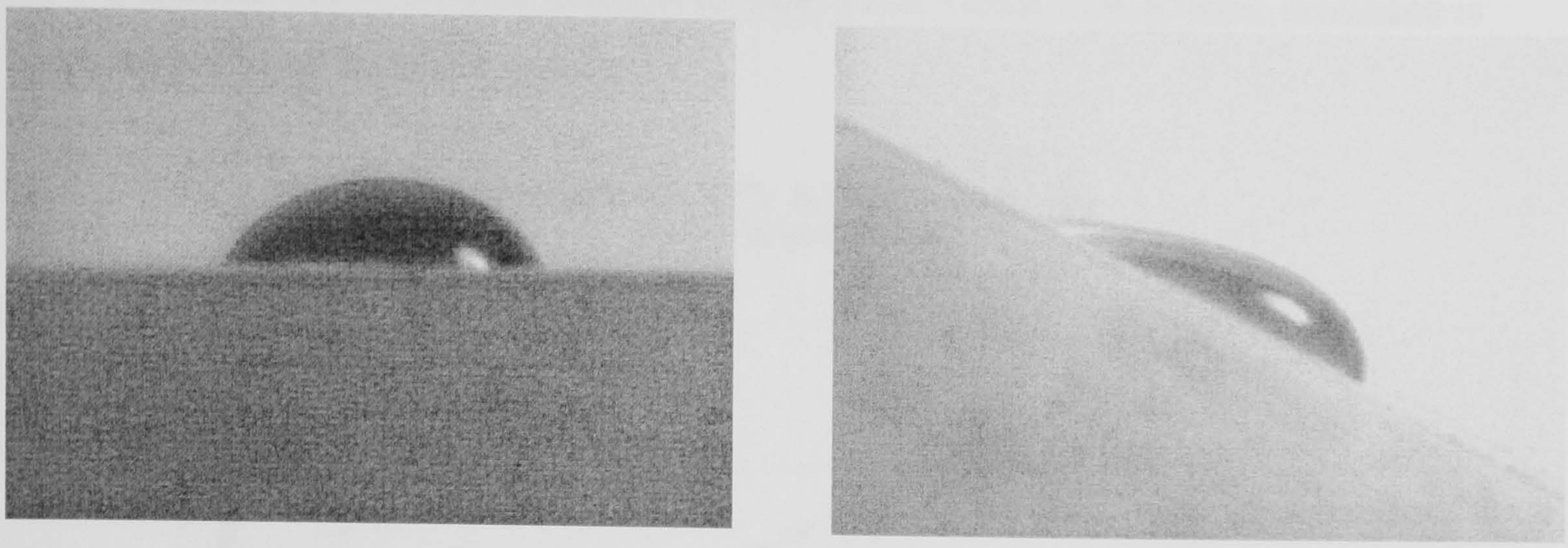


Figure 6.4 – Illustration of the image analysis technique showing the position of the glycerine droplet relative to the Perspex surface in *x*-*y* coordinates.

Table 6.1 – Contact angle of glycerine on a Perspex surface.

	Average Contact Angles (°)	
	Left	**Right**
Horizontal Surface	61 (equilibrium)	64 (equilibrium)
Inclined at point of slipping (surface inclination = 30°)	23 (receding)	77 (advancing)



Figures 6.5 – Glycerine droplet on a flat (a) and inclined (b) Perspex surface.

When the fluid is moving relative to the solid, as occurs during impregnation, the contact angle is different from the contact angle at equilibrium. The advancing and receding contact angles are very important in the impregnation stage of RTM.

Using the same technique as above the average equilibrium contact angles of corn syrup and Derakane 411-C50 on glass fabric were determined and are summarised in Table 6.2.

Table 6.2 – Average equilibrium contact angles.

Liquid/Surface	Average Equilibrium Contact Angles (°)	
	Left	Right
Corn syrup - Glass fabric	67	63
Derakane 411-C50 – Glass fabric	28	39

The results presented in Table 6.2 show that the contact angle of corn syrup on glass fibres is higher than the contact angle of Derakane 411-C50 on glass fibres, suggesting that the wetting of Derakane 411-C50 on glass fibres is better than corn syrup on glass fibres. Also, comparison of Table 6.1 and Table 6.2 suggests corn syrup on glass fabric has an equilibrium contact behaviour similar to that of glycerine on Perspex. Unfortunately it was not possible to obtain advancing/receding contact angles for the glass fibres.

6.3. Surface Tension Measurement

Surface energy changes as a system reacts. Figure 6.6 shows the surface energy of Dow Derakane 411 C-50 as a function of time under various conditions. Derakane is composed of vinyl ester and styrene.

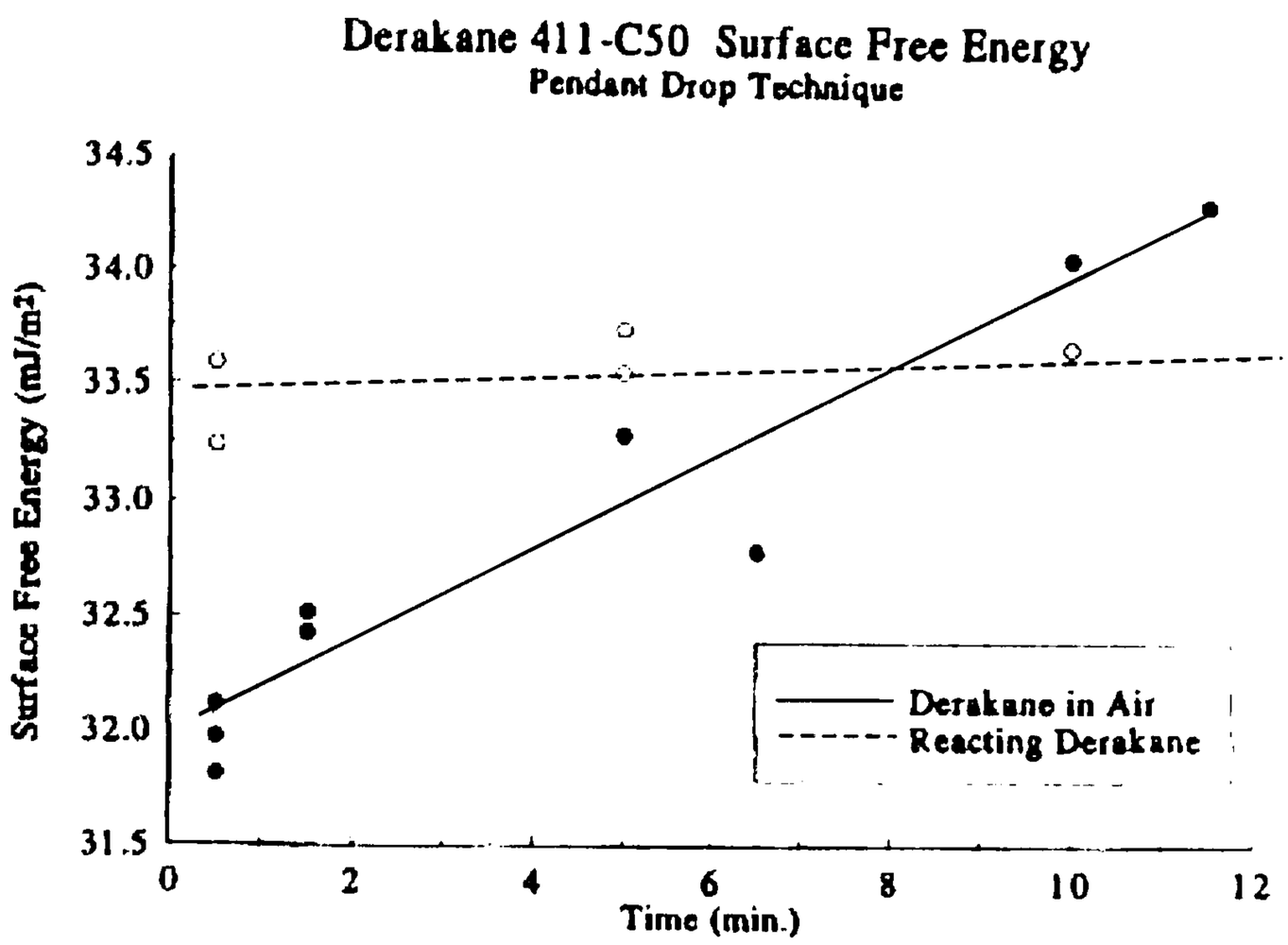


Figure 6.6 – Surface free energy of Derakane 411–C50[a].

The surface energy increases with time in the case where polymerization of Derakane is carried out under vacuum. The increasing surface energy makes it harder for the resin to wet the fibers. The reason for this increase is that the vacuum evaporates the styrene. The styrene is responsible for Derakane's fairly low surface energy. This example shows how changes in reaction environment can affect resin properties such as surface tension.

Table 6.3 shows some surface free energies for fibers. Notice the range in surface free energy value for typical reinforcements. Polyethylene fiber has very low surface energy and will not be wetted well by any of the resins typically used in RTM. Aramid is slightly better because it has more constituents on its surface.

---

[a] Source: *Intelligent Systems Laboratory*, Michigan State University, US

Table 6.3 - Surface free energy of typical reinforcing fibres[a]:

Material Surface	Free Energy (mN/m)
Carbon (intermediate modulus)	50 - 56
Carbon (high modulus)	40 - 50
Glass (bare)	55 - 65
Glass (sized)	30 - 46
Aramid	~30
Polyethylene	~22

A *KRUSS* (K10T) digital tensiometer was used to measure the surface tension for the fluids used in the experiments using the pendant drop technique.

Table 6.4 - Surface tension results.

Liquid	Surface Tension (mN/m)	Viscosity (Pa.s)
Corn syrup with 10% water	49 @ 25.7°C	0.26 @ 25.5°C
Glycerine solution with dye	59.7 @ 25°C	0.03 @ 30°C
Derakane 411-C50	33.2 @ 24.8°C	0.45 @ 25°C

The results in Table 6.4 are consistent with those presented in section 6.2. The lower value of surface tension of Derakane 411-C50 compared to corn syrup correlates with the better wetting with glass fibres.

6.4. Flow Front Tracking for a Hexagonal Array of Cylinders - Results

The behaviour of a glycerine flow front as it progressed through a hexagonal array of Perspex cylinders was observed. Figure 6.7 shows an overall image of the flow front during the filling process. The flow front is from bottom to top in each image. The different parts of the flow front are all very similar, which gives confidence when a particular part of the front is chosen as a representative of the results for further

analysis. Three flow rates were used and for each flow rate the contact angle between the cylinders and the flow front was determined at several positions during filling.

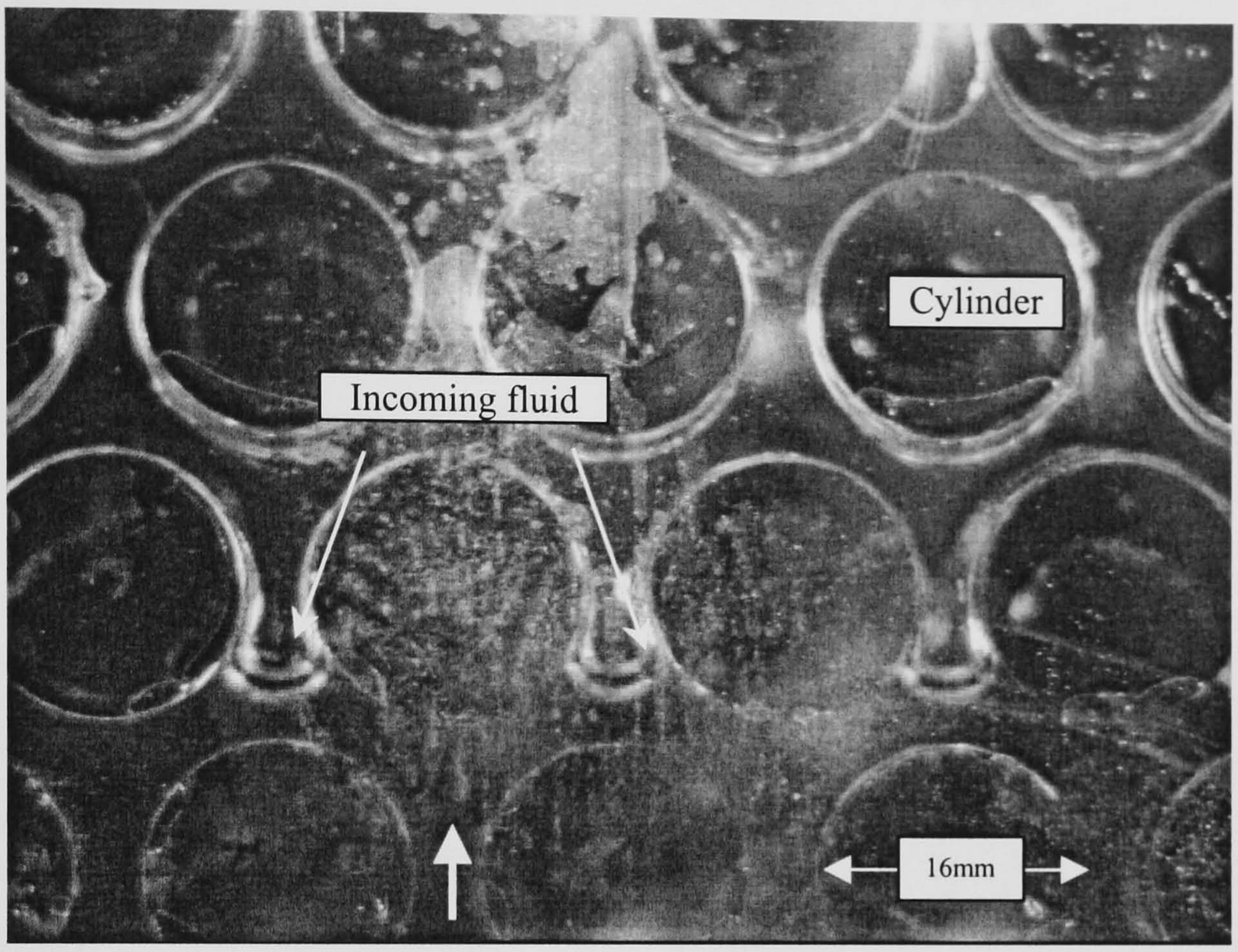


Figure 6.7 - Overall image of the flow front passing through a hexagonal array.

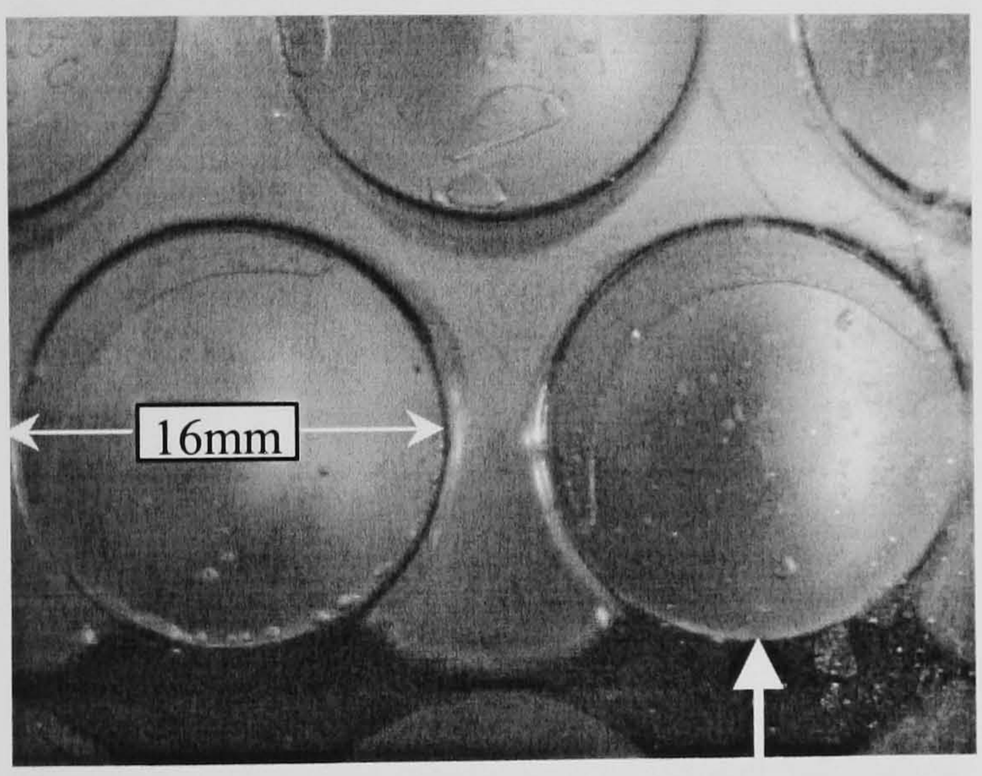
Table 6.5 summarises the velocities and Reynolds number at each respective flow rate. The superficial velocity is defined as the total volumetric flow rate divided by the total cross-sectional area. The pore velocity is defined as the total volumetric flow rate divided by the average pore cross-sectional area. The maximum velocity is the velocity within the narrowest gaps and is defined as the total volumetric flow rate divided by the minimum pore cross-sectional area. The Reynolds number is based on the superficial velocity.

Table 6.5 – Summary table of flow rates and Reynolds number.

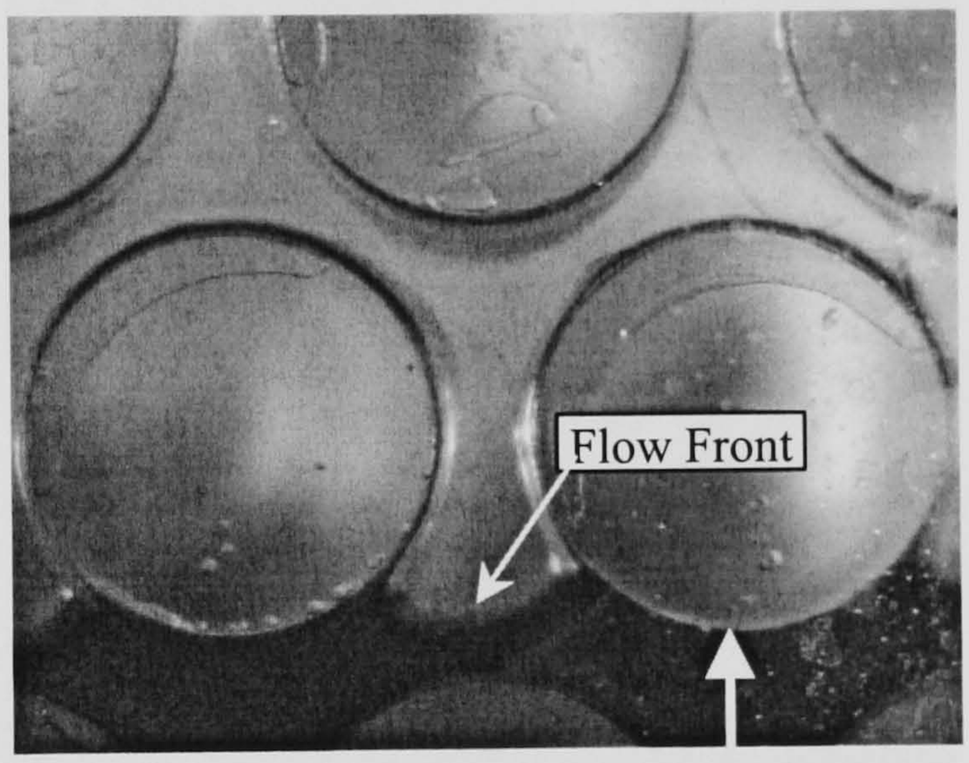
Experiment	Flow rate (cm^3/s)	Superficial Velocity (cm/s)	Pore Velocity (cm/s)	Maximum Velocity (cm/s)	$Re_{(superficial)}$
1	5.5	0.28	0.65	6.88	0.44
2	8.9	0.45	1.06	11.13	0.71
3	12.5	0.63	1.49	15.63	1

The sequence of images shown in Figure 6.8 display the flow front showing how the shape changes as it progresses through the cell.

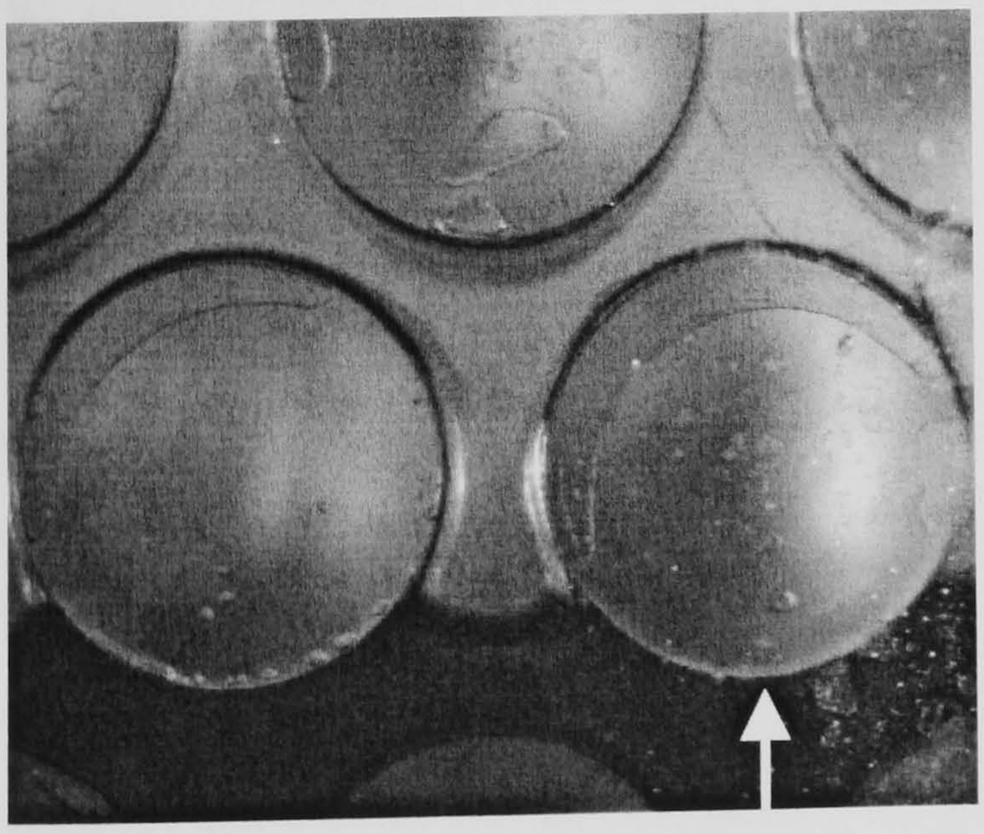
a) 0s



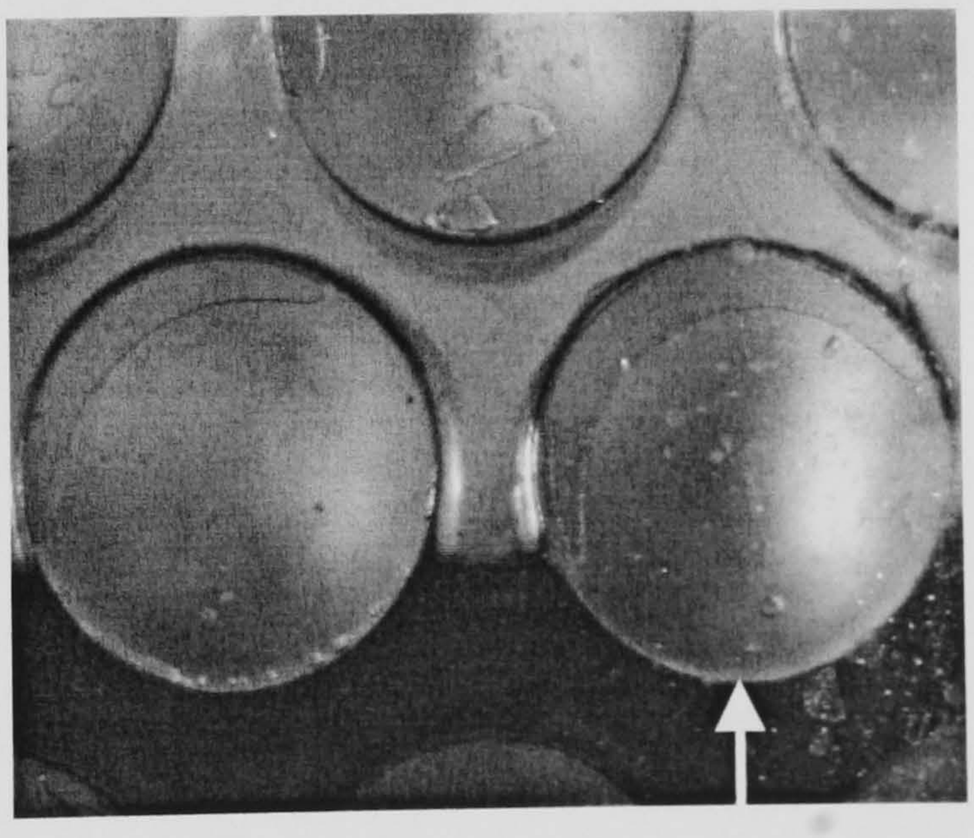
b) 0.2s



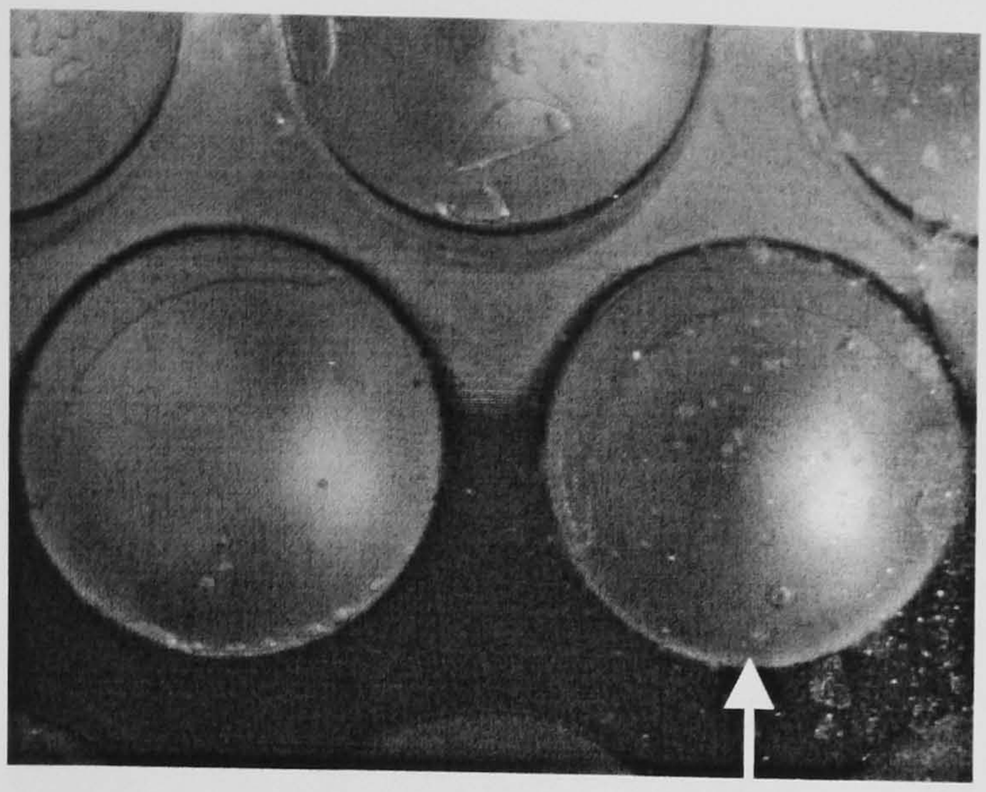
c) 0.4s



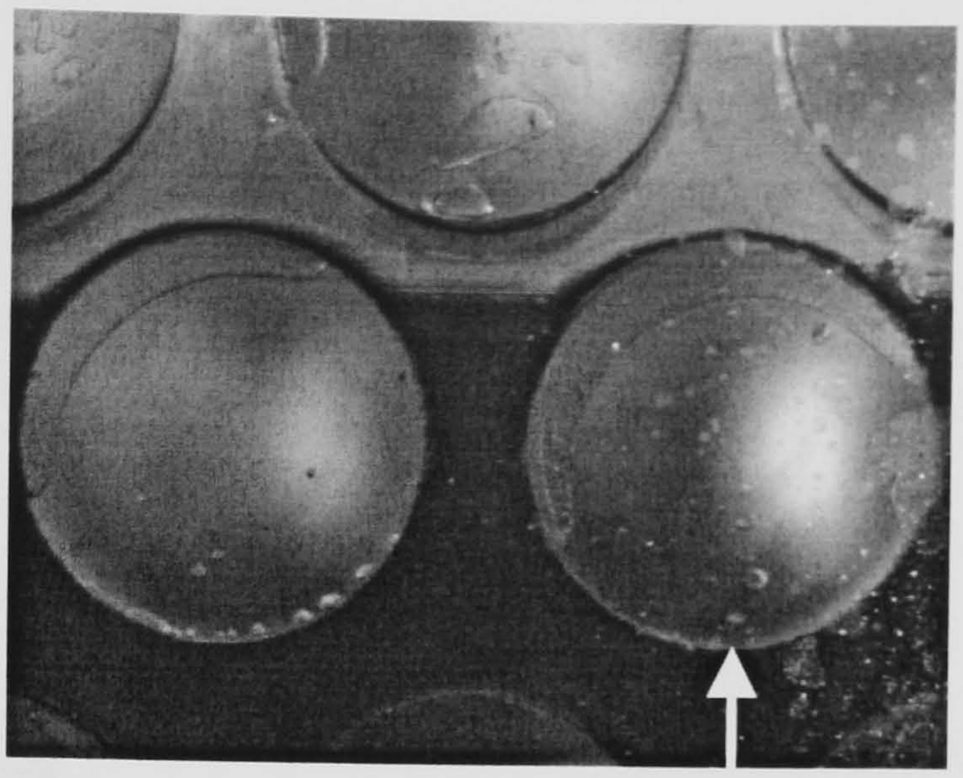
d) 0.6s



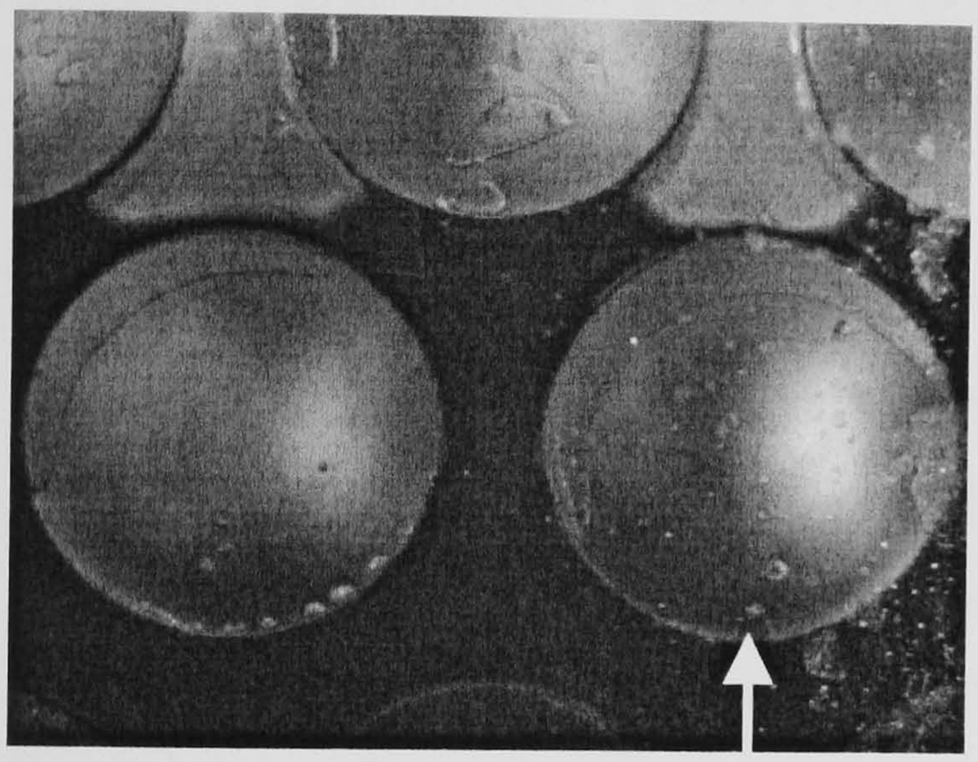
e) 0.8s



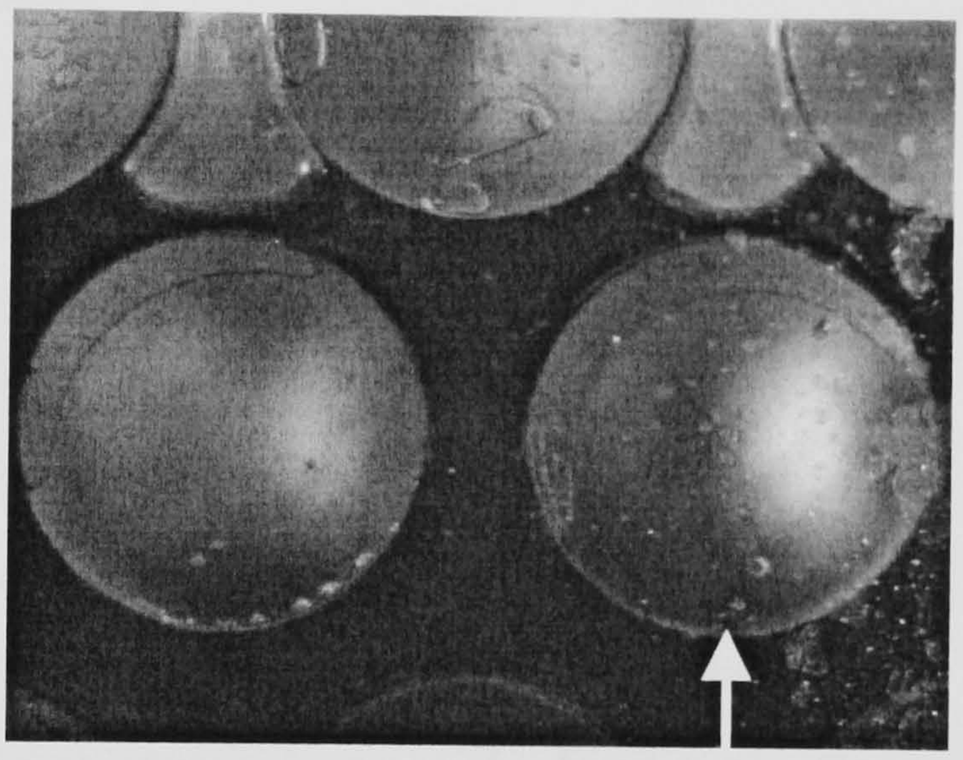
f) 1s



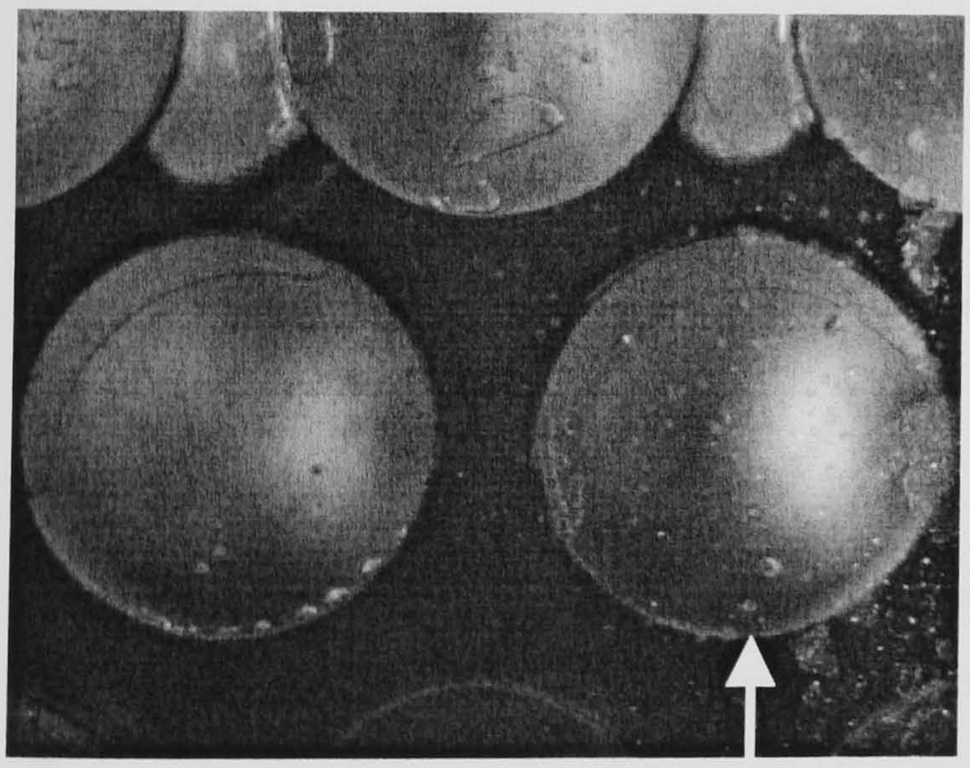
g) 1.2s



h)1.4s



i)1.6s



j) 1.8s

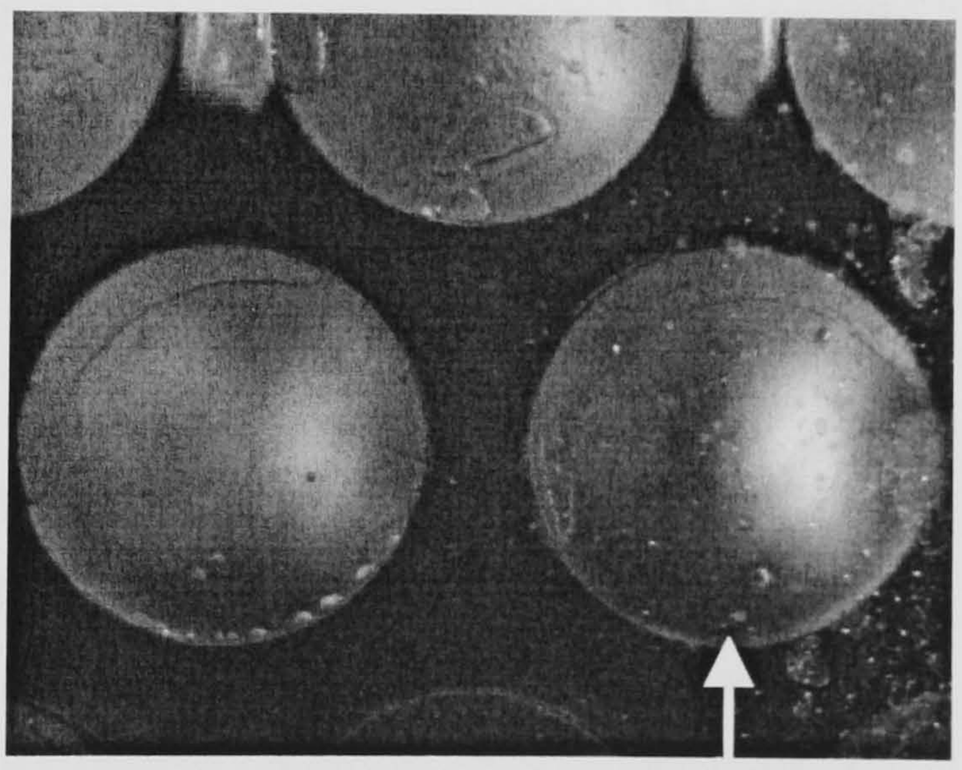


Figure 6.8(a-j) - Sequence of images of the progressing flow front at a superficial velocity of 0.45cm/s and a frame rate of 0.2s/frame.

Figure 6.9 shows a close-up of the image sequences from Figure 6.8 from 0.4s to 1s giving a clearer indication of the behaviour of the flow front as it progresses through the flow cell.

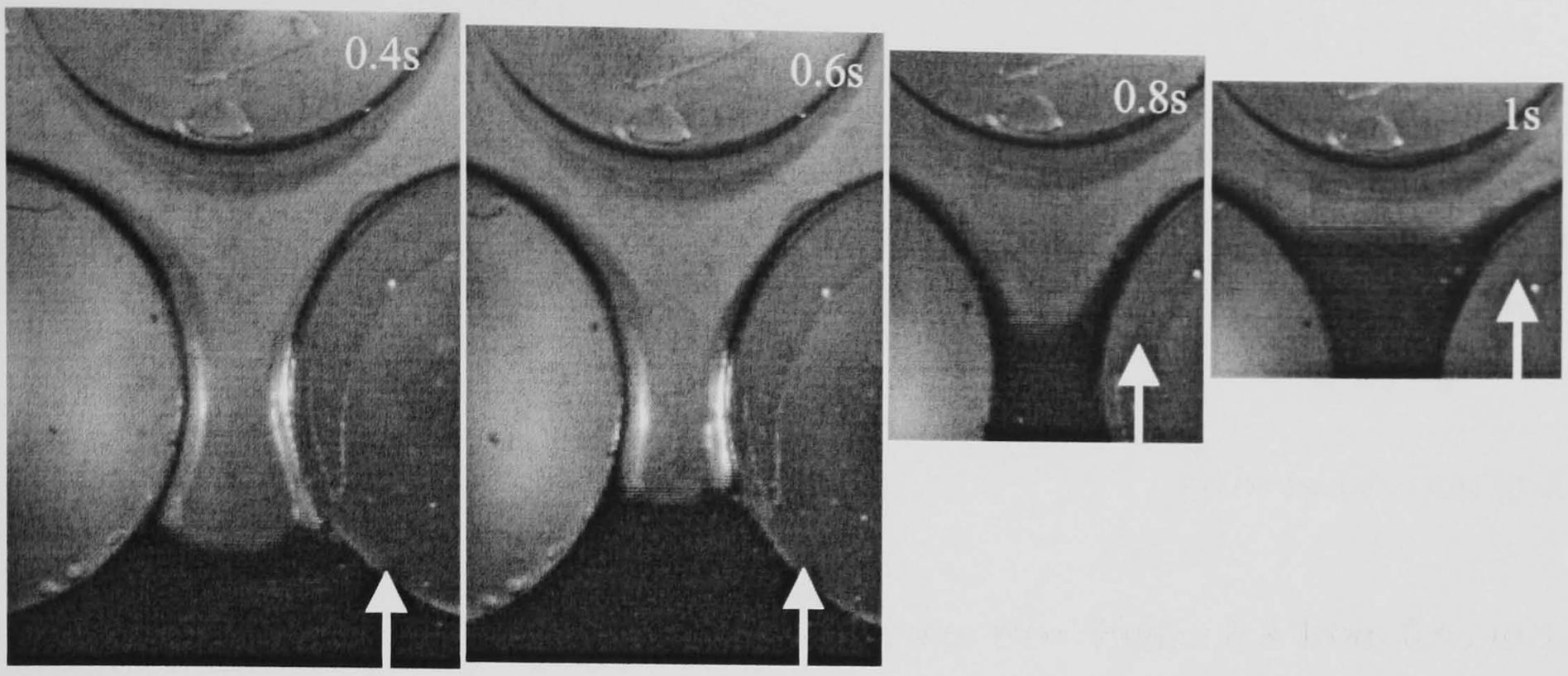


Figure 6.9 – Close-up of image sequences in Figure 6.8 from 0.4s to 1s showing more clearly the shape of the flow front.

In this example, there is a very clear indication that the shape of the flow front varies in the different stages of filling between the cylinders but generally the meniscus is concave in shape. After the front has passed the narrowest point and continues to progress through the widening gap, the front then starts to flatten out leading to a lower degree of curvature but it seems that both contact lines of the front are pulled around the cylinder surfaces stretching the front as the gap size increases. To quantify this the contact angles were determined by quantifying the position of the cylinders and the front in *x-y* coordinates using '*ImageTool*' then fitting a curve for each and hence evaluating the dynamic contact angles.

Three different sets of results at different superficial velocities (see Table 6.5) were obtained and are summarised in the three separate images shown in Figure 6.10(a-c). Since they are taken under the same frame rate, direct comparison is possible. Obviously the lower the pump speed the more flow front positions are obtained. An interesting feature is that the flow front is non-symmetrical in Figures 6.10a and b. This should not happen in the ideal situation but based on the observation during the experiment, the bottom of this flow front seemed to 'peel' off asymmetrically from the cylinder below thus causing this sideways movement of the front. The hexagonal arrangement of the cylinders played a role in this case because the bottom of the front

seems to be 'sticking' to the surface of the cylinder below for a short period of time and hence the degree of curvature is increased as a result.

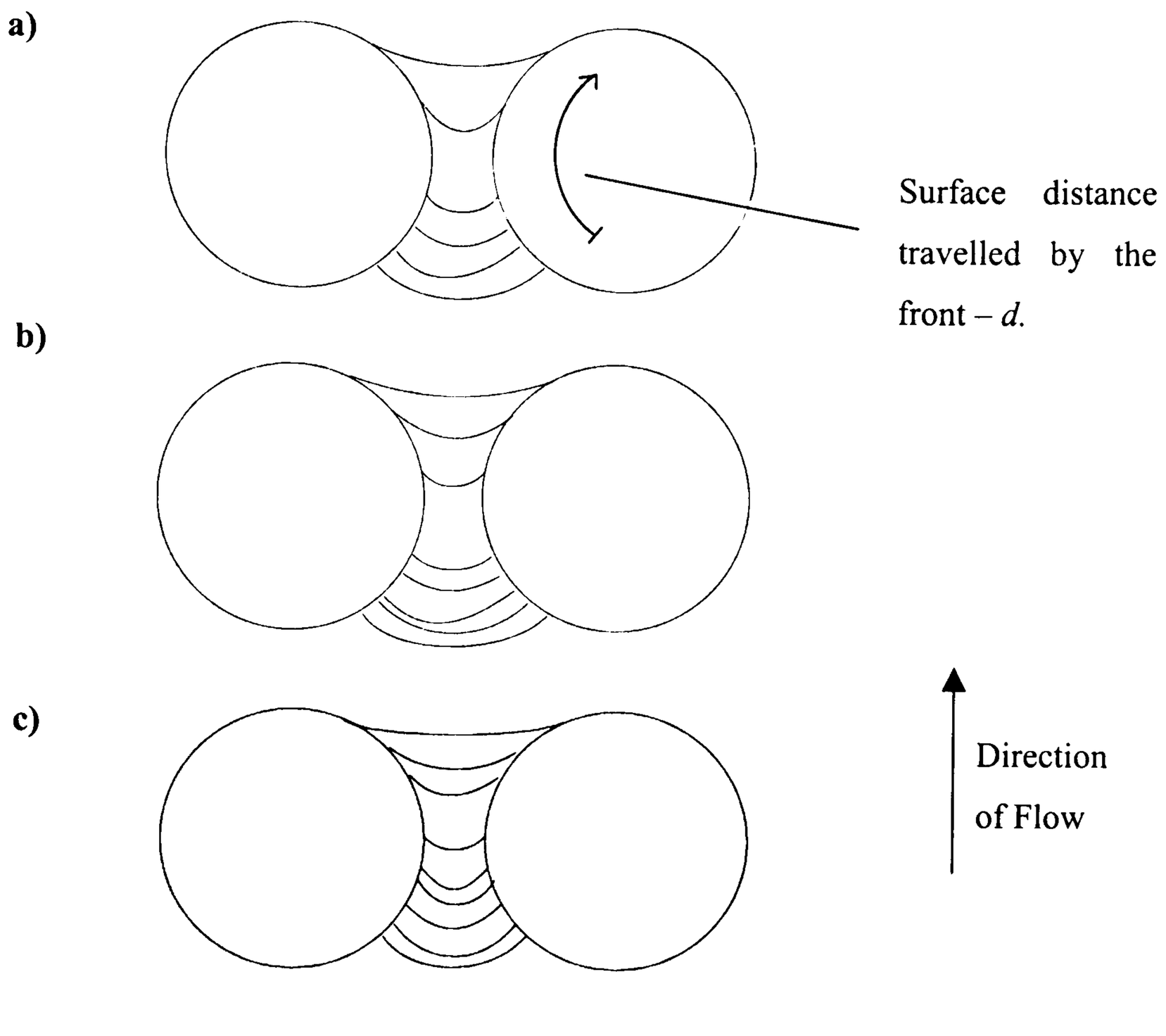


Figure 6.10(a-c) - Flow front profiles for 3 different superficial velocities (a = 0.63cm/s, b = 0.45cm/s and c = 0.28cm/s).

The dynamic contact angles are summarised in Table 6.6. There is a clear trend showing that the contact angles on both sides decrease as the flow front progresses through the gap between the two cylinders. Secondly the contact angle values between the left and the right side are consistently similar to each other, with a few non-symmetrical exceptions, indicating the flow front is generally symmetrical throughout the filling process. The bulk flow rate of the fluid is calculated based on the information from the flow front profiles since the actual dimension of the cylinders, frame rate and the functions which describe the front and the cylinders are known. Hence the area that the fluid has passed can be calculated by integrating the functions between them and then dividing by the time to give the bulk flow rate.

Table 6.6 – Listing of the contact angles between the progressing flow front and the cylinder surface.

Superficial Velocity = 0.28cm/s		Superficial Velocity = 0.45cm/s		Superficial Velocity = 0.63cm/s	
Left (°)	**Right (°)**	**Left (°)**	**Right (°)**	**Left (°)**	**Right (°)**
107.2	110.5	109.5	111.1	102.1	102.5
98.1	102.2	97.8	93.6	94.3	80.2
88.4	93.3	93.7	82.5	72.5	70.3
80.9	80.7	83.9	81.8	56.5	54.0
74.8	74.8	72.7	72.4	16.1	12.2
63.4	68.0	26.7	25.4	8.3	15.4
54.1	56.7	7.7	7.5	-	-
47.8	50.5	4.4	4.4	-	-
26.7	28.0	-	-	-	-
13.6	15.1	-	-	-	-
12.4	21.0	-	-	-	-
9.0	14.5	-	-	-	-
8.6	9.8	-	-	-	-

A graph of the contact angle versus the surface distance of the cylinder travelled by the front (d – indicated on Figure 6.10) is plotted in Figure 6.11. Generally, the contact angle decreases in a fairly linear manner as the distance increases but there seems to be a transition point appearing at the mid-section causing a change in the gradient of this line. This trend certainly suggests that the contact angle is decreasing linearly when approaching the narrowest gap and also coming out from this point, but the changes in these two regions occur at different rates.

The contact angle did not show any relationship with the flow velocity as all three curves in Figure 6.11 have a similar range of contact angles throughout the filling process. However, it is difficult to draw a definitive conclusion on this because the difference between the lowest flow rate and the highest is just over 50%. This is due to the limitation of the current set-up as it was not possible to get a higher frame rate which hindered the testing range of the flow rate. Hence the flow rate could have an effect on the flow front at a higher value.

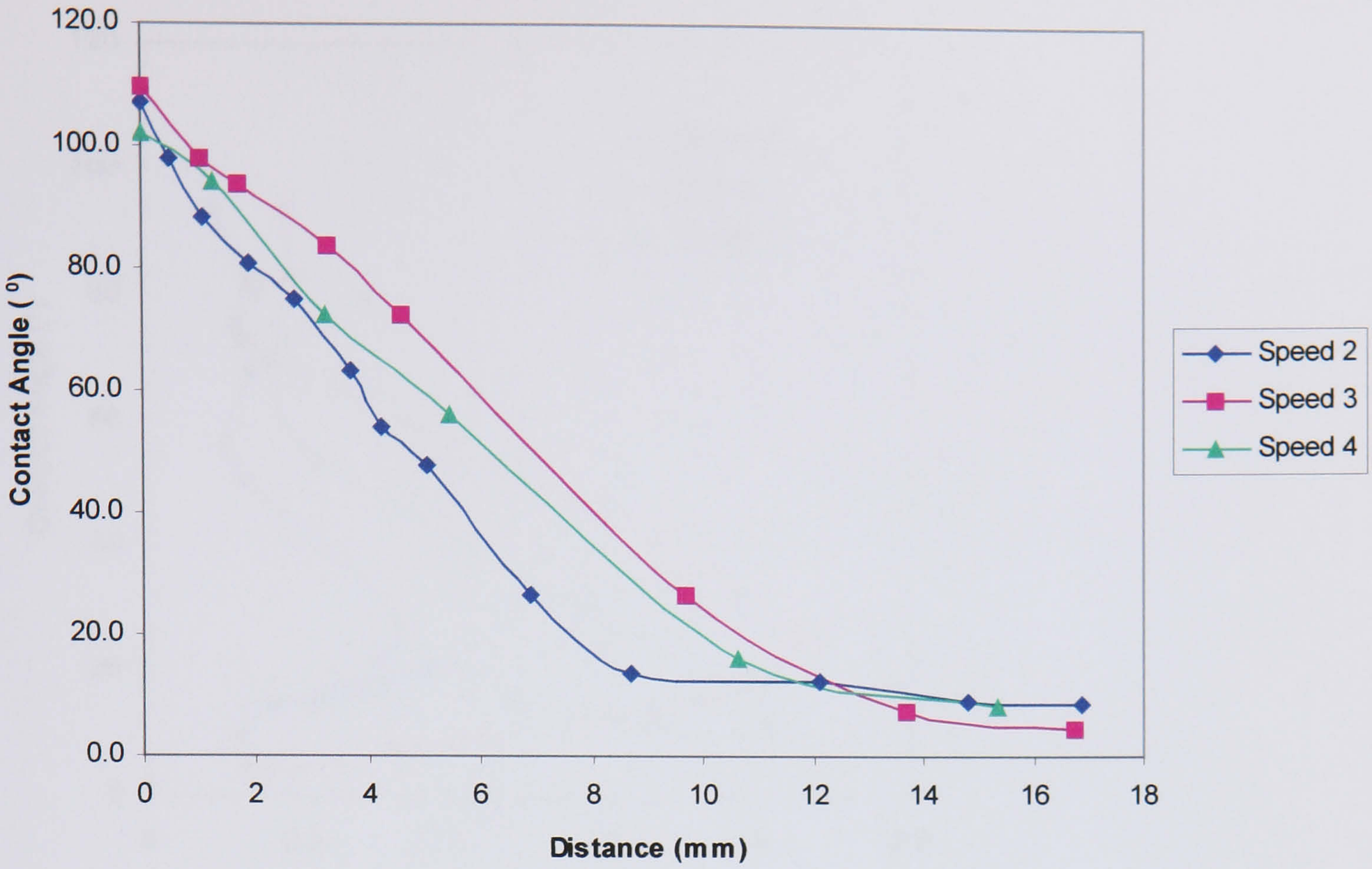


Figure 6.11 - Graph showing the average contact angle vs. the surface distance of cylinder.

Figure 6.12 shows the relationship between the contact angle and the contact line speed (U_{cl}) at each point for the three flow rates used. This relationship is consistent with the observations made above. The contact line speed generally shows little change in the region where a linear relationship occurs in the contact angle versus distance curve (Figure 6.11) and peaks at the point where a change is observed in the gradient of the contact angle versus distance curve. The highest contact line speed occurs at the point of narrowest gap.

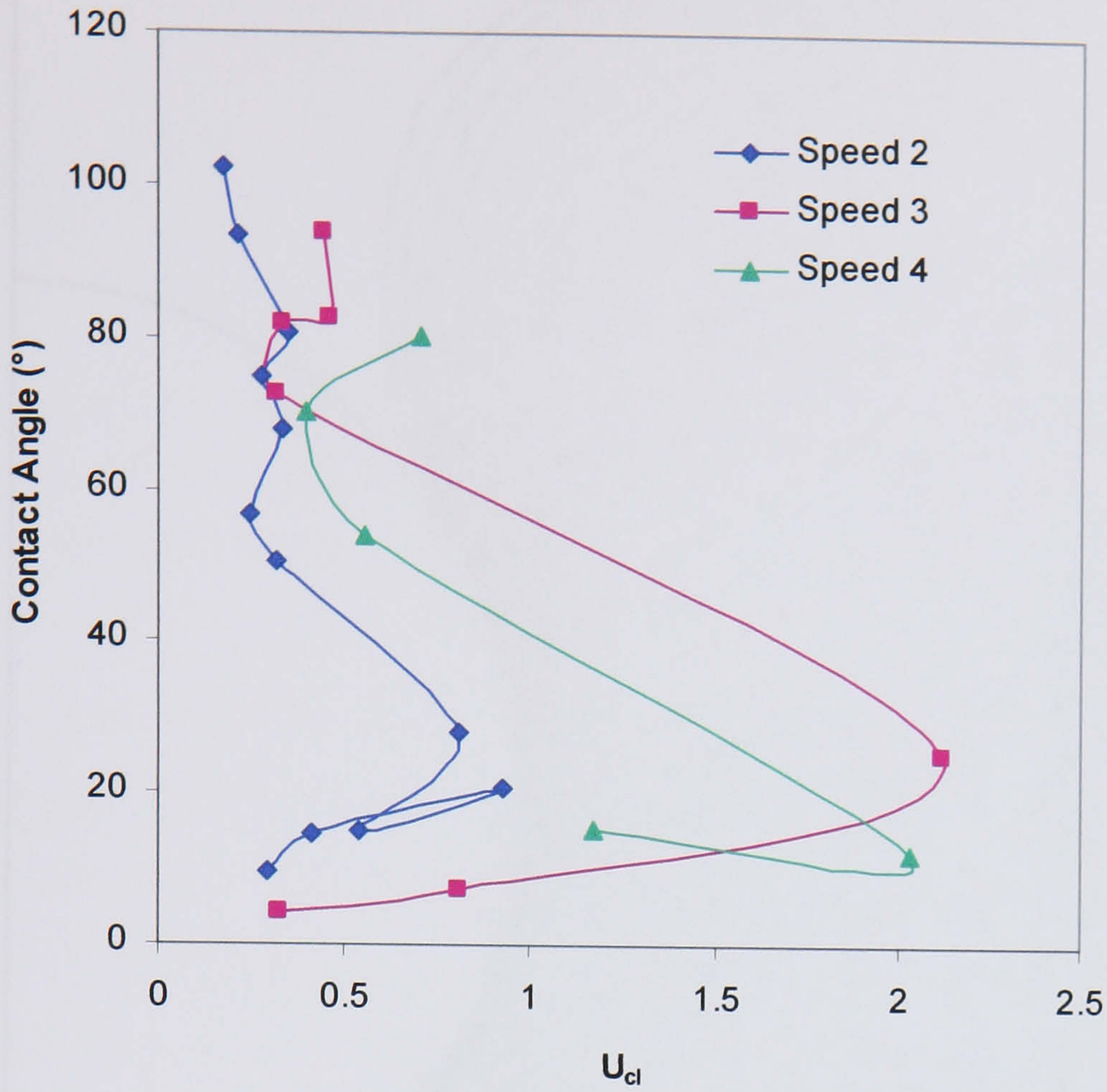


Figure 6.12 - Graph showing the contact angle vs. the contact line speed for each point (U_{cl}).

6.5. Comparison with Numerical Simulation Results

A flow front tracking simulation code has been developed by Spelt et al.[10]. In its current form, the code simulates flow through a periodic square array of cylinders as distinct from the hexagonal matrix used in the experimental studies. Even so, a qualitative comparison of these simulation results can be made with the experimental results highlighted in this chapter. Creeping flow was simulated and therefore the Reynolds number was zero, the volume fraction used was 0.3 and the Capillary Number was large (approximately 100), therefore indicating very weak surface tension effects. The simulation does not, however, account for the dynamic contact angle between the flow front and the cylinders. Figure 6.13 shows the simulation results for the profile of the flow front at different times as it passes between two cylinders.

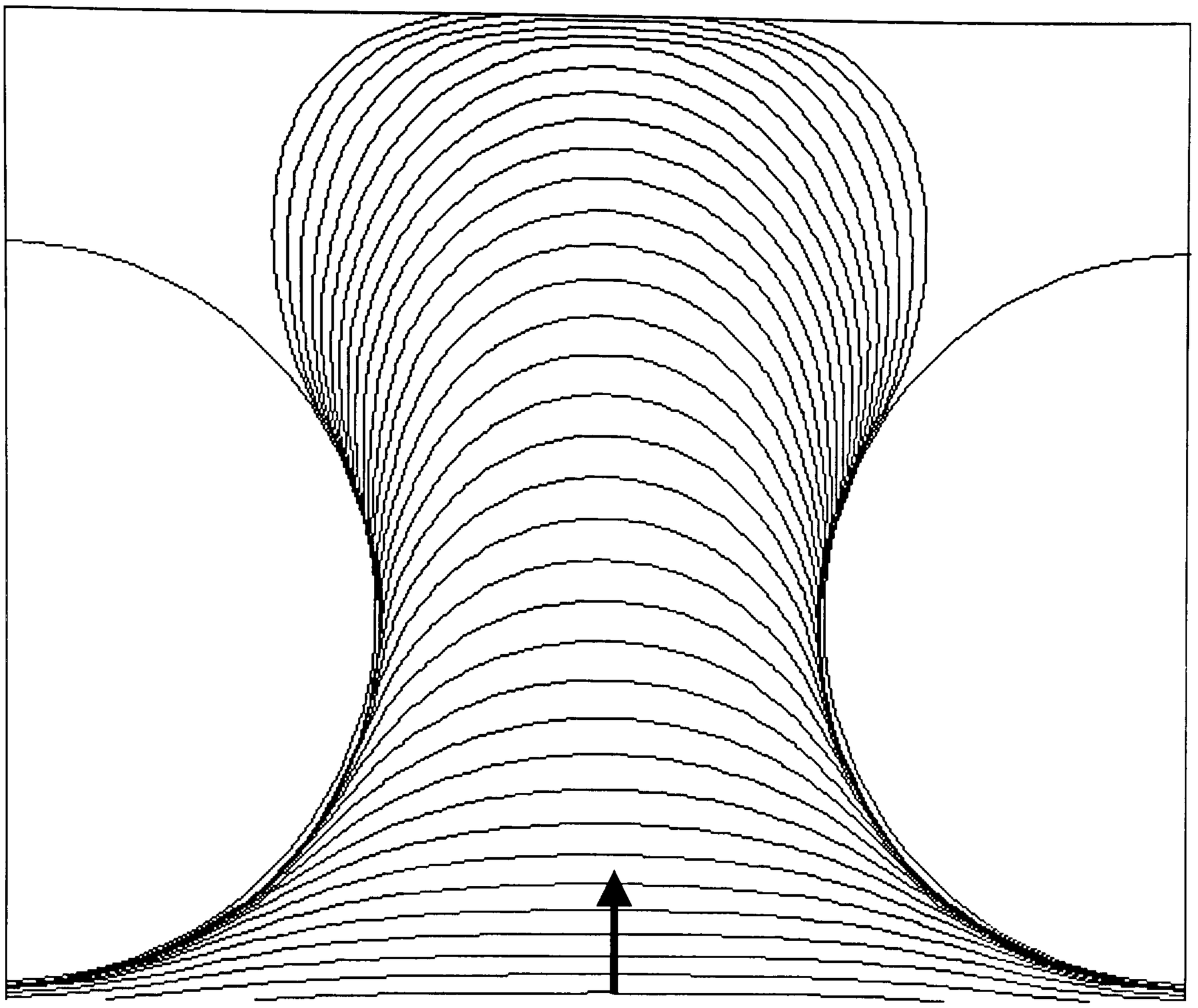


Figure 6.13 - Flow front tracking simulation result from Spelt et al.[10] showing the shape of the flow front at different times as it progresses through the gap between two cylinders. Creeping flow simulation through a periodic square array of cylinders. The volume fraction is 0.3, the Capillary Number is large (i.e. weak surface tension effects), the gas density is 0.1 of the liquid density, the gas viscosity is 0.01 of the liquid viscosity.

The front in Figure 6.13 is propagating from bottom to top. The shape of the flow front profile at the latest time shown in Figure 6.13 should be ignored as the flat shape of the flow front in this region is an artefact of the boundary conditions used. The general shape of the flow front as it progresses through the gap between the two cylinders is convex in nature. A comparison of this simulation result with a typical experimental result can be made by considering Figure 6.14.

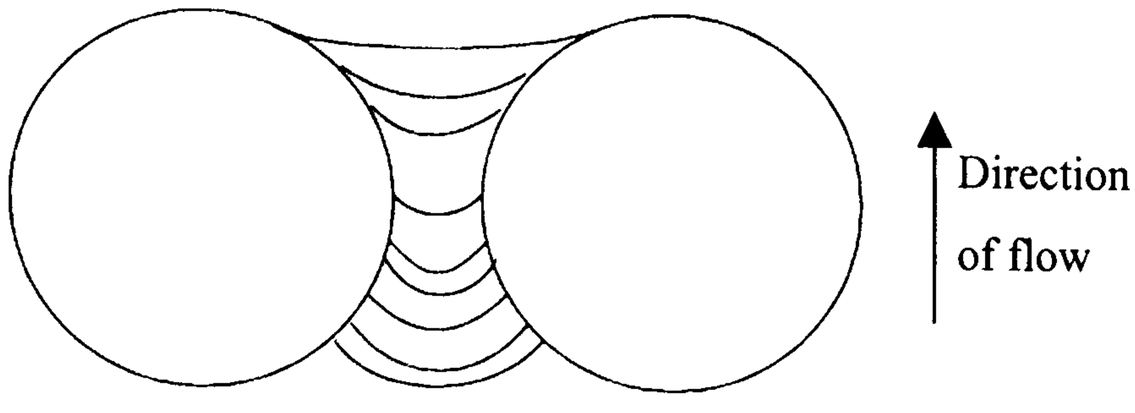


Figure 6.14 – Experimentally determined positions for the flow front at different times for flow between two cylinders within a hexagonal cylindrical array with a volume fraction of 58% (Superficial velocity = 0.63cm/s, $Re_{superficial}$ = 1).

One obvious distinction between the experimental and model results is the general shape of the flow front as it progresses through the gap between the cylinders. In the model the flow front is observed to be convex in nature whilst in the experiment the flow front is concave. Also, the apparent contact angle between the flow front and the cylinders in the model increases as the flow front progresses whilst this dynamic contact angle was observed to decrease as the flow front progressed in the experiment (see Figure 6.11).

These distinct differences between the model and the experiments are due to several effects. Firstly, as mentioned previously, the model does not account for the dynamic contact angle between the flow front and the cylinders. Clearly, as observed in the experimental study, this dynamic contact angle plays a significant role in the development of the flow front profile. Secondly, the concave nature of the flow front in the experimental study was believed to be partly due to an electrostatic interaction between the fluid and the surface of the cylinders. No account of this electrostatic field is made in the model. Another observation made in the experimental study was the 'sticking' of the central part of the flow front on the cylinder below the gap (not shown in Figure 6.14) for a short period of time, thus pulling the flow front back and enhancing its concave shape.

6.6. Summary

The results of a micro-scale flow filling experimental study have been presented in this chapter. An analysis of the flow front profiles indicates that the contact angle between the cylinders and flow front decreases as the front progresses through the channel between the cylinders. The rate of decrease in contact angle is generally

linear with position but changes after the front passes the narrowest region of the gap. The general shape of the flow front meniscus is concave. This is believed to be partly due to an electrostatic interaction between the fluid and the surface of the cylinders. Also, the central part of the front was observed to 'stick' on the surface of the cylinder below it for a short period of time thus 'pulling' the flow front back and enhancing the concave nature of the front.

Results are also presented for the contact angle and surface tension of the different liquids and surfaces used in both these micro-scale experiments and industrial scale RTM applications. The relatively short amount of time available for fibre wetting and the development of a strong fibre-matrix interface makes the understanding of the wetting process an important factor in optimising the mechanical performance of composites. However, it is important to note that the short length of time available for impregnation would have a more significant effect on the porosity.

A comparison of these experimental results against a flow front tracking model proposed by Spelt et al.[10] reveals the need for the model to account for certain important parameters. The model considers a creeping flow simulation through a periodic square array of cylinders. No account is yet made in the model of the dynamic contact angle between the flow front and the cylinders, whilst the surface tension effects are assumed to be very weak. However, the experimental study highlights the significant role played in the development of the flow front profile by the dynamic contact angle between the flow front and the cylinder surface. Surface tension effects are also observed to play a significant role in the experiments, implying the need to allow a lower value for the Capillary Number in the model.

6.7. References

[1] Darcy, H., "Les Fontaines Publiques de la Ville de Dijon", Dalmont, Paris, (1856).

[2] Amico, S., Lekakou, C., "An Experimental Study of the Permeability and Capillary Pressure in Resin Transfer Moulding", Composites Science and Technology, **61**, 1945–1959, (2001).

[3] Visconti, I.C., Langella, A., Durante, M., "The Influence of Injection Pressure on the Permeability of Unidirectional Fibre Preforms in RTM", In: 8th European Conference on Composite Materials, ECCM-8, Naples, Italy, 737–43, (1998).

[4] Gauvin, R., Trochu, F., Lemenn, Y., Diallo, L., "Permeability Measurement and Flow Simulation Through Fibre Reinforcement", Polymer Composites, **17**(1), 34–42, (1996).

[5] Griffin, P.R., Grove, S.M., Russell, P., Short D., Summerscales, J., Guild, F.J., Taylor, E., "The Effect of Reinforcement Architecture on the Long-range Flow in Fibrous Reinforcement", Composites Manufacturing, **6**(3-4), 221–35, (1995).

[6] Steenkamer, D.A., Wilkins, D.J., Karbhari, V.M., "Influence of Test Fluid on Fabric Permeability Measurements and Implications for Processing of Liquid Moulded Composites", Journal of Materials Science Letters, **12**(13), 971–3, (1993).

[7] Parnas, R.S., Salem, A.J., Sadiq, T.A.K., Wang, H.P., Advani, S.G., "The Interaction Between Micro and Macroscopic Flow in RTM Preforms", Composite Structures, **27**, 93–107, (1994).

[8] Potter K.D., "Resin Transfer Moulding", 1st Edition, Chapman & Hall, London, (1997).

[9] Sadiq, T.A.K., Advani, S.G., Parnas, R.S., "Experimental Investigation of Transverse Flow Through Aligned Cylinders", Int. J. Multiphase Flow, **21**(5), 755 – 774, (1995).

[10] Spelt, P.D.M., Selerland, T., Lee, P.D., Lawrence, C.J.L., Internal Report, *Imperial College of Science, Technology and Medicine*, London, (2002).

7. SEMI INDUSTRIAL SCALE RTM

This chapter presents the results of semi-industrial scale RTM experimental studies of the flow front behaviour during filling using the *SMARTweave* flow monitoring system. This work focuses on the production of thick composite parts and hence a 30mm thick mould was used for the study. Flow of a model fluid, corn syrup, through a unidirectional glass fibre material was monitored. Also presented are dielectric cure monitoring results for the impregnation and post-impregnation stages of the RTM experiment.

7.1. Introduction

Production of thick composite components is becoming one of the major trends in aerospace as well as other areas like armour and weapon design. Efficient and low cost production of these components requires both a clear understanding of the major factors and phenomena involved and a reliable simulation program which can act as a design tool.

There is considerable experience in modelling and numerical techniques within composite component manufacturers and the research community. There are currently a few commercially available simulation packages (e.g. LCMFLOT[a] and LIMS[b])

---

[a] L'Ecole Polytechnique de Montreal, Canada

[b] Suresh G. Advani and Pavel Simacek, University of Delaware

which are based on Darcy's law to describe flow of viscous resin through the fibre reinforcement[1,2]. However, current experiments at BAe Systems and Qinetiq show that in the production of "thick" components the impregnation process, cure characteristics, void formation and growth criteria and the final shape of the product are substantially different from what is predicted by the conventional models and simulation packages mentioned above.

The SMARTweave system was used to monitor the progression of the flow front during filling in a Resin Transfer Moulding (RTM) process. The system provides valuable information such as the dynamics of the mould filling process and information of dry spots.

SMARTweave sensing is based on an embedded gridwork of conducting wires which act as sensing and excitation line sensors. The arrival of the fluid is sensed by multiplexing through the grid, by monitoring the voltage as the fluid flows and thereby closes open circuits through the preform[3]. Associated instrumentation detects the signal and hence infers the liquid location. This information is useful in the manufacturing process, for quality control, for the design of moulds and control strategies, and in the present case for the development of models for flow and cure.

Some of the alternative techniques for monitoring the flow front in RTM include a dielectric sensor proposed by Skordos et al.[4]. Skordos et al. report that experiments confirmed the flow front position can be located continuously with a satisfactory accuracy. The sensor set-up also enabled cure monitoring of the resin once the mould filling stage was complete. Mathur et al.[5] propose a flow sensor based on evanescent wave fluorescence for locating the position of the flow front.

Studies were performed[6] to sense the flow of low-resistance model fluids, such as corn syrup through glass fabric preform. Also, studies have been performed on the application of *SMARTweave* for cure and position monitoring of several high-resistance resins. Through parametric studies including the influence of resin type, the use of single and multiple *SMARTweave* planes, the use of carbon and insulated copper sensors and the stitching versus non-stitching of the preform, it was

demonstrated that the *SMARTweave* technique of resin position monitoring had definite advantages over traditional sensing techniques.

7.2. Background

In 1956 Aukward and Warfield presented the first monitoring device for the investigation of resin resistivity[7]. The *SMARTweave* (Sensors Mounted As Roving Threads) system was subsequently developed by the US Army Research Laboratory (ARL) and the University of Delaware, Centre for Composite Materials (CCM) and patented in May 1993[8,9]. The system consists of a sensor grid, an electronics package designed to detect signals from the sensing grid and a computer and software to control and record the signals and display the output data. The sensor grid includes two orthogonal sets of conductive threads separated by one or more isolating textile layers. As the liquid fills the mould, the gaps between the filament planes are filled with conductive fluid which sequentially completes the many possible electrical circuits.

7.3. Experiments

Details of the materials, equipment and lay-up procedure are given in Chapter 3. A series of 9 experiments was conducted and aimed at assessing the effects of the following process parameters:-

i. The fill pattern in thick composites.
ii. The effects of variations in preform (fibre fraction, flow direction relative to fibre alignment).
iii. Race-tracking (unfilled section of the mould).
iv. Influence of the orientation of the tool i.e. horizontal or vertical filling.

Table 7.1 – Summary table of all the experiments performed.

Run	Fibre orientation	V_f	θ	Fabric dimensions (mm)	Grid (*X*,*Y*)	No. of Planes	Inlet Pressure (Bar gauge)
1	[0°]	0.43	90°	330x360	5×5	3	1.23
2	[0°]	0.49	90°	360x360	5×5	3	1.51
3	[0°]	0.55	90°	330x360	5×5	3	1.54
4	[90°]	0.43	90°	360x330	5×5	3	1.5
5	[90°]	0.43	90°	360x330	5×5	3	0.79
6	[90°]	0.55	90°	360x330	5×5	3	1.14
7	[0°]	0.43	0°	360x360	5×5	3	1.21
8	[0°,0°,90°]	0.43	90°	360x360	3×3	5	1.15
9	[0°,90°,0°]	0.43	90°	360x360	3×3	5	1.51
10	[90°]	0.49	90°	360x360	0	1	1.52

Table 7.1 summarises the experiments performed. In the Table,

- Fibre orientation refers to the direction of the fibres relative to the main flow direction i.e. 0° indicates that the fibres lie parallel to the main flow direction and 90° implies the fibres lie transverse to the main flow direction.
- V_f is the volume fraction based on an area density of 723.75g/m^2 for the glass fabric and a glass density of 2570kg/m^3.
- θ indicates the orientation of the RTM tool during filling i.e. 90° implies vertical filling and 0° horizontal filling.
- The grid refers to the numbers of wires per plane in the *X*,*Y* coordinates, described in Chapter 3.
- The number of planes refers to the number of planes through the thickness of the mould where sensing elements were placed.

Vertical filling was used in all the tests apart from run 7 where the RTM tool was reconfigured for horizontal filling. Uni-directional glass fabric was used for all tests, with diluted corn syrup (10% water by weight) as the fluid system. However, the final

run, 10, was performed using the resin system Dow Derakane 411-C50[c] to produce a composite part for analysis. Further details are given in Chapter 3.

7.4. Error Analysis

The main sources of error in this series of experiments can be divided into two groups;

i. Time errors
ii. Location errors

The time errors can be divided further into the following sub groups:-

- The time lag in registering the contact time of the liquid at each node. It was observed that a delay existed between the liquid making contact with each node and the *SMARTweave* system recording a change in voltage. However, this is a consistent error throughout the data set and therefore does not affect the relative timing of data points. A time lag of approximately 2 seconds was observed.

The location errors can also be divided into the following subgroups:-

- Longitudinal errors - these are due to (i) errors in the nodal positioning within the tool and (ii) deformation of the fabric and hence nodal position. The wires could be placed in the tool with an accuracy of ± one stitch width or 2mm. The error due to deformation of the fabric is much larger and is estimated to be 5mm.
- Lateral errors – due to (i) variation in packing density and (ii) wire nesting within the fabric. Depending on the orientation of the fabric during lay-up, the packing density changed. The estimated lateral error associated with this change is 1mm. Also, it was observed that in some cases the wires nested within the tows hence changing the lateral position. This error is also estimated to be of the order of 0.5mm.

Thus the estimated global errors of the results presented are of order 4% in position and 2s in time.

---

[c] Manufactured by *Dow Chemicals*, Kings Lynn, Norfolk PE30 2JD, UK

7.5. Results

Figures 7.1 and 7.2 display photographs showing the lay-up of the fabric within the RTM tool and the positioning of the wiring within the tool.

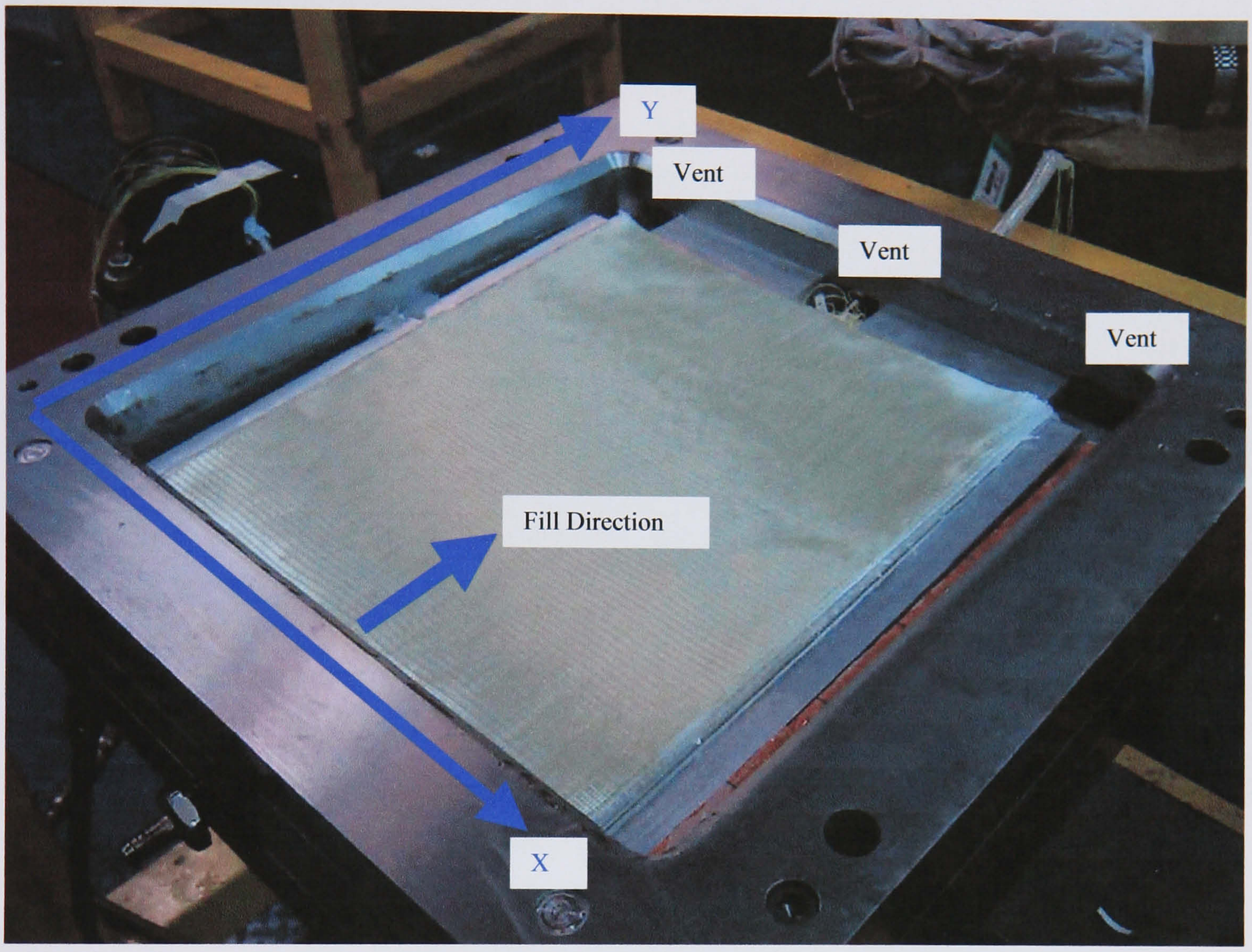


Figure 7.1 - Fabric lay-up in tool, showing the *X* and *Y* coordinates relative to the main flow direction. The fibres are parallel to the fill direction. The transverse lines are the stitching.

Figure 7.1 shows the ***X***, ***Y*** coordinates relative to the main flow direction. The fabric was laid-up with the fibres either parallel, transverse or a combination of these relative to the main flow direction. The mould had a single inlet port and three vent ports as indicated on Figure 7.1.

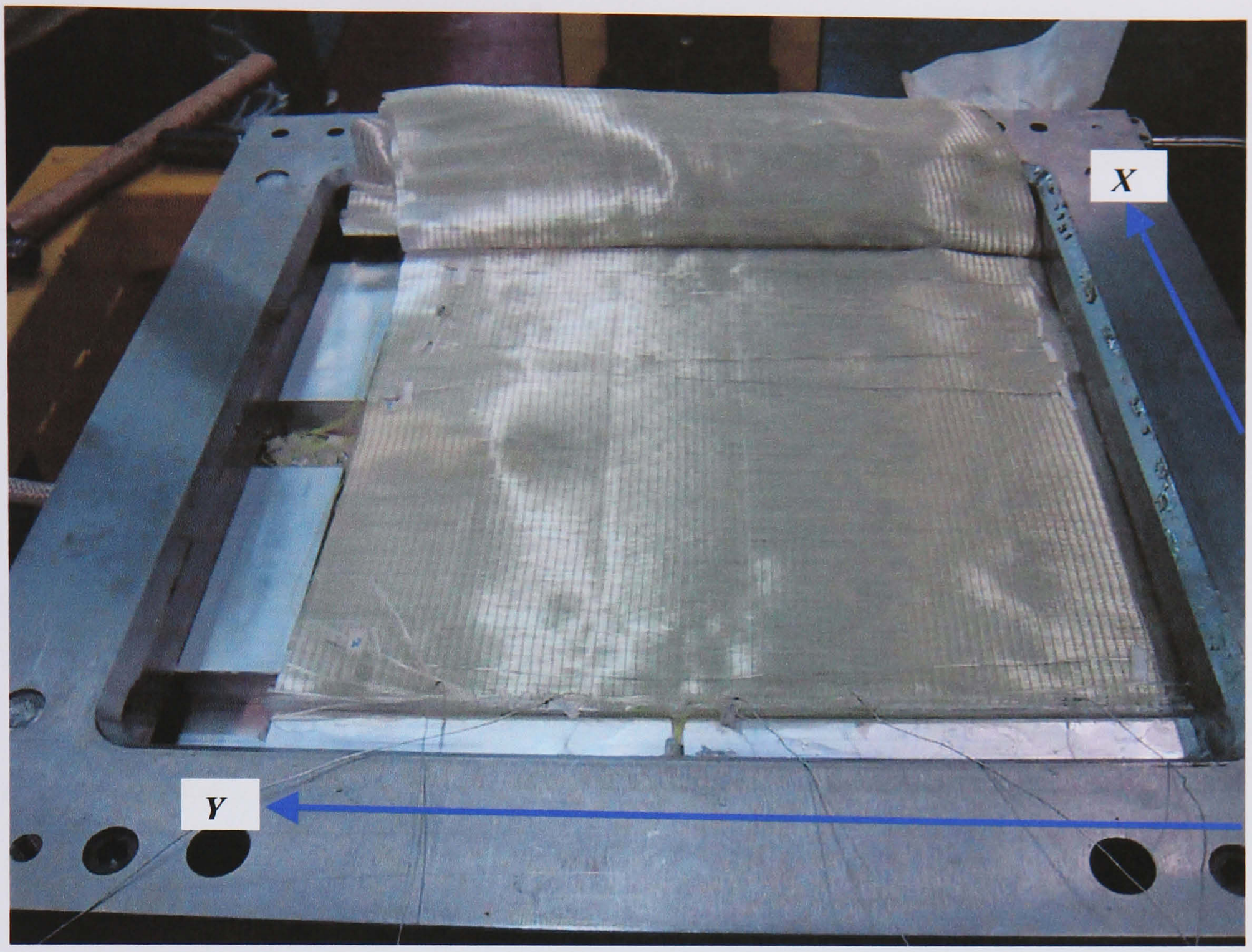


Figure 7.2 - *SMARTweave* wiring inside the mould. The *Y* coordinate wires run from right to left and *X* coordinate wires run from the front of the picture to the back. The wires were stitched into the fabric and taped at each end. One layer of fabric was used to separate the *X*,*Y* coordinate wires.

Figure 7.2 shows the lay-up of the wiring system within the tool. The ***X*** and ***Y*** coordinate wires were stitched into the fabric to hold them in position and a small piece of tape was placed on each end. One layer of fabric was used to separate the ***X*** coordinate wires from the ***Y*** coordinate wires. The wires in the photograph are seen to lie in loose curves across the fabric. They were pulled tight (and straight) prior to the experiment.

A typical voltage history pattern at constant ***X*** and increasing ***Y*** (the main flow direction) is shown in Figure 7.3. This shows how the voltage changes as the flow front progresses through the mould since ***Y*** is the direction of the front propagation. Firstly, from Figure 7.3 it is seen quite clearly how the voltage rises sharply from $0V$ to approximately $9.8V$ when the flow front reaches each node. This is good as it gives a clear indication of the arrival time of the front at each node. There is a small

precursor signal before full wetting of the node. This arrives at the first node about 10 seconds before the main front and at node 5 about 50 seconds before the main front. It is probably due to wicking in the fibres of the layer of fabric between the planes of *SMARTweave* sensors. The second point to highlight is how the flow front velocity decreases as it progresses through the mould. This is indicated by the fact that the interval time between each node progressively increases with ***Y***.

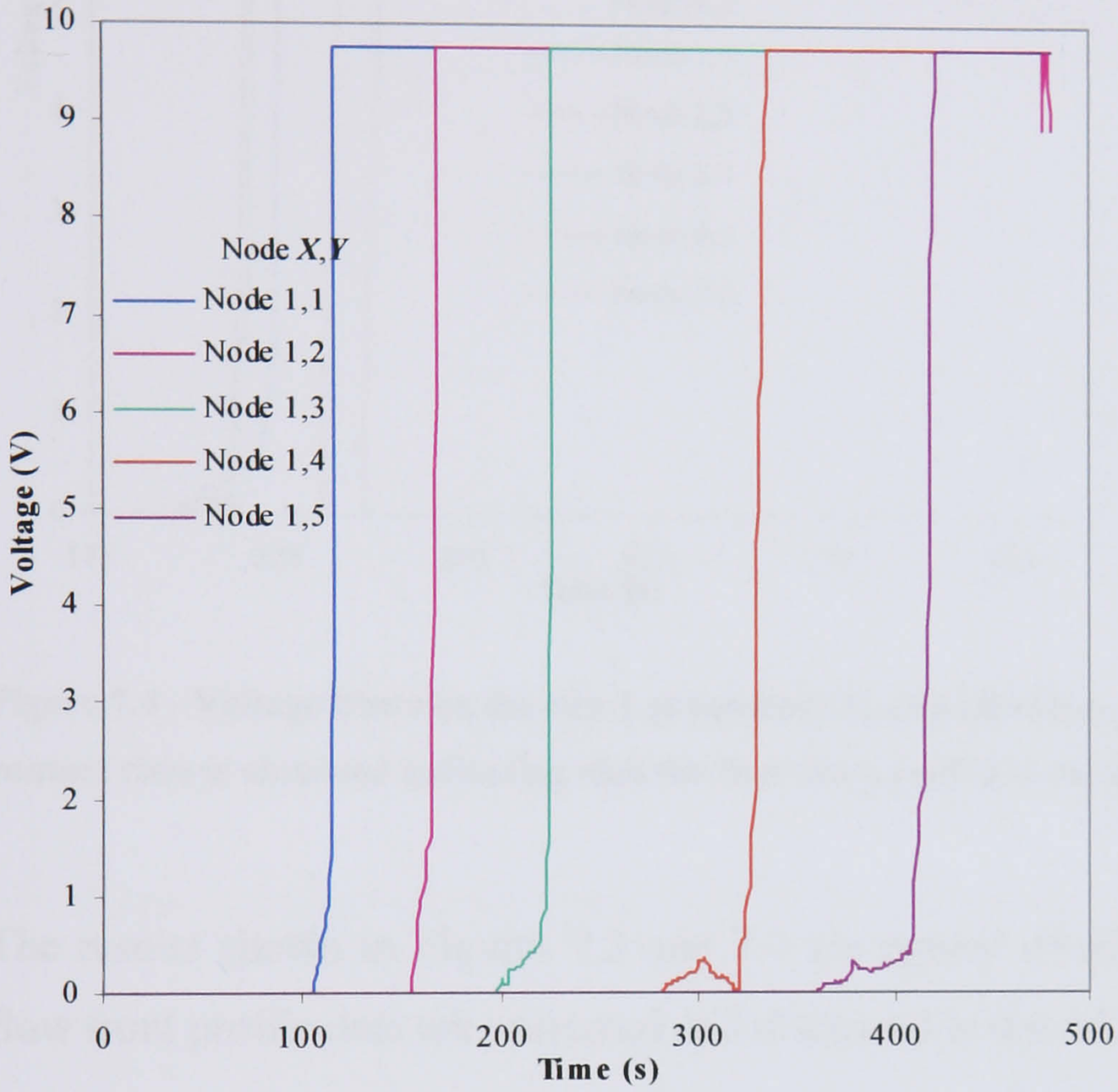


Figure 7.3 - Voltage history for run 1 at X_1 and increasing *Y*. The voltage rises sharply from 0V to 9.8V when liquid contact is made at each node.

Figure 7.4 shows a voltage history plot for the various ***X*** wires. For a flat flow front profile we would expect the front to arrive at each ***X*** node simultaneously for any given value of ***Y***. However the flow front is not flat, which is indicated by the different voltage-time history curves at each node. In this case the front arrives in the order X_2, X_3, X_1, X_4, X_5. In the case of X_5, the voltage does not quite reach the peak value of 9.8V. Some of the other nodes also show decreasing voltage at later times.

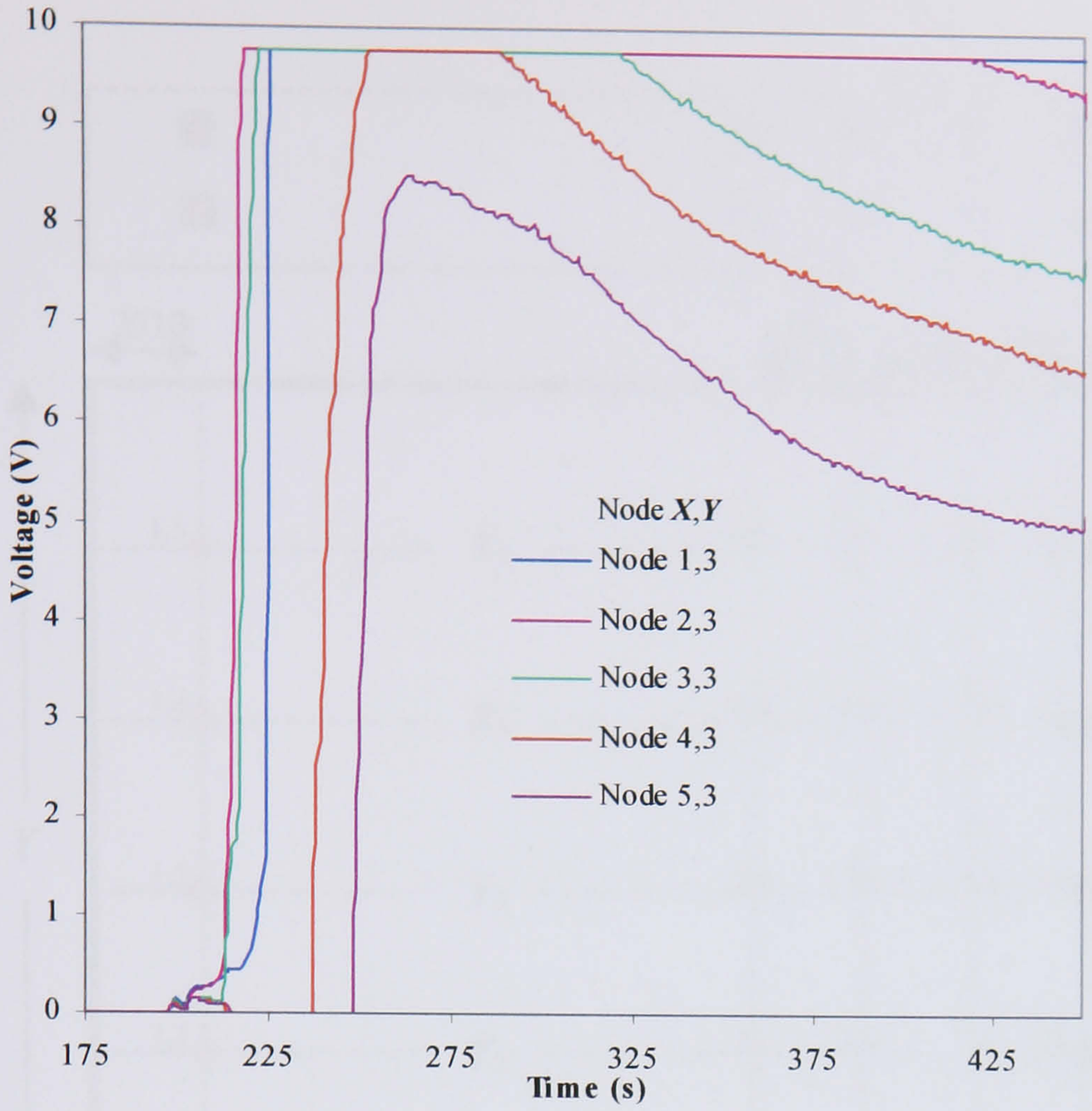


Figure 7.4 - Voltage histories for run 1 at constant Y_3 and all values of X. A variation in the nodal contact time is observed indicating that the flow front profile is not flat.

The results shown in Figures 7.3 and 7.4 are typical of all the runs performed. The flow front profile data are presented and discussed in the following sections.

7.5.1. Run 1

Run 1 simulated flow parallel to the fibre direction with a fibre volume fraction (V_f) of 43% (see Table 7.1). Three planes of wires were used to monitor the flow with 5***X*** and 5***Y*** wires in each plane (refer to Chapter 3 for details). The raw data extracted from the *SMARTweave* system was the arrival time of the flow front at each node. Figure 7.6 shows the position-time data for each plane. The ♦ symbols denote the nodes on the other half of the mould that have been directly reflected in the mid-y plane (see Chapter 3 for sensor positioning data) as illustrated in Figure 7.5 where the nodes (♦) on the left are reflected to the right-hand side.

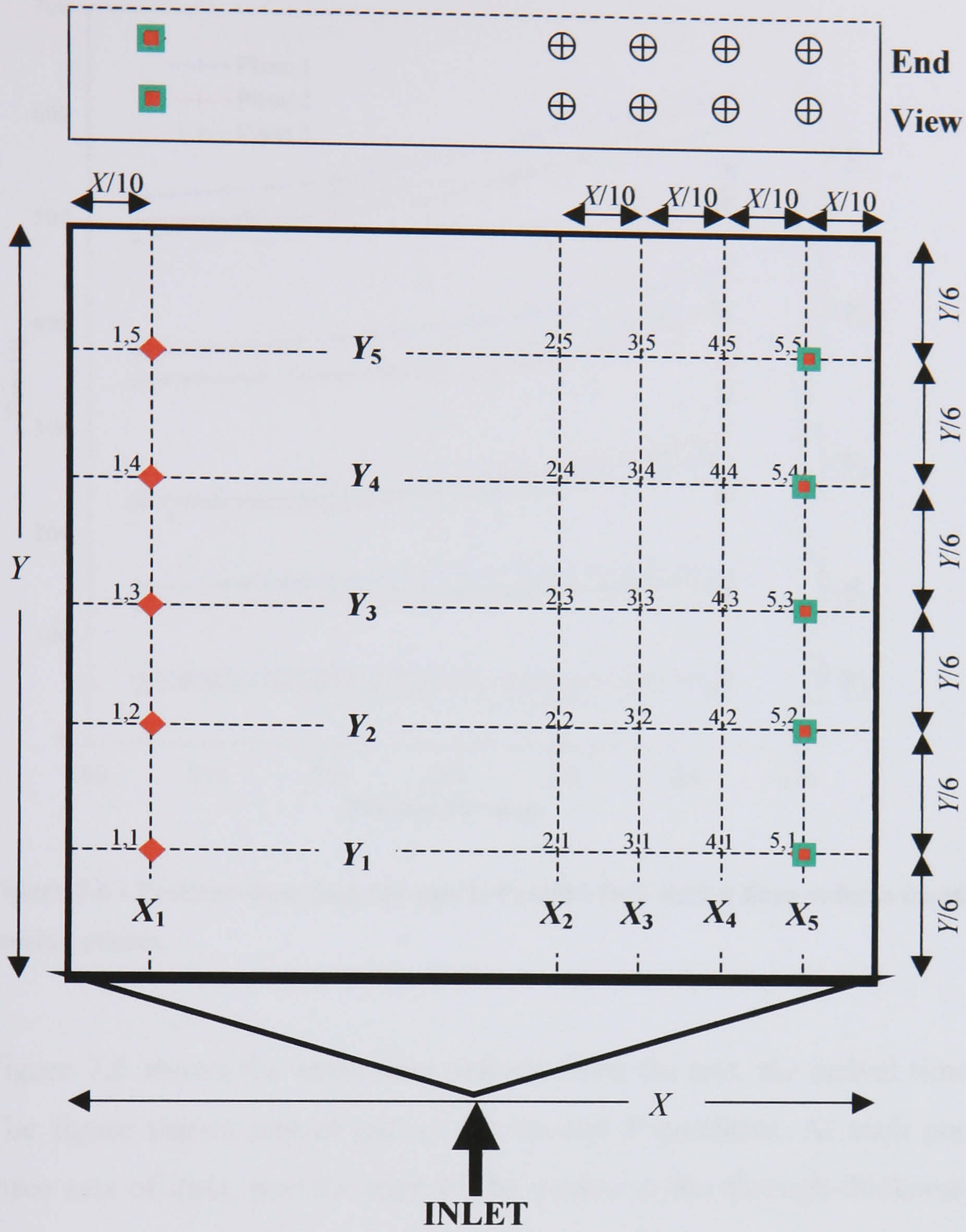


Figure 7.5 – Schematic diagram showing nodal positions within the mould. The symbols, ♦, on the left-hand side of the mould denote nodes that are reflections of the ones indicated by ■ on the right-hand side. The length scale is dimensionless and can thus be applied to the corresponding fabric dimensions (360mm or 330mm).

Figure 7.5 shows the nodal positions in the ***X***, ***Y*** plane. The nodes on the far left-hand-side of the mould can be reflected directly through the mid-*x* plane to the right-hand-side of the mould. Therefore node [1,1] can be mapped directly onto node[5,1] etc. This is done in the graphs of results presented below, where the nodes on the far left are presented by the ♦ symbol and thus only the right-hand-side of the mould is shown.

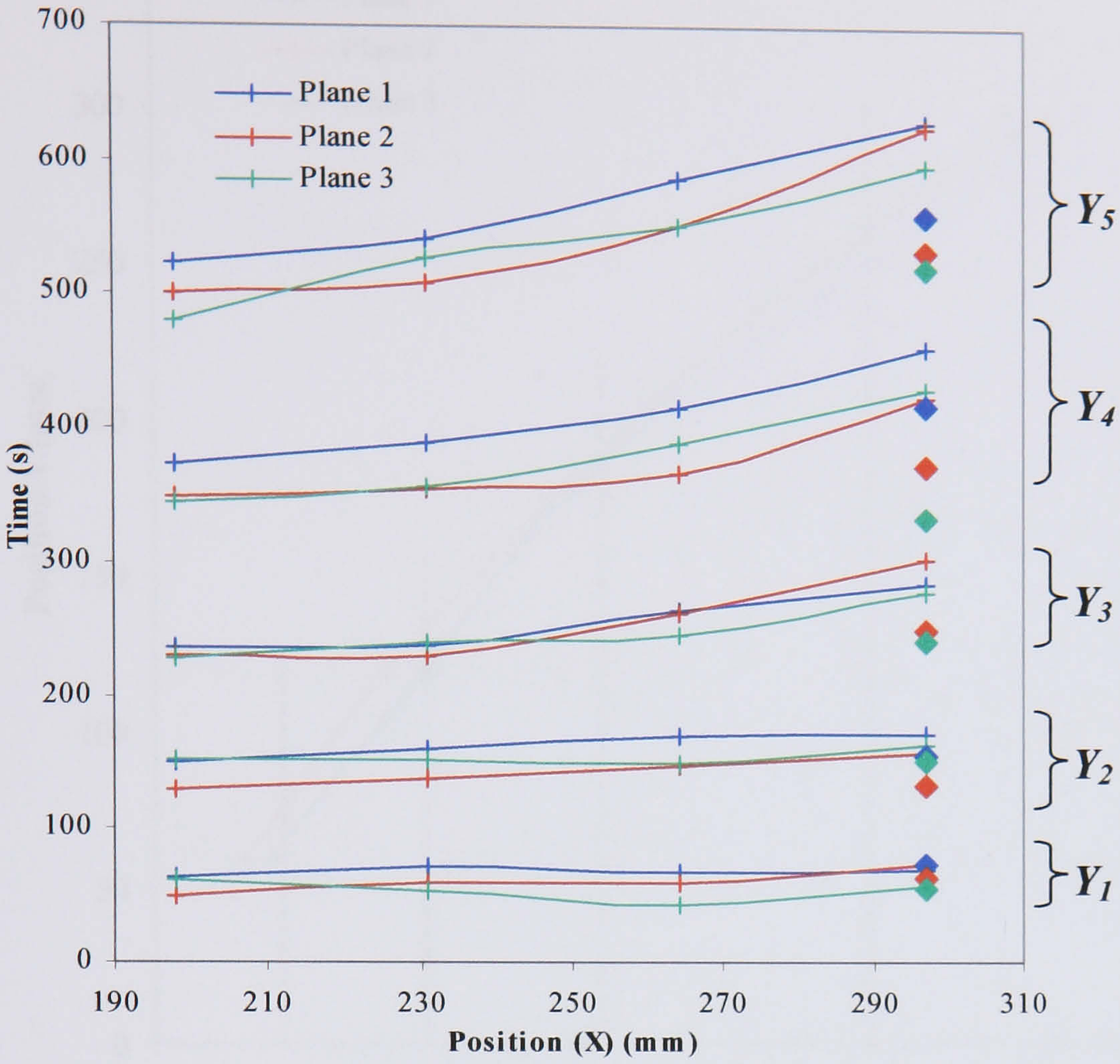


Figure 7.6 - Position-time data for run 1. Parallel flow with a fibre volume fraction of 43% and 3 sensing planes.

Figure 7.6 shows the main data derived from the test, the arrival time at each node. The figure shows sets of curves for several ***Y*** positions. At each position there are three sets of data, one for each of the planes in the through-thickness direction. For this particular run (1), it is seen that the flow front is not symmetric left to right, but that the left half of the mould fills earlier than the right. It is also clear that plane 1 (closest to the mould wall) tends to fill later than planes 2 and 3 (away from the walls).

From these raw data of time and position, graphs of position ***Y*** versus flow front arrival time were plotted for each value of ***X*** in each plane (see Figure 7.7). A second order polynomial fit was applied to each curve for the different planes. Hence, by selecting a fixed time on each curve, the position of the flow front in the ***Y*** coordinate could be estimated. An example of these at specific time is shown in Figure 7.8.

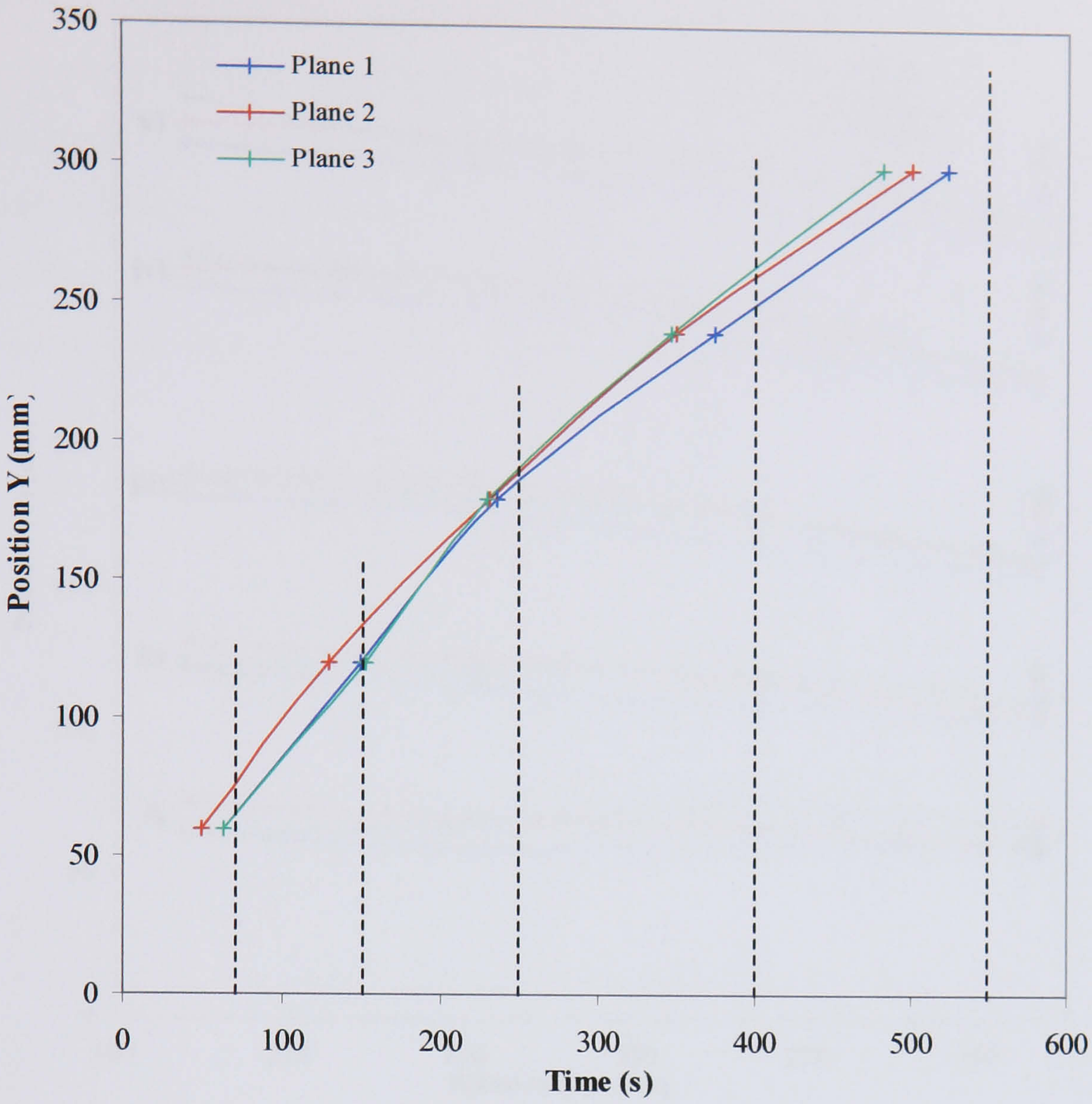


Figure 7.7 - Position *Y* versus flow front arrival time at each node in each plane for X_2 in Run 1. Parallel flow with a fibre volume fraction of 43%.

Figure 7.7 displays the change in the position of the flow front along wire X_2 for increasing ***Y*** in the three planes for run 1. In the ideal case of plug flow, the three curves for the different planes would collapse onto one curve. However due to the through-thickness variations in the behaviour of the flow front this is not case. Similar graphs to Figure 7.7 were plotted for each ***X*** wire in each plane (X_1 to X_5). The times selected for plotting Figure 7.8 are shown by vertical lines in Figure 7.7. In each case, the times correspond roughly to arrival at one of the ***Y***-positions monitored, so that the effects of interpolation should be minimal.

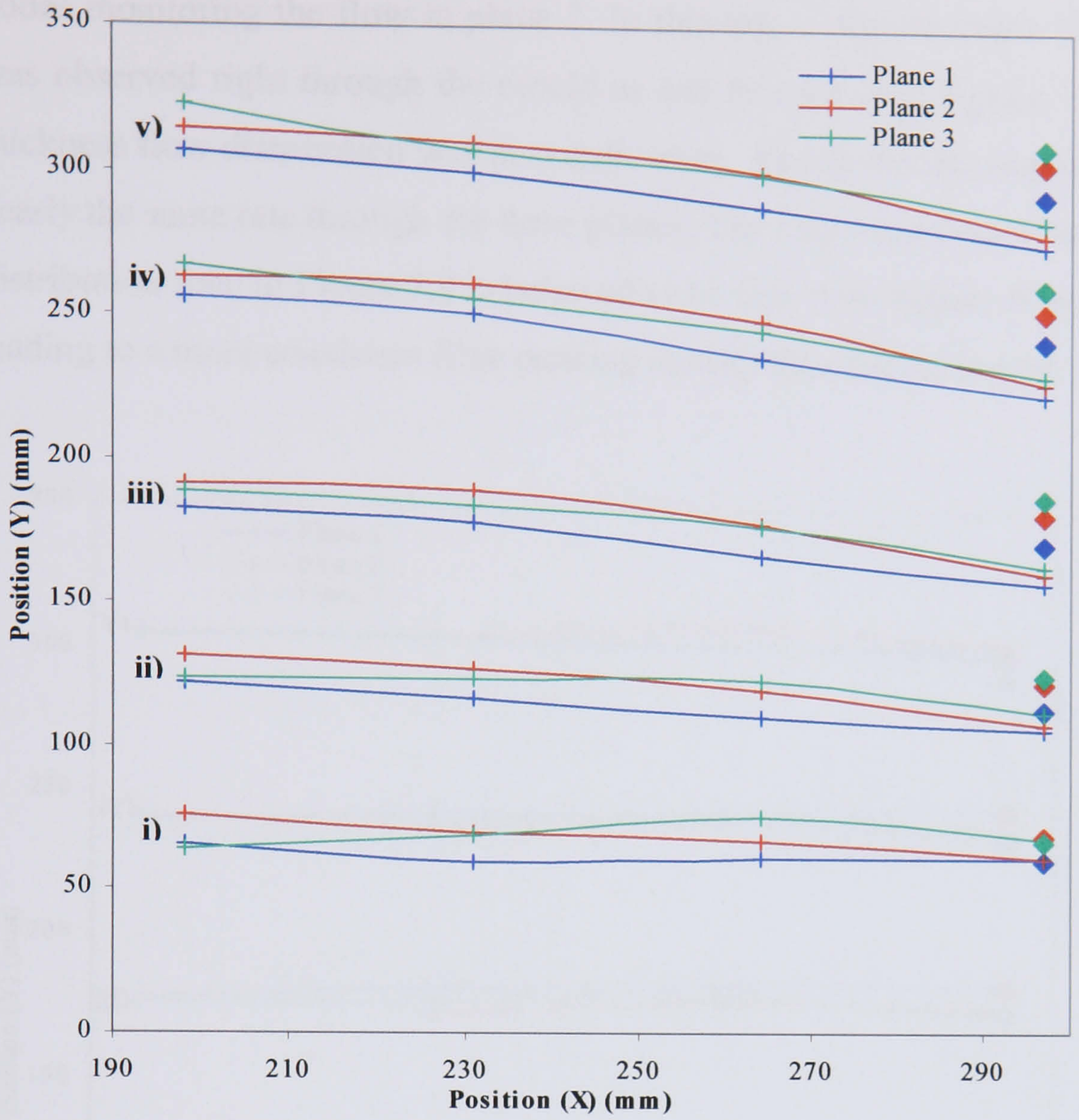


Figure 7.8 - Flow front profile for run 1. Interpolated times i) 70s, ii) 150s, iii) 250s, iv) 400s and v) 550s. Parallel flow with a fibre volume fraction of 43%. Vertical filling.

Figure 7.8 shows faster filling in the middle and left-hand-side of the mould. The degree of non-uniformity is observed to increase as the flow front progresses through the mould. Through the thickness, the flow in plane1 tends to lag behind planes 2 and 3. The through-thickness flow distribution also gets progressively worse as the flow front progresses further up the mould especially along the left-hand-side of the mould.

The observed variations are not severe and can largely be accounted for by the low fibre volume fraction which leads to an inconsistent packing density through the mould.

7.5.2. Run 2

Parallel flow at a fibre volume fraction of 49% was monitored in run 2. However, a technical fault was encountered with wire X_2 in plane 2 which reduced the number of

nodes monitoring the flow in plane 2. In this test, a flat/rectilinear flow front profile was observed right through the mould as can be seen from Figure 7.9. The through-thickness flow distribution was also quite even. The flow was observed to progress at nearly the same rate through the three planes. The improved flow front shape and flow distribution seen in Figure 7.9 is believed to be due to the higher fibre volume fraction leading to a more consistent fibre packing density through the mould.

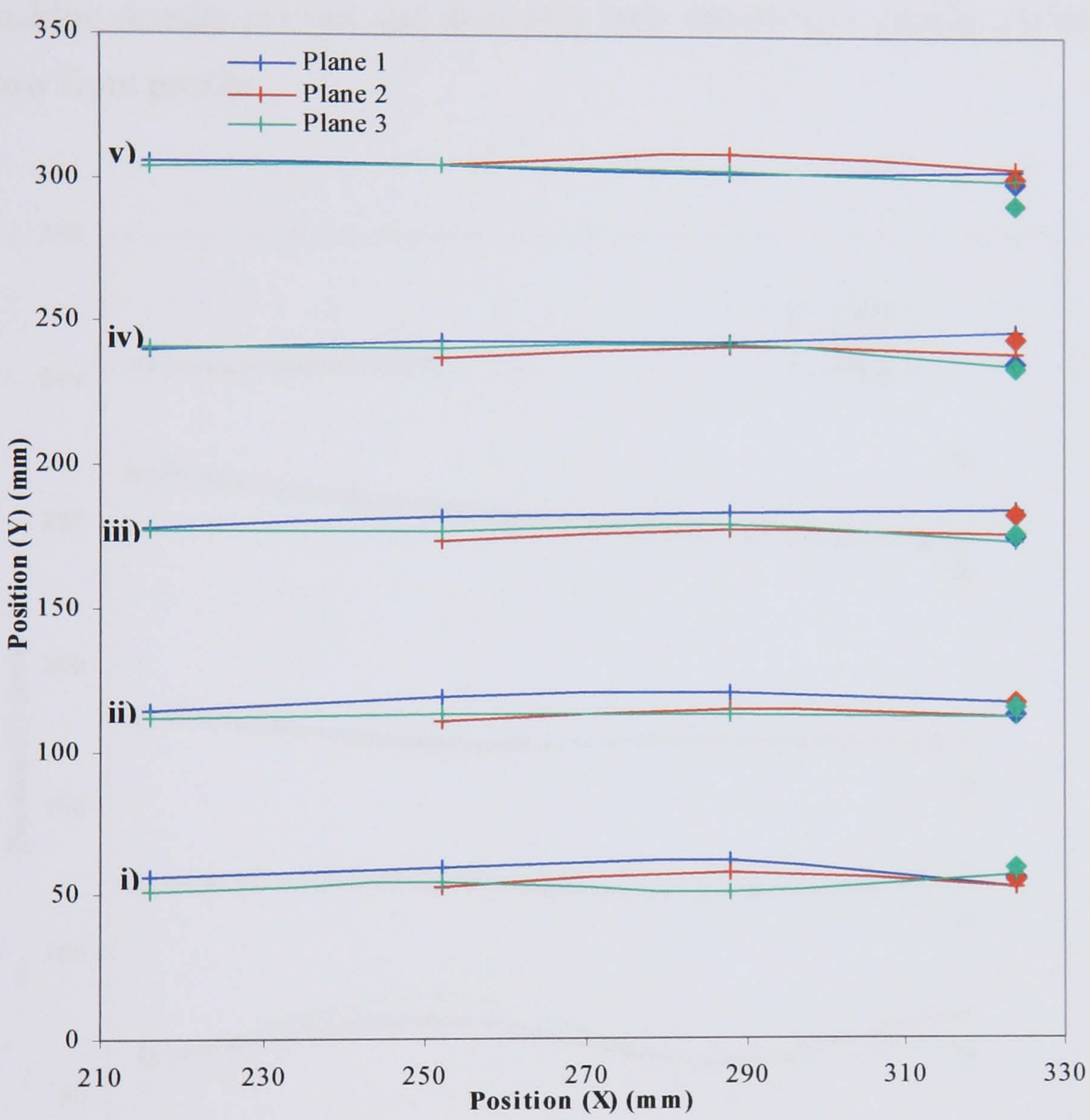


Figure 7.9 - Flow front profile for run 2. Interpolated times i) 65s, ii) 140s, iii) 230s, iv) 330s and v) 450s. Parallel flow with a fibre volume fraction of 49%. Vertical filling.

7.5.3. Run 3

Parallel flow was performed at a volume fraction of 55%. Due to a technical fault nodes (X_4,Y_5) and (X_5,Y_5) did not register a voltage in any of the three planes. Figure 7.10 shows the flow front profile which is seen to be quite uneven when it arrives at the first row of sensors in all three planes. This behaviour can be accounted for by the

slight fabric shifting and deformation adjacent to the inlet port caused by the relatively high inlet pressure used (1.54 bar gauge). However, the flow variation through the thickness remains minimal along the length of the mould. The overall shape of the flow front as it progresses through the mould becomes convex with the fastest flow in the centre, and the flow on the left-hand-side of the mould lagging slightly behind the right-hand-side. This overall convex shape of the flow front is believed to be largely due to the higher inlet pressure. However, due to the high fibre volume fraction the packing density is even and thus very little variation is seen in the through-thickness flow front profile.

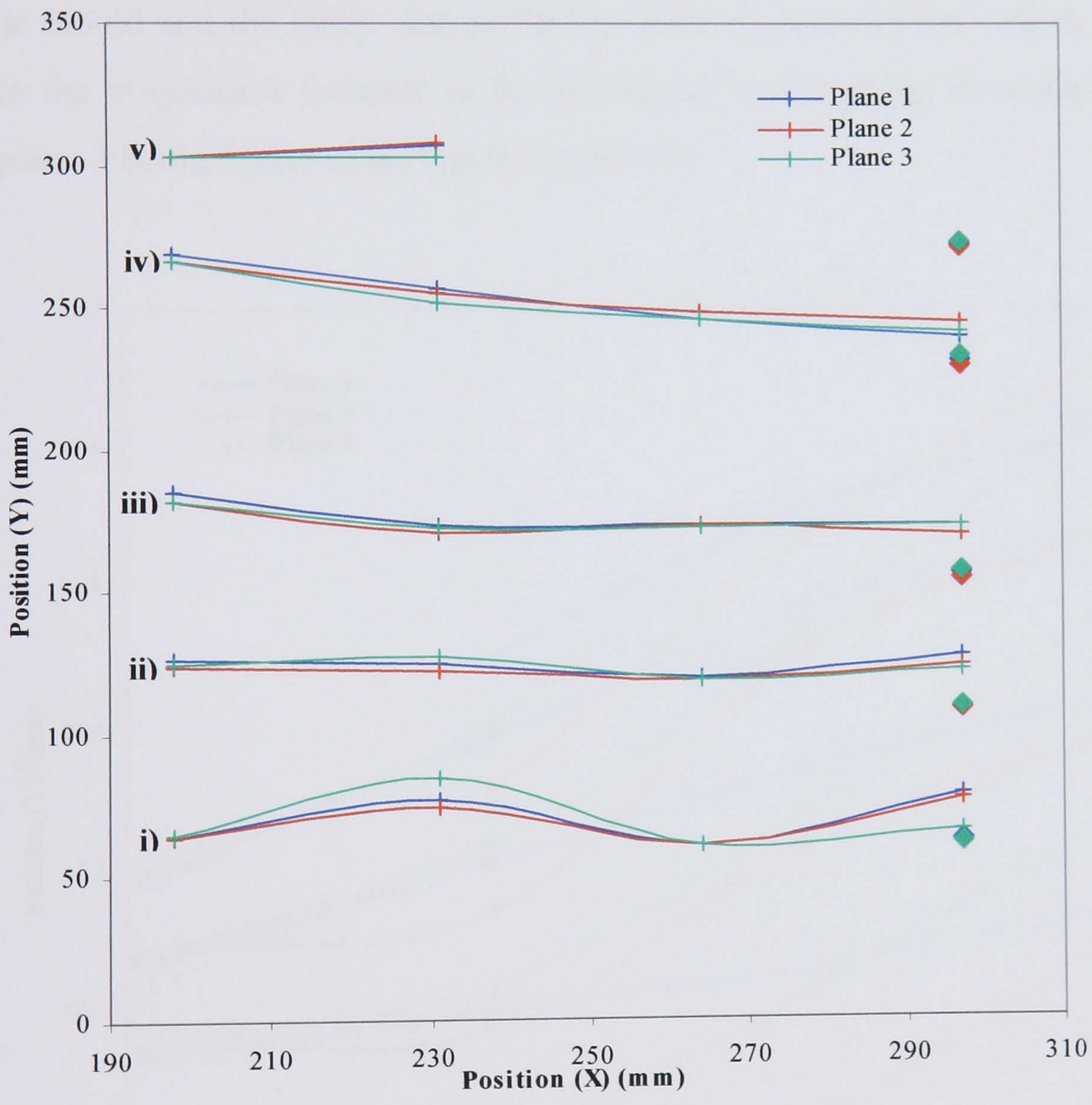


Figure 7.10 - Flow front profile for run 3. Interpolated times i) 60s, ii) 150s, iii) 250s, iv) 450s and v) 600s. Parallel flow with a fibre volume fraction of 55%. Vertical filling.

7.5.4. Run 4

In run 4, transverse flow was monitored at a fibre volume fraction of 43%. Nodes (X_1,Y_4), (X_1,Y_5) and (X_2,Y_5), in each plane did not register a voltage due to a technical fault. The same applied to node X_2, Y_2 in plane 2. Fabric deformation occurred adjacent to the inlet port (by approximately 15mm) which caused kinking of the X wires. Because of these problems, the data derived from arrivals near Y_5 are not shown in Figure 7.11. The figure shows significant race-tracking along the right-hand side of the mould with a progressively increasing amount of race-tracking from plane 1 to plane 3. Some of this race-tracking can be attributed to the fabric deformation. Another major cause of race-tracking could be a lack of tight fit between the top of the mould and the fabric due to the low fibre volume fraction which would account for the progressive increase in the amount of race-tracking from plane 1 to plane 3 (plane 3 being nearer to the top of the mould).

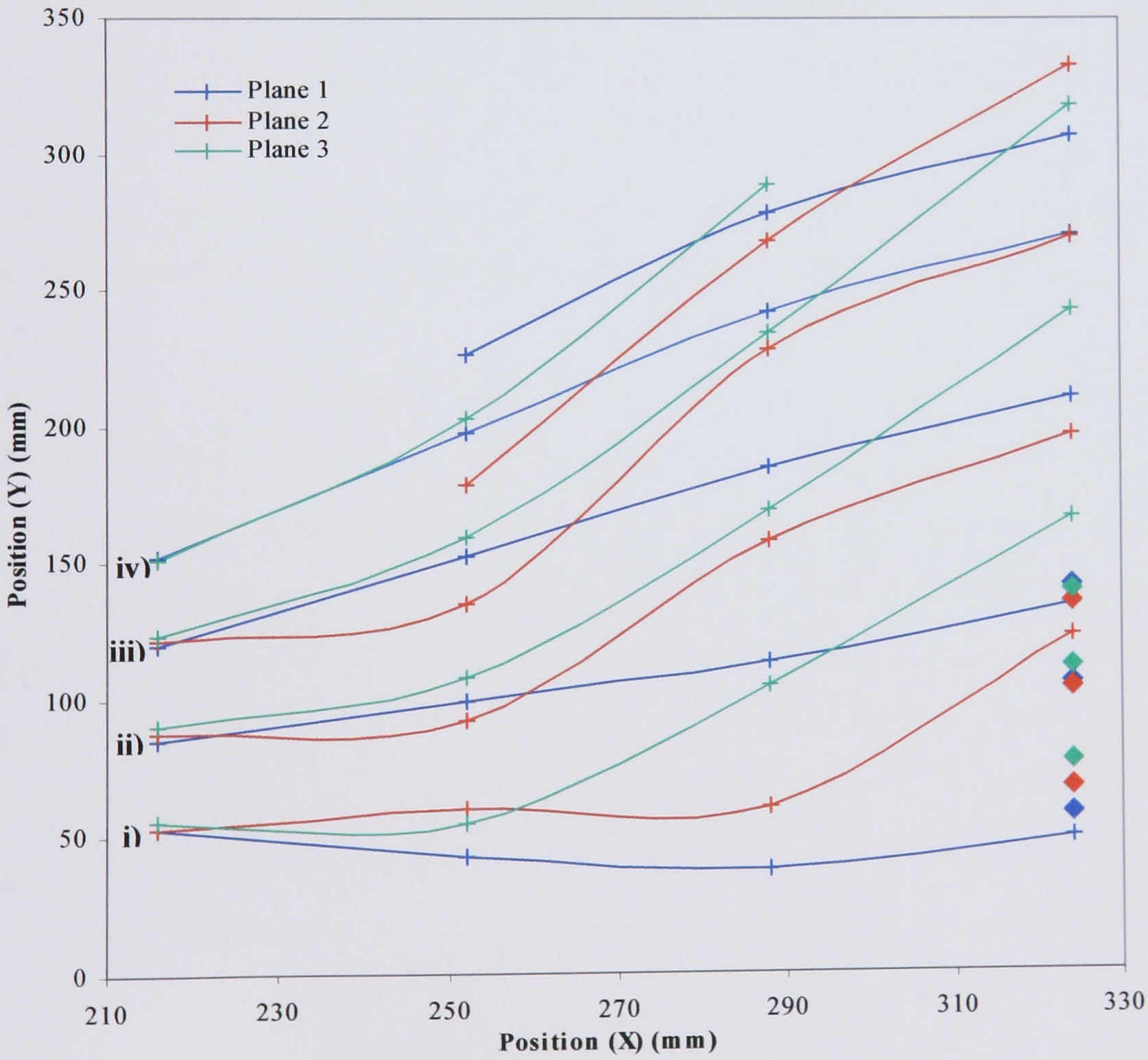


Figure 7.11 - Flow front profile for run 4. Interpolated times i) 80s, ii) 150s, iii) 220s, iv) 280s and v) 320s. Transverse flow with a fibre volume fraction of 43%. Vertical filling.

7.5.5. Run 5

Transverse flow at 43% fibre volume fraction was attempted again but to avoid the problem of fabric deformation observed in run 4, a wooden insert was placed at the top end of the mould to prevent the fabric from shifting. This helped to reduce the amount of fabric deformation but did not completely eliminate it. Figure 7.12 shows an improvement in the amount of race-tracking observed although a significantly faster flow still occurred along both edges. Due to the much lower degree of fabric deformation in this run the variation of the flow front through the thickness was also much lower. The overall shape of the flow front as it progresses through the mould is concave in nature. The deformation of the fabric contributes to this in two ways. First, the compression of the fabric around the centre of the mould reduces the permeability there. Second, the actual position in Y is shifted upwards slightly compared to the original wire position which is used to produce the figure.

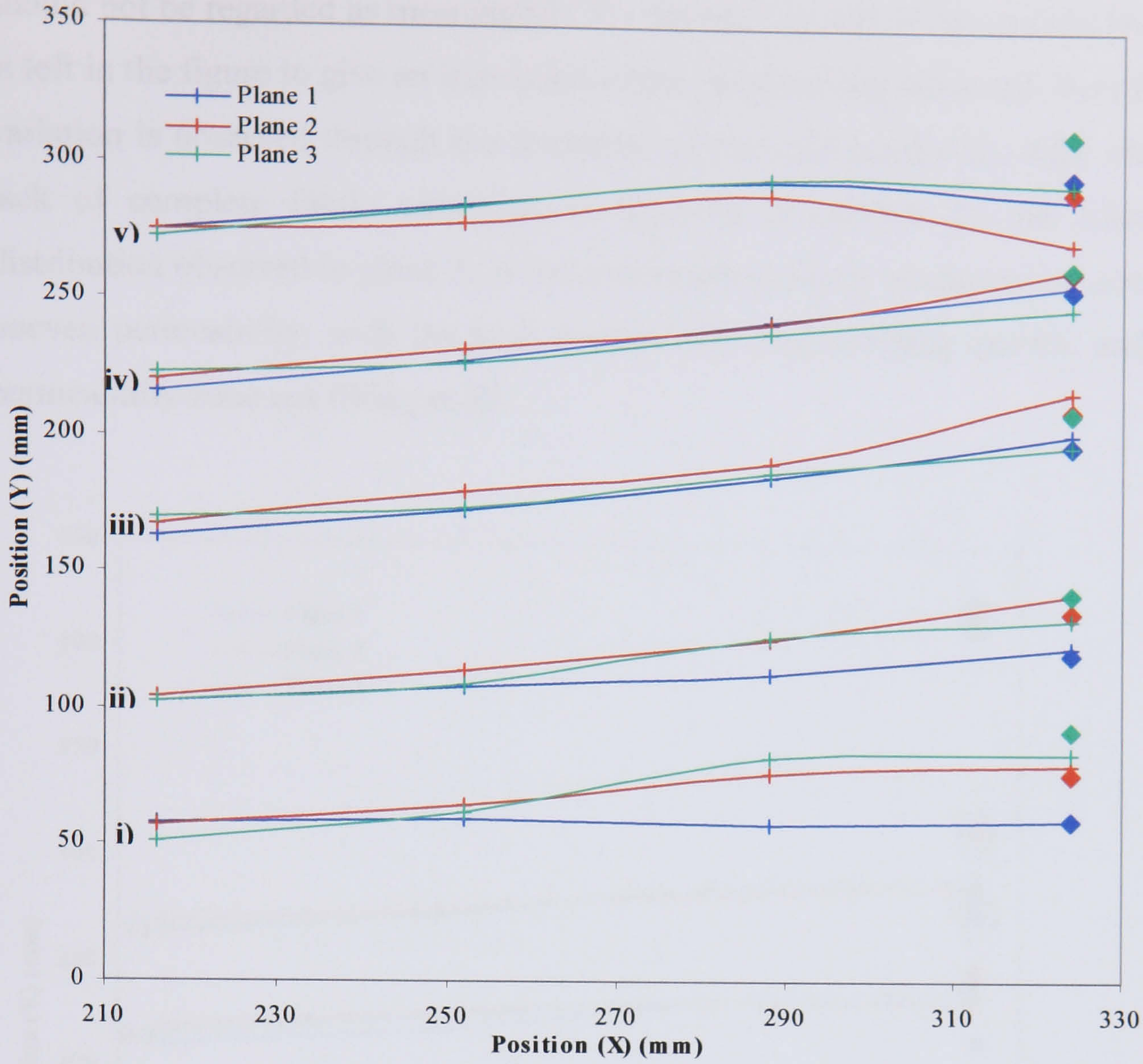


Figure 7.12 - Flow front profile for run 5. Interpolated times i) 150s, ii) 330s, iii) 610s and iv) 900s and v)1340s. Transverse flow with a fibre volume fraction of 43%. Vertical filling.

7.5.6. Run 6

Run 6 simulated transverse flow again but at a higher fibre volume fraction of 55%. The ***Y*** wires were observed to shift away from the inlet port by approximately 10mm whilst the ***X*** wires crimped by approximately 5mm. This was all caused by shifting and deformation of the fabric. Also, fabric saturation was not fully achieved. Dry spots were present around the central region of the mould. A slightly faster fill is observed in Figure 7.13 along both edges of the mould. However in the top plane, plane 3, a significant level of race-tracking is observed on the left-hand-side of the mould in the late stages of filling. Very little race-tracking occurs in the first three rows of sensors but in the 4^{th} and 5^{th} rows a significant level of race-tracking is observed in plane 3 on the left-hand-side of the mould. The symbol for ***X*** at time (v) appears at greater than 400mm. This represents an extrapolation of the data, and

should not be regarded as meaningful (it is beyond the end of the mould). However, it is left in the figure to give an indication of the race-tracking observed. Very little flow variation is observed through the thickness on the right-hand-side of the mould. The lack of complete fabric saturation is believed to account for the uneven flow distribution observed in plane 3. A lack of complete fabric saturation can occur due to uneven permeability, with the high permeability region filling quickly and the low permeability zone not filling at all.

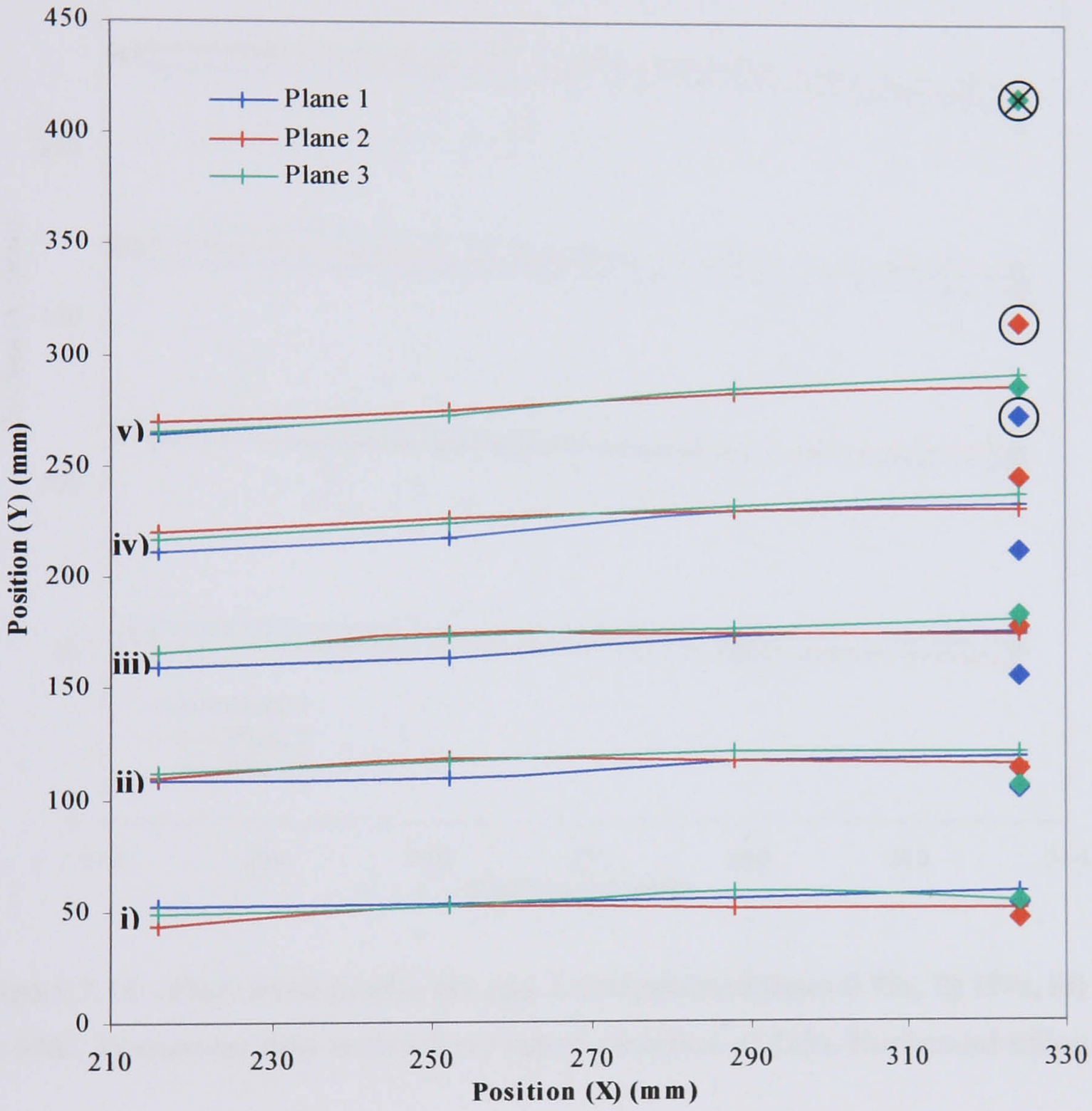


Figure 7.13 - Flow front profile for run 6. Interpolated times i) 160*s*, ii) 600*s*, iii) 1000*s*, iv) 1400*s* and v) 1800*s*. Transverse flow with a fibre volume fraction of 55%. Vertical filling. The symmetric nodes at time (v) are indicated by open symbols O for clarity.

7.5.7. Run 7

In this case the mould filling was performed with the mould aligned horizontally. The fibres were arranged parallel to the flow with a volume fraction of 43%. Nodes (X_5, Y_5) in planes 1 and 2 did not activate due to a technical fault. Figure 7.14 shows the flow front profile observed through the mould. The fabric adjacent to the inlet

deformed by approximately 5mm. A flat flow front profile is observed along the length of the mould. The variation of the flow front through the thickness is generally quite low. In this case the fabric deformation adjacent to the inlet seemed to have very little effect on the flow front, presumably because the magnitude of the fabric deformation was quite low.

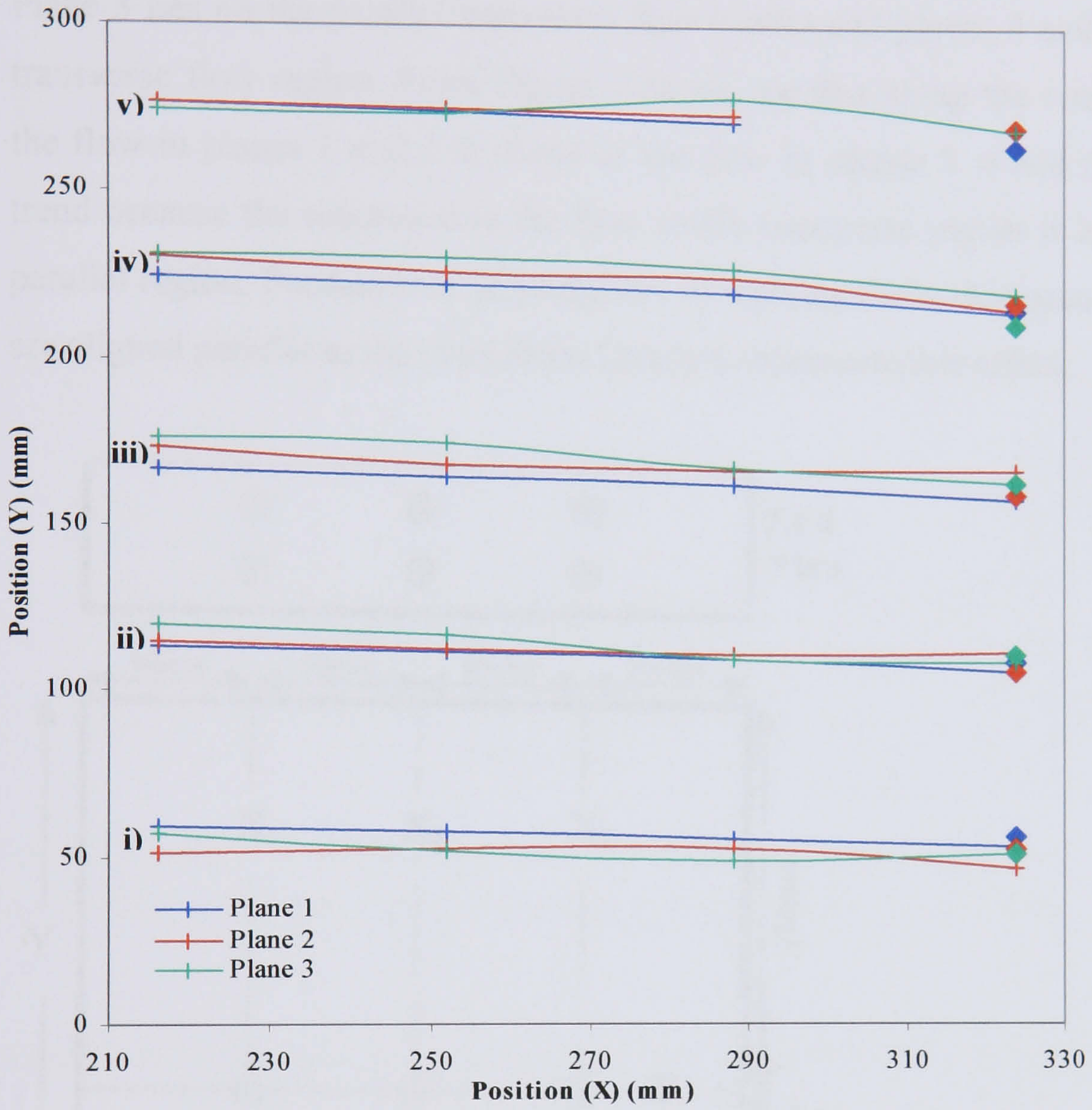


Figure 7.14 - Flow front profile for run 7. Interpolated times i) 90*s*, ii) 190*s*, iii) 290*s*, iv) 400*s* and v) 500*s*. Transverse flow with a fibre volume fraction of 43%. Horizontal filling.

7.5.8. Run 8

In this run the fibre lay-up orientation was varied through the thickness. The bottom two-thirds of the mould had fibres aligned parallel to the main flow direction whilst the top third had fibres aligned transverse to the flow. Five planes of sensing wires were used to monitor the flow with three ***X*** and three ***Y*** wires in each plane. However no results were recorded in plane 5 along the top end of the mould due to a technical fault. Figure 7.15 displays a schematic diagram showing the nodal positions within

the mould in a single plane. Figure 7.16 shows the shape of the flow front profile in each plane as it propagates through the mould. A flat flow front profile (left to right) is observed in all the five sensing planes. Generally the variation of the flow through the thickness is as expected with the flow front in the parallel regions ahead of the flow front in the transverse region. Planes 1 and 2 are within the parallel flow region. Plane 3 lies on the parallel/transverse flow border and planes 4 and 5 are within the transverse flow region. From Figure 7.16 we see that along the length of the mould the flow in planes 1 and 2 is ahead of the flow in planes 3, 4 and 5. We expect this trend because the resistance to the flow in the transverse region is higher than in the parallel region. Furthermore, the capillary or wicking flows that occur when the fibres are aligned parallel to the main flow direction accentuate this effect.

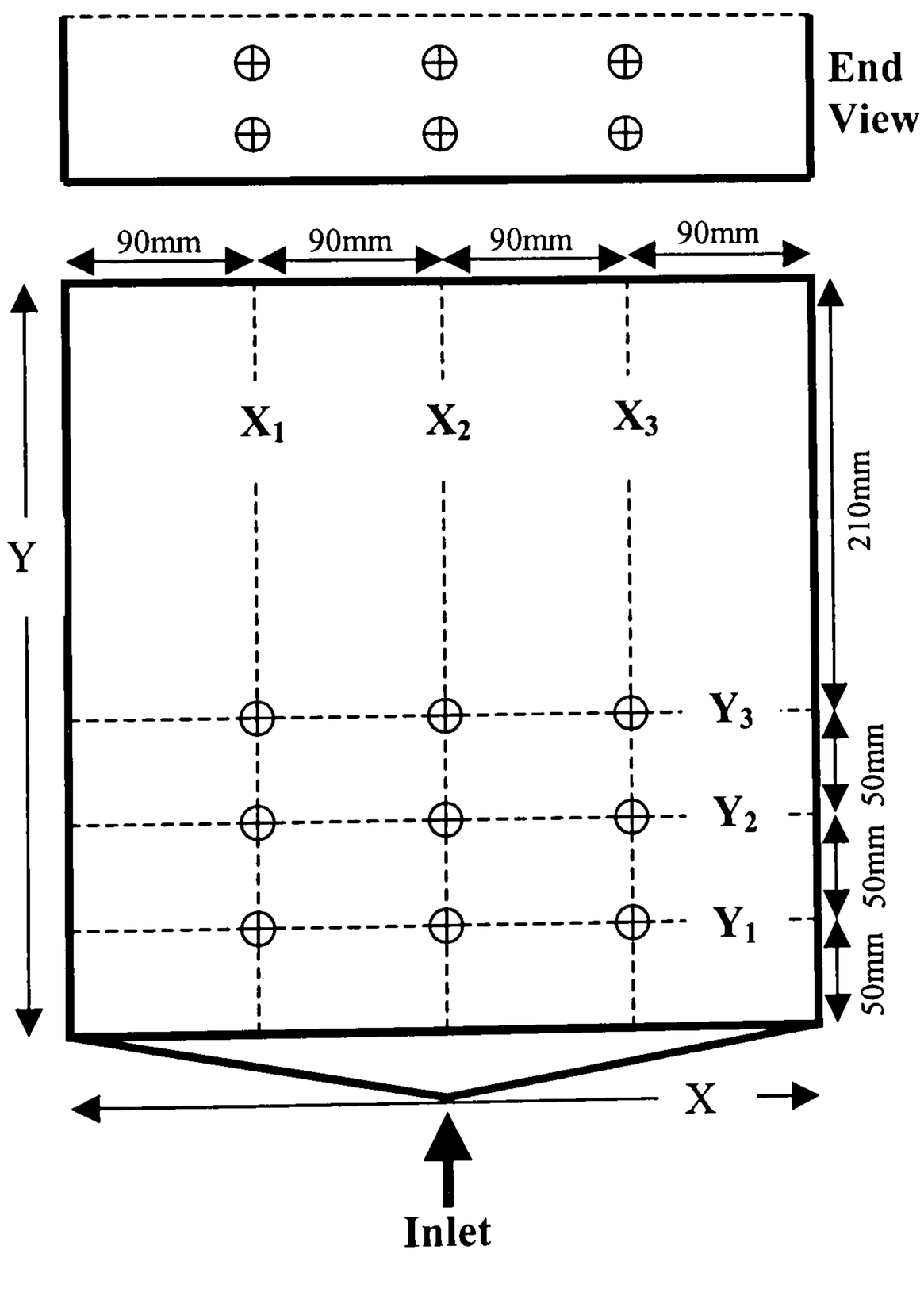


Figure 7.15 – Schematic diagram showing nodal positions within the mould for runs 8 and 9.

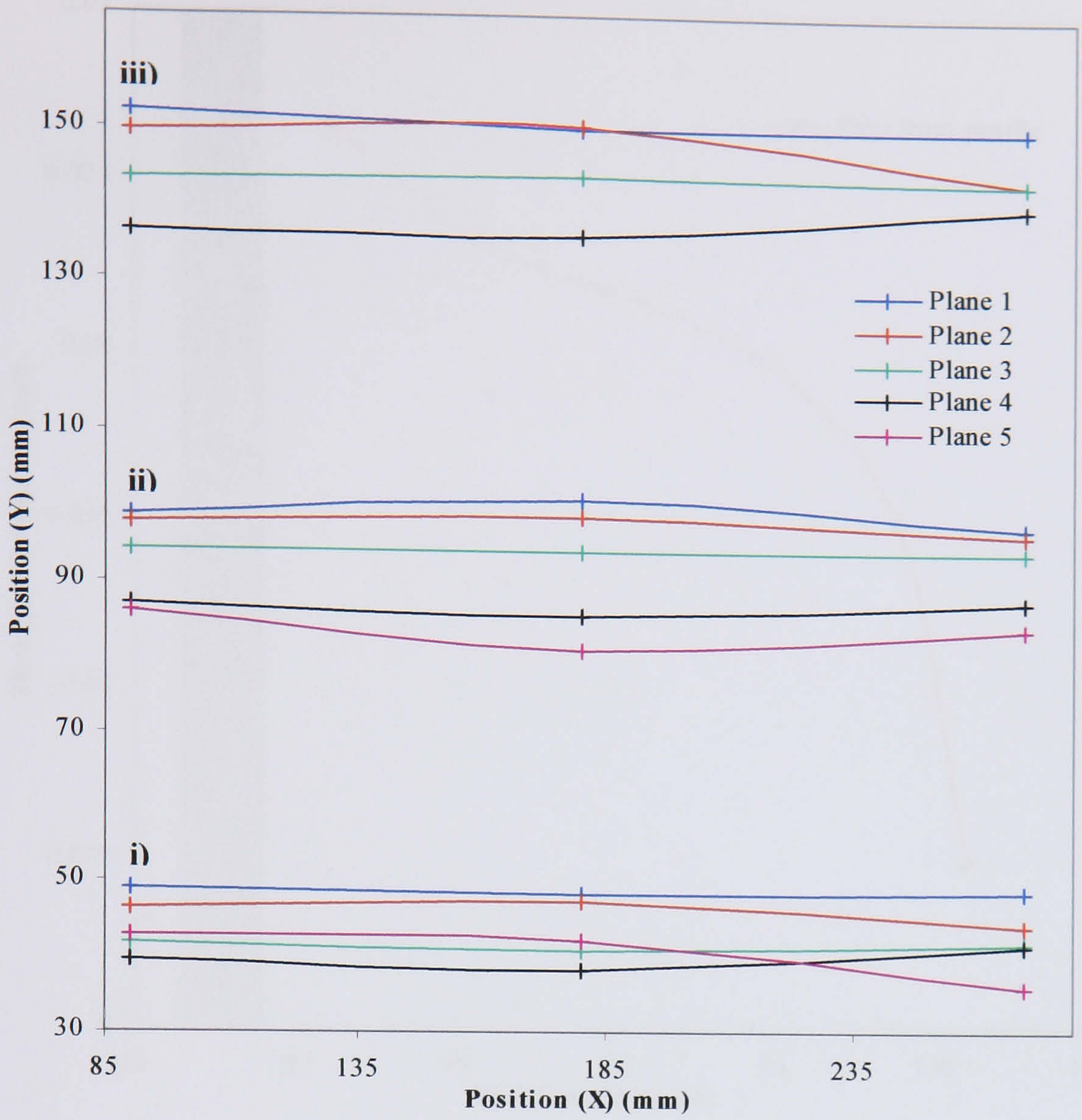


Figure 7.16 - Flow front profile for run 8. Interpolated times i) 85*s*, ii) 165*s* and iii) 255*s*. Fibre lay-up sequence of [0°, 0°, 90°] with a volume fraction of 43%. Vertical filling.

Figure 7.17 displays a cross-sectional view of the flow front through the thickness of the mould at X_2, Y_2. It is clearly observed that the flow front progresses faster in the region where the fibres are aligned parallel to the flow. Lower resistance to the flow (coupled with capillary effects) is largely responsible for this trend. However, the cross-sectional shape of the flow front does vary depending on the location within the mould. For example, Figure 7.18 shows a cross-sectional view of the flow front at X_2, Y_1. The shape of the flow front observed in this case is somewhat different from Figure 7.17, presumably due to slight local variations in fibre packing. However, the general trend is consistent with the flow propagating faster in the parallel flow regions than in the transverse flow regions.

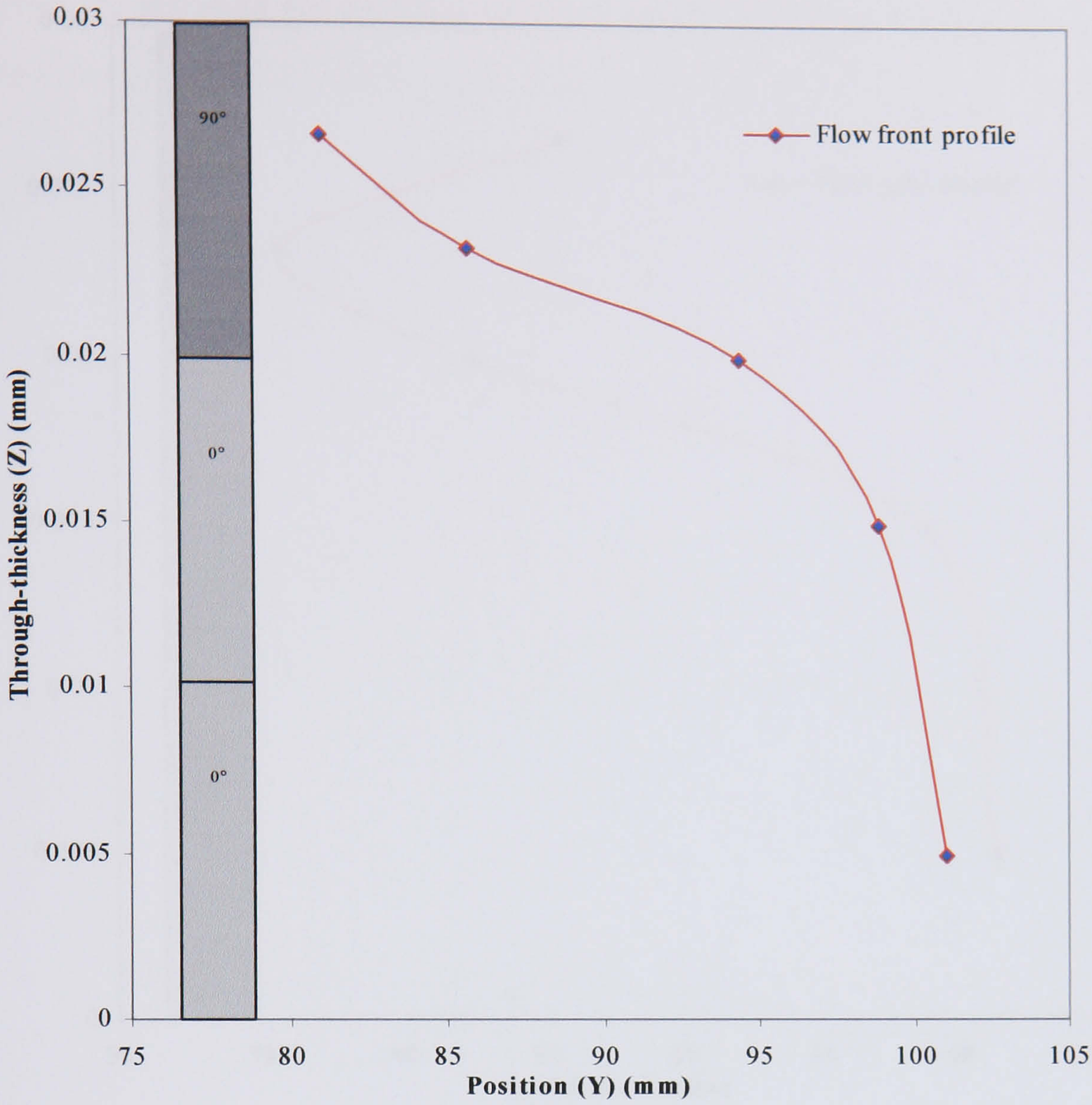


Figure 7.17 - Through-thickness front profile for run 8 at X_2, Y_2. Fibre lay-up sequence of [0°, 0°, 90°] with a volume fraction of 43%. Vertical filling.

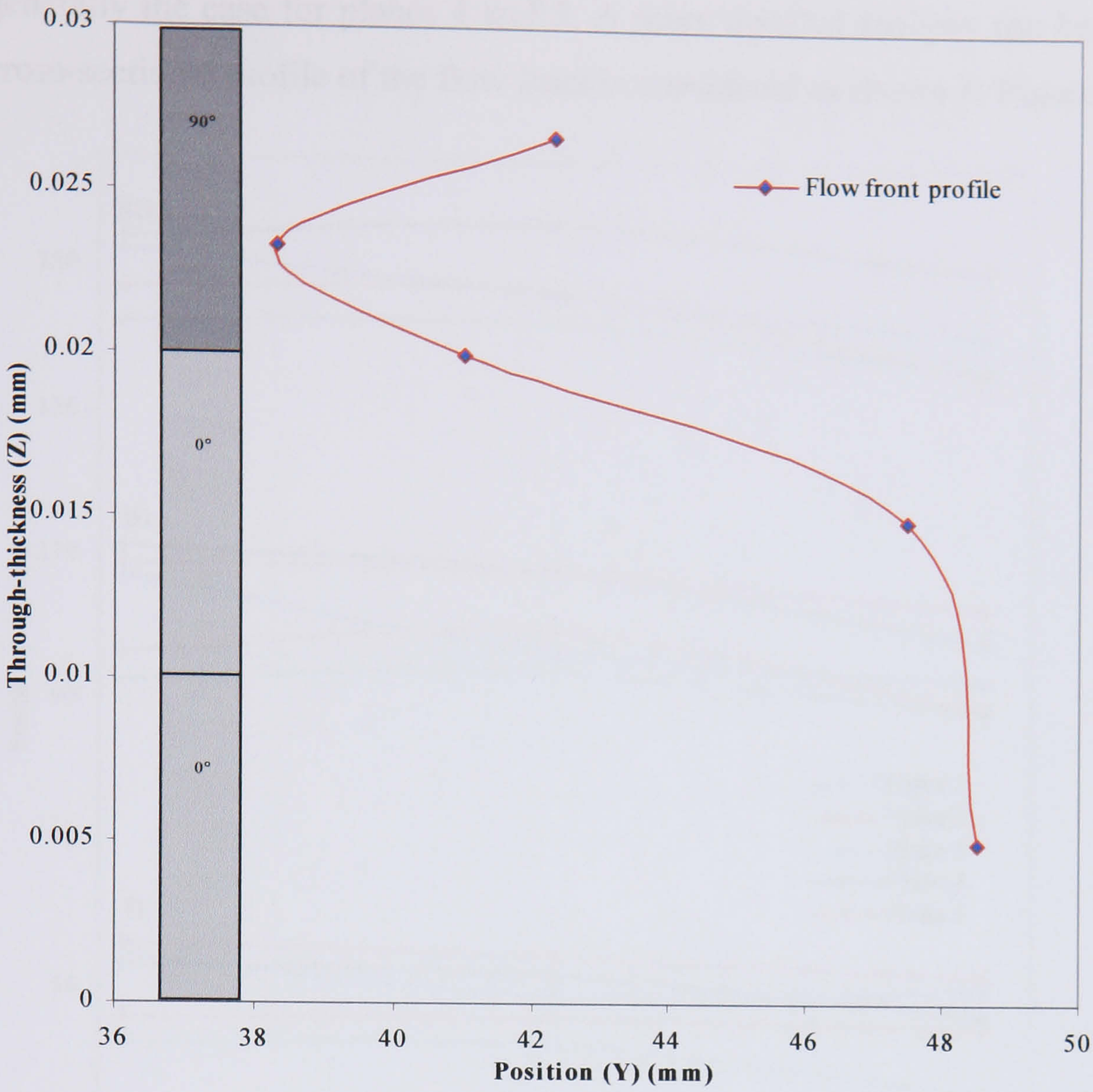


Figure 7.18 - Through-thickness front profile for run 8 at X_2, Y_1. Fibre lay-up sequence of [0°, 0°, 90°] with a volume fraction of 43%. Vertical filling.

7.5.9. Run 9

The fibre orientation was again varied through the thickness in run 9. The bottom third of the mould had fibres aligned along the flow direction, the middle third had fibres aligned transverse whilst the top third was longitudinal again. The location of the planes of the wires was the same as for run 8 shown in Figure 7.15. Due to a technical problem, plane 5 did not register a voltage along the top end of the mould. The transverse layers adjacent to the inlet deformed by approximately 5mm. Figure 7.19 shows the flow front profiles achieved. The flow front profile is observed to be quite flat with no severe race-tracking regions. In Figure 7.19 plane 1 is within the parallel flow region, plane 2 is within the transverse flow region, plane 3 is on the transverse/parallel region border and planes 4 and 5 are within the parallel flow region. Therefore we would expect the flow in planes 1, 4 and 5 to lead. This is

generally the case for planes 4 and 5. A more detailed analysis can be made when a cross-sectional profile of the flow front is considered as shown in Figure 7.20.

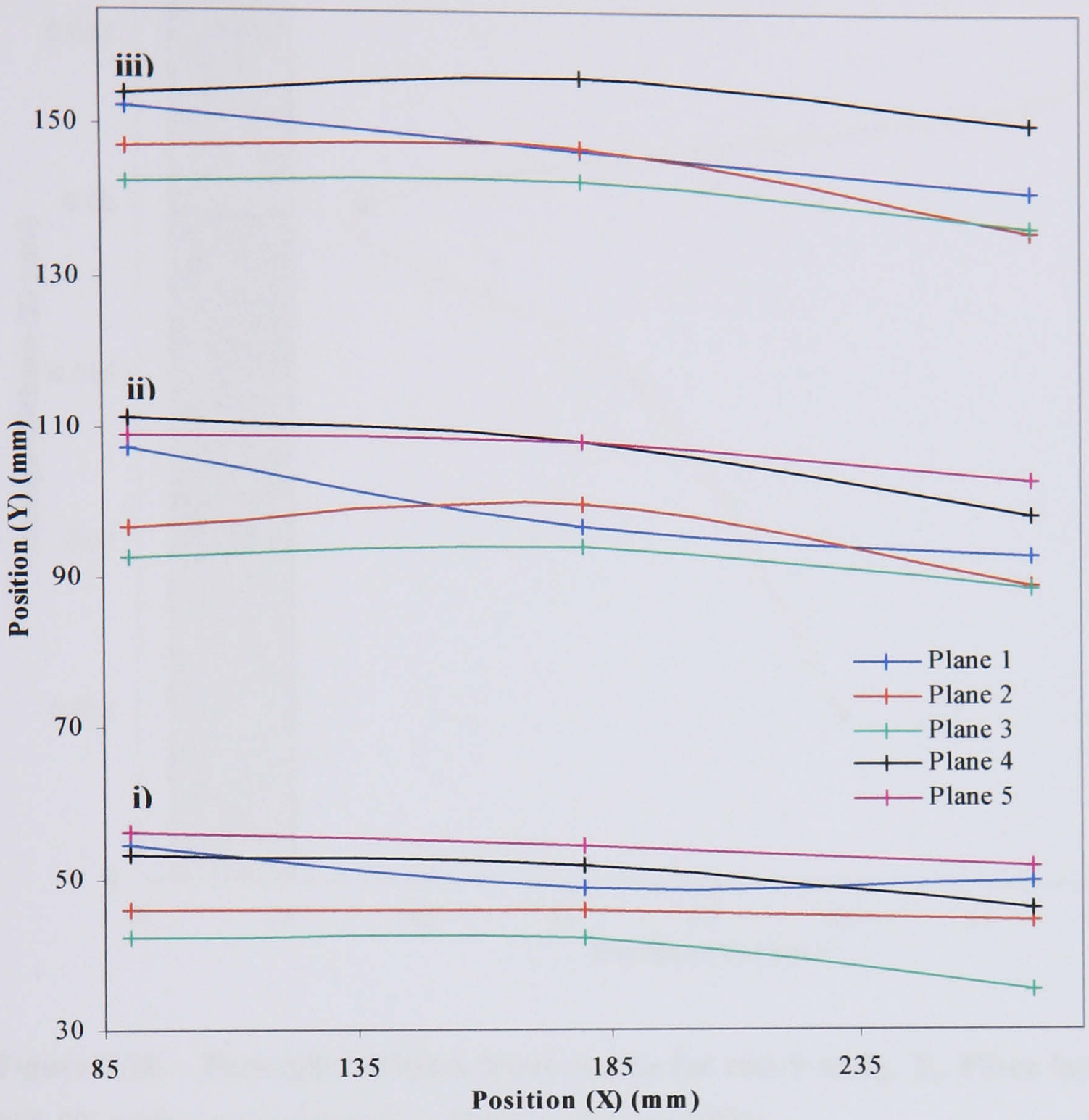


Figure 7.19 - Flow front profile for run 9. Interpolated times i) 60*s*, ii) 115*s* and iii) 175*s*. Fibre lay-up sequence of [0°, 90°, 0°] with a volume fraction of 43%. Vertical filling.

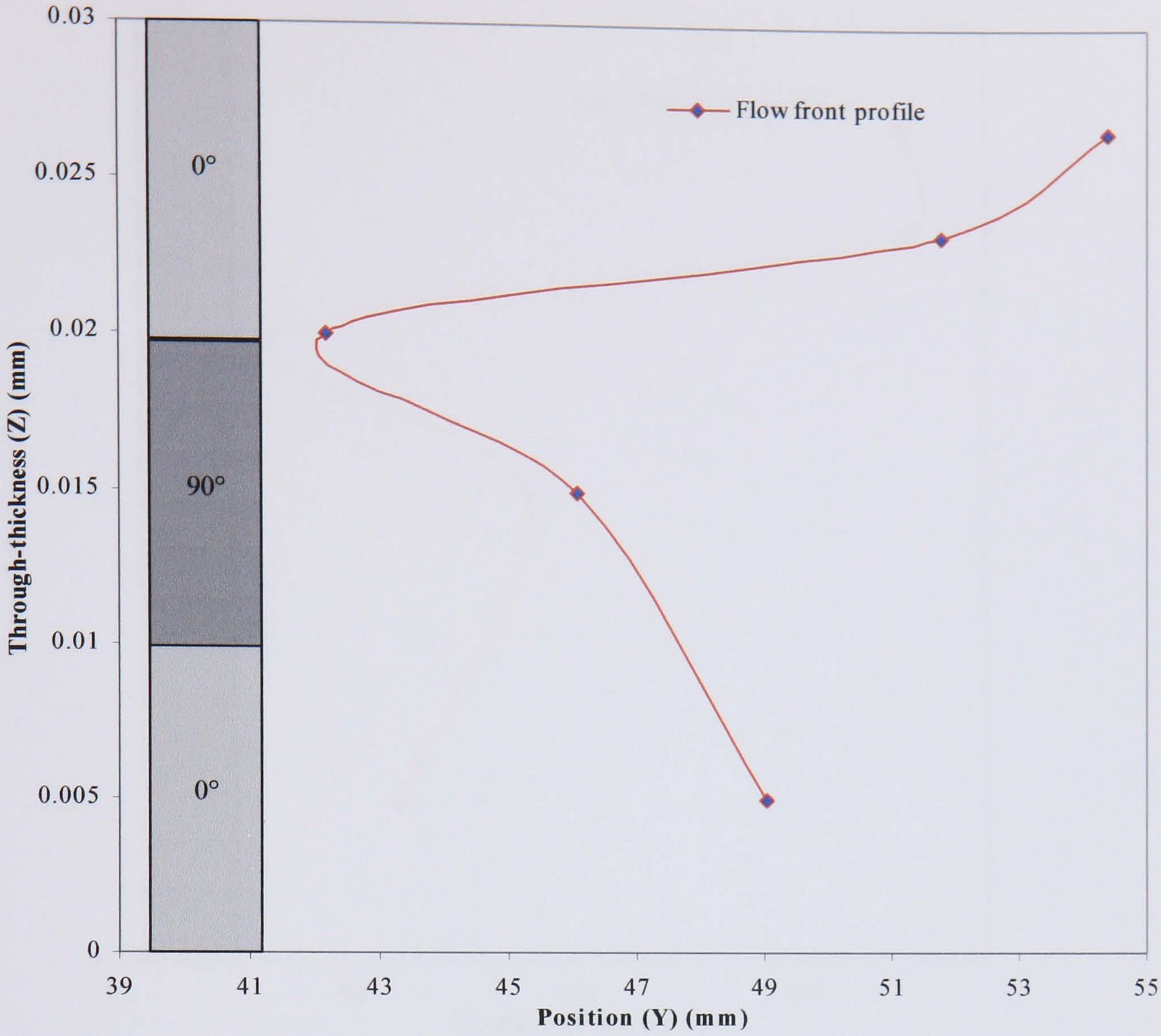


Figure 7.20 - Through-thickness front profile for run 9 at X_2, Y_1. Fibre lay-up sequence of [0°, 90°, 0°] with a volume fraction of 43%. Vertical filling.

From Figure 7.20 it is observed that the flow progresses faster in the parallel flow regions than in the transverse flow regions. In this case, the flow progresses most slowly on the transverse/parallel flow region interface. This could partly be due to the packing density in this region forming an area of higher resistance to the flow. Capillary effects are believed to contribute to the higher permeability in the parallel flow regions. However, along the transverse/parallel fibre interface, the transverse fibres may disrupt the capillary effects and hence decrease the permeability.

The cross-sectional profile of the flow front observed at a different location is shown in Figure 7.21.

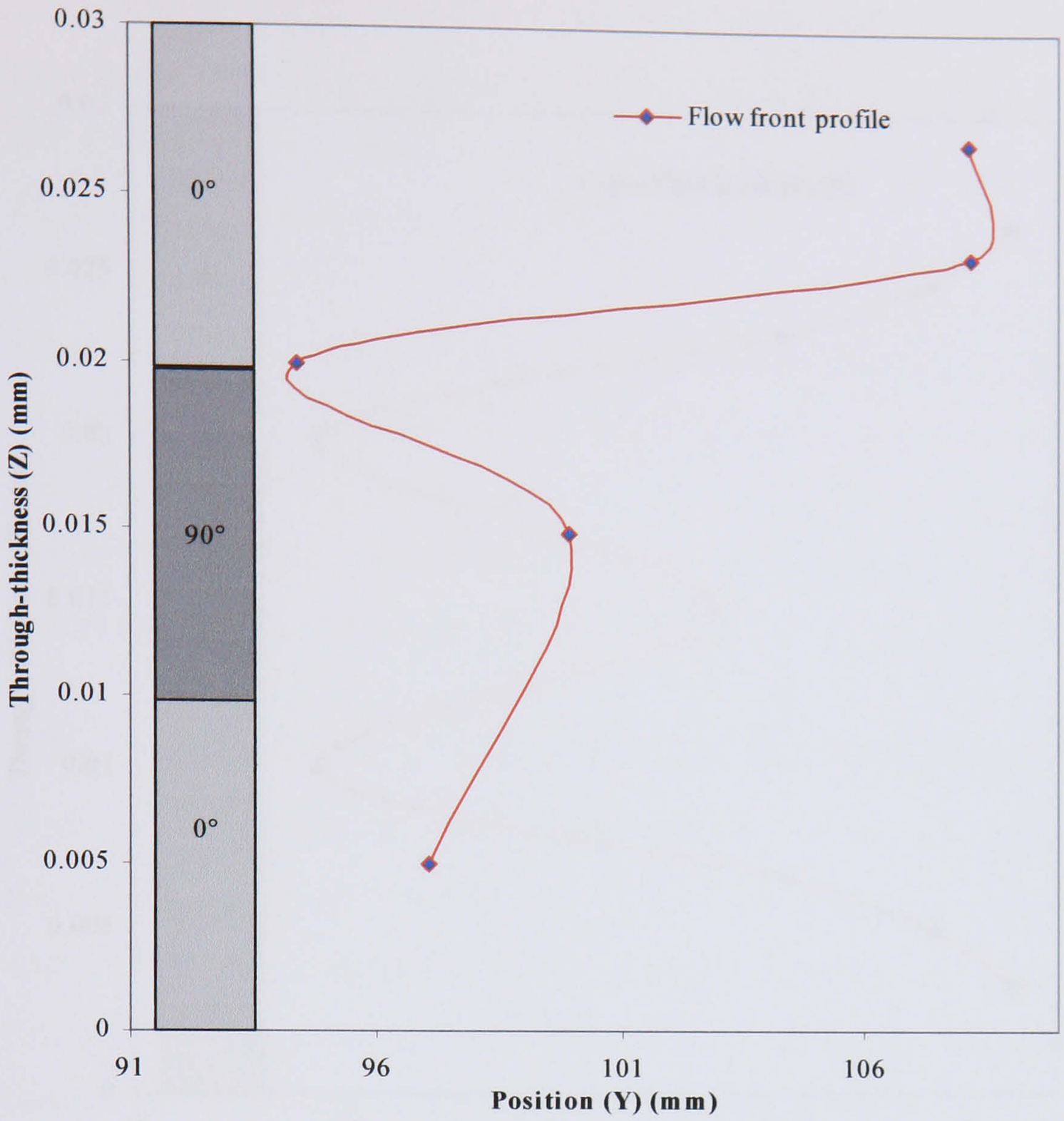


Figure 7.21 - Through-thickness front profile for run 9 at X_2, Y_2. Fibre lay-up sequence of [0°, 90°, 0°] with a volume fraction of 43%. Vertical filling.

Figure 7.21 shows the cross-sectional profile of the flow front at location X_2, Y_2. The flow front is observed to progress faster in the parallel flow region at the top of the mould. The flow progresses slowest on the transverse/parallel interface which is consistent with the results observed in Figure 7.20. However in this case the flow propagates more slowly than expected in the parallel flow region at the bottom of the mould. This trend is not global as in Figure 7.22 we see a profile that is more consistent with Figure 7.20. Slight variations in packing density or capillary flow effects could account for the profile observed in Figure 7.21.

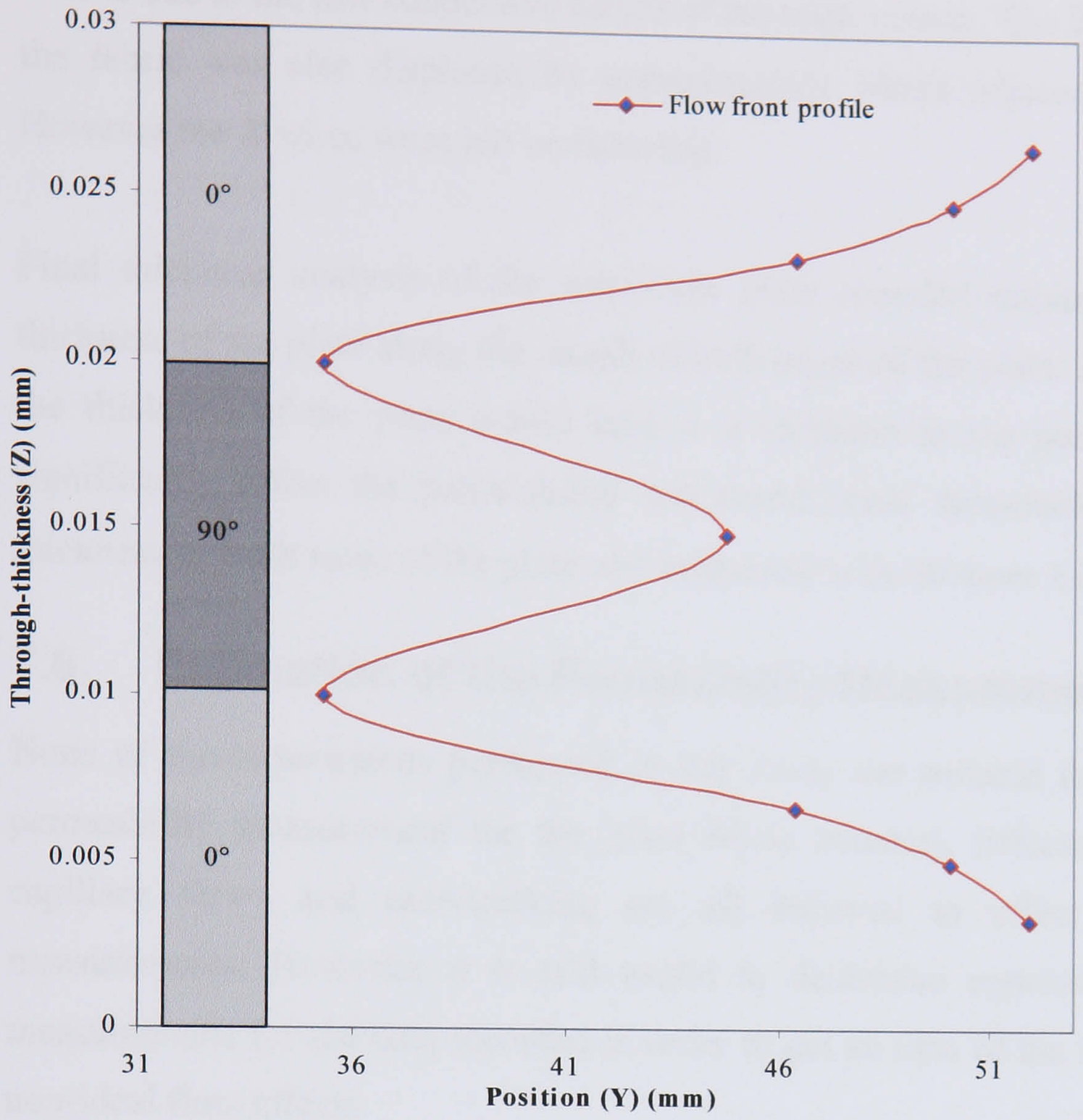


Figure 7.22 - Through-thickness front profile for run 9 at X_3, Y_1. Fibre lay-up sequence of [0°, 90°, 0°] with a volume fraction of 43%. Vertical filling.

The flow front profile in Figure 7.22 at X_3, Y_3 is more consistent with the observations drawn from Figure 7.20. The flow progresses faster in the parallel flow region where capillary flows play a significant role and the tortuousity is lower. The flow at the transverse/parallel flow interface propagates most slowly due to the dense packing conditions in this region, with the transverse fibres disrupting the capillary flows within the parallel region.

7.5.10. Run 10

In Run 10, the resin system Dow Derakane 411-C50 was used in place of the model fluid, corn syrup, to produce a composite plate for final analysis. The fibres were arranged transverse to the filling direction with a volume fraction of 49%. This filling was performed with the RTM tool set-up vertically. As expected, no voltage was

registered by the *SMARTweave* system at normal sensitivity and threshold values. This is due to the low conductive nature of the resin system. The ***Y*** wires distorted and the fabric was also displaced by approximately 10mm adjacent to the inlet port. However the ***X*** wires were left undisturbed.

Final thickness analysis of the composite plate revealed minimal variation in the thickness of the plate along the length of both edges of the plate. A small variation in the thickness of the plate would lead to a variation in the porosity which would significantly affect the permeability and could cause race-tracking. However, the thickness on both sides of the plate was measured to be $30.4mm \pm 0.5mm$.

7.6. Estimation of the Permeability Measurement

None of the experiments performed in this study are suitable for making accurate permeability measurement for the glass fabric material. Effects such as wicking, capillary flows and race-tracking are all believed to affect the permeability measurements. However, it is still useful to determine approximate permeability measurements for the data recorded in order to get an idea of the magnitude of these non-ideal flow effects.

The permeability measurement is estimated from experimental data by using Darcy's law, which can be expressed as:

$$U_i = -\frac{K_{ij}}{\eta}\frac{\partial P}{\partial x_j} \qquad [7.1]$$

where, U_i is the superficial velocity, K_{ij} is the Darcy permeability tensor of the porous medium, η is the dynamic viscosity and P is the pressure. To determine the permeability from experimental data [7.1] was rearranged in the form:

$$K = \frac{\eta \Delta x^2}{2\Delta P.\Delta t} \qquad [7.2]$$

A comparison of this experimental value of permeability is made with the permeability estimated by the Carman-Kozeny equation, which can be written as (for flow along the fibre direction):

$$K_x = \frac{r_f^2}{4k_x}\frac{(1-V_f)^3}{V_f^2} \qquad [7.3]$$

where K_x is the permeability in the fibre direction, r_f is the fibre radius, k_x (=0.4) is the Kozeny constant determined experimentally and V_f is the fibre volume fraction. For flow transverse to the fibre bundle, the same expression is used but the Kozeny constant is changed to k_z (=0.6) to match with experimental measurements[10]. In this case, the values of k_x and k_z used were taken from literature for similar experimental conditions[10].

This comparison was made for two of the runs that showed more uniform filling and the results are given in Table 7.2.

Table 7.2 – Comparison of experimentally determined permeability versus Carman-Kozeny prediction. Experimental permeability values are for the length of the mould along wire X_2.

Run	Fibre orientation	θ	V_f	Experimental Permeability (m^2) ±40%	Carman-Kozeny permeability (m^2)
2	[0°]	90°	0.49	1.7×10^{-9}	2.2×10^{-10}
5	[90°]	90°	0.43	5.5×10^{-10}	2.6×10^{-10}

From Table 7.2 it is seen that the experimentally determined permeability values are higher than those predicted by the Carman-Kozeny equation. This could be due to effects such as wicking and race-tracking during the impregnation process. Figures 7.23 and 7.24 display the permeability values between the sensor rows along the length of the mould at position X_2 for plane 2. Quite a large variation in permeability values (upto 200%) is observed at the different locations. This is evidence of the changes in porosity at different locations within the mould. There are numerous explanations for this occurrence such as variations in the fibre compaction at different locations due to changes in the clamping pressure or small variations in the orientation of the fibre lay-up.

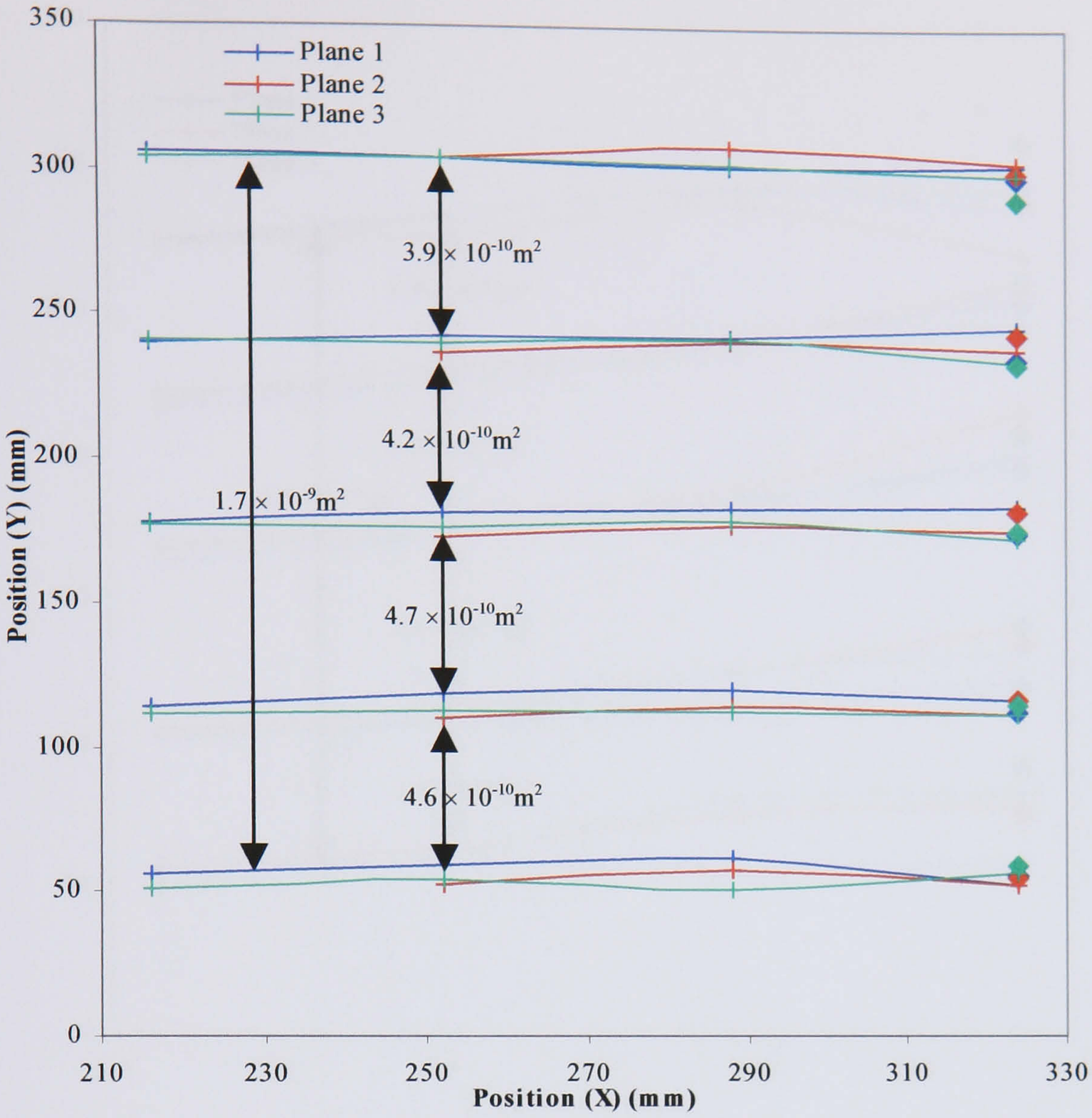


Figure 7.23 - Flow front profile for run 2 showing calculated permeability values along different lengths of the mould at X_3 in plane 2. Darcy's law was used in calculating the permeability. The Carman-Kozeny estimate of the permeability in this case is $2.2\times10^{-10}m^2$ with a Kozeny constant of 0.4. Parallel flow with a fibre volume fraction of 49%. Vertical filling.

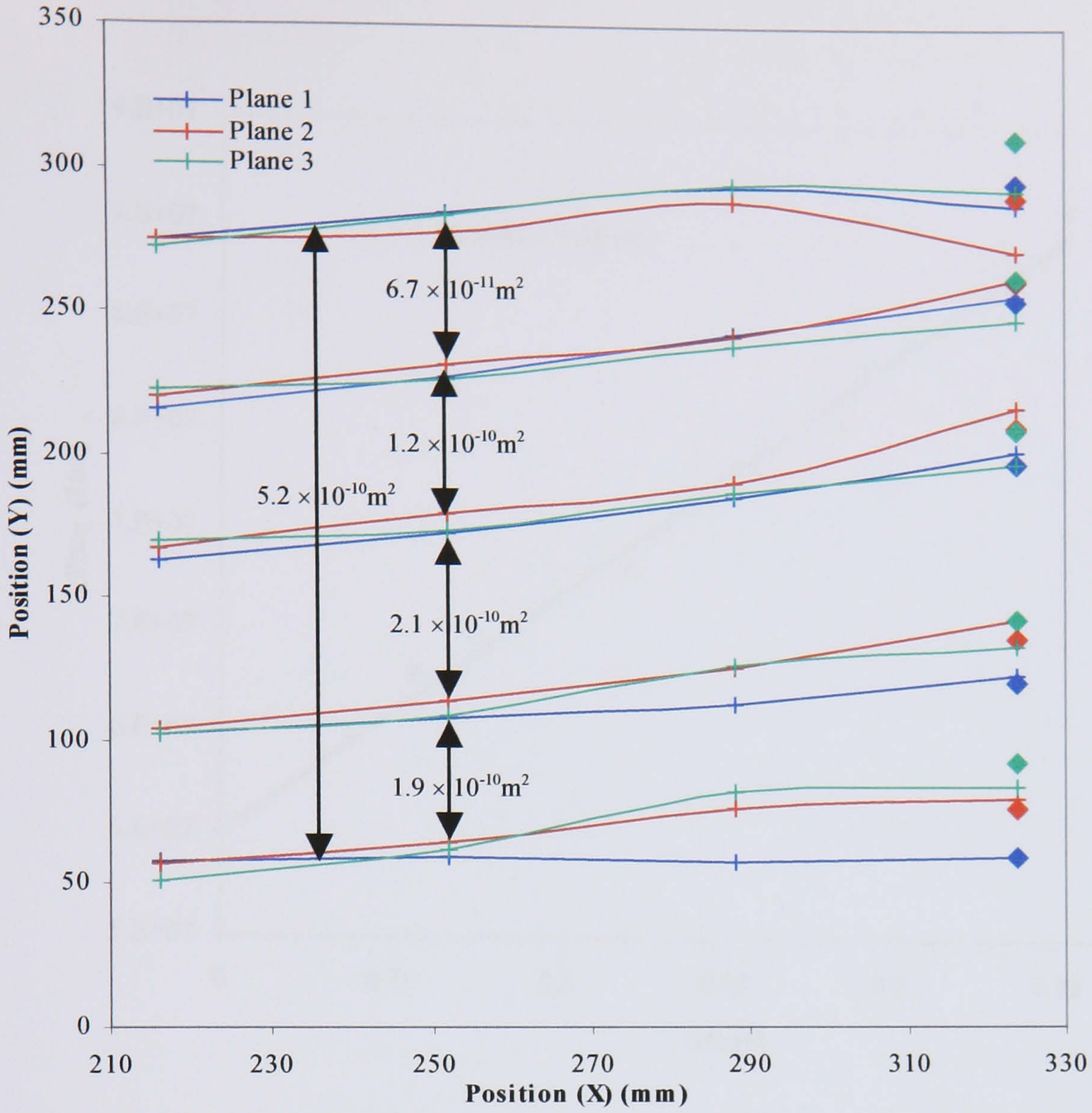


Figure 7.24 - Flow front profile for run 5 showing calculated permeability values along different lengths of the mould at X_3 in plane 2. Darcy's law was used in calculating the permeability. The Carman-Kozeny estimate of the permeability in this case is $2.6\times10^{-10}m^2$ with a Kozeny constant of 0.6. Transverse flow with a fibre volume fraction of 43%. Vertical filling.

The results presented in Figures 7.23 and 7.24 can be analysed in a slightly different manner by rearranging [7.2] and plotting $\Delta P/u\eta$ vs. Δx where ΔP is the measured pressure drop, u is the local velocity, η is the viscosity and Δx the filled length. This plot has a gradient equal to $1/2k$ where k is the permeability. Figures 7.25 and 7.26 display these results.

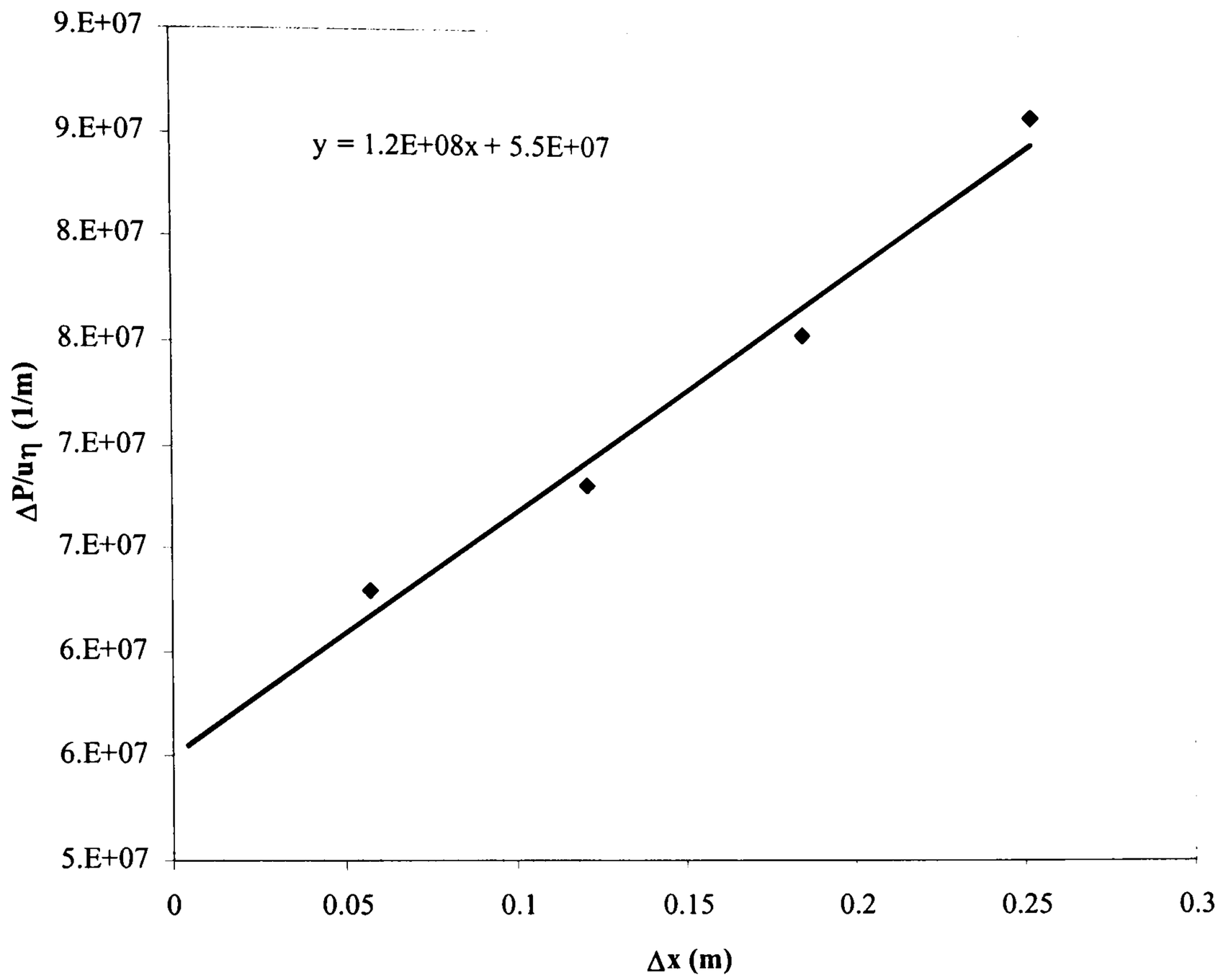


Figure 7.25 – Graph of $\Delta P/u\eta$ vs. Δx the filled length for run 2 for data at position X_3 in the mould and plane 2. ΔP is the measured pressure drop, u is the local velocity, η is the viscosity and Δx is the filled length. The slope of curve is equal to $1/2k$ where k is the permeability (refer to [7.2]).

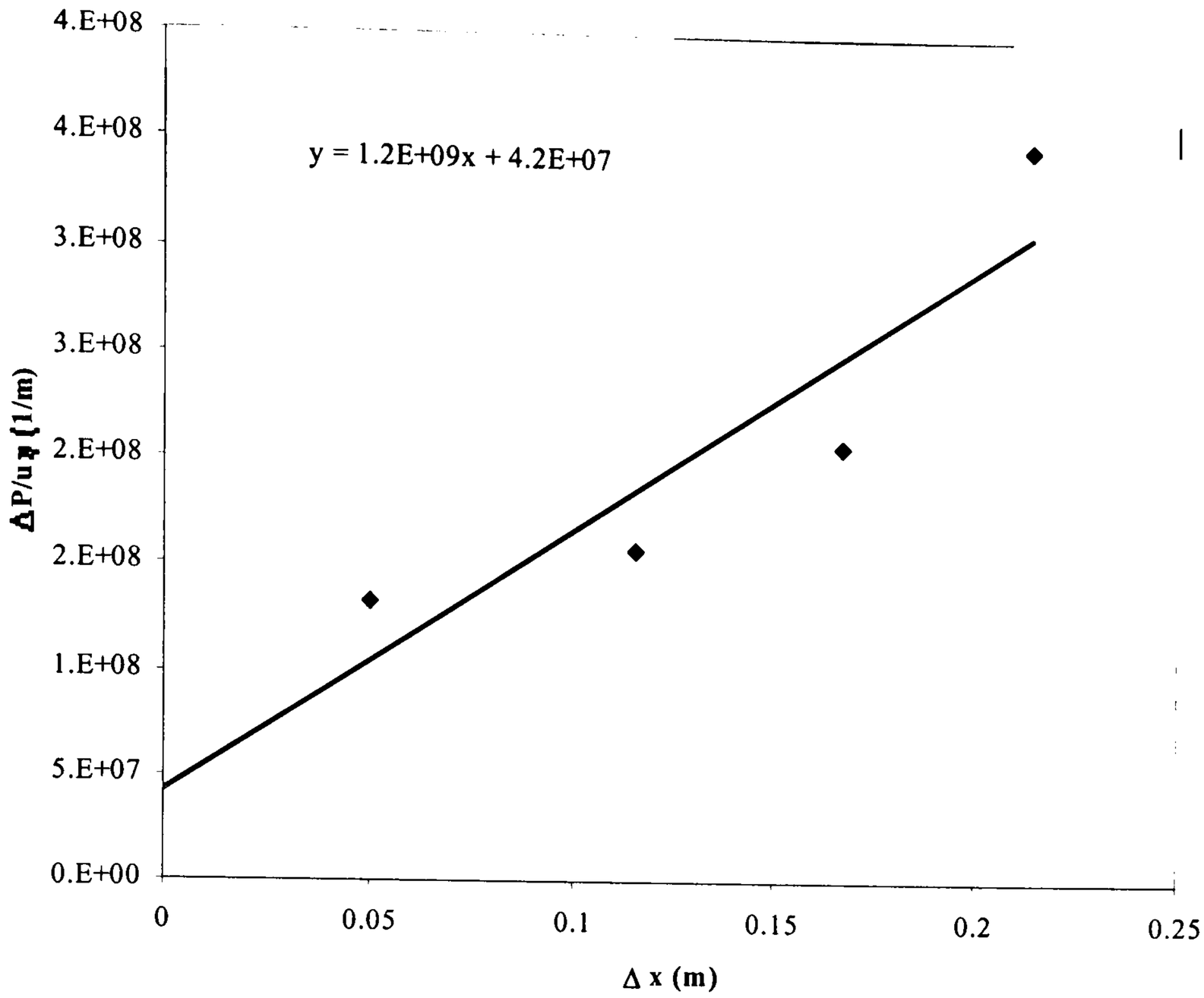


Figure 7.26 - Graph of $\Delta P/u\eta$ vs. Δx the filled length for run 5 for data at position X_3 in the mould and plane 2. ΔP is the measured pressure drop, u is the local velocity, η is the viscosity and Δx is the filled length. The slope of curve is equal to $1/2k$ where k is the permeability (refer to [7.2]).

The data for run 2 is more consistent than that of run 5 which is indicated by the better linear fit to the data in Figure 7.25 than in Figure 7.26. From these graphs the permeability in run 2 is estimated to be $4.2\times10^{-9}m^2$ and in run 5 $4.2\times10^{-10}m^2$.

7.7. Discussion

The fill pattern in thick composites has been presented and discussed in the sections above. In this section the effects of variations in the preform properties such as the fibre fraction and the direction of flow relative to the fibre alignment are discussed. Also the influence of the orientation of the tool (either horizontal or vertical) is assessed.

7.7.1. Effect of Variations in Preform Properties

The two main variations in preform properties considered were the fibre volume fraction and the fibre alignment. Firstly, considering the variation in the fibre volume fraction, runs 1, 2 and 3 which all incorporated parallel flow with vertical filling at fibre volume fractions of 0.43, 0.49 and 0.55 respectively can be compared. Comparison of these three runs highlights that as the fibre volume fraction increases, the variation in flow through the thickness decreases. Figure 7.27 shows the flow front profiles of runs 1 and 3 where it can be seen that the through-thickness variation in the flow front profile decreases with increasing fibre volume fraction. The same trend is also observed when runs 4, 5 and 6 are analysed. Runs 4, 5 and 6 incorporate transverse flow with vertical filling at fibre volume fractions of 0.43, 0.43 and 0.55 respectively. This decrease in variation of flow through-thickness when the fibre volume fraction increases is largely due to more uniform compaction at higher fibre volume fractions leading to a more consistent global porosity and hence less local variation in the permeability.

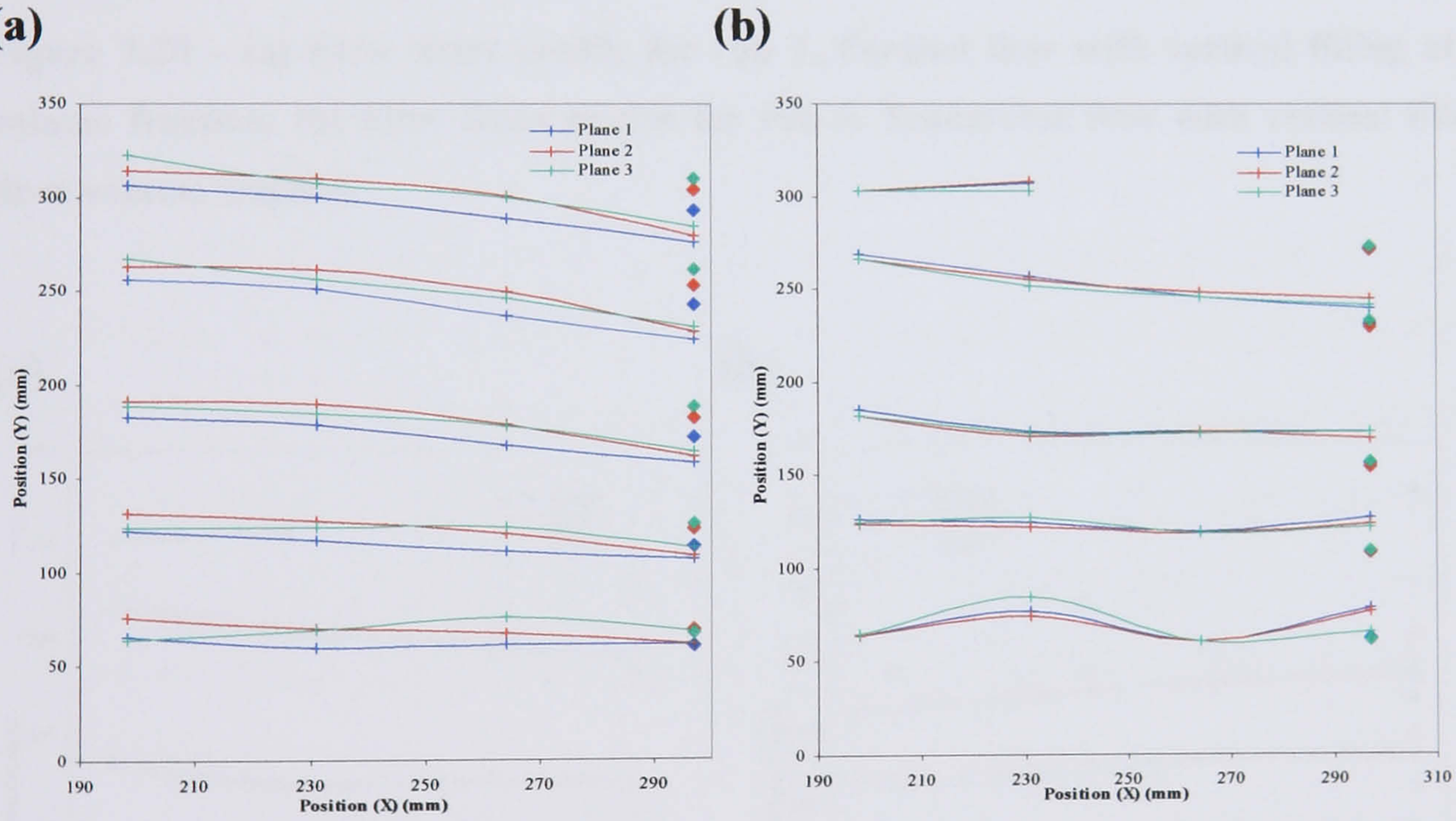


Figure 7.27 – (a) Flow front profile for run 1. Parallel flow with vertical filling at 43% fibre volume fraction. (b) Flow front profile for run 3. Parallel flow with vertical filling at 55% fibre volume fraction.

To determine the effects of the fibre orientation, a comparison is made of runs with a similar fibre volume fraction and tool orientation but different fibre alignment. For example runs 1 and 5 both incorporate vertical filling with fibre volume fraction of 43% but the fibre orientations are parallel and transverse respectively. For parallel flow the general shape of the flow front is observed to be convex in nature. However,

for transverse flow the shape of the flow front is concave. This can be seen in Figure 7.28. The same observation can be made by comparison of runs 3 and 6 which are both at a fibre volume fraction of 55% and for parallel and transverse flows respectively as seen in Figure 7.29.

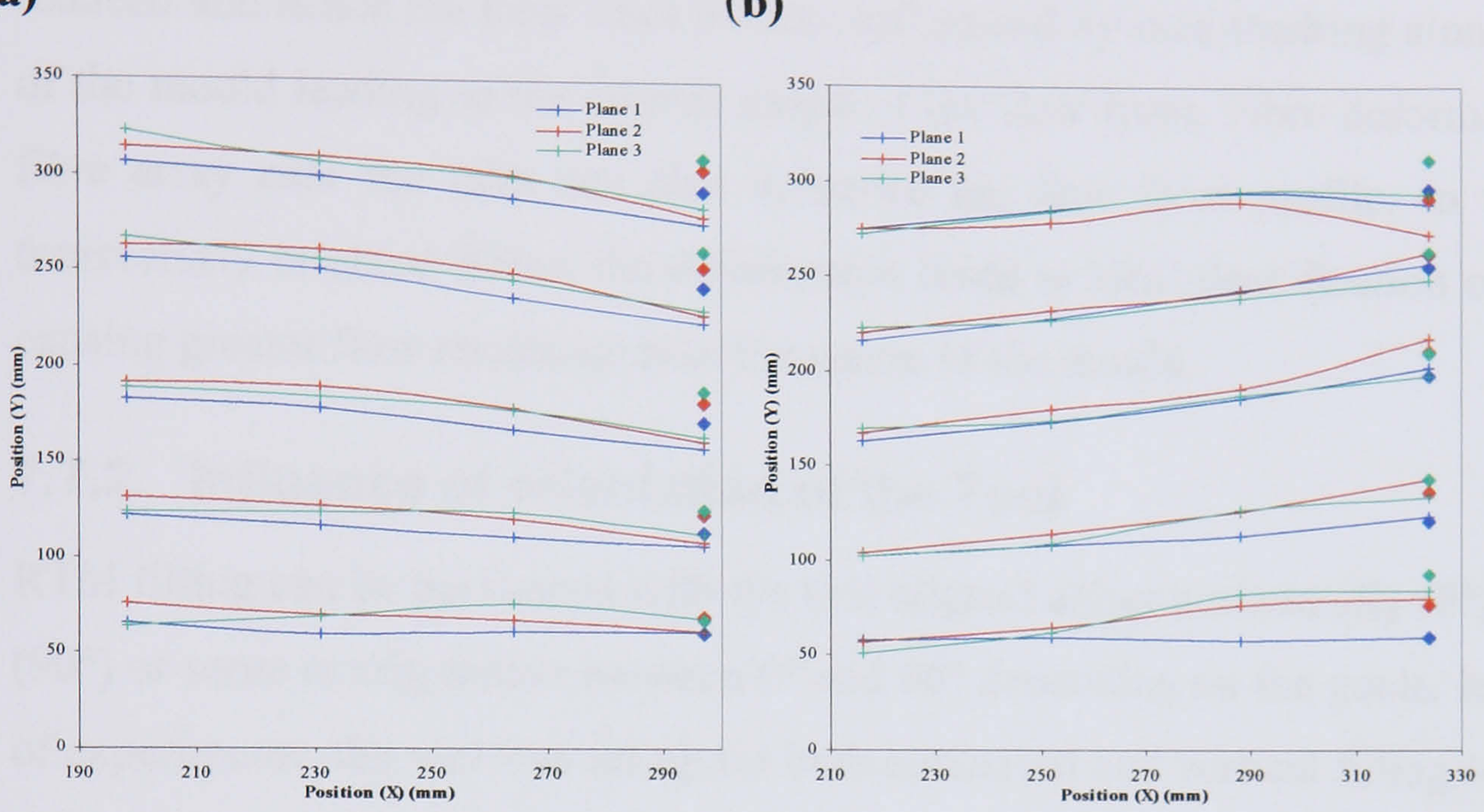


Figure 7.28 – (a) Flow front profile for run 1. Parallel flow with vertical filling at 43% fibre volume fraction. (b) Flow front profile for run 5. Transverse flow with vertical filling at 43% fibre volume fraction.

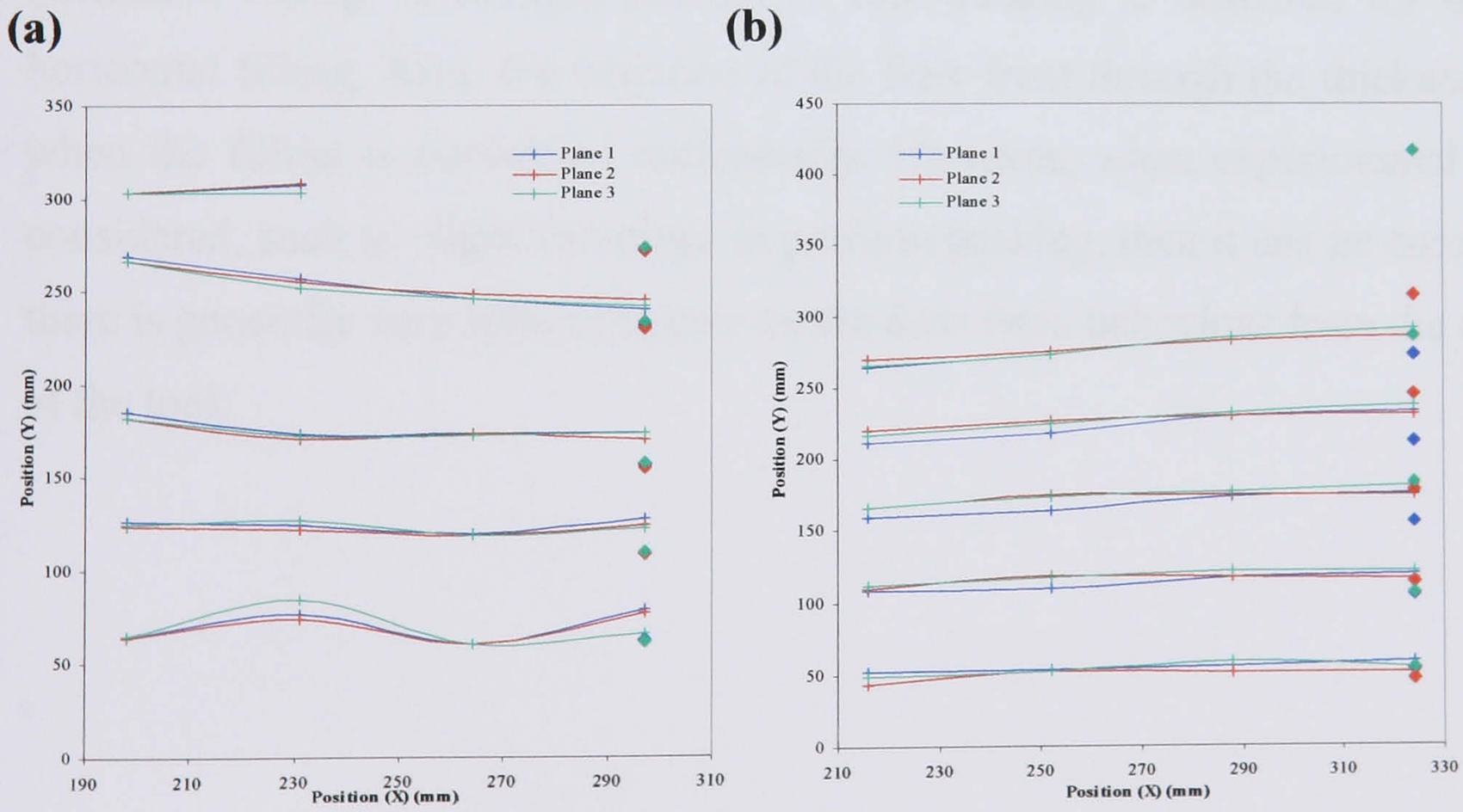


Figure 7.29 – (a) Flow front profile for run 3. Parallel flow with vertical filling at 55% fibre volume fraction. (b) Flow front profile for run 6. Transverse flow with vertical filling at 55% fibre volume fraction.

This trend in the shape of the flow front for the different flow configurations, parallel and transverse, is due to the different flow phenomena occurring in the different configurations. When the fibres are aligned parallel to the flow, the flow front profile is highly influenced by capillary flows within the fabric system. However, in the case of transverse flow, the capillary flows in the main flow direction are drastically reduced and hence the flow front is more influenced by race-tracking along the edges of the mould leading to the convex shape of the flow front. Fibre deformation of the fibre array near the inlet can also influence the flow front profile. In the case of transversely oriented fibres, the deformation leads to local densification of the array, causing greater flow resistance near the centre of the mould.

7.7.2. Influence of orientation of the Tool

RTM filling can be performed with the tool aligned either horizontally (0°), vertically (90°) or some configuration between 0° and 90° depending on the goals. In this series of experiments, the tool was set-up for both horizontal and vertical filling to study any effects of orientation on the filling behaviour.

Figure 7.30 shows the flow front profiles for runs 1 and 7. Both runs are for parallel flow at 46% fibre volume fraction but run 1 incorporates vertical filling and run 7 horizontal filling. A reduced amount of race-tracking is observed for the case of horizontal filling. Also, the variation of the flow front through the thickness is lower when the filling is performed horizontally. However, when experimental errors are considered, such as slight variations in preform packing, then it can be concluded that there is generally very little influence on the flow front behaviour from the orientation of the tool.

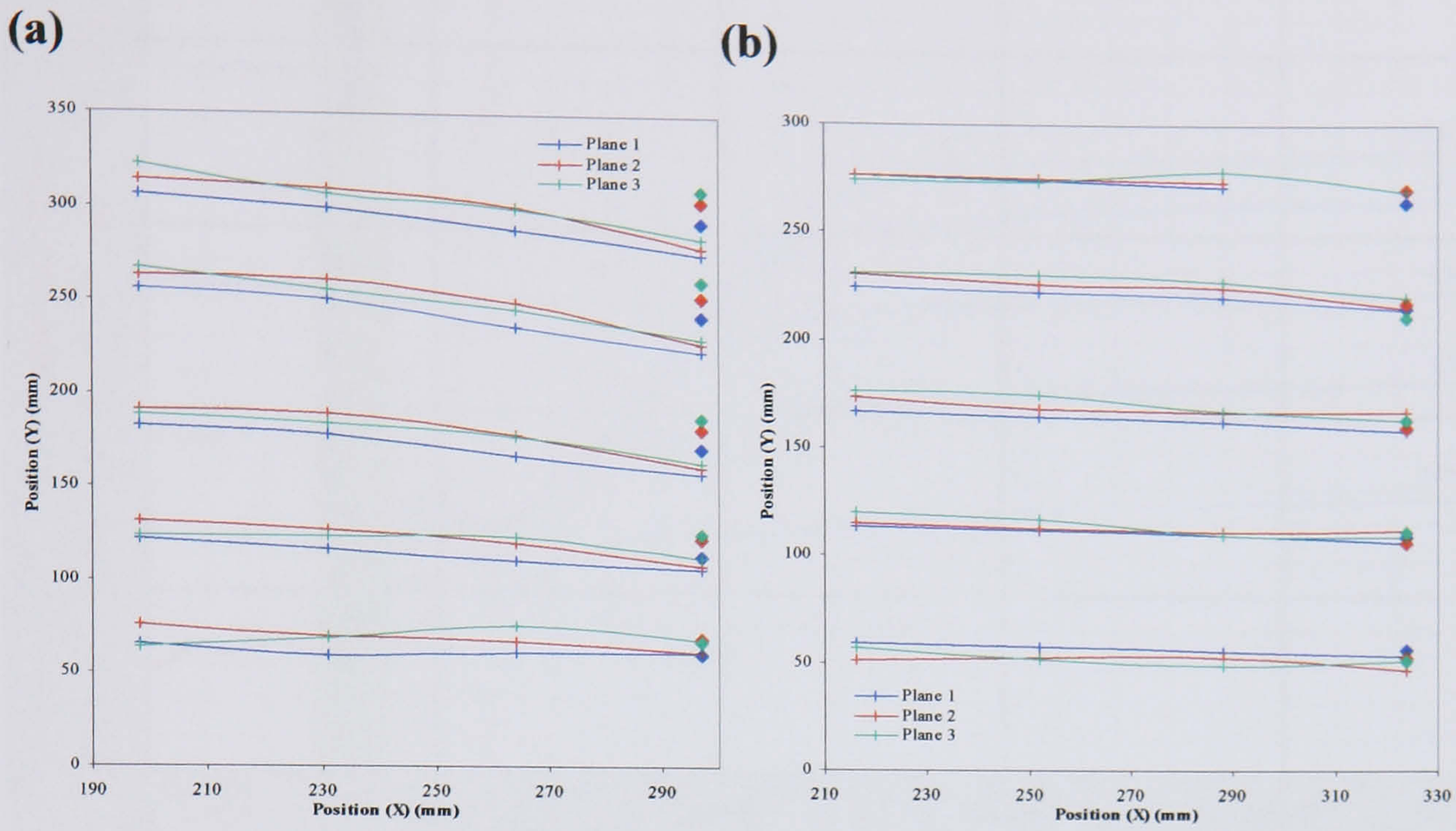


Figure 7.30 – (a) Flow front profile for run 1. Parallel flow with vertical filling at 43% fibre volume fraction. (b) Flow front profile for run 7. Parallel flow with horizontal filling at 43% fibre volume fraction.

7.8. Dielectric Cure Monitoring

The dielectric cure monitoring results obtained from the RTM experimental run are presented in Figure 7.31.

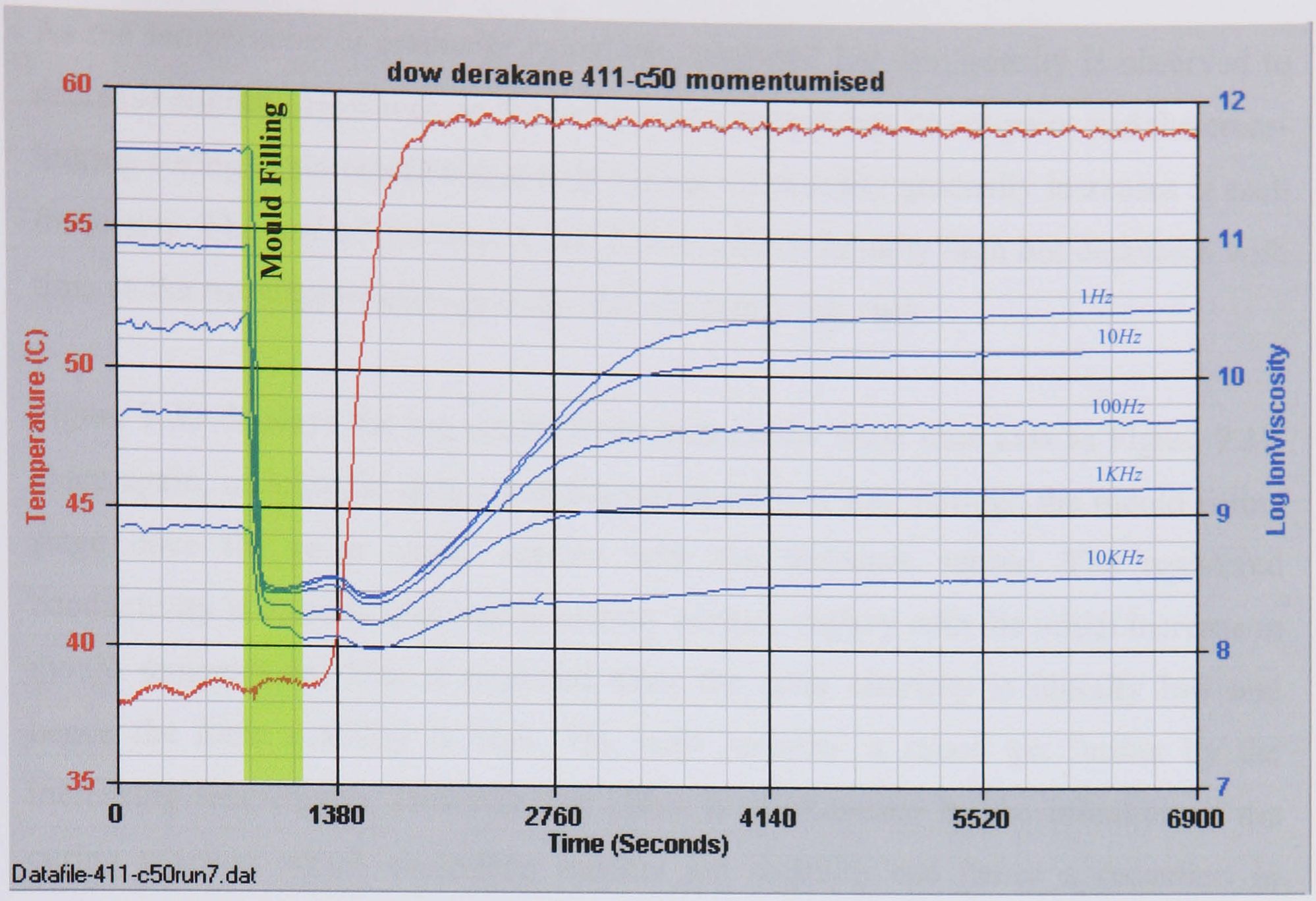


Figure 7.31 - Dielectric cure monitoring results obtained from the RTM experimental run showing the temperature and log ionviscosity curves. The green shaded area shows the duration of the mould filling stage. Each log ionviscosity curve corresponds to a different frequency (1Hz, 10Hz, 100Hz, 1kHz, 10kHz).

The mould filling was performed at 38°C, 1.5Bar and lasted approximately six minutes. Once the mould was completely saturated with resin the post injection pressure was set to 3Bar and the temperature to 59°C. The system was then held under these conditions for two hours. As can be seen in Figure 7.31, the temperature rose rapidly to 55°C over a period of about 10 min and then took a further 5 min to achieve the set value.

Figure 7.31 displays the log ionviscosity curves for each sampling frequency used. The log ionviscosity data prior to the mould filling process can be ignored since no contact had yet been made between the resin and the dielectric sensor. The sensor was positioned in the centre of the mould and close observation of Figure 7.31 shows that there is a change in the log ionviscosity measurement part way through the mould filling process when the fluid reaches the sensor.

As the temperature is gradually raised the measured log ionviscosity is observed to decrease slightly. However, as the temperature approaches its set-point and the cross-linking curing chain reaction proceeds the log ionviscosity gradually increases at each frequency. The rate of increase in log ionviscosity is initially high but decreases with time as the resin approaches gelation and ultimately full cure.

Figure 7.32 displays the log conductivity data on the same time axis as Figure 7.31. Once again, meaningful data are registered about half way through the mould filling stage once the resin makes contact with the dielectric sensor. The registered conductivity is initially high and is seen to increase slightly with the initial increase in mould temperature. This is expected since the resin viscosity is initially low and hence the ionic mobility is high. The ionic mobility is raised yet further by the increasing temperature. However this effect is counteracted by the initiation of the curing reaction which essentially hinders ion mobility and hence a reduction in conductivity is observed.

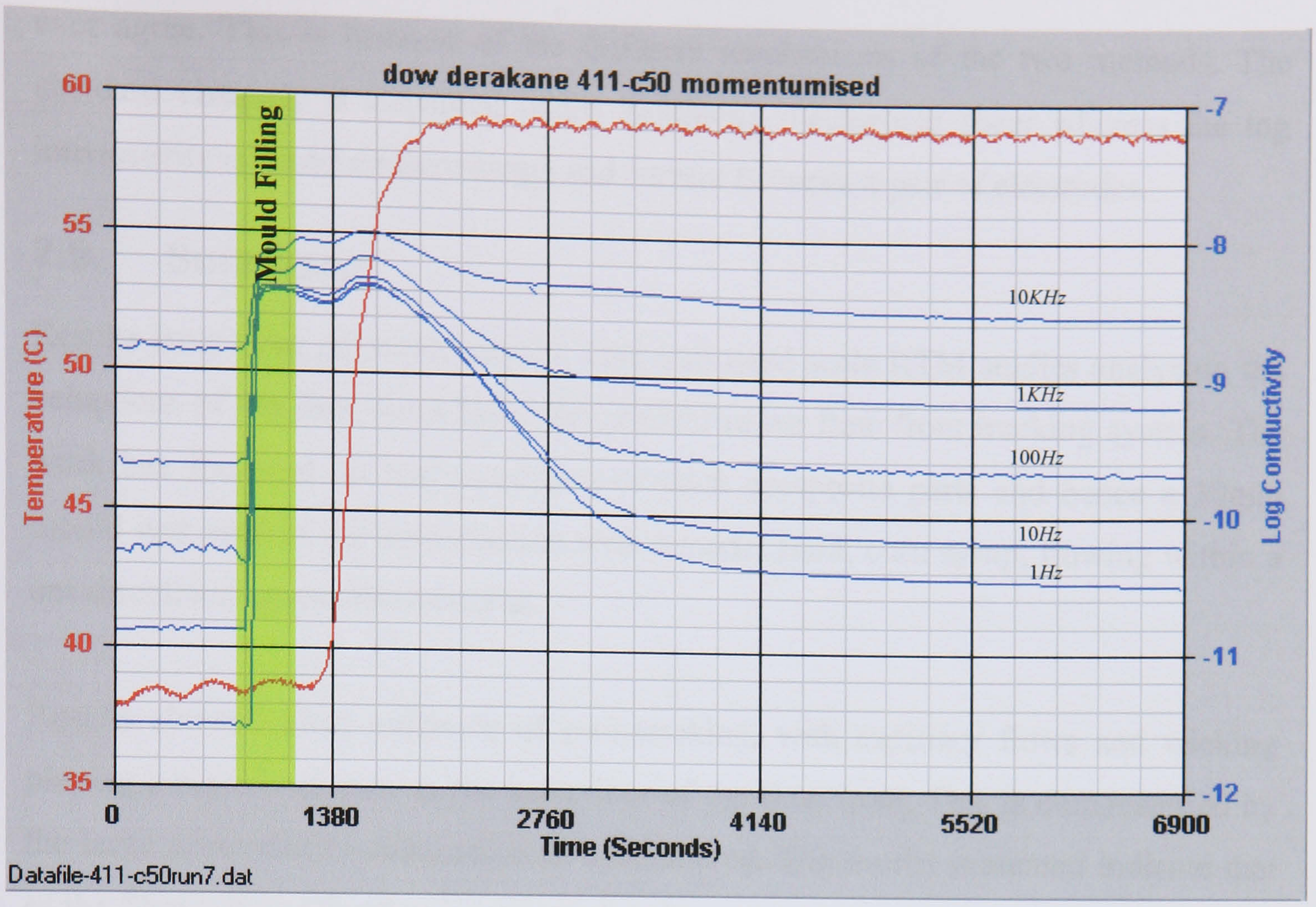


Figure 7.32 - Cure monitoring results showing the changes in resin Conductivity during the experiment at various frequencies (1Hz, 10Hz, 100Hz, 1kHz, 10kHz).

In order to apply the viscosity model presented in Chapter 4 to these results it is necessary to convert the log ionviscosity data to units of Pa.s. However, attempts to perform this operation failed to yield any consistent results. This suggests the need to perform in-situ conversion of log ionviscosity to units of Pa.s. The reason for this is that log ionviscosity measurements are based on a cure kinetics model and therefore follow a degree of cure curve i.e. a measure of the number of epoxide groups consumed, whereas the model presented in Chapter 4 models the viscosity curve itself. Consequently, a relationship between the extent of cure and the viscosity would be required in order to make a direct comparison of the two results.

The proposed viscosity model is optimised for operation in the low extent of cure range, which is of significance during the mould-filling stage in Resin Transfer Moulding. At high extents of cure, such as those achieved in the dielectric cure measurements, it is not envisaged that the model would give accurate results. Hence it is not possible to link the log ionviscosity data to the model presented in Chapter 4. Furthermore, it is not envisaged that the log ionviscosity and standard viscosity will

ever agree. This is because of the different mechanisms of the two methods. The standard viscosity is measured under oscillating mechanical shear whereas the log ionviscosity is based on the voltage and current between a pair of electrodes.

7.9. Summary

Results have been presented for the semi-industrial scale RTM studies analysing the behaviour of the flow front using the *SMARTweave* flow front tracking system. The work has focussed on the production of thick composite parts and hence a 30mm mould was used in the investigation with a model fluid, corn syrup, flowing within a uni-directional glass fibre material.

Results showed clear evidence of race-tracking, with capillary flows and wicking playing a significant role in the behaviour of the flow front. This is demonstrated by the large permeability measurements encountered. The results presented indicate that as the fibre volume fraction is increased an improvement is observed in the uniformity of the flow front in the through-thickness direction. This is largely due to better compaction at higher fibre volume fractions leading to a more consistent porosity and hence less local variation in the permeability. The results clearly demonstrate that the flow propagates faster in regions where the fibres are aligned parallel to the main flow direction than in regions where the fibres are transverse to the flow. However, the highest resistance to flow was observed at the transverse/parallel flow interface. This is believed to be due to the better compaction achieved and also the transverse fibres disrupting any capillary flows. The results also demonstrate that there is generally very little influence on the flow front behaviour from the orientation of the tool.

7.10. References

[1] Adams, K.L., Miller, B., and Rebenfeld, L., "Forced In-Plane Flow of an Epoxy Resin in Fibrous Networks", Polymer Eng. Sci., **26**(20), 1434-1441, (1986).

[2] Um, M. K., Lee, W. I., "A Study on the Mould Filling Process in Resin Transfer Moulding", Polym. Eng. Sci., **31**(11), 765-771, (1991).

[3] Bradley, J.E., Fink, B.K., Gillespie, J.W., "On-line Process Monitoring and Analysis of Large Thick Section Composite Parts Utilising *SMARTweave* In-Situ Sensing Technology", Proc. 43rd Int. SAMPE, 254-67, (1998).

[4] Skordos, A.A., Karkanas, P.I., Partridge, I.K., "A Dielectric Sensor for Measuring Flow in Resin Transfer Moulding", Meas. Sci. Technol., **11**, 25-31, (2000).

[5] Mathur, R., Advani, S.G., Parnas, R.S., Fink, B.K., "Evanescent Wave Fluorescence Fibre Optic Flow Sensor for Resin Transfer Moulding", Proc. Conf. 29th Soc. Adv. Mater. Proc. Eng., Covina, CA, (1997).

[6] Vaidya, U.K., Gillespie, J.W., "Assessment of Flow and Cure Monitoring using Direct Current and Alternating Current Sensing in Vacuum-assisted Resin Transfer Moulding", Smart. Mater. Struct., **9**, 727-736, (2000).

[7] Aukward, J., Warfield, R., "Monitoring Device for Investigation of Encapsulating Resins", Rev. Sci. Instrum., 413-414, (1956).

[8] Shepard, D., "A New Instrument for Monitoring the Resin Flow Front in RTM and other Resin Infusion Processes", Proc. 43rd Int. SAMPE, 1302-1309, (1998).

[9] England, K., "Direct Current Sensing of Viscosity and Degree of Cure of Vinylester", Tech. Rep. University of Delaware Centre for Composite Materials, (1997).

[10] Lam, R.C., Kardos, J.L., "The Permeability of Aligned and Cross-Plied Fibre Beds During Processing of Continuous Fibre Composites", Proc. American Society for Composites, Third Tech. Conf., Seattle, WA, 3-11, (1988).

8. CONCLUSIONS AND RECOMMENDATIONS FOR FUTURE WORK

8.1. Summary

The work presented in this thesis helps in providing a knowledge base to validate models of the RTM process. The ultimate objective is to (i) develop accurate simulation models that can be used for mould design applications and (ii) to develop control systems, based on real-time monitoring, that accurately ensure the manufacture of quality parts.

In developing any mould filling control system (or simulation tool) it is important to understand, amongst other things, (i) both the micro and macro flow parameters, (ii) to be able to accurately predict the velocity field in both saturating and saturated media and (iii) to be able to predict the change in viscosity of the resin with time during mould filling. A flow cell was constructed in order to physically model the micro-scale phenomena. A careful similarity analysis was performed to ensure a virtually two-dimensional flow field was obtained with a hexagonal arrangement of spherical rods and a volume fraction of 58%.

Comparison of experimental results of the velocity field in saturated media obtained using the flow cell with those generated by the numerical simulation model proposed

by Spelt et al.[1,2] showed reasonable agreement (within 60%) in the velocity field data. Generally the flow is observed to be of low magnitude in the boundary layer close to the cylinder surfaces and of highest magnitude in the central region of the unit cell. Reasonable agreement was also observed between the experimental and model results in the trajectory of the velocity vectors within the flow field.

The physical modelling for micro-scale filling around tows indicated that the contact angle between the cylinders and flow front decreases as the front progresses through the channel between the cylinders. The rate of decrease in contact angle is generally linear but changes after the front passes the narrowest region of the gap. The general shape of the flow front meniscus was concave. This was believed to be partly due to an electrostatic interaction between the fluid and the surface of the cylinders. A comparison was made between the physical model and a flow front tracking model proposed by Spelt et al.[1]. This revealed the need for the model to account for the dynamic contact angle between the flow front and the cylinders, and strong surface tension effects by lowering the value of the Capillary Number.

Rheological characterisation of the RTM resin systems LY5052/HY5052[i], LY564/HY2954[i], RTM6[ii], Derakane Momentum 411-C50[iii] and PR500[iv] highlighted the Newtonian behaviour of the uncured resin systems over an appreciable intermediate shear stress range. Estimates of applicable shear stress/shear rate values during RTM processing indicated that yield stress behaviour is not critical as this is only important at much lower values of shear rate (< 1/s). Elasticity was not dominant at relevant frequency values (1Hz) but was observed to become dominant at much higher frequencies (10Hz).

A non-parametric viscosity model was developed. It provides an important first step in developing predictive/analytical models and hence real-time monitoring of the viscosity and ultimately using this information for control systems. Furthermore, the model could be used to determine the processing window (for impregnation purposes)

---

[i] Manufactured by *Ciba-Geigy*, Macclesfield, Cheshire SK10 2NY, UK
[ii] Manufactured by *Hexcel Composites*, Duxford, Cambridge CB2 4QD, UK
[iii] Manufactured by *Dow Chemicals*, Kings Lynn, Norfolk PE30 2JD, UK
[iv] Manufactured by *3M*, Bracknell, Berkshire RG12 1JU, UK

and optimum processing temperature (based on viscosity) for each specific resin system/chemistry. The key advantage of this model is that it is not explicitly dependent upon the extent of cure. This is a general methodology that can be adapted to a range of curing kinetics (which depend on the chemical structure of the resin system), with an accuracy that can be increased depending on the order of the fitting equation used. The success of the model is governed to an extent by the selection of the functional forms of the uncured viscosity, $\eta_0(T)$, the rate constant, $k(T)$, the viscosity master curve, $f(\tau)$, and of their parameters. An advantage of the methodology proposed is that it gives the flexibility to choose optimal forms for these functions (the criterion of optimality being the existence of a master curve $f(\tau)$) which can be exploited for the modelling of the viscosity of different resin systems. Indeed the form of the viscosity master curve is strongly dependent upon the chemical structure of the polymer and the associated reaction kinetics. Since the rheology of the resin is so sensitive to the extent of reaction, the proposed methodology could be used to gain insight into the reaction kinetics in the early stages of cure, well before gelation has been achieved.

Semi-industrial scale RTM studies were performed, analysing the behaviour of the flow front using the *SMARTweave* flow front tracking system and showed clear evidence that race-tracking and capillary flows play a significant role in the behaviour of the flow front. This was further demonstrated by the high permeability measurements encountered. The results also indicated that as the fibre volume fraction was increased an improvement was observed in the through-thickness uniformity of the flow front. This was largely due to better compaction at higher fibre volume fractions leading to a more consistent porosity and hence less local variation in the permeability. The results also confirmed that there was generally very little influence on the flow front behaviour from the orientation of the tool with respect to gravity, for the conditions studied.

In conclusion, the semi-industrial scale studies reveal the need to understand both the macro scale phenomena, due to race-tracking, fabric deformation, dry-spot formation etc. and the micro scale aspects in the development of the flow front. Additionally, the early stages of resin cure and the concurrent increase in viscosity strongly influence

these processes. This thesis has addressed all these variables, from the large-scale experiments to the physical model of meso-scale parameters and provides an important tool for comparing and validating RTM simulation models or model-based process controllers.

8.2. Future Work

The following suggestions are recommended for the focus of future studies relating to the work presented in this field.

- The currently proposed cure model is only applicable at the low extent of cure range where the fluid is Newtonian. However, future studies could focus on applying the same methodology to develop a model for much higher extents of cure, where non-Newtonian effects become significant.
- The micro-scale experimental studies of the velocity field within a saturated medium in this work considered the flow across a hexagonal arrangement of cylindrical rods. Circular cylinders are a reasonable approximation, but tows are not likely to be this shape inside the mould. Reinforcement plies undergo compression when the mould is closed and this causes the cross-sections of the tows to form elliptical shapes rather than circular. Saunders et al.[3] investigated the effect of compression on the microstructure of fibre plain-woven cloths. Their studies showed that the tows approximated an elliptical shape. The width of these ellipses increased with increasing pressure and the height decreased, i.e. the ellipses became more elongated. To improve the accuracy of the computer simulations it is important to obtain the aspect ratios and spacing of the ellipses formed by the tows in order to produce realistic meshes. Therefore, a similar experimental investigation to that carried out in this work but which utilises elliptical rods as opposed to circular rods is recommended.
- An alternative technique to Particle Image Velocimetry (PIV) is proposed for the visualisation of the flow in a saturated medium for a more accurate representation of the velocity field. The Photochromic Dye Activation technique is a non-intrusive visualisation tool unlike PIV. The distinguishing factor between a photochromic dye and other types of dye is that some wavelength of light causes a change of colour in the dye, and that the reaction that occurs is reversible. Two dyes are proposed for use in future experiments, namely, Acid Violet 19 (Triarylmethane) which is an aqueous soluble dye and

1,3,3-trimethylindoline-6-nitrobenzospiropyran (spiropyran), shown in Figure 8.1, which is soluble in organic phases. However, the geometrical arrangement for flow visualisation is all-important. Curved boundaries and the mismatch of refractive indices can lead to a loss of information through image distortion. It is therefore critical that the refractive index of the solution under study matches that of the material from which the flow cell is constructed.

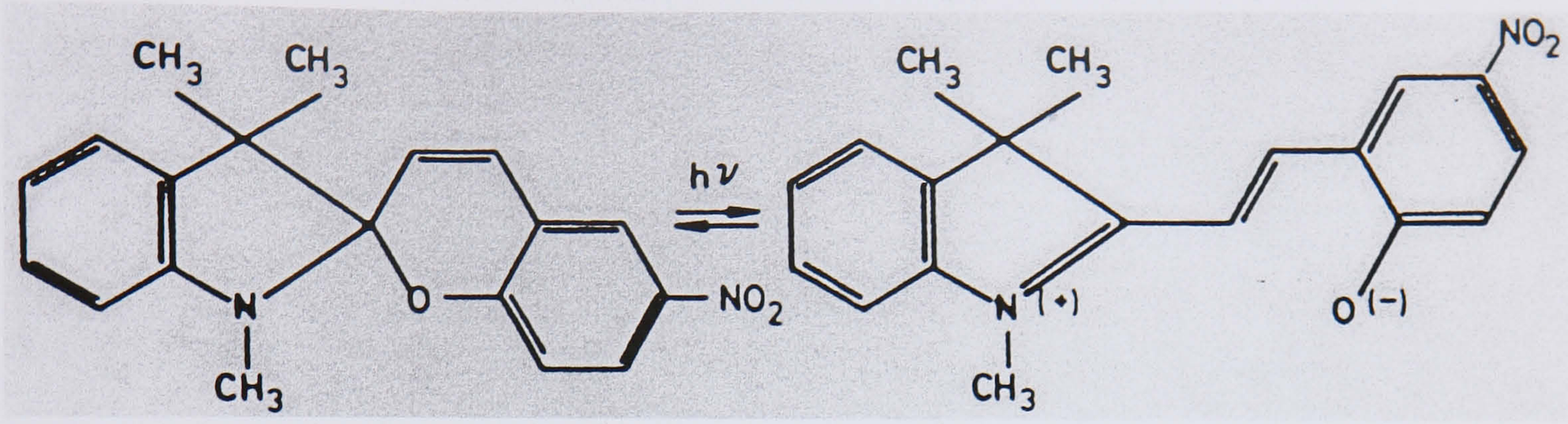


Figure 8.1 - 1,3,3-trimethylindoline-6-nitrobenzospiropyran (spiropyran)[4]

- The *SMARTweave* flow front monitoring experiments described in Chapter 7 utilised a uni-directional glass fibre material. This material provided the simplest flow geometry and hence was a good option to use for comparison of the experimental measurements with simulation results. However, it would be useful to consider experiments that utilise more complicated fabric systems, such as woven cloths. This would require fully three-dimensional micro simulations, both experimental and computational.

8.3. References

[1] Spelt, P.D.M., Selerland, T., Lee, P.D., Lawrence, C.J.L., Internal Report, Dept. of Materials, *Imperial College of Science, Technology and Medicine*, London, (2002).

[2] Spelt, P.D.M., Selerland, T., Lawrence, C.J., Lee, P.D., "Flow of Inelastic Non-Newtonian Fluids Through Arrays of Aligned Cylinders. Part 1. Creeping Flow", Submitted to Journal of Fluid Mechanics (2003).

[3] Saunders, R.A., Lekakou, C., Bader, M.G., "Compression in the Processing of Polymer Composites. Part 1: A Mechanical and Microstructural Study for Different Glass Fabrics and Resins", Comp. Sci. Tech., **59**, 983-993, (1999).

[4] Fogwell, T.W., Hope, C.B., "Water Soluble Photochromic Dyes for Flow Visualisation", AERE, (1987).

BI
LC
UNIV.